UNIVERSIDADE DO PORTO

Compensation of Fibre Impairments in Coherent Optical Systems

by

Luís Manuel de Sousa Pessoa

A thesis submitted in candidature for the
degree of Doctor of Philosophy

in the
Faculdade de Engenharia
Departamento de Engenharia Electrotécnica e de Computadores

September 2010

Thesis Identification

Title:	Compensation of Fibre Impairments in Coherent Optical Systems
Keywords:	Coherent Systems, Feedforward phase estimation, Wiener filtering, Kalman filtering, Parallel algorithms, OFDM, Back-propagation, Four Wave Mixing, Cross Phase Modulation
Start:	October 2006
Duration:	4 years
Candidate information:	
Name:	Luís Manuel de Sousa Pessoa
e-Mail:	luis.pessoa@fe.up.pt
Curriculum Vitae:	http://www.fe.up.pt/~dee06001/cv.pdf
Supervisor information:	
Name:	Henrique Manuel de Castro Faria Salgado
e-Mail:	hsalgado@fe.up.pt
Curriculum Vitae:	http://www.fe.up.pt/~hsalgado/cv.pdf
Co-supervisor information:	
Name:	Izzat Darwazeh
e-Mail:	i.darwazeh@ee.ucl.ac.uk
Curriculum Vitae:	http://www.ee.ucl.ac.uk/~idarwaze/cv.pdf
Educational Establishment:	Faculdade de Engenharia da Universidade do Porto
Research Institution:	Inesc Porto

Statement of Originality

The work presented in this thesis was carried out by the candidate. It has not been presented previously for any degree, nor is it at present under consideration by any other degree awarding body.

Candidate:

(Luís Manuel de Sousa Pessoa)

Advisor:

(Henrique Manuel de Castro Faria Salgado)

Statement of Availability

I hereby give consent for my thesis, if accepted, to be available for photocopying and for interlibrary loan, and for the title and summary to be made available to outside organizations.

Candidate: _____

(Luís Manuel de Sousa Pessoa)

"We shall not cease from exploration
And the end of all our exploring
Will be to arrive where we started
And know the place for the first time."

Four Quartets - Little Gidding, T.S. Eliot, 1942

Acknowledgements

I would like to thank to my supervisor, Prof. Henrique Salgado, for his continuous support, encouragement and availability, and also to my co-supervisor, Prof. Izzat Darwazeh, for his guidance and insightful comments.

I also acknowledge the support from João Oliveira and Mário Pereira for valuable discussions.

I acknowledge the support from FCT (Foundation for Science and Technology) for the PhD scholarship.

Finally, I am infinitely grateful to my wife, Anabela, for being a constant source of moral support.

Summary

Optical fiber backbone networks are increasingly demanding new ways of supporting the continuous growth in worldwide data traffic. In this context, a study on digital signal processing (DSP) techniques enabling the improvement of currently installed optical fiber systems, in terms of throughput and distance reach, becomes relevant. Coherent systems are seen today as a means of enabling the usage of complex modulation formats, increasing the spectral efficiency of transmission, and employment of advanced DSP functions that subsequently allow for the mitigation of impairments stemming from both the system optical sources (phase noise) as well as the transmission channel (noise, chromatic dispersion, polarization mode dispersion and nonlinearity).

This work discusses the main digital signal processing functions inherent to a coherent optical receiver, where the main focus is directed to the topics of equalization, carrier recovery and nonlinearity mitigation. The least mean squares (LMS) and constant modulus algorithm (CMA) equalizer functions are investigated, and their performance is assessed in terms of integration with carrier phase estimation algorithms. Thereby, the decision directed and the non-data-aided approaches are analyzed, and possibilities of configuration with equalization algorithms are evaluated. Although the speed of digital electronics is continuously increasing, it is still approximately one order of magnitude behind the speed of optical circuits and therefore it is relevant to study the issues associated with a parallel implementation of the discussed algorithms, in order to determine the restrictions and strategies that allow for an effective practical implementation.

The joint mitigation of both dispersion and nonlinear effects is critical in systems employing arbitrary dispersion maps. In this context, the back-propagation algorithm provides a means of partially solving this problem in the digital domain, allowing for an improvement of system performance. In fact, this document presents an analysis between both the performance and computational complexity requirements of the symmetric and asymmetric implementation of the back-propagation algorithm, as well as a study on optimum design options regarding the dispersion map characteristics.

Polarization multiplexed quadrature phase shift keying (PM-QPSK) and coherent optical orthogonal frequency division multiplexing (CO-OFDM) modulation formats are seen today as the main candidates for future optical networks. Moreover, their power efficiency should be maximized in order to minimize fiber nonlinearities. In this context, the performance of these modulation formats is also studied in terms of nonlinear tolerance, in order to investigate design issues regarding the compensation of these impairments. Moreover, an investigation concerning the compensation of nonlinear impairments for multi-band OFDM signals is presented, where the back-propagation algorithm through the total field and coupled field approaches is analyzed, and new simplified compensation schemes are proposed.

Sumário

As actuais redes de fibra óptica necessitam cada vez mais de novas estratégias para suportar o crescente tráfego de dados a nível mundial. Neste contexto, torna-se relevante um estudo sobre técnicas de processamento digital de sinal que permitam melhorar as actuais redes de fibra óptica, tanto em termos de débito máximo como em termos de distância máxima. Actualmente, os sistemas ópticos coerentes tornam possível a utilização de formatos avançados de modulação, o aumento da eficiência espectral da transmissão, bem como o uso de avançadas funções de processamento de sinal que permitem mitigar penalidades introduzidas pelas fontes ópticas (ruído de fase), bem como pelo canal de transmissão (ruído, dispersão cromática, dispersão modal de polarização e não-linearidades).

Este trabalho discute as principais funções de processamento digital de sinal inerentes a um receptor óptico coerente, onde são focados principalmente os aspectos de igualização, recuperação de portadora e compensação de não-linearidades. Os algoritmos de igualização dos mínimos quadrados médios ("LMS") e o algoritmo de módulo constante ("CMA") são investigados, e o seu desempenho é avaliado em termos de integração com algoritmos de estimação de fase da portadora. Assim, o algoritmo dirigido à decisão - *decision directed* - bem como o algoritmo não dirigido à decisão - *non-data-aided* - são analisados, e as possibilidades de configuração com algoritmos de igualização são avaliadas. Embora a velocidade de relógio dos circuitos electrónicos digitais esteja em constante crescimento, esta está ainda cerca de uma ordem de magnitude abaixo da velocidade dos circuitos ópticos, sendo por isso relevante estudar as implicações associadas a uma implementação em paralelo, dos algoritmos discutidos.

A compensação simultânea de efeitos não-lineares e dispersivos assume um papel crítico em sistemas que usam mapas de dispersão. Neste contexto, o algoritmo *back-propagation* resolve parcialmente este problema no domínio digital, permitindo melhorar o desempenho do sistema. Com efeito, este documento apresenta um estudo comparativo entre a abordagem simétrica e assimétrica de implementação do algoritmo *back-propagation*, ao nível do desempenho e complexidade computacional, bem como uma análise em termos de opções óptimas de projecto em relação aos mapas de dispersão. Os formatos de modulação "QPSK" multiplexado em polarização e multiplexagem por divisão ortogonal da frequência ("OFDM") em sistemas ópticos coerentes são actualmente vistos como os principais candidatos para as redes ópticas futuras. Assim, é fundamental maximizar a sua eficiência em potência, por forma a minimizar as não-linearidades na fibra. Neste contexto, o desempenho dos formatos de modulação referidos será estudado em termos de tolerância a não-linearidades. Adicionalmente, será apresentada uma investigação acerca da compensação de efeitos não-lineares em sinais "OFDM" multi-banda, onde o algoritmo *back-propagation* será considerado, através das abordagens de campo total e de campos acoplados, sendo proposto um novo esquema simplificado de compensação.

Contents

List of Figures

Abbreviations

AA	Anti-Aliasing
AC	Amplitude Correction
ADC	Analogue to Digital Conversion
ANDA	Alternative Non Decision Aided
ASE	Amplified Spontaneous Emission
ASIC	Application Specific Integrated Circuit
ASK	Amplitude Shift Keying
AWGN	Additive White Gaussian Noise
BER	Bit Error Rate
BP	Backward Propagation
BPSK	Binary Phase Shift Keying
CD	Chromatic Dispersion
CMA	Constant Modulus Algorithm
CO-OFDM	Coherent Optical Orthogonal Frequency Division Multiplexing
CP	Cyclic Prefix
CPE	Carrier Phase Estimation
CW	Continuous Wave
DAC	Digital to Analog Conversion
DCF	Dispersion Compensating Fiber
DD	Decision Directed
DFB	Distributed Feedback
DFT	Discrete Fourier Transform
DPSK	Differential Phase Shift Keying
DSP	Digital Signal Processing
EDFA	Erbium Doped Fiber Amplifier
EFC	Electric Field Component
E/O	Electrical to Optical conversion
FBG	Fiber Bragg Grating
FF	Feed-Forward
FFT	Fast Fourier Transform
FIR	Finite Impulse Response

FPGA	Field Programmable Gate Arrays
FSK	Frequency Shift Keying
FWM	Four Wave Mixing
GNSE	Generalized Nonlinear Schrödinger Equation
GVD	Group Velocity Dispersion
ICI	Inter-Carrier Interference
IFFT	Inverse Fast Fourier Transform
IIR	Infinite Impulse Response
IM/DD	Intensity Modulation / Directed Detection
IO-OFDM	Incoherent Optical Orthogonal Frequency Division Multiplexing
IQ	In-phase and Quadrature
ISI	Inter Symbolic Interference
LD	Laser Diode
LMS	Least Mean Squares
LO	Local Oscillator
LPF	Low Pass Filter
LUT	Look-Up-Table
LW	Line-Width
MB	Multi-Band
MMA	Multi-Modulus Algorithm
MSE	Mean Squared Error
MZI	Mach-Zehnder interferometer
MZM	Mach-Zehnder Modulator
NDA	Non Decision Aided
NLPN	Non-Linear Phase Noise
NLSE	Nonlinear Schrödinger Equation
NRD	Net Residual Dispersion
NRZ	Non Return-to-Zero
OA	Optical Amplifier
OBM	Orthogonal Band Multiplexing
O/E	Optical to Electrical conversion
OFDM	Orthogonal Frequency Division Multiplexing
OPLL	Optical Phase Locked Loop
OR	Oversampling Rate
OSNR	Optical Signal to Noise Ratio
PAPR	Peak-to-Average Power Ratio
PBC	Polarization Beam Combiner
PBS	Polarization Beam Splitter
PC	Polarization Controller
PD	Photodiode

PDM	Polarization Division Multiplexing
PMD	Polarization Mode Dispersion
PSK	Phase Shift Keying
QAM	Quadrature Amplitude Modulation
QPSK	Quadrature Phase Shift Keying
RDPS	Residual Dispersion Per Span
RF	Radio Frequency
RIN	Relative Intensity Noise
RLS	Recursive Least Squares
ROADM	Reconfigurable Optical Add/Drop Multiplexer
RZ	Return-to-Zero
SC	Single Channel
SMF	Single Mode Fiber
SNR	Signal to Noise Ratio
SOP	State Of Polarization
SPM	Self-Phase Modulation
SSB	Single Side Band
SSFM	Split-Step Fourier Method
TI	Time Interleaved
UWB	Ultra Wide Band
WDM	Wavelength Division Multiplexing
XPM	Cross-Phase Modulation

Symbols

a_s	Magnitude of the transmitted signal electric field
$a(t)$	Anti-alias filter impulse response
$a_e(t)$	Magnitude of the information complex envelope
$a_{lo}(t)$	Magnitude of the local oscillator electric field
A_{eff}	Fiber effective core area
A	One-dimensional amplitude of the transmitted constellation points
$A(z,t)$	Electric field of pulse envelope propagating on the optical fiber
$B_n(\omega)$	Birefringence matrix of n-th segment of fiber
c	Speed of light in vacuum
C	Total number of computations of algorithm
d_k	Training sequence for LMS equalizer
D	Dispersion parameter
$\hat{D}$	Differential operator accounting for dispersion and attenuation
D_{PMD}	Polarization mode dispersion coefficient of the optical fiber
e_k	Error signal used to adapt equalizer coefficients
E	Electric field, expected value of a random variable
$E(z,t)$	Electric field of pulse envelope, in back-propagation
$\tilde{E}(z,t)$	Estimated electric field of pulse envelope, in back-propagation
E_b	Average bit energy in a single carrier signal
E_i	Electric field of the optical signal at the output of a device
E_{LO}	Electric field of the local oscillator optical carrier at the receiver local oscillator port
E_o	Electric field of the optical signal at the output of a device
E_{out}	Electric field of the optical signal at the output of an optical hybrid
E_s	Average symbol energy in a single carrier signal
$E_S(t)$	Electric field of the optical signal at the receiver input
f_d	Frequency separation between OFDM subcarriers
f_s	Sampling frequency
F	Amplifier noise figure
$F_{n,m}$	Related to the FWM nonlinear interaction between n neighboring channels

G	Kalman gain, amplifier gain
h	Segment length considered in the split step Fourier method, Planck constant
h_n	Segment of fiber of index n
$h(t)$	Fiber impulse response in a singly polarized system
$H(t)$	Fiber impulse response in a dually polarized system
$H(\omega)$	Fiber transfer function in a dually polarized system
$H_{CD}(\omega)$	Fiber transfer function only due to chromatic dispersion
$H_{\text{bessel}}(f)$	Transfer function of Bessel filter
i_k	In-phase component of complex transmitted symbol of information
$I(t)$	In-phase component of the transmitted complex envelope
$I^*(t)$	In-phase component of the electrical current at the photodiode output
j	$\sqrt{-1}$
k	Discrete time index of sampled signal
k_0	Wavenumber
k_m	Propagation constant of channel m
K	Denominator of the fractional oversampling ratio, autocorrelation matrix of the soft estimate ψ
K_p	Autocorrelation of θ_k
$K_{n'}$	Autocorrelation of n'_k
l	Index of fiber input polarization, channel index
L	Fiber length
L_{eff}	Effective length due to attenuation influence over nonlinearity
L_{FWM}	Nonlinear length scale associated with four wave mixing
L_{NL}	Nonlinear length scale associated with self phase modulation
L_{wo}	Nonlinear length scale associated with walk-off stemming from chromatic dispersion
m	Index of fiber output polarization, general discrete index, channel index
M	Length of the alphabet of information to be transmitted, numerator of the fractional oversampling ratio
M_s	Oversampling ratio due to zero-padding in a OFDM signal
n	Discrete time index
$\tilde{n}$	Total refractive index
n_k	Discrete noise sample at the receiver
$\boldsymbol{n}_k$	Oversampled representation of discrete noise sample at the receiver
n_{sp}	Spontaneous emission factor in an optical amplifier
$n_{r,2}$	Nonlinear part of optical fiber refractive index

$n(t)$	Gaussian noise added along the transmission channel
$n_l^{'}(t)$	Anti-alias filtered gaussian noise added along the transmission channel, on polarization l
$n_r(w)$	Linear part of optical fiber refractive index
N	Length of Wiener filter, number of WDM channels
$\hat{N}$	Nonlinear operator governing nonlinear effects in the propagating signal
N_0	Noise power spectral density
N_c	Number of subcarriers of OFDM signal
N_f	Number of feed-forward taps of equalization filter
$\boldsymbol{N}_k$	Oversampled representation of $\boldsymbol{n}_k$ generalized over the equalizer length
N_{PMD}	Number of fiber segments in PMD model
N_{pre}	Number of subcarriers corresponding to cyclic prefix extension in a OFDM signal
N_{span}	Number of spans of the long haul fiber optic link
N_{win}	Number of subcarriers corresponding to windowing terms in a OFDM signal
N_u	Number of subcarriers effectively used to transmit information in a OFDM signal
$p(t)$	Pulse shape of the transmitted signal
P	Refers to the *a posteriori* error covariance matrix in the Kalman estimator
P_c	Dispersion pre-compensation value, normalized to the dispersion of a span of single mode fiber
P_{LO}	Continuous wave power of the local oscillator laser
P_{NL}	Induced nonlinear polarization due to four wave mixing
P_p	Peak signal power
P_{out}	Optical power at the output of photo-detector
P_S	Continuous wave power of the transmitter laser
P_s	Average symbol power for a subcarrier in a OFDM signal
P_{Sum}	Power summation from the electric field of all WDM channels
P_{tx}	Average symbol power in a single carrier signal
q	Represents the ratio between mean value and the standard deviation in a constellation cloud
q_k	Quadrature component of complex transmitted symbol of information, sampled combined impulse response
$\boldsymbol{q}_k$	Oversampled representation of q_k at the receiver
Q	Q factor in decibels, related with the bit error rate performance of the system

$\boldsymbol{Q}$	Oversampled representation of $\boldsymbol{q}_k$ generalized over the equalizer length
$q(t)$	combined impulse response of the transmitter pulse shape, channel impulse response and anti-alias filter
$Q(t)$	Quadrature component of the transmitted complex envelope
$Q^*(t)$	Quadrature component of the electrical current at the photodiode output
r	Parameter that determines rate of decay of Wiener filter coefficients, channel index
R	Photodiode responsivity
R_2	Constant used for the error calculation in the CMA equalizer
$R_{a,b}$	Cross correlation between elements a and b
R_s	Symbol-rate
$R(\alpha_n)$	Matrix of a rotator representing coordinate transformation in the fiber axis
$r(t)$	Received signal, before the anti-alias filter, in the system canonical model
s	Index of subcarrier in OFDM symbol, channel index
$S_{\text{ofdm}}(\omega)$	Power spectrum of OFDM signal
t	Time
T	Sample period of signal
T_b	Bit period
T_s	Symbol period
T_{ofdm}	Effective duration of OFDM symbol
T_{pre}	Duration of cyclic prefix in a OFDM symbol
T_{sym}	Duration of whole OFDM symbol including cyclic prefix and windowing
T_{win}	Duration of windowing in a OFDM symbol
$T(\omega)$	Fiber Jones matrix
$u(\omega)$	Elements of the fiber Jones matrix
$u_{x,y}$	Pulse envelope in the coupled nonlinear equations in a linearly bi-refringent optical fiber
v_g	Group velocity
$V(t)$	Amplitude of an electric voltage at the arms of a Mach-Zehnder modulator
V_π	Voltage required to turn the modulator from minimum to maximum optical intensity
w_n	Set of Wiener filter coefficients
W	Set of equalizer coefficients in a singly polarized system

$\boldsymbol{W}$	Transposed 2×2 equalizer coefficient matrix, in a dually polarized system
$W(Z)$	Z transform of set of Wiener filter coefficients
x_k	Complex transmitted symbol of information
$\hat{x}_k$	Decided complex symbol at DSP output
$\tilde{x}_k$	Estimated complex symbol at the equalizer output
$X_{s,k}$	Represents the s-th subcarrier constellation symbol transmitted on the k-th OFDM symbol
$\boldsymbol{X}_k$	Representation of x_k generalized over the equalizer length
$x(t)$	Complex envelope of the transmitted signal including pulse shape
$x_I(t)$	In-phase component of complex envelope of the transmitted signal including pulse shape
$x_Q(t)$	Quadrature component of complex envelope of the transmitted signal including pulse shape
y_k	Sampled discrete domain signal at the input of DSP, in the system canonical model
$\boldsymbol{Y}_k$	Representation of y_k generalized over the equalizer length
$y(t)$	Continuous time domain signal after the anti-alias filter in the system canonical model
z	Propagation distance
$z_{1,2}$	Poles of the Wiener filter
α	Fiber attenuation, parameter related with the Wiener filter coefficients
$\beta(\omega)$	Fiber mode propagation constant
β_m	Fiber mode propagation constant of order m in the Taylor series expansion
δk	Phase mismatch parameter
Δ	delay
$\Delta V(t)$	Differential amplitude of an electric voltage between the arms of a Mach-Zehnder modulator
Δt	Pulse rise time
$\Delta\phi(t)$	Phase error at the coherent receiver
Δh	Deviations in length of segments of fiber in PMD model
$\Delta\nu$	Combined line-width of both transmitter and local oscillator lasers
$\Delta\nu_{\text{ref}}$	Frequency separation between two reference spectral components of interest
$\Delta\omega$	Channel spacing in terms of angular frequency
Δf	Channel spacing in terms of frequency
ϵ	Parameter related with the accuracy of the split step Fourier method

ϵ_0	Vacuum permitivity
γ	Fiber nonlinear parameter
λ	Wavelength of optical carrier
μ	Step size for LMS coefficient update, mean value of a constellation cluster
ν	Finite length where the response of q(t) is non-negligible, frequency of optical carrier
ν_k	Independent identically distributed Gaussian variable
ω	Angular frequency of a generic signal
ω_0	Center angular frequency of optical carrier
ω_S	Angular frequency of the signal optical carrier
ω_{LO}	Angular frequency of the local oscillator optical carrier
ω_{BW}	Angular frequency bandwidth between nulls of OFDM signal
ϕ_S	Initial phase of the signal optical carrier
ϕ_s	Total phase of the signal complex envelope
ϕ_{LO}	Initial phase of the local oscillator optical carrier
ϕ_{lo}	Total phase of the local oscillator complex envelope
ϕ_n	Phase accounting for temperature fluctuation in fiber PMD model
ϕ_{NL}	Nonlinear phase shift induced by self phase modulation
$\phi_e(t)$	Phase of the information complex envelope
$\phi_{NS}(t)$	Phase noise of the signal optical carrier
$\phi_{NLO}(t)$	Phase noise of the local oscillator optical carrier
ψ	Phase shift due to IQ unbalancing in an optical hybrid, soft estimate of θ_k (ψ_k)
σ_p	Standard deviation of phase noise
$\sigma_{n'}$	Standard deviation of the phase of Gaussian noise
τ	Differential group delay owning from PMD
$\theta(t)$	Phase noise from combined line-width of transmitter and LO lasers
θ_k	Phase noise in the discrete domain
$\tilde{\theta}_k$	Estimated phase noise in the discrete domain
ξ	Empirical parameter to control the amount of FWM compensation in back-propagation
ζ	Nonlinear phase rotation parameter in back-propagation

Chapter 1

Introduction

1.1 Background and motivation

Recently, the main challenge faced by optical engineers has been increasing the throughput and distance limitation of existent long-haul transmission systems, without doing signal regeneration. Coherent systems are seen today as the the key in order to accomplish these requirements. These systems were a topic of intense research during the 80's, essentially because of their great sensitivity and capability of narrowband channel selection, until the emergence of Erbium Doped Fiber Amplifiers (EDFA) in the early 90's. Recently, they have gained renewed interest, essentially because of the ability of linearly transferring the signal from the optical to the electrical domain, combined with the availability of high speed digital signal processing, which allows for the signal to be digitized and processed in the electrical domain. The lower price of electrical components, partly relaxed receiver requirements at high data rates and capability of pushing the spectral efficiency limits beyond, while maximizing the power efficiency, also intensified the interest in this topic. In fact, if the outputs of a coherent homodyne receiver are sampled at the Nyquist rate, the digitized waveform contains full information of the electric field, preserving the amplitude, phase and polarization from the optical domain to the electrical domain, enabling new potential of multi-level signaling (M-ary Phase Shift Keying – PSK – and M-ary Quadrature Amplitude Modulation – QAM), as well as the possibility of exploring polarization multiplexing [2]. Therefore the symbol rate can be reduced while keeping the bit rate, increasing the spectral efficiency and easing the complexity of analogue to digital (A/D) circuits used in demodulation/compensation

schemes. Additionally, it enables *quasi*-exact compensation of linear transmission impairments such as Chromatic Dispersion (CD) and Polarization Mode Dispersion (PMD) by a linear filter [3], which can operate adaptively to overcome time-varying impairments. Furthermore, Orthogonal Frequency Division Multiplexing (OFDM) provides inherent high spectral efficiency due to orthogonal subcarrier overlapping, and subcarrier based easiness of equalization. Recently, it has received a lot of attention from the fiber optics community. In fact, OFDM can take advantage of long symbol times associated with a large number of subcarriers to allow for time domain guard intervals to be assigned in between symbols, enabling single-tap frequency domain equalization of several sources of Inter Symbolic Interference (ISI), such as CD and PMD [4], opposed to a multi-tap equalization system used for single carrier modulation formats [5]. It is in this context that the main objective of this work is to investigate the compensation of fiber impairments in coherent optical systems by electronic domain equalization using digital processor technology.

1.2 State of the art

The most common type of optical communication systems are Intensity Modulation / Directed Detection (IM/DD) based, essentially due to their cost, simplicity and effectiveness. Yet, dispersion compensation in IM/DD systems is not very efficient due to the non-linear optical to electrical (O/E) conversion in the photodiode (PD), with loss of phase information. However, single side band (SSB) transmission allows the square law detection to largely preserve the phase, therefore being a technique of high interest. Moreover, maximum likelihood sequence estimation (MLSE) is the most effective means of impairments mitigation in these systems [6].

In contrast to IM/DD systems, complete equalization of transmission impairments is possible in coherent systems, in the electrical domain, as the equalizer operates on signals proportional to the electric field. Additionally, zero penalty dispersion compensation may also be achieved in the optical domain. However, adaptive schemes are rather complicated because the error signal is obtained after square-law detection in the photodiode [6].

Considering coherent receiver implementation, homodyne receivers are superior to their heterodyne counterparts, and seem to be the choice for future networks. However, as they are sensitive to phase noise, an elegant technique called phase diversity emerged,

but only applicable to 2-level modulation signals. Therefore, for higher order modulation signals, an optical phase locked loop (OPLL) is necessary, which nowadays is still very difficult to implement. A turnaround to this problem is the usage of DPSK modulation, where the information is encoded by changes in phase from one symbol to the next, and differential detection, which consists in pair-wise comparison of sample phases, assuming the optical carrier phase varies much more slowly than the phase modulation. However, this detection scheme is less performing than synchronous detection [7], where the decoding of data is performed on the basis of comparison of consecutive quadrant numbers, but requiring that the phase of the signal is tracked. Thereafter, the option is to cope with phase noise through digital phase estimation, using a DSP to track the signal phase [8].

In recent experiments, the typical receiver is based on a phase and polarization diversity configuration [9]. Considering that the Local Oscillator (LO) phase needs to be locked to the signal phase, to avoid the difficulties associated with the OPLL, the synchronization can be done in the DSP, by digital phase estimation techniques, allowing for a free running LO.

The main goal of the algorithms used in coherent receivers is to perform equalization and phase recovery. Equalizers can achieve adaptation of their coefficients either by transmitting a training sequence, known symbol statistics or decision-directed (DD) adaptation. When no training sequence is transmitted, the operation is referred to as blind equalization and the constant modulus algorithm (CMA) introduced by Godard and Treichler [10] is the most used, essentially because of its robustness and ability to converge prior to phase recovery [11]. However, for non-constant modulus constellations such as QAM, the multimodulus algorithm (MMA) introduced by Yang [12] improves the performance of CMA by obtaining low steady-state mean-squared error (MSE) [13], but its cost function is not carrier phase independent. In order to cope with laser phase noise, an elegant solution consists in using the CMA for initial adaptation, avoiding bandwidth consuming training sequences, and enabling subsequent independent carrier phase estimation (CPE). Once equalizer convergence has been achieved, there is a great benefit if the equalizer switches to DD mode, whereby the error signal is derived from the error between the baseband signal and the nearest, ideal point of the constellation, improving the demodulator Signal to Noise Ratio (SNR) performance [11]. However, at this point, the phase must be estimated and its value considered in the error signal, precluding the use of independent CPE.

Additionally, equalization should be combined with nonlinearity mitigation, whenever nonlinear impairments are present due to high power in the transmission fiber. In fact, as nonlinearity constrains the usable launch power, the maximum achievable capacity depends on the algorithm used to mitigate its impact. The best method known for fiber nonlinearity mitigation is backward propagation (BP) [14], which consists in passing the received signal through a virtual fiber with opposite signs of dispersion and nonlinearity, yielding an estimate of the transmitted signal. In fact, back-propagation has been proposed as a universal technique for jointly compensating linear and nonlinear impairments for WDM systems using coherent detection, DSP and Dispersion Compensating Fiber (DCF), enabling higher launched power and longer transmission reach. It has been proposed independently by [15] and [16]. Since the BP algorithm works with the electric field of the signal, it can be applied to both single carrier and multi-carrier signals. Furthermore, a detailed study on the back-propagation algorithm performance for dispersion managed systems, combined with more efficient signaling schemes has not been done yet, being therefore performed in the present work.

1.3 Relevance of the subject

The impairments associated with currently installed fiber become significant at high data-rates and fiber lengths. Therefore, in order to cope with the bandwidth restrictions of optical fibers and amplifiers, maximizing the system spectral efficiency turns out to be mandatory. Moreover, the power efficiency should also be maximized in order to avoid fiber nonlinearities, which corresponds to minimizing the required transmitted energy per bit. DSP emerges in this context as a flexible tool to allow the manipulation of the signal in the digital domain, in order to compensate for all the distortion caused by the fiber channel (linear and non-linear) as well as distortions stemming from the lasers used in both transmitter and receiver ends. Therefore, the algorithms to be developed will take even further both the data-rates and system reach of currently deployed networks. These requirements are expected to become even more stringent with time due to the growing demands on broadband services, such as high definition multimedia contents. DSP has been evolving as a practical solution for robust optical long-haul transmission, and it is expected that data converters will be able to satisfy the required high sampling rates in the near future. In 2007, a 90 nm 20 M gate ASIC with 4 integrated A/D converters (> 20 GSa/s) has been reported [17]. On the other hand, as soon as sufficiently high

speed data converters are available, field programmable gate arrays (FPGA) propose to be a very flexible and fast time to market design tool, to implement the developed algorithms.

1.4 Author contributions

The main objective of this work is the investigation of suitable digital signal processing algorithms to compensate for relevant impairments in the scope of coherent optical systems. In the context of this work several contributions were added to the state-of-the art in this field, namely:

- Assessment of the performance of the IIR implementation (Kalman) of the zero delay Wiener filter.
- Evaluation of quantization issues on the performance of the Kalman filter.
- Improvement of the phase unwrapping function associated with the non-decision-aided phase estimation algorithm.
- Investigation of parallelization issues associated with both equalization and phase estimation algorithms, and subsequent identification of optimized design options.
- Identification of Equalizer/Estimation filter feedback configurations, and corresponding benefits and limitations.
- Assessment on the influence of dispersion map characteristics over the performance of back-propagation algorithm.
- Evaluation of the back-propagation algorithm performance for both single channel and OFDM transmission.
- Investigation of the performance/computational complexity for both coupled and total field compensation methods for multi-band OFDM transmission.
- Proposal of a reduced complexity back-propagation method for multi-band OFDM signals, with the inclusion of four wave mixing interaction between neighbor channels.
- Derivation of the back-propagation equations for polarization multiplexed transmission, considering both single channel and WDM scenarios.

- Identification of optimum dispersion map characteristics over polarization multiplexed multichannel back-propagation.
- Investigation of oversampling issues for both coupled and total field algorithms in WDM signal transmission.

As an outcome of this work, several publications in conference proceedings have been made, as well as a publication in an international journal indexed by the ISI Web of Science.

1. L. M. Pessoa, H. M. Salgado and I. Darwazeh, "Adaptive Electrical Equalization of Optical Impairments in Coherent Optical Systems", in Proc. Symposium on Enabling Optical Networks and sensors, Aveiro, 28th June 2007.

2. L. M. Pessoa, H. M. Salgado and I. Darwazeh, "Algorithms for DSP implementation in coherent optical systems", Cranfield Multi-Strand Conference, Cranfield, United Kingdom, 5-6 May 2008.

3. L. M. Pessoa, H. M. Salgado and I. Darwazeh, "Joint Mitigation of Optical Impairments and Phase Estimation in Coherent Optical Systems", IEEE/LEOS Summer Topical Meetings 2008, Acapulco, Mexico, 21-23 July 2008.

4. L. M. Pessoa, H. M. Salgado and I. Darwazeh, "Simplified backpropagation equalization in wdm coherent polarization multiplexed systems", In Proc. 11th International Conference on Transparent Optical Networks (ICTON) 2009, pages 1-5, June 2009.

5. L. M. Pessoa, H. M. Salgado and I. Darwazeh, "Assessment of parallel equalizer/phase estimation algorithms in coherent optical systems", In Proc. IEEE/LEOS Summer Topical Meeting LEOSST 09, pages 79-80, July 2002, 2009.

6. L. M. Pessoa, H. M. Salgado and I. Darwazeh, "Performance evaluation of phase estimation algorithms in equalized coherent optical systems", IEEE Photonics Technology Letters, 17:1181-1183, 2009.

7. N. M. Pinto, H. M. Salgado, Ferreira J. C. and L. M. Pessoa, "Implementação de algoritmos em FPGA para estimação de sinal em sistemas ópticos coerentes", In Proc. Digest of REC 2010, pages 33-39, 2010.

8. J. M. B. Oliveira, L. M. Pessoa, H. M. Salgado, and I. Darwazeh, "Signal Processing Techniques for Transmission Impairments Compensation in Optical Systems", In Proc. 12th International Conference on Transparent Optical Networks ICTON 10, pages 1-4, June 2010.

1.5 Thesis outline

This document is organized as follows: The first chapter gives a review of coherent optical systems, and provides an explanation on the relevance of the subject, in order to determine the principal motivations leading to the execution of this work. Chapter 2 presents the principles of a coherent optical transmission system, analysis of coherent optical receiver structures, and optical modulation techniques with special attention on the fundamental principles of OFDM modulation, considering both coherent and incoherent transmission models, and its associated practical implementation constraints. Chapter 3 provides an investigation on the main types of linear fiber impairments, inherent to the implementation of a valid computer simulation model. Additionally, equalization algorithms suitable for implementation in a digital coherent receiver are studied and associated theoretical performance bounds are obtained. Chapter 4 focus on the topic of carrier phase estimation and equalization algorithms. Decision directed and non-decision-aided phase estimation algorithms are analyzed for both 4 and 16-QAM modulation formats. Then the issues associated with the combination of equalization and carrier phase estimation are investigated, in terms of performance and parallelization possibilities. Chapter 5 addresses the back-propagation algorithm, specifically, the

symmetric and asymmetric implementation of the nonlinear propagation equation. Additionally, the simulation model of a long-haul transmission system is analyzed, results being presented on the optimized dispersion map characteristics for an amplified long-haul channel, and theoretical performance bounds are obtained for both single channel and OFDM modulation formats. Furthermore, the back-propagation algorithm is analyzed in detail, and optimum design rules are determined from simulation results, where the dispersion map, oversampling rate, launched power and computational complexity parameters are considered in the investigation. This chapter ends with a comparison on the performance of the back-propagation algorithm between single channel and OFDM transmission formats. The back-propagation algorithm studied in this chapter is used in chapter 6 to analyze OFDM multi-band transmission performance focusing on the comparison between coupled field and total field back-propagation, where computational complexity and dispersion management are considered as variables. Additionally, four wave mixing is considered within the coupled field method to provide simplified means of multichannel nonlinearity compensation. A compensation method is proposed for multi-band OFDM signals. Then chapter 7 presents an analysis on the back-propagation algorithm performance for polarization multiplexed transmission, focusing on the comparison between single channel and WDM transmission, as well as the influence of the system dispersion map. Finally chapter 8 summarizes and concludes the thesis, outlining directions for further research.

Chapter 2

Coherent optical systems

2.1 Introduction

The two main categories of optical receivers are based on both direct detection and coherent detection. In direct detection systems the receiver directly converts the modulated optical signal to a baseband electrical signal through a photodiode, as shown in Fig. 2.1 (a). Therefore, the receiver makes decisions based on the detected signal power, which limits such a system to signals which encode only one degree of freedom per polarization per carrier, translating into a poor spectral efficiency [3]. In a coherent receiver, the incoming modulated optical signal is mixed with an optical local oscillator signal in a photodiode. This operation is accomplished through an optical down-converter (Fig. 2.1 (b)) which might be implemented in different ways, as will be shown in the following sections. The output of the signal downconversion generates the sum and difference of the two optical frequencies (intermediate frequencies).

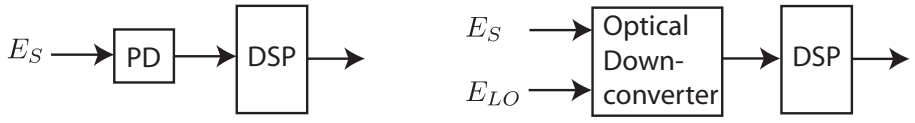

(a) Direct Detection (b) Coherent Detection

FIGURE 2.1: Simplified schematic of a direct detection receiver (a) and coherent detection receiver (b).

If the LO frequency is different from the carrier frequency, the system is said to be heterodyne, while if the LO frequency is matched to the optical carrier, the intermediate frequency falls at zero, and the optical signal is mapped to baseband, the system being called homodyne. The heterodyne down-converter has the advantage of avoiding the

need for phase tracking the optical carrier, and finds applications in RF based electrical phase correction techniques to combat dispersion induced distortions [18]. However, the heterodyne down-converter requires at least twice as much bandwidth compared to the homodyne counterpart, in order to avoid distortions from overlapping side-lobes, which is a major disadvantage. Homodyne receivers allow for digital signal processing operations at baseband, which is the case of interest within the scope of this thesis. In the early nineties, when coherent systems became popular, the main advantages they provided were the sensitivity improvement of approximately 20 dB, compared with direct detection without pre-amplification, and the possibility of finer optical frequency division multiplexing due to greater channel selectivity [19].

2.2 Single branch receiver

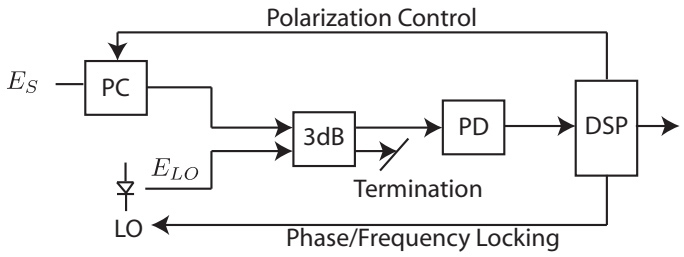

FIGURE 2.2: Single branch coherent optical receiver. PC - Polarization Controller. PD - Photodetector.

The most simple coherent receiver structure, the single branch receiver (Fig. 2.2), most early used by [20], uses a fiber coupler having the optical modulated signal and the LO laser signal at each of its inputs, and having a single photodetected output (while the other coupler output is terminated). This configuration requires the polarization state of the incoming optical signal to be matched to the LO, to allow for optimal signal mixing. This can be achieved by using a complex automatic polarization control system. Additionally, the LO laser is also required to be matched in phase (for homodyne) or frequency (for heterodyne) systems. The operations of phase and frequency locking are rather complex, requiring an optical phase locked loop and an automatic frequency control scheme, respectively. Typically, a single branch receiver is limited by the noise stemming from the LO source, either from an amplifier (used to boost the power of the LO) or from the relative intensity noise (RIN) of the LO itself. However, it is possible to use a balanced detection approach that cancels the noise stemming from the LO laser.

2.3 Balanced receiver

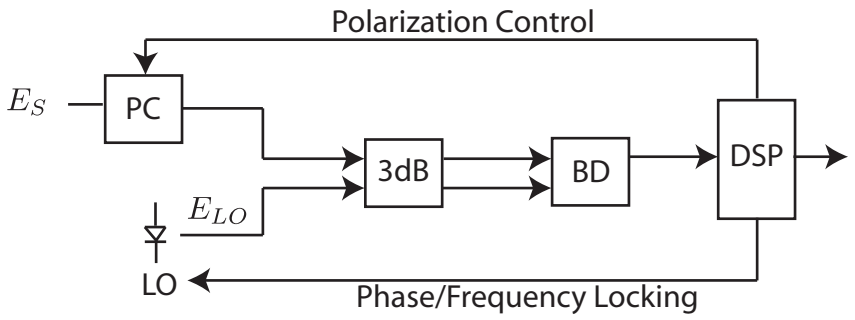

FIGURE 2.3: Dual photodiode balanced coherent optical receiver. BD - Balanced Detector.

The balanced receiver approach (Fig. 2.3), introduced by [21], uses the signal difference from two photodiodes present at each of the outputs of the optical fiber coupler, providing twice the power than the single branch counterpart, and eliminating the noise from the LO laser source. However, the downsides concerning polarization control and phase/frequency matching still persist in this configuration.

2.4 Phase diversity receiver

According to the terminology of Proakis [22], a system is called coherent if the receiver performs tracking of the phase of a LO. However, within coherent optical communications terminology, the system is considered synchronous or asynchronous depending on whether phase tracking is being performed, and the coherent term always applies as long as a LO laser is used to mix with the incoming optical signal. ASK and FSK signal formats might be used with both synchronous or asynchronous approaches, while PSK can only be used with synchronous detection. In fact, a differential version of PSK is required in order to avoid the need for phase tracking. The phase diversity receiver (Fig. 2.4) is based on an asynchronous homodyne quadrature receiver, which allows the extraction of the in-phase and quadrature components of the optical signal, dispensing phase tracking when a 2-level modulation signal is used.

This type of receiver was first used in 1985 by Hodgkinson [23] for DPSK signals and thoroughly reviewed by Kazovsky [24] in 1989. Additionally, the quadrature receiver is based on a 90° optical hybrid, which has 4 output ports, possibly featuring 2 balanced photodetector pairs, in order to take advantage of the good performance of the balanced

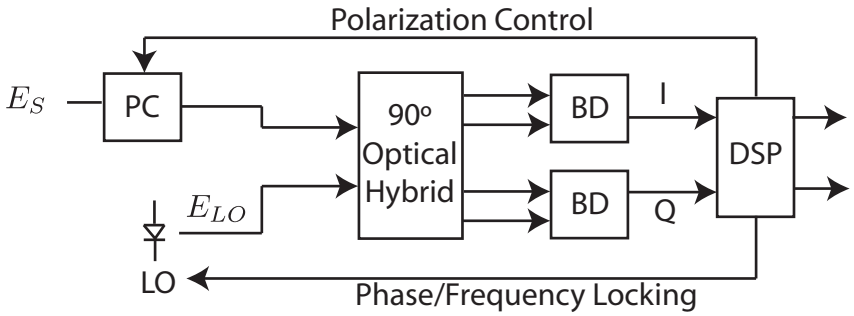

FIGURE 2.4: Phase diversity coherent optical receiver.

configuration concerning LO noise. A detailed analysis of the principles by which the 90° optical hybrid operates is conveyed in the subsequent section of the present chapter. The quadrature receiver, if operated in an homodyne configuration, allows for the possibility of receiving M-ary PSK or QAM signals. The quadrature receiver was first used by Walker [25] in 1984 to measure the phase and amplitude of an electric field. The main advantage of the phase diversity receiver is related with the reduced bandwidth requirement, providing close channel spacing.

2.5 2×4 90°-hybrid

The 2×4 90°-hybrid is a fundamental component of a coherent optical receiver, allowing the translation of the input signal electric field information from the optical domain to the electrical domain, since it enables the separate detection of the in-phase and quadrature components of the optical signal. A coherent receiver takes as its inputs both the incoming optical signal and the receiver laser LO. One of the key components within a 2×4 90°-hybrid is the 3 dB coupler. The input-output characteristic of a single lossless 3 dB coupler is given as:

$$\begin{bmatrix} E_{o,1} \\ E_{o,2} \end{bmatrix} = \frac{1}{\sqrt{2}} \begin{bmatrix} 1 & j \\ j & 1 \end{bmatrix} \begin{bmatrix} E_{i,1} \\ E_{i,2} \end{bmatrix} \tag{2.1}$$

The 2×4 90°-hybrid can be implemented in several ways [26]. Here two different implementation schemes are analyzed. One of the possibilities consists in using four 3 dB couplers, with an additional 90 degrees phase shift in one branch. The schematic in Fig. 2.5 shows the necessary configuration.

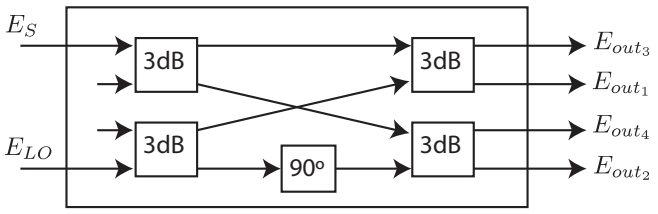

FIGURE 2.5: Diagram of a 2×4 90°-hybrid using four 3 dB couplers

A simplified representation of the signals at the input of the receiver, can be written as follows:

$$E_S = a_s \exp(j\phi_s) \tag{2.2}$$

$$E_{LO} = a_{lo} \exp(j\phi_{lo}) \tag{2.3}$$

where E_S and E_{LO} represent the electric field of the input optical signal and local oscillator waves. In this way, the signal electric field at each of the 4 outputs of the hybrid is given as

$$\begin{bmatrix} E_{out_3} \\ E_{out_1} \\ E_{out_4} \\ E_{out_2} \end{bmatrix} = \frac{1}{2} \cdot \begin{bmatrix} E_S - E_{LO} \\ jE_S + jE_{LO} \\ jE_S + jE_{LO} \cdot \exp(90°) \\ -E_S + E_{LO} \cdot \exp(90°) \end{bmatrix} \tag{2.4}$$

where de additional 90 degrees phase shift is written separately. Each of the hybrid output electric field signals will be squared by the photodiode response, and therefore it is relevant to write the optical power output at each branch $n \in \{1, 2, 3, 4\}$:

$$P_{out_n} = E_{out_n} \cdot E^*_{out_n} = \frac{1}{4}|E_S|^2 + \frac{1}{4}|E_{LO}|^2 + \frac{1}{2}|E_S||E_{LO}| \cdot \cos(\phi_s - \phi_{lo} - n \cdot 90° + \psi) \tag{2.5}$$

where the phase ψ traduces a small quantity related with a possible phase shift away from 90° between the upper to the lower branches of the hybrid. Commercial hybrids provide external control of this phase shift, which might be used to rotate the received constellation diagram into the correct position. However, only 90° of relative phase shift between the upper to the lower branches guarantees orthogonality of the in-phase and quadrature components. Therefore, any imprecise relative phase shift leads to a degradation of the IQ balance.

As seen in equation (2.5), adjacent optical outputs of the hybrid are in quadrature, which can be used in balanced photo-detection. Therefore, the 4 output fields are combined in pairs using balanced photodetectors, the fields E_3 and E_1 being detected

by the upper and E_4 and E_2 being detected by the lower balanced detector. Moreover, assuming perfect balancing in the hybrid, the photocurrents obtained in the upper and lower BD, I^* and Q^*, are proportional to the I and Q electric field components of the received signal, respectively, as follows:

$$I^* = R \cdot (E_{out_3} \cdot E^*_{out_3} - E_{out_1} \cdot E^*_{out_1}) = R \cdot |E_S||E_{LO}| \cdot \cos(\phi_s - \phi_{lo}) \tag{2.6}$$

$$Q^* = R \cdot (E_{out_4} \cdot E^*_{out_4} - E_{out_2} \cdot E^*_{out_2}) = R \cdot |E_S||E_{LO}| \cdot \sin(\phi_s - \phi_{lo}) \tag{2.7}$$

where R denotes the photodiode responsivity. Furthermore, imprecisions in the symmetry of the 3 dB couplers lead to asymmetries in the output power of the hybrid branches, and subsequent asymmetries in the balanced photo-detection process [27].

Another possibility of building a 2×4 90°-hybrid consists in using a single 3 dB coupler in conjunction with two polarization beam splitters (PBS), as shown in Fig. 2.6. However, this approach requires a specific polarization state of the hybrid input signals,

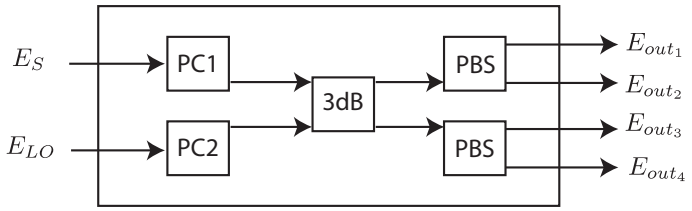

FIGURE 2.6: Diagram of a 2×4 90°-hybrid using the polarization splitting technique

such that the input optical signal electric field should be linearly polarized at 45 degrees from the PBS reference, while the LO electric field should be circularly polarized, holding that:

$$E_S = \frac{1}{\sqrt{2}} a_s \exp(j\phi_s) \begin{bmatrix} \hat{x} \\ \hat{y} \end{bmatrix} \tag{2.8}$$

$$E_{LO} = \frac{1}{\sqrt{2}} a_{lo} \exp(j\phi_{lo}) \begin{bmatrix} \hat{x} \\ j\hat{y} \end{bmatrix} \tag{2.9}$$

In this way, the output electric fields, after the PBS are given as:

$$\begin{bmatrix} E_{out_1} \\ E_{out_2} \\ E_{out_3} \\ E_{out_4} \end{bmatrix} = \frac{1}{2} \cdot \begin{bmatrix} \hat{x}(E_S + jE_{LO}) \\ \hat{y}(E_S - E_{LO}) \\ \hat{x}(jE_S + E_{LO}) \\ \hat{y}(jE_S + jE_{LO}) \end{bmatrix} \tag{2.10}$$

Finally, balanced photo-detection is used to combine signals in the same polarization, yielding the in-phase and quadrature components of the optical received signal identically to the previous approach.

2.6 Polarization diversity receiver

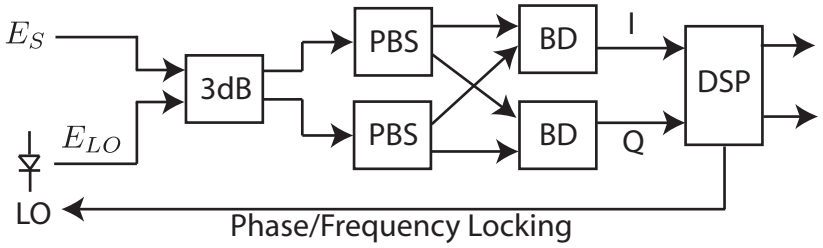

FIGURE 2.7: Polarization diversity coherent optical receiver.

All of the previously mentioned single branch, balanced, and phase diversity receivers require some sort of polarization control at the receiver, in order to guarantee the alignment between the polarization of the LO and the incoming optical field. However, this requirement might be overcome if a polarization diversity configuration is used (Fig 2.7). This consists in using a 3-dB coupler having as inputs the incoming optical signal (with no polarization control) and the LO signal polarized at 45 degrees. Then each output of the coupler features a polarization beam splitter, which separates orthogonal signals either to the in-phase (polarization x) or to the quadrature (polarization y) pair of balanced photodetectors. In this way, depending on the polarization of the incoming optical signal, the output signal will have its x and y polarization components divided by the two outputs. Therefore, the data might be demodulated by combining information from both branches, and no penalty is incurred relative to the case where physical polarization control is used.

In fact, both phase and polarization diversity concepts can be combined in a single receiver, which is able to cope with the random variations in the state of polarization of the received signal, without requiring polarization control, while being also able to

receive asynchronous modulation formats. Additionally, if independent data is to be transmitted in each polarization, the received signal must be treated as a four dimensional vector, allowing the DSP to handle the polarization demultiplexing. In order to be able to receive synchronous modulation formats an optical phase locked loop is necessary, which nowadays is still very difficult to implement. A turnaround to this problem is possible using DPSK modulation (asynchronous), where the information is encoded by changes in phase from one symbol to the next, and differential detection, which consists in pair-wise comparison of sample phases, assuming the optical carrier phase varies much more slowly than the phase modulation. However, this detection scheme is less performing than synchronous detection [6], where the decoding of data is performed on the basis of comparison of consecutive quadrant numbers, but requiring the phase of the signal to be tracked. Thereafter, the option is to cope with phase noise through digital phase estimation, using a DSP to track the signal phase.

2.7 Mathematical analysis of the coherent receiver

At this point, it is of relevance to provide a perspective on the mathematical operations associated with a coherent receiver. In the following analysis, the coherent optical receiver structure given in Fig. 2.4 is analyzed assuming that the signal is aligned in SOP with the LO in the optical hybrid. The complex envelope of the incoming optical multi-level modulation signal, and local oscillator laser are:

$$\begin{aligned} E_S(t) &= a_e(t) \cdot e^{j\phi_e(t)} \cdot \sqrt{P_S} \cdot e^{j(\omega_S t+\phi_S+\phi_{NS}(t))} = \\ &= [I(t) + jQ(t)] \cdot \sqrt{\frac{P_S}{2}} \cdot e^{j(\omega_S t+\phi_S+\phi_{NS}(t))} = \end{aligned} \tag{2.11}$$

$$E_{LO}(t) = \sqrt{P_{LO}} \cdot e^{j(\omega_{LO} t+\phi_{LO}+\phi_{NLO}(t))} \tag{2.12}$$

where ω_S and ω_{LO} are the angular frequencies, P_S and P_{LO} the CW power, ϕ_S and ϕ_{LO} initial phases, and $\phi_{NS}(t)$ and $\phi_{NLO}(t)$ the phase noise of the signal optical carrier and local oscillator, respectively. $I(t)$ and $Q(t)$ are the in-phase and quadrature components of the information complex envelope, and $a_e(t)$ and $\phi_e(t)$ its magnitude and phase. The signal wave and the LO wave combine in an optical 2×4 90°-hybrid, yielding 4 output fields. The electric field components (EFCs) at the output of the hybrids are detected by means of balanced photodiodes, which has the advantage of suppressing the

relative intensity noise (RIN) [6]. The in-phase and quadrature photocurrents are given as follows:

$$I^*(t) = R_e \cdot (I(t) \cdot \cos(\Delta\phi) + Q(t) \cdot \sin(\Delta\phi)) \quad (2.13)$$

$$Q^*(t) = R_e \cdot (-I(t) \cdot \sin(\Delta\phi) + Q(t) \cdot \cos(\Delta\phi)) \quad (2.14)$$

with $R_e = R \cdot \sqrt{P_{LO}P_S/2}$, when neglecting shot noise. In the above equations, R is the responsivity of the photodiodes, and $\Delta\phi$ is the phase error due to frequency offset, phase offset and laser phase noise, which is given by

$$\Delta\phi(t) = (\omega_S - \omega_{LO})t + (\phi_S - \phi_{LO}) + (\phi_{NS} - \phi_{NLO}) \quad (2.15)$$

Therefore, in order to extract the modulation information the total phase error must be controlled. Moreover, for zero phase error, the in-phase and quadrature components of the transmitted complex envelope are obtained separately in the two arms.

2.8 Optical modulation techniques

The function of generating a signal to carry the information to be transmitted in a system is a fundamental operation. A typical digital transmission system carries the information in one or multiple degrees of freedom provided by the optical carrier characteristics, namely, amplitude, phase, frequency and even polarization [26], when considering a coherent optical system. While basic modulation formats can be used, such as amplitude shift keying (ASK), phase shift keying (PSK) and frequency shift keying (FSK), respectively based on the amplitude, phase and frequency of the optical carrier, more complex formats can be constructed by adding more levels into the basic signal or by combining different components of a signal, leading to the generation of multi-level signals. Furthermore, by exploiting the fact that single mode optical fibers support two orthogonal polarizations, it is possible to transmit independent data streams orthogonally polarized, which is called polarization division multiplexing (PDM). Additionally, both non-return-to-zero (NRZ) and return-to-zero (RZ) line codes are suitable for transmission in a coherent optical system. The most commonly used light source for coherent optical systems is the semiconductor laser diode [28], essentially because of its small size, low power consumption, reliability and compatibility with electronic circuits. The semiconductor laser uses a Fabry-Perot cavity resonator with two reflective mirrors at

both ends in order to provide optical feedback. However, as this configuration supports a high number of modes, there is an alternative which employs a fiber Bragg grating (FBG), the distributed feedback laser (DFB) so that the optical feedback is strongest at the Bragg wavelength, restricting the number of modes in propagation inside the cavity to a single mode.

2.8.1 The Mach-Zehnder modulator

Mach-Zehnder modulators (MZM) are external modulators typically used for long haul, high capacity systems, essentially due to their superior signal quality when compared with less performing direct modulation or electroabsorption modulators, providing a smaller chirp, narrower spectrum and higher resilience to chromatic dispersion [28]. The most commonly used material to fabricate a MZM is Lithium Niobate, which is an electro-optical crystal, whose refractive index changes in response to an applied electric field. Therefore, the speed of the lightwave in propagation is higher or lower as the refractive index decreases or increases, respectively, as a result of the applied voltage from the modulating signal. The Mach-Zehnder interferometer (MZI) is the fundamental structure on the basis of the external MZM. The MZI can be used to provide intensity modulation, since a waveguide coupler splits the optical signal into two optical paths, each going through a different phase modulator, as shown in Fig.2.8.

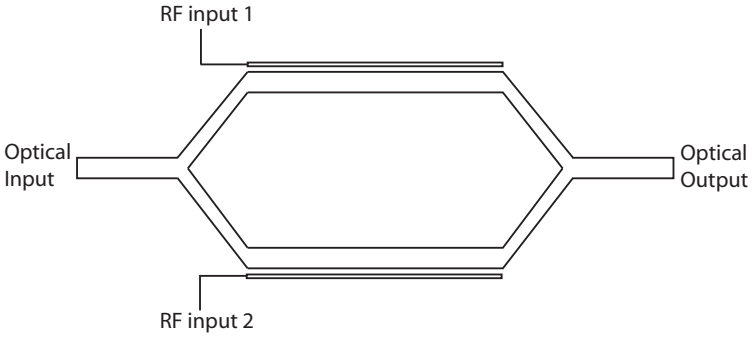

FIGURE 2.8: Diagram of a Mach-Zehnder Interferometer

The optical signal is affected by a phase shift which is a function of the applied voltage in each optical path, through RF inputs 1 and 2. The two optical paths are then recombined using another waveguide coupler. Constructive or destructive interference results depending on the lightwaves being in-phase or out-of-phase, respectively. The output intensity will vary between these two extreme cases according to the phase

difference between both arms. The electric field at the output of the MZM is given by:

$$E_o = \frac{E_i}{2}\left[\exp\left(j\pi\frac{V_1(t)}{V_\pi}\right) + \exp\left(j\pi\frac{V_2(t)}{V_\pi}\right)\right] \tag{2.16}$$

where E_o and E_i denote the the electric field amplitude of the optical wave at the output and input of the modulator, respectively. $V_1(t)$ and $V_2(t)$ represent the electric voltages applied to RF inputs 1 and 2 of Fig. 2.8, respectively. The V_π parameter corresponds to the total input voltage required to turn the modulator from the minimum to the maximum optical intensity. Equation (2.16) can be rewritten in the following manner:

$$\frac{E_o}{E_i} = \cos\left(\frac{\pi}{2}\frac{V_1(t) - V_2(t)}{V_\pi}\right)\exp\left(j\frac{\pi}{2}\frac{V_1(t) + V_2(t)}{V_\pi}\right) \tag{2.17}$$

From this equation it is clear that the output of the optical modulator is composed by an amplitude modulation given by the cosine term and a phase modulation given by the complex exponential. If the modulating signals have equal amplitude and opposite phase, the phase modulation term disappears. This mode of operation is referred as "push-pull", corresponding to the typical operation of a balanced single drive modulator, which produces zero chirp. The MZM input output intensity relationship becomes:

$$\frac{|E_o|^2}{|E_i|^2} = \cos^2\left(\frac{\pi}{2}\frac{\Delta V(t)}{V_\pi}\right) \tag{2.18}$$

with,

$$\Delta V(t) = V_1(t) - V_2(t) \tag{2.19}$$

and,

$$V_1(t) = -V_2(t) \tag{2.20}$$

The relationship between the optical output of the modulator and the drive voltage (ΔV), is shown in Fig. 2.9, in terms of both intensity and optical field.

The relationship between the modulating signal and the intensity of light at the output of the modulator is a nonlinear sinusoidal function. In this way, the typical mode of operation consists in adding a bias voltage to the modulating signal in order to move the region of operation into the quasi-linear region, referred as quadrature-point, and then keeping the amplitude of the driving voltage small.

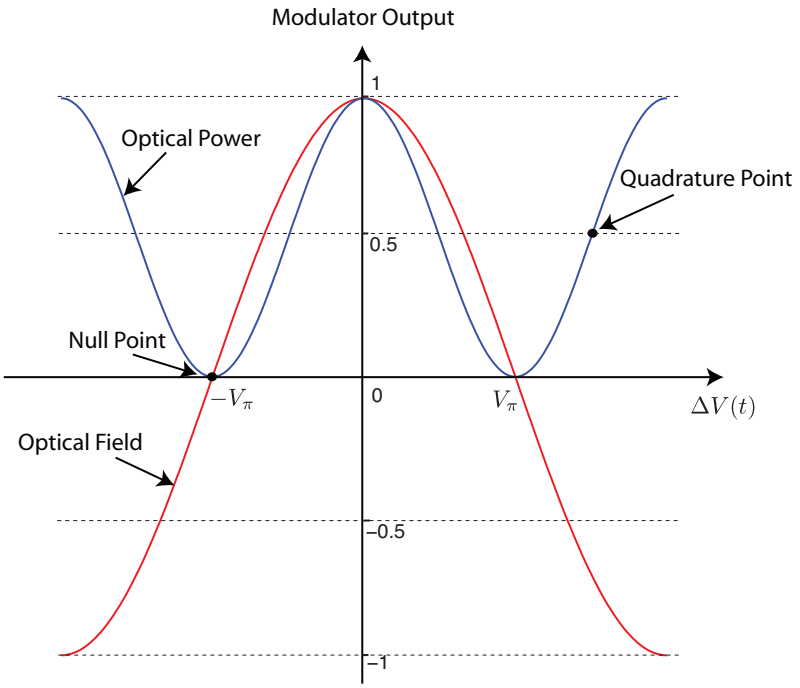

FIGURE 2.9: Representation of both optical power and optical field at the modulator output as a function of the input drive voltage

While the quadrature bias point has been extensively used in direct-detection systems, the typically used bias point for coherent systems is the null point, which corresponds to the point of minimum optical intensity, also referred as minimum transmission. This is explained by the fact that a coherent optical system is based in the transformation between electrical drive voltage into optical field, while a conventional direct-detection system is based in the transformation between electrical drive voltage into optical intensity. Fig. 2.9 clearly indicates that the optimal bias point is always in the quasi-linear region of the sinusoidal function, being the quadrature point for the optical intensity modulation and the null point for the optical field modulation.

2.8.2 Multi-level modulation

A multi-level digital transmission system requires the mapping of bits into symbols from a constellation diagram [22]. Depending on the length of the alphabet M, $m = \log_2(M)$ bits can be mapped into complex symbols. The symbols to be transmitted can be defined as:

$$x_k = i_k + jq_k \tag{2.21}$$

where the i_k and q_k represent the in-phase and quadrature components of the complex symbol. These components can be obtained for the complex envelope of the transmitted signal $x(t) = x_I(t) + jx_Q(t)$, which can be determined by including the pulse shape $p(t)$ and time repetition, as follows [8]:

$$x_I(t) = \sum_k i_k \cdot p(t - kT_s) \tag{2.22}$$

$$x_Q(t) = \sum_k q_k \cdot p(t - kT_s) \tag{2.23}$$

where T_s represents the symbol period. The typical structure of a multi-level modulation transmitter is based on an IQ-modulator consisting of two arms having single drive modulators with two orthogonal carriers applied in each arm. The in-phase component of the complex envelope is applied to the optical carrier passing through the I-arm, while the quadrature component is applied to the 90° phase shifted optical carrier passing through the Q-arm, as depicted in Fig. 2.10.

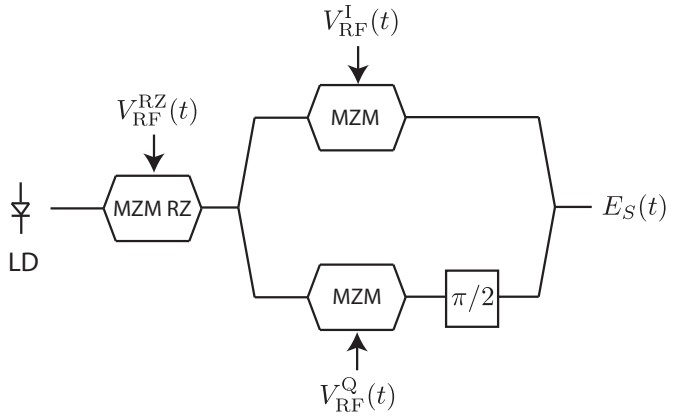

FIGURE 2.10: Structure of an IQ modulator

In Fig. 2.10 the RF driving voltages for the I and Q arms is represented by $V_{\mathrm{RF}}^{\mathrm{I}}$ and $V_{\mathrm{RF}}^{\mathrm{Q}}$, respectively. Single drive MZMs are used, in the minimum transmission bias point, as previously explained. The signal at the output of the modulator is represented by $E_s(t)$. The first Mach-Zehnder referred as "MZM RZ", is typically known as a pulse carver and is responsible for providing a return-to-zero profile. The RZ profile corresponds to a pulse train which is obtained as a result of a modulation from a sine wave, represented by $V_{\mathrm{RF}}^{\mathrm{RZ}}$. The swing excursion of the sine wave over the modulator driving voltage determines the duty cycle of the pulse train. For a 50% RZ signal, the excursion of the driving voltage should go from 0 to V_π, yielding the following signal

electric field at the output of the "MZM RZ" [29]:

$$E_{50}(t) = \frac{1}{\sqrt{E_{\text{pulse}}}} \sin\left(\frac{\pi}{4}\left[1+\cos\left(\frac{2\pi t}{T_s}\right)\right]\right), \text{ with } -\frac{T_s}{2} \leqslant t \leqslant \frac{T_s}{2} \tag{2.24}$$

where E_{pulse} is a constant used to obtain a pulse with normalized unit energy. The pulse power corresponding to the RZ profile is shown in Fig. 2.11. The MZMs within the IQ modulator are driven by the NRZ electrical waveforms V_{RF}^{I} and V_{RF}^{Q}, which encode the data to be transmitted. These waveforms will be modulated over the RZ pulse train, if RZ format is considered for transmission. The typically considered pulse shape $p(t)$ in the NRZ electrical waveforms corresponds to the output of a Bessel low pass filter having a rectangular pulse as input. Driving the MZM with such type of pulse has shown good results [30, 31].

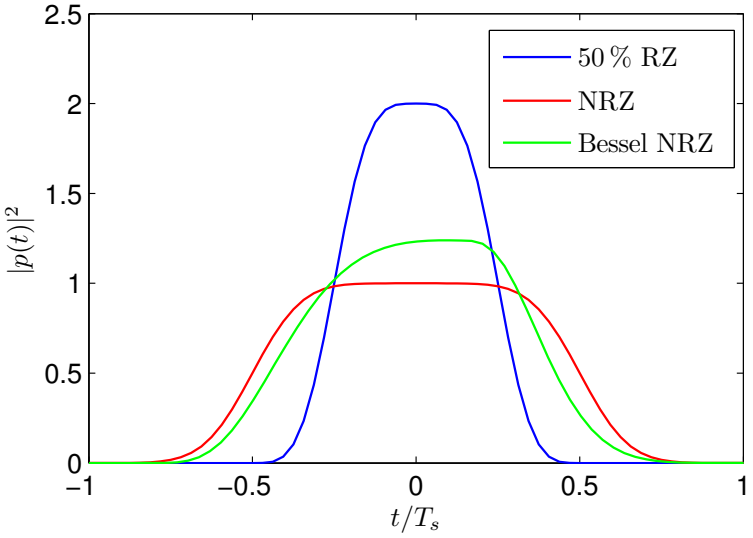

FIGURE 2.11: Pulse shape comparison

The Bessel filter considered in this work corresponds to a third order low-pass filter, having the following transfer function:

$$H_{\text{bessel}}(f) = \frac{15}{15+15p+6p^2+p^3}, \text{ with } p = j1.75f/f_{3\text{dB}} \tag{2.25}$$

where $f_{3\text{dB}}$ corresponds to the cut off frequency at -3 dB, which is set at 80 % of the symbol rate [31]. In [30] it is shown that lower filtering bandwidths can be used, specifically up to 50 % of the symbol rate, at the expense of an higher receiver bandwidth requirement in order to preserve the eye opening at the decision circuit. Fig. 2.11 shows

the intensity profile of the Bessel filtered pulse. For comparison purposes a representation of an ideal NRZ pulse shape is also depicted, having a rise time of 25 % of the symbol period, which can be obtained by the following expression [8]:

$$|E_{\mathrm{NRZ}}(t)|^2 = \frac{1}{2} \cdot \left(\mathrm{erfc}\left(\frac{2(t-T_s)}{4/3 \cdot \Delta t} \right) - \mathrm{erfc}\left(\frac{2t}{4/3 \cdot \Delta t} \right) \right) \tag{2.26}$$

where Δt represents the pulse rise-time.

2.8.3 Compensation of the nonlinear MZM characteristic

As studied in [8], one could theoretically apply an ideal driving signal to the MZM, in order to completely compensate for its nonlinear characteristic. Such a signal is given by:

$$\Delta V(t) = 2\frac{V_\pi}{\pi} \left[\arcsin\left(\sum_k i_k \cdot p(t - kT_s) \right) - \frac{\pi}{2} \right] \tag{2.27}$$

However, such type of signal is not very practical to generate, unless digital signal processing is used. Therefore an easier signal to generate would be [8]:

$$\Delta V(t) = 2\frac{V_\pi}{\pi} \left[\sum_k \arcsin(i_k) p(t - kT_s) - \frac{\pi}{2} \right] \tag{2.28}$$

which does not compensate completely the cosine modulator characteristic, but still yields the correct optical constellation diagram, while small differences occur during symbol transitions.

2.9 OFDM transmission

Orthogonal Frequency Division Multiplexing was introduced in 1966 as a technique of multichannel modulation that divides a given channel into many parallel subchannels or subcarriers, so that multiple symbols are sent in parallel [32]. Furthermore, by using the fast Fourier transform (FFT) algorithm and its inverse (IFFT), OFDM can be implemented with moderate computational complexity. OFDM provides inherent high spectral efficiency due to orthogonal subcarrier overlapping, and subcarrier based easiness of equalization. These characteristics stimulated extensive investigations on the topic and lead to its deployment in wireless and wireline communications. Recently, it has received a lot of attention from the fiber optics community. In fact, OFDM can take advantage of long symbol times associated with a large number of subcarriers to allow

for time domain guard intervals to be assigned in between symbols, which is achieved through cyclic prefix (CP), enabling single-tap frequency domain equalization of several sources of Inter Symbolic Interference (ISI), such as CD and PMD [4], opposed to a multi-tap equalization system used for single carrier modulation formats [5]. Laser phase noise also affects the performance of OFDM proportionally to the number of subcarriers, N_c. Therefore, reducing N_c will avoid Inter Carrier Interference (ICI) problems caused by the misalignment of orthogonality induced by phase noise [4].

This section provides a reasonably complete analysis on OFDM transmission, including state-of-the-art references in terms of transmission setup, sampling requirements and real-time implementation possibilities.

2.9.1 OFDM theory

An OFDM signal can be viewed as an analog multi-carrier signal, where instead of using analog I/Q modulation/demodulation, the inverse discrete Fourier transform (DFT) and forward DFT operations are used to modulate/demodulate the data on the subcarriers, translating these operations into the digital domain. The analog multi-carrier approach uses non-overlapped band-limited signals, and requires a bank of oscillators and filters at both transmit and receive ends, which demands high complexity. Additionally, the channel spacing is required to be a multiple of the symbol-rate in order to allow for a cost-effective design of those filters and oscillators, which subsequently uses an excessively high bandwidth. Opposed to the multi-carrier approach, OFDM employs overlapped, yet orthogonal carriers. In fact, any two subcarriers in the signal are orthogonal to each other, having frequencies spaced at multiples of the inverse of the symbol rate, which allows them to be recovered without ICI. The OFDM signal can be written as:

$$x(t) = \sum_{k} \sum_{s=0}^{N_c-1} X_{s,k} p(t - kT_{\text{sym}}) \exp(j2\pi s f_d t) \tag{2.29}$$

where $X_{s,k}$ denotes the s-th subcarrier constellation symbol transmitted on the k-th OFDM symbol and $p(t)$ is the pulse shape (carrier waveform). The frequency separation between carriers is $f_d = 1/(N_c T)$ where T is the sample period. The duration of the whole symbol can be written as:

$$T_{\text{sym}} = (N_c + N_{\text{pre}} + N_{\text{win}})T \tag{2.30}$$

$$= T_{\text{ofdm}} + T_{\text{pre}} + T_{\text{win}} \tag{2.31}$$

including the OFDM symbol itself plus the cyclic prefix N_{pre} and windowing N_{win} terms. Notice that N_c, N_{pre} and N_{win} are integers.

Cyclic prefix (CP) was proposed to resolve the channel dispersion induced ISI and ICI. It consists of a cyclic extension of the OFDM waveform into the guard interval, this waveform being essentially a time shifted identical copy of that in the DFT window. In this way, the sequence of received samples in one symbol is equivalent to one period of a circular convolution between the transmitted OFDM symbol and the samples of the channel impulse response. In the frequency domain, this corresponds to the multiplication of each subcarrier by the corresponding sample of the channel frequency response. The cyclic prefix length should be sufficient to accommodate the duration of the channel impulse response associated with dispersion, in order to avoid ISI and ICI. In wireless systems, it is typically selected to be greater than the maximum delay of the channel [33]. Additionally, the performance is generally improved by increasing the number of subcarriers, so that the transmission channel affects each subcarrier as a flat channel; however, as the peak-to-average power ratio (PAPR) is proportional to N_c [34], it is desirable to minimize the number of subcarriers employed because of the peak-limited transfer characteristics of typically used Mach-Zehnder modulators, so that the power efficiency of the modulator can be maximized.

The windowing terms can be used to provide an extra control to the pulse shape, in addition to the pulse shaping induced by the transmitter, which might be required to reduce the spectrum sidelobes when considering a rectangular window ($N_{\text{win}} = 0$). Considering this window and the transmitted symbols as independent identically distributed, the power spectrum of the OFDM signal can be written as [35]:

$$S_{\text{ofdm}}(\omega) = \frac{T_{\text{sym}}}{N_c^2} \sum_{s=0}^{N_c-1} P_s \text{sinc}^2 \left(\frac{T_{\text{sym}}}{2\pi} (\omega - 2\pi s f_d) \right) \tag{2.32}$$

where $P_s = E[|X_s|^2]$ is the average symbol power for subcarrier s. Fig. 2.12 represents the power spectrum of an OFDM signal having an arbitrary number of subcarriers. The power corresponding to each subcarrier is represented in blue lines, so that the summation of the power from all subcarriers leads to the result represented by the red line.

One of the advantages of OFDM corresponds to its very confined spectrum, which tends to a rectangular shape with increasing number of subcarriers. The signal bandwidth from the first to the last null can be shown to be:

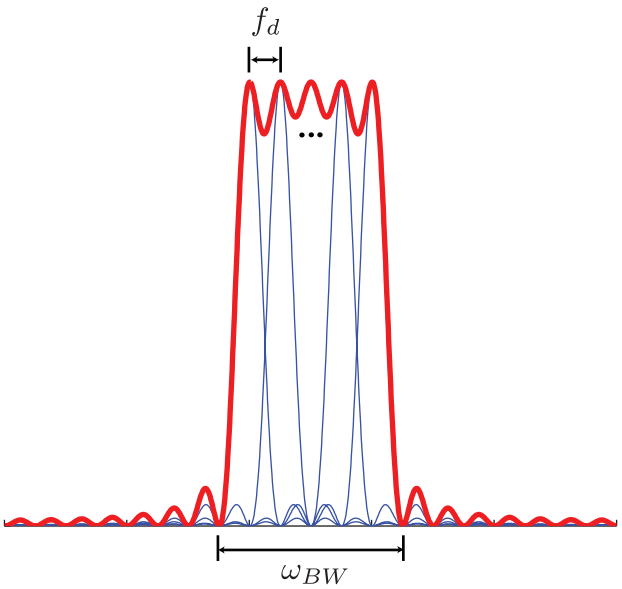

FIGURE 2.12: Power spectrum of the OFDM signal given by $S_{\text{ofdm}}(\omega)$, represented by the red line.

$$\omega_{BW} \approx 2\pi \left((N_c - 1) f_d + \frac{2}{T_{\text{sym}}} \right) \tag{2.33}$$

In order to satisfy a specified requirement for the symbol rate R_s, the frequency separation between carriers needs to obey the following condition:

$$f_d = \frac{(N_c + N_{\text{pre}}) R_s}{N_c^2} \tag{2.34}$$

Cyclic prefix and windowing bring several benefits, but on the other hand they limit the maximum achievable transmission rate, since they represent information that in spite of being transmitted, is not useful at the receiver, and therefore is discarded. In this sense, a power penalty is incurred deriving from the energy used for the transmission of these symbol extensions, and additionally, a sampling penalty stems from the fact that the sampling frequency needs to be higher than the symbol rate by an amount proportional to the length of symbol extensions. The power penalty is reflected in the SNR as a loss [33]:

$$\text{SNR}_{\text{LOSS}} = \left[1 - \frac{T_{\text{pre}} + T_{\text{win}}}{T_{\text{ofdm}}} \right] \tag{2.35}$$

In fact, the sampling frequency can be written in the following way:

$$f_s = 1/T = \frac{(N_c + N_{\text{pre}} + N_{\text{win}}) R_s}{N_c} \tag{2.36}$$

Furthermore, the previously derived OFDM bandwidth can be largely approximated as $\omega_{BW} \approx 2\pi \times R_s$ while for a single carrier system the occupied bandwidth tends to $\omega_{BW} \approx 2\pi \times 2R_s$, which represents an advantage of 2 times fold for OFDM. Additionally OFDM benefits from another inherent advantage regarding the oversampling ratio, which can be equal to an arbitrary rational value, since it is achieved by transmitting unmodulated subcarriers in the edges of the spectrum. In this way, the oversampling ratio is equal to the total number of subcarriers over the number of subcarriers effectively used to transmit information, $M_s = N_c/N_u$. Although a rational value of the oversampling rate is possible for single carrier systems, this would require highly complex signal processing. It has been shown in [35] and [31] that oversampling rates of 1.2 and 1.5/2 for OFDM and SC, respectively, are required to avoid aliasing, when pulse-shaping and anti-alias filters are properly selected. Finally, the previously shown formulas are also valid when oversampling is used, as long as the symbol extensions and the sampling frequency are adequately scaled by the oversampling ratio.

2.9.2 Coherent vs incoherent approaches

OFDM is used in both coherent (Coherent Optical-OFDM) and incoherent (Incoherent Optical-OFDM) optical systems, with the fundamental difference being that a signal proportional to the optical field is received in one case while a signal proportional to the optical power is received in the other, respectively. It has been shown by [36] that both CO-OFDM and IO-OFDM provide large tolerance to linear impairments, especially chromatic dispersion. However, IO-OFDM does not provide an optimal performance with respect to optical signal to noise ratio (OSNR); the main limitation for IO-OFDM is the requirement for a guard band between the optical carrier and the OFDM signal [4], providing lower spectral efficiency than coherent detection; The bandwidth occupied by the guard band is typically equal to the signal bandwidth, in order to avoid the second-order inter-modulation distortion near the optical carrier due to the square law photo-detector [37]. Subsequently, increased bandwidth requirements of both optical and electrical components needs to be considered, which lowers the maximum achievable data rate. However, an improved technique was published recently [38] that lowers the guard-band requirement and provides increased receiver sensitivity, tolerance to chromatic dispersion and laser line-width. This technique uses an algorithm to iteratively estimate the beat interference, therefore tolerating a reduced frequency gap, which

allows for the spectral efficiency to be almost doubled. The downside is related with the processing burden associated with the iterative algorithm, which might compromise a real-time implementation, rendering this technique useless. On one hand, the superior performance of CO-OFDM with respect to OSNR, its increased PMD tolerance and spectral efficiency makes it an excellent candidate for long-haul transmission systems. However, OFDM is very sensitive to phase and frequency offset [36], and therefore, very narrow line-width lasers are necessary at both transmitter and receiver, associated with appropriate algorithms to track the signal frequency, phase and polarization. On the other hand, IO-OFDM is more suitable for cost effective short reach applications, since OSNR performance and PMD tolerance are not issues for these short lengths. Furthermore, compensation of both transmitter and receiver lasers phase noise and frequency offset are not necessary for direct detection, avoiding additional overheads and increased algorithms complexity.

2.9.3 OFDM transmitter

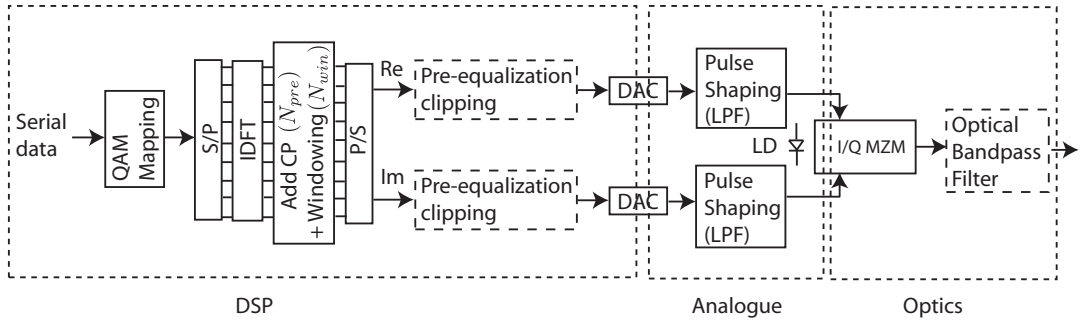

FIGURE 2.13: Digital implementation of an OFDM transmitter. S/P - Serial to Parallel. LPF - Low Pass Filter.

Figure 2.13 represents the architecture for the OFDM transmitter. A typical OFDM transmitter is comprised by three main parts: DSP, Analogue and Optics. In the DSP part, the information bits are mapped onto the corresponding data symbols of the subcarriers within one OFDM symbol, according to the constellation type used. Then the digital domain signal is obtained by using the IDFT operation, after which the guard interval is inserted, through cyclic prefix extension. Pre-equalization and clipping modules might be used to compensate for the frequency response of the subsequent DAC, and reducing optical nonlinearities (through PAPR reduction), respectively. Finally, the analog waveform is obtained through a DAC. In the analogue part, a low pass filter (LPF)

removes the DAC image frequency bands, resulting in pulse shaping. This sequence generates the baseband signal, which can be up-converted into a RF band by using an electrical I/Q mixer, so that the DAC bandwidth requirements are minimized [39]. Another technique to provide an efficient use of the DAC bandwidth uses a virtual carrier generated by a RF tone, allowing direct detection of the signal. These two techniques will be further explained in greater detail in the next section. Finally an optical filter may be employed to eliminate one of the sidebands from the signal, generating an optical SSB signal, which avoids phase distortion in the square law photo-diode (using direct detection), enabling effective compensation of transmission impairments in the electrical domain, and overcoming the power fading inherent in a double-sideband system. This filter might not be required if the transmitted OFDM signal and its Hilbert Transform are fed to an I/Q modulator [36]. Coherent detection and other techniques such as the virtual carrier approach can also dispense the optical filter.

2.9.4 Reducing DAC requirements

The OFDM multiband technique proposed by [39] in which the spectrum is divided into multiple orthogonal OFDM bands, can relax the speed and bandwidth requirement of the signal converters while providing finer switching granularity and more network service flexibility. Data rates of 107 Gb/s have been demonstrated over 1000 km of uncompensated fiber, using this technique. The multiple OFDM bands can be multiplexed/demultiplexed without interband interference due to the orthogonality between bands. In [40] it is shown that a fraction of the OFDM spectrum can be received at a fraction of the overall data rate. This is shown in real-time using an FPGA to receive a 3.55 Gb/s subband of a 54 Gb/s multi-band signal, using 2.5 GSamples/s signal converters.

A recent work proposed a different technique of reducing the required sample rate of DACs, without needing RF mixers and maintaining a colorless design [41]. This technique uses the signal at baseband, making an efficient use of the modulator's bandwidth, and by adding a high frequency RF waveform to the signal (virtual carrier), allows the signal to be direct detected with a single photodiode. A 24 Gb/s transmission was shown (with 8-QAM modulation over OFDM) with a simple direct detection receiver and 5 GHz bandwidth DACs. This work has also been extended to include a polarization-multiplexed receiver with a 90 degrees optical hybrid, which uses the transmitted generated carrier as a local oscillator [42]. While enabling the transmission of

polarization-multiplexed signals, this approach, known as self-coherent, has the advantage that phase noise is less critical than in CO-OFDM systems. Furthermore, the frequency gap (between the virtual carrier and the OFDM signal) might be reduced due to the photodiodes balanced configuration, increasing the spectral efficiency.

2.9.5 Adaptively modulated OFDM

The OFDM technique allows the employment of an additional level of flexibility and robustness. The individual carriers of an OFDM signal might be manipulated by using different modulation formats according to the frequency response at that particular frequency, so that the modulation format can range from 256-QAM to BPSK, or even the carrier being dropped, depending on the transmission loss [43]. This scheme might operate adaptively if the frequency response is changing with time (due to multimode fiber links/PMD issues), or just be subject to an initial negotiation. This method is capable of exploiting the fiber bandwidth to its full potential, since compared to existing schemes it has higher transmission capacity, greater spectral efficiency, and is more tolerant to different launching conditions, modal dispersion and fiber types. Furthermore, it has been found that a 15-dB bandwidth specification is more adequate to describe the transmission capacity when using this technique than the typical 3-dB bandwidth. Additionally, an arbitrary amount of modal dispersion might be tolerated since the OFDM cyclic prefix length might be specified by design, originating a tradeoff with the maximum bandwidth achievable.

2.9.6 Real-time operation

Although a lot of progress in the optical OFDM range has been reported, with data rates in excess of 100 Gb/s, the majority of achievements rely on using off-line experiments with arbitrary waveform generators at the transmitter and fast sampling oscilloscopes at the receiver associated with offline signal processing. However, recently some progress has been shown concerning real-time implementations of these systems, which is pertinent to confirm the viability of deploying OFDM in real systems. The main limitations imposed on the implementation of real-time transceivers are related to the speed of signal converters (ADC/DAC) and DSP circuits, in particular FPGAs. In fact, although 50 GS/s capability has been commercially available in fast sampling scopes

since 2007 [44], they operate in burst mode. Presently, the fastest commercial continuous operation standalone ADC operates at 30 GS/s [45], while DACs are available for 25 GS/s. Nortel's commercial coherent receiver uses an application specific integrated circuit (ASIC) with four embedded 20 GS/s 6 bit ADCs [46]; this ASIC dissipates 21 Watts, whereas the complete modem dissipates 140 Watts. This circuit performs the functions of clock recovery, carrier recovery, polarization and PDM tracking; dispersion compensation is accomplished within the circuit using a FIR filter with 152 effective taps, which is able to compensate for over 3000 km of SMF with negligible degradation, making this kind of system very well suited to long haul transmission. Several works have already shown real-time implementations of transmitters, receivers and even transceivers.

2.9.6.1 Real-time transmitters

A research group at University College London has focused its research on the transmitter design, including pre-distortion to avoid receiver based equalization [47, 48]. The modulator drive voltage required to generate the pre-distorted waveform was obtained using non-linear digital filters implemented with a look-up table (LUT) and stored in a high speed SRAM of the FPGA. The nonlinear digital filter inverts the nonlinear characteristic of the MZM and provides appropriate biasing of the signal. The pre-distorted waveform was calculated offline for the central bit-period of each possible 11 bit sequence, accounting for fiber dispersion and nonlinearity. The main advantages of doing pre-distortion are the availability of a suitable clock for the DSP circuits at the transmitter avoiding clock recovery units [47], and the possibility of employing a direct-detection receiver which is simpler than a coherent receiver required to linearly translate the signal phase to the optical domain with subsequent compensation of fiber impairments. Transmission results obtained with this technique showed a BER of 10^{-3} after 641 km of non zero dispersion shifted fiber, with the maximum distance limited by the size of the Look Up Table (LUT) used for the compensating filters, which is limited by FPGA resources.

2.9.6.2 Real-time transceivers

A 6 Gb/s IM/DD transceiver based on FPGA was reported in [49], using 16-QAM encoded optical OFDM modulated data transmitted through 300 meters of multi-mode

fiber and a directly modulated laser. The design uses commercial off-the-shelf components such as the FPGA, ADC and DAC operating at 4 GS/s, low cost DFB laser, worst case multi-mode fiber and a simple single channel IM/DD system. This design is versatile in the sense that it could also be used with plastic optical fiber or single mode fiber, and both coherent and IM/DD systems, after some modifications. Additionally, experimental measurements suggest that higher data rates could be attainable with the same FPGA, potentially in excess of 40 Gb/s.

2.10 Summary

This chapter reviewed the fundamental principles of coherent optical transmission systems, possibilities of coherent optical receiver structures and optical modulation techniques with special attention to external modulation and multi-level signal generation. Finally, special attention has been directed to the fundamental principles of OFDM modulation, where both coherent and incoherent transmission models were discussed as well as its associated practical implementation constraints.

Chapter 3

Digital signal processing for coherent optical systems

3.1 Introduction

The previous chapter focused on the principles of coherent optical systems, stressing the possibilities enabled by the linear translation of the signal electric field from the optical to the electrical domain. In fact, the signal processing operations performed over a signal which is proportional to the electric field have the potential to effectively compensate any distortions suffered by the signal. Therefore, this chapter addresses the investigation of signal processing algorithms suitable for the compensation of transmission impairments, and the respective computer modeling of those impairments.

In coherent optical systems, the compensation of fiber impairments in the digital domain implies that, in principle, any linear distortion can be compensated in the DSP at 1 sample/symbol, as long as an analog matched filter precedes the sampler. However, the matched filter has several drawbacks: It may be more difficult to design than its digital equivalent and the exact phase of sampling is required to be known to sample the signal at its maximum energy. Moreover, if the channel response is unknown or time-varying, an adaptive equalizer is necessary whereas an adaptive analog matched filter may be difficult to design [31]. Even if the sample time is optimum, spectral overlap always occurs unless the system impulse response is a sinc function, which is not realizable in practice. A fractionally spaced equalizer (FSE) implements the matched filter and equalizer as a single unit [50]. The model of a system employing a FSE is shown in Fig. 3.1, where the following sequence of blocks is depicted: transmitter pulse

shape, channel impulse response, noise, anti-alias filter, sampling and finally the FSE.

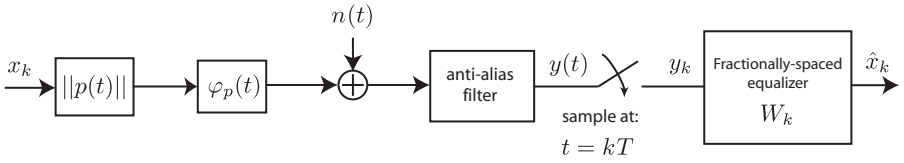

FIGURE 3.1: Modeling of a communication system, with transmitter pulse shape ($||p(t)||$), channel impulse response ($\varphi(t)$), noise ($n_p(t)$), anti-alias filter, sampling and fractionally spaced equalizer W_k

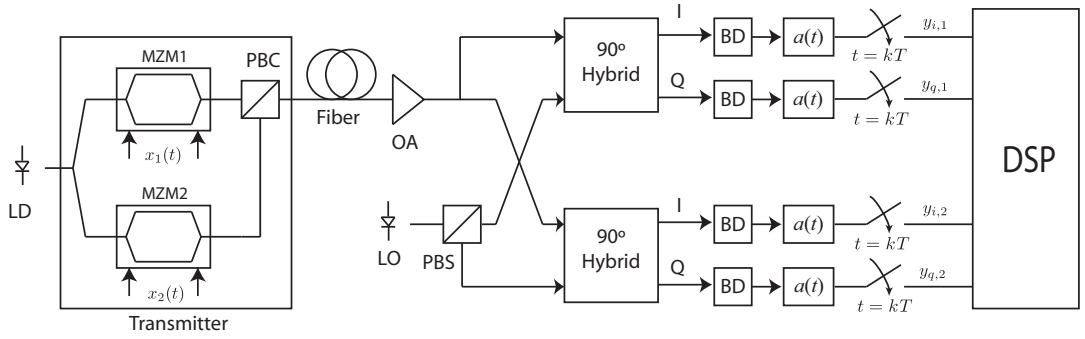

FIGURE 3.2: Coherent transmission system employing a phase and polarization diversity homodyne receiver. LD - Laser Diode, PBC - Polarization Beam Combiner, OA - Optical Amplifier, PBS - Polarization Beam Splitter, BD - Balanced Detector.

Although the system model shown in Fig. 3.1 reflects the basic blocks required to implement a simulation model in order to evaluate the performance of different DSP algorithms, it is pertinent to establish a relation between this model and the real set of devices necessary in order to effectively implement a long-haul optical communication system. Figure 3.2 represents a diagram of the optical coherent transmission system under study [51]. In the transmitter optical IQ-Modulators are used whereby the laser signal light is split into two orthogonal carriers and then modulated by Mach-Zehnder-Modulators, biased at minimum transmission, and driven by multi-level RF signals. For 16-QAM these RF signals have 4-levels. Then, the two data streams, polarized in orthogonal directions, are combined in a Polarization Beam Combiner and launched into the transmission channel (optical fiber). The signal is amplified to overcome attenuation in the long haul transmission. Additive White Gaussian Noise (AWGN) comes from the amplified spontaneous emission (ASE) of optical amplifiers which dominates over LO shot noise and thermal noise [28]. The mentioned MZM based transmitter, the optical fiber channel and the OA generated noise, correspond, respectively, to the transmitter pulse shape $||p(t)||$), channel impulse response ($\varphi(t)$), and noise ($n_p(t)$) parameters of

the model represented in Fig. 3.1. The optical multi-level modulation signal can be detected by an homodyne IQ-receiver, whose general configuration is valid for any M-PSK and M-QAM modulation format. Coherent detection involves beating the incoming signal with light from a LO laser [52], of near-identical wavelength and similar state of polarization (SOP), generating a photocurrent in the detector that corresponds to the beat product of the two lightwaves. Figure 3.2 shows how the signal is mixed with the LO in a phase/polarization diverse hybrid, therefore no polarization controllers being present, due to the polarization diversity configuration, where both signal and LO waves are separated by polarization beam splitters into orthogonal components, each going to a separate 90°-hybrid, where the signal is coherently detected using four balanced photodiodes. The four electrical output signals correspond to the I and Q components associated with the parallel and orthogonal LO polarizations. Finally, the signals are low-pass filtered by anti-aliasing filters $a(t)$ and sampled at the Nyquist rate or above, with $1/T = M/KT_s$, in order to be processed by in the DSP. It should be noticed that M/K relates to the fractional oversampling ratio, and its numerator M should not be confused with the alphabet of the constellation, since the meaning should always be obvious in each context. In terms of correspondence between the real set of devices and its model, the coherent detection approach using balanced photo-detectors can be simply modeled as an ideal linear translation of the electric field from the optical domain to the electrical domain. Finally, a direct correspondence can be established between the anti-alias filter and sampler of Fig.3.2 with their corresponding models in Fig. 3.1; the generic DSP element in the real system might implement a fractionally spaced equalizer, as well as additional compensation algorithms, if necessary.

3.2 Simulation model description

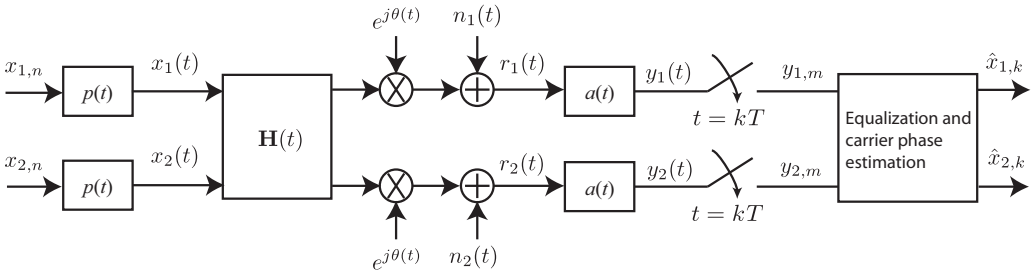

FIGURE 3.3: System canonical model

Rather than dealing with the complexities associated with practical implementations of coherent transmission systems, simulation platforms are a very effective way to allow the assessment of different fiber impairments mitigation algorithms. Therefore an investigation of the major issues concerning the modeling of the whole transmission system is pertinent. Figure 3.3 represents the canonical model of a coherent optical system employing polarization multiplexing [53]. The transmitted signals, in each polarization are given by:

$$x_l(t) = \sum_n x_{l,n} p(t - nT_s) \tag{3.1}$$

where $x_{l,n}$ is the n^{th} symbol transmitted in the l^{th} input polarization and $p(t)$ is the transmitted pulse shape. The received signal is then of the form:

$$\begin{bmatrix} r_1(t) \\ r_2(t) \end{bmatrix} = \left(\begin{bmatrix} h_{11}(t)\ h_{12}(t) \\ h_{21}(t)\ h_{22}(t) \end{bmatrix} \otimes \begin{bmatrix} x_1(t) \\ x_2(t) \end{bmatrix} \right) \cdot e^{j\theta(t)} + \begin{bmatrix} n_1(t) \\ n_2(t) \end{bmatrix} \tag{3.2}$$

where $r_m(t)$ and $n_m(t)$ denote the received signal and the channel noise on the m-th output polarization, respectively. The matrix $\mathrm{H}(t)$ represents the fiber impulse response, completely describing a dually polarized channel, which is mathematically represented as a 2×2 Multiple Input Multiple Output (MIMO) channel [17], including the effects of fiber chromatic dispersion and polarization mode dispersion. Notice that h_{ml} represents the fiber impulse response given from input polarization l to the output polarization m.

3.2.1 Fiber chromatic dispersion

Fiber chromatic dispersion manifests as a frequency dependence of the refractive index $n_r(\omega)$, leading to the propagation at different speeds from the different spectral components of an optical pulse, which leads to pulse broadening. Each spectral component travels at a speed of $c/n_r(\omega)$, c being the speed of light. In a mathematical perspective, the Taylor series expansion of the fiber mode-propagation constant $\beta(\omega)$ around the center frequency ω_0, gives a clear description on the effects of the several orders of fiber dispersion [54]:

$$\beta(\omega) = n(\omega)\frac{1}{c} = \beta_0 + \beta_1(\omega - \omega_0) + \frac{1}{2}\beta_2(\omega - \omega_0)^2 + \frac{1}{6}\beta_3(\omega - \omega_0)^3 + ..., \tag{3.3}$$

where

$$\beta_m = \left(\frac{d^m \beta}{d\omega^m} \right)_{\omega = \omega_0} \quad m \in \{0, 1, 2, 3, ...\} \tag{3.4}$$

The parameter β_1 is related with the inverse of the group velocity, so that $\beta_1 = 1/v_g$. Therefore, an optical pulse moves at the group velocity, while parameter β_2 represents the dispersion of the group velocity, a phenomenon called group-velocity dispersion (GVD). β_2 is the known as the GVD parameter. The dispersion parameter D is commonly used to describe the amount of fiber dispersion of a given system, which takes the value of $D = 17\,\mathrm{ps/nm{\cdot}km}$ for a typical single mode fiber, for a wavelength, λ, of 1550 nm. Parameter D is related with β_2 in the following way:

$$D = \frac{d\beta_1}{d\lambda} = -\frac{2\pi c}{\lambda^2}\beta_2 \tag{3.5}$$

The group velocity dispersion parameter is approximately $\beta_2 = -22\,\mathrm{ps}^2/\mathrm{km}$, for the typical case given above. In order to model the effect of fiber chromatic dispersion, the following partial differential equation may be written [5]:

$$\frac{\partial A(z,t)}{\partial z} = j\frac{D\lambda^2}{4\pi c}\frac{\partial^2 A(z,t)}{\partial t^2} \tag{3.6}$$

where A represents the pulse envelope, z the propagation distance and t is the time variable referenced to the moving pulse. Therefore, by taking the Fourier transform of equation (3.6), it is possible to obtain the frequency domain transfer function H_{CD} as follows:

$$H_{CD}(\omega) = \exp\left(j\frac{1}{2}\beta_2 L\omega^2\right) \tag{3.7}$$

where ω is the angular frequency and L represents the length of fiber. Effectively, fiber chromatic dispersion manifests as a phase shift and therefore it can be compensated using an all-pass filter having a transfer function of $1/H_{CD}(\omega)$, which can be approximated using both linear finite impulse response (FIR) and infinite impulse response (IIR) filters, which are non-recursive and recursive, respectively. Fig. 3.4 represents the coefficients of a FIR filter, calculated to invert the frequency response of a length of 100 km of single mode fiber having chromatic dispersion.

3.2.2 Polarization mode dispersion

The polarization reflects a fundamental property of an optical signal, the orientation of the electric field. An optical fiber can propagate two nearly degenerate modes, orthogonally polarized into the two principal axes of the fiber, the principle states of polarization. However, due to birefringence, these two modes suffer different phase delays during

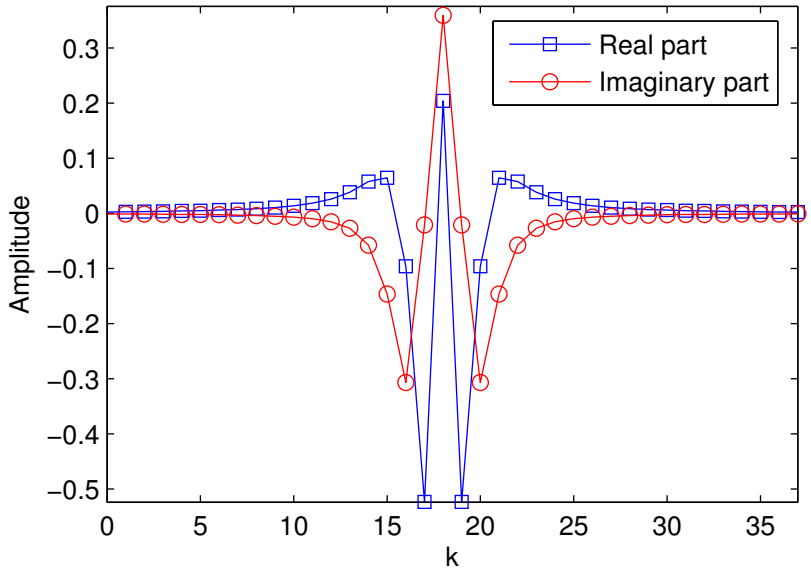

FIGURE 3.4: Impulse response (real and imaginary parts) of the filter which compensates the equivalent to 100 km of fiber chromatic dispersion, with 2 samples per symbol.

propagation, leading to output pulse broadening [55]. Birefringence is a result of both intrinsic factors, such as geometric irregularities of the fiber core or internal stresses on it, but also external factors such as bending or twisting of the fiber, which vary with distance [56]. Since the signal energy at a given wavelength occupies two orthogonal polarizations modes, the fiber varying birefringence leads the two modes to travel with different group velocities and the polarization orientation to rotate with distance. The resulting difference in propagation times, $\Delta\tau$, which corresponds to the differential group delay (DGD), results in pulse spreading. This reflects the so called polarization mode dispersion effect. Additionally, since the physical perturbations causing birefringence are temperature dependent, PMD is a time-varying effect. Therefore, the mean value of the differential group delay is a useful means of characterizing the total fiber PMD after a given distance, and can be expressed as:

$$\langle \Delta\tau \rangle \approx D_{\mathrm{PMD}} \sqrt{L} \tag{3.8}$$

where L represents the fiber length and D_{PMD} is the PMD coefficient of the fiber in $\mathrm{ps}/\sqrt{\mathrm{km}}$. Typical values of D_{PMD} range from 0.1 to 1.0 $\mathrm{ps}/\sqrt{\mathrm{km}}$ [56], with most single mode fibers having approximately 0.1 $\mathrm{ps}/\sqrt{\mathrm{km}}$. When the polarization of the fiber is taken into account, the frequency response of the fiber can be described by:

$$H(\omega) = T(\omega) \times \exp\left(j\frac{1}{2}\beta_2 L\omega^2\right) \tag{3.9}$$

where chromatic dispersion is accounted up to second order and $T(\omega)$ is the fiber Jones Matrix accounting for PMD. $T(\omega)$ is given by:

$$T(\omega) = \begin{bmatrix} u_1(\omega) & u_2(\omega) \\ -u_2^*(\omega) & u_1^*(\omega) \end{bmatrix} \tag{3.10}$$

where $|u_1(\omega)|^2 + |u_2(\omega)|^2 = 1$. The numerical modeling of the Jones matrix is obtained by a concatenation of unequal sections of birefringent fiber, which can be expressed as [57]:

$$T(\omega) = \prod_{n=1}^{N_{\text{PMD}}} B_n(\omega) R(\alpha_n) \tag{3.11}$$

where

$$B_n(\omega) = \begin{bmatrix} \exp\left(j\frac{1}{2}\sqrt{\frac{3\pi h_n}{8}}\omega D_{\text{PMD}} + j\phi_n\right) & 0 \\ 0 & \exp\left(-j\frac{1}{2}\sqrt{\frac{3\pi h_n}{8}}\omega D_{\text{PMD}} + j\phi_n\right) \end{bmatrix} \tag{3.12}$$

$$R(\alpha_n) = \begin{bmatrix} \cos\,\alpha_n & \sin\,\alpha_n \\ -\sin\,\alpha_n & \cos\,\alpha_n \end{bmatrix} \tag{3.13}$$

N_{PMD} is the number of fiber segments ($N_{\text{PMD}} = 80$ in the simulated model) and $B_n(w)$ represents the birefringence matrix of the n-th segment of length h_n. $R(\alpha_n)$ is the matrix of a rotator that represents the random coordinate transformation of the birefringent segment axes, producing therefore, a frequency independent differential group delay in each section. The phase angle ϕ_n accounts for the small temperature fluctuation along the fiber, being a stochastic variable with a uniform distribution between 0 and 2π. For a given total PMD $\langle\tau\rangle$ and fiber length L, the size of each segment was randomly generated from a Gaussian distribution around the mean length $h_n = L/N_{\text{PMD}}$ with standard deviations Δh varying from $0 - 30\%$ of the mean length, in order to produce non-periodic variations of the DGD over the frequency spectrum, and achieve a Maxwellian distribution. Furthermore, as the variation of $T(\omega)$ as a function of frequency is very slow on the length scale given by h_n, it is only necessary to evaluate it at a few frequencies, intermediate values being obtained through interpolation [58].

3.2.3 Phase noise

After adding the channel distortion effect, the signal is noise loaded, with both Gaussian noise and phase noise. In semiconductor lasers, phase noise results from spontaneous emission of the laser gain medium into the resonator modes, so that the signal amplified on each pass through the laser cavity has slightly different phase, leading to a random evolution of the signal phase at the laser output [59]. This translates into random fluctuations of the instantaneous frequency of the laser, which is expressed by its finite line-width. Phase noise is usually characterized as a Wiener process [60], described in the discrete domain as:

$$\theta_k = \sum_{-\infty}^{k} \nu_m$$

where the ν_m's are independent identically distributed (i.i.d.) Gaussian random variables with zero mean and variance $\sigma_p^2 = 2\pi\Delta\nu T_s$. $\Delta\nu$ is generally assumed to be the combined line-widths of the signal and LO lasers (also known as the beat line-width), and T_s is the symbol period [1]. The laser line-width parameter is considered to be measured at full width at half maximum, also referred to as 3-dB line-width. In the considered numerical model, the LO laser is assumed to be ideal, whereas the transmitter laser is assumed to have a phase noise equal to the sum of the line-widths of the two lasers. Such approximation is valid given that the phase noises of the lasers in the transmitter and receiver are uncorrelated [3], and provided that optical chromatic dispersion is used, so that the phase noise variation is negligible within the memory length of the channel impulse response [61], allowing the commuting between the channel pulse response ($\mathrm{H}(t)$) and the transmitter phase noise ($e^{j\theta(t)}$). In fact, when no optical dispersion compensation is used, a penalty of 0.5 dB and 1.2 dB would be incurred in a system having a LO laser line-width of 1.3 MHz for 4000 km and 10000 km of length, respectively, stemming from the receive laser phase noise enhanced by the electronic equalization.

3.2.4 Receiver based compensation

With reference to Fig. 3.3, letting $q(t) = a(t) \otimes h(t) \otimes p(t)$ and $n_l^{'} = a(t) \otimes n_m(t)$ the received signal $y_m(t)$ after the anti-alias filters can be written as:

$$y_m(t) = r_m(t) \otimes a(t) = \sum_{n} \sum_{l=1}^{2} x_{l,n} q_{ml}(t - nT_s) e^{j\theta(t)} + n_l^{'}(t) \tag{3.14}$$

The sampling occurs at a rate of 2 samples per symbol, which was previously shown to be sufficient. In fact, [31] has shown that a small penalty can be obtained if 1.5 samples per symbol are used in conjunction with a 5-th order Butterworth anti-aliasing filter. In this way, the results become almost insensitive to the sampling time error, since the FSE synthesizes, via its transfer characteristic, the necessary phase adjustment [50].

The subsequent operation consists in linear equalization, where blocks of samples of the incoming signal are taken (with a size equal to the equalizer length) and the minimum-mean-squared-error (MMSE) estimate of the k^{th} symbol $\tilde{x}_k$ is calculated. The optimum solution for the coefficients is obtainable by the Wiener-Hopf equation [31]. The equalizer can be efficiently implemented if partitioned in two parts as depicted in Fig. 3.5 [5]. The first part is responsible for fixed impairments, such as chromatic disper-

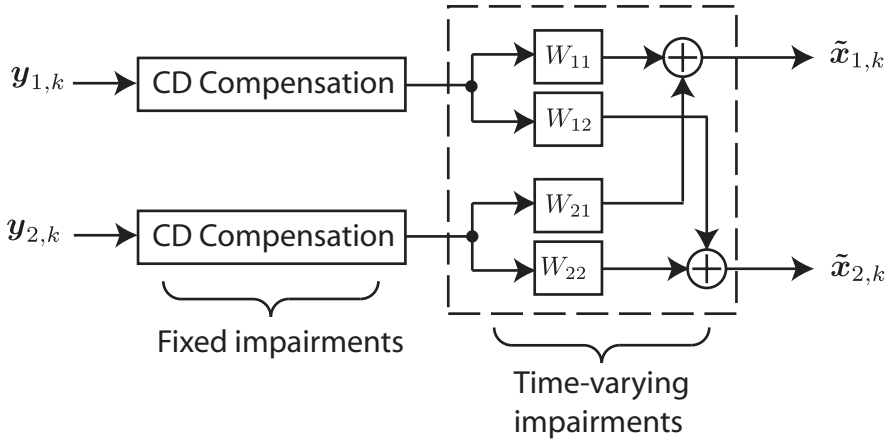

FIGURE 3.5: Equalizer butterfly structure

sion, as well as pulse shape matching (which synthesizes the sampling phase adjustment). Additionally, time-varying impairments such as polarization rotations and PMD might be compensated by the second part, which is performed through the convolution of the signal with a bank of four complex valued FIR filters, arranged in a butterfly structure, in order to allow for polarization demultiplexing. This implementation sectioning is a potential advantage for a practical implementation, since the first block allows for large amounts of CD to be compensated without requiring permanent updates, which eases the DSP implementation complexity.

3.2.4.1 MMSE mathematical description

As denoted previously, the combined impulse response of the transmitter pulse shape, channel impulse response and anti-alias filter is represented by $q(t)$. The mathematical analysis provided here neglects the effect of polarization for simplicity, so that the received signal can be represented by:

$$y(t) = \sum_{n} x_n \cdot q(t - nT_s)e^{j\theta(t)} + n'(t) \tag{3.15}$$

The continuous signal $y(t)$, when sampled at instants $t = (k - iK/M)T_s$, $i = 0, ..., M/K-1$ where M/K represents the oversampling ratio, is represented by a column vector $\boldsymbol{y}_k$ having a length equal to the oversampling ratio, $\boldsymbol{q}_k$ and $\boldsymbol{n}_k$ being analogously the oversampled vectorial representation of $q(t)$ and $n'(t)$. Therefore, when neglecting the phase noise, the sampled $y(t)$ signal can be written as:

$$y([k - iK/M]T_s) = \sum_{n=-\infty}^{\infty} x_n \cdot q([k - iK/M - n]T_s) + n'([k - iK/M]T_s) \tag{3.16}$$

According to [50], assuming the combined response $q(t)$ extends only over a finite interval $0 \leqslant t \leqslant \nu T_s$. This assumption requires any nonzero component of $q(t)$ outside of this time interval to be negligible, so that $\boldsymbol{q}_k = 0$ for $k < 0$ and for $k > \nu$. Therefore, $\boldsymbol{y}_k$ is the result of the convolution of the input signal x_k with the combined response $\boldsymbol{q}_k$, calculated only over its the non-zero extension:

$$\boldsymbol{y}_k = \sum_{n=0}^{n=\nu} x_{k-n} \cdot \boldsymbol{q}_n + \boldsymbol{n}_k \tag{3.17}$$

where $\boldsymbol{y}_k$, $\boldsymbol{q}_k$ and $\boldsymbol{n}_k$ are vectors having a length equal to the oversampling ratio, with indexes on the form of $\{kT_s, kT_s - K/MT_s, ..., kT_s - (M/K - 1)/(M/K)T_s\}$. Equation (3.17) can be represented as a vectorial multiplication, such that:

$$\boldsymbol{y}_k = \begin{bmatrix} \boldsymbol{q}_0, & \boldsymbol{q}_1, & ..., & \boldsymbol{q}_\nu \end{bmatrix} \begin{bmatrix} x_k \\ x_{k-1} \\ \vdots \\ x_{k-\nu} \end{bmatrix} + \boldsymbol{n}_k \tag{3.18}$$

The expression in equation (3.18) can be generalized in order to be defined over the

length of the equalizer which takes $\boldsymbol{y}_k$ as input. Assuming an equalizer having $N_f \cdot M/K$ coefficients, the oversampled y(t) can be represented by N_f successive M/K-tuples of samples:

$$\begin{aligned}
\boldsymbol{Y}_k &= \begin{bmatrix} \boldsymbol{y}_k \\ \boldsymbol{y}_{k-1} \\ \vdots \\ \boldsymbol{y}_{k-N_f+1} \end{bmatrix} \\
&= \begin{bmatrix} \boldsymbol{q}_0 & \boldsymbol{q}_1 & \cdots & \boldsymbol{q}_\nu & 0 & \cdots & 0 \\ 0 & \boldsymbol{q}_0 & \boldsymbol{q}_1 & \cdots & \boldsymbol{q}_\nu & \cdots & 0 \\ \vdots & \vdots & \ddots & \ddots & \ddots & \vdots & \vdots \\ 0 & \cdots & 0 & \boldsymbol{q}_0 & \boldsymbol{q}_1 & \cdots & \boldsymbol{q}_\nu \end{bmatrix} \begin{bmatrix} x_k \\ x_{k-1} \\ \vdots \\ x_{k-N_f-\nu+1} \end{bmatrix} \\
&+ \begin{bmatrix} \boldsymbol{n}_k \\ \boldsymbol{n}_{k-1} \\ \vdots \\ \boldsymbol{n}_{k-N_f+1} \end{bmatrix}
\end{aligned} \tag{3.19}$$

The expression of $\boldsymbol{Y}_k$ accommodates the oversampled representation of the transmission channel, and can be written in a simplified manner:

$$\boldsymbol{Y}_k = \boldsymbol{Q}\boldsymbol{X}_k + \boldsymbol{N}_k \tag{3.20}$$

where matrix $\boldsymbol{Q}$ has a size of $(N_f \cdot M/K) \times (N_f + \nu)$, $\boldsymbol{X}_k$ denotes the data vector and $\boldsymbol{N}_k$ denotes the noise vector. In the case of M/K being a rational fraction, the rows of $\boldsymbol{Q}$ become independent from each other, becoming dependent on the specific sampling instants. The vector $\boldsymbol{Y}_k$ is the input to the equalizer having a $N_f M/K$-dimensional set of coefficients W, such that its output can be defined by:

$$\tilde{x}_k = W\boldsymbol{Y}_k \tag{3.21}$$

A typical delay Δ of half the equalizer filter length is generally selected, in order to allow for causality. Therefore, the error at the output of the equalizer can be shown to be:

$$e_k = x_{k-\Delta} - \tilde{x}_k = x_{k-\Delta} - W\boldsymbol{Y}_k \tag{3.22}$$

The minimum squared error can be minimized when the equalizer incoming signal becomes uncorrelated with the error signal, according to the orthogonality principle [22], such that:

$$E\{e_k \boldsymbol{Y}_k^*\} = E\{x_{k-\Delta} \boldsymbol{Y}_k^*\} - W E\{\boldsymbol{Y}_k \boldsymbol{Y}_k^*\} \tag{3.23}$$

Equation (3.23) is composed by a cross-correlation vector (left term) and a autocorrelation matrix (right term). Therefore, it can be easily solved to give the optimum coefficients (Wiener-Hopf equation):

$$W_{\text{opt}} = R_{x\boldsymbol{Y}} R_{\boldsymbol{YY}}^{-1} \tag{3.24}$$

where $R_{ab} = E\{ab^*\}$ denotes the cross-correlation function between signals a and b. Additionally, $R_{x\boldsymbol{Y}}$ can be decomposed in the following manner:

$$\begin{aligned} R_{x\boldsymbol{Y}} &= E\{x_{x-\Delta} \boldsymbol{Y}_k^*\} = E\{x_{k-\Delta} \boldsymbol{X}_k^*\} \boldsymbol{Q}^* + E\{x_{k-\Delta} \boldsymbol{N}_k^*\} \\ &= E_x \mathbf{1}_\Delta \boldsymbol{Q}^* + 0 \end{aligned} \tag{3.25}$$

which results from the expansion of the equalizer input signal using the result $\boldsymbol{Y}_k = \boldsymbol{Q}\boldsymbol{X}_k + \boldsymbol{N}_k$. E_x represents the average energy of the transmitted signal, and $\mathbf{1}_\Delta$ is a vector of length $N_f + \nu$, being 0 for every coefficient except the central coefficient which is one. Furthermore, the autocorrelation of the equalizer input signal can also be decomposed as:

$$\begin{aligned} R_{\boldsymbol{YY}} &= E\{\boldsymbol{Y}_k \boldsymbol{Y}_k^*\} = \boldsymbol{Q} E\{\boldsymbol{X}_k \boldsymbol{X}_k^*\} \boldsymbol{Q}^* + E\{\boldsymbol{N}_k \boldsymbol{N}_k^*\} \\ &= E_x \boldsymbol{Q}\boldsymbol{Q}^* + R_{\boldsymbol{NN}} \end{aligned} \tag{3.26}$$

where $R_{\boldsymbol{NN}}$ represents the noise autocorrelation matrix. It can be obtained by filtering the channel noise $n(t)$ with the anti-alias filter $a(t)$, which gives $n'(t)$, and then computing the Inverse Fourier Transform of its power spectral density.
The previous analysis can be extended to include both polarizations, by writing the equalizer output signal as:

$$\tilde{\boldsymbol{x}}_k = \begin{bmatrix} \tilde{\boldsymbol{x}}_{1,k} \\ \tilde{\boldsymbol{x}}_{2,k} \end{bmatrix} = \begin{bmatrix} W_{11}\ W_{21} \\ W_{12}\ W_{22} \end{bmatrix} \begin{bmatrix} \boldsymbol{y}_{1,k} \\ \boldsymbol{y}_{2,k} \end{bmatrix} = \boldsymbol{W}^T \boldsymbol{Y}_k \tag{3.27}$$

where $\boldsymbol{W}^T$ is the 2×2 equalizer coefficient matrix, each of its 4 elements W_{ml} consisting

of a set of coefficients calculated to compensate the channel impulse response given from input polarization l to the output polarization m.

Although the details involved in the calculation of the optimum set of coefficients that compensate the combined system impulse response have been presented, this is only applicable as long as the channel stays static in time. However, in practice, H is time-varying due to PMD, and an adaptive equalizer is necessary. Therefore, the least mean square (LMS) or the recursive least squares (RLS) algorithms [22] can be used to update the coefficients, and track the time varying minimum of the cost function.

3.2.4.2 The LMS algorithm

Fig. 3.6 describes a diagram block of a transmission system employing a LMS equalizer. For simplicity, the diagram shows only the implementation for a single polarization, its extension to both polarizations being straightforward, consisting of the repetition of the "Symbol Decision" and error calculation blocks for the equalizer output corresponding to the orthogonal polarization.

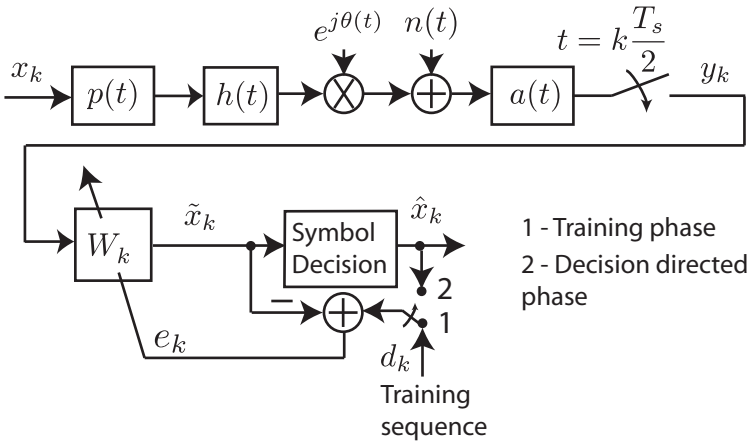

FIGURE 3.6: Diagram of a transmission system employing a LMS equalizer

The LMS coefficient update equation is given by [22]:

$$W_{k+1} = W_k + \mu \cdot e_k^* \cdot y_k \tag{3.28}$$

where W_k is the varying set of equalizer coefficients, which should be initialized to a set of zeros equal to the equalizer length, μ is the algorithm step size, e_k is the error signal and y_k is the equalizer input signal. These variables are defined in the following matrix

form:

$$e_k = \begin{bmatrix} e_{1,k} \\ e_{2,k} \end{bmatrix} \quad y_k = [y_{1,k}\ y_{2,k}] \tag{3.29}$$

The equalizer will try to minimize, in a mean squares sense, the error signal e_k. For the standard LMS algorithm, the error signal can be defined in the following way:

$$e_k = d_k - \tilde{x}_k \tag{3.30}$$

where $\tilde{x}_k$ is the equalizer output symbol, which is an estimate of the transmitted symbol x_k, d_k is the desired signal, which can be associated with a training sequence (typically before convergence), or with a decided output of the equalizer (after convergence), which is called LMS decision directed mode (LMS-DD). However, training sequences represent an additional overhead in terms of transmission, and could be required frequently if the characteristics of the channel vary significantly in time, as an example, due to time varying impairments. In this way, it is relevant to analyze an alternative method for adapting the equalizer coefficients, the constant modulus algorithm.

3.2.4.3 The CMA algorithm

The CMA algorithm is a variation of the LMS algorithm, which allows the recovery of the signal in blind mode. A diagram of a transmission system employing CMA equalization is described in Fig. 3.7.

This approach exploits the properties of data, namely for the typical transmission modulation of polarization division multiplexed QPSK (PDM-QPSK), where the signal for each polarization should have constant modulus. Fig. 3.8(a) shows the constant modulus of the QPSK constellation. However, when the constellation in consideration does not have constant modulus, as in the case of higher order modulation (Fig. 3.8(b)), the CMA algorithm has also been shown to provide good results [10].

Although the amplitude and frequency of an M-PSK signal are nominally constant, channel distortion lead to interferences that change these properties. In this way, the CMA algorithm operates by tracking the variability of the signal amplitude, and permanently trying to restore the amplitude to its nominal value, which eventually leads to an improved quality of the received signal and consequently to more correct decisions.

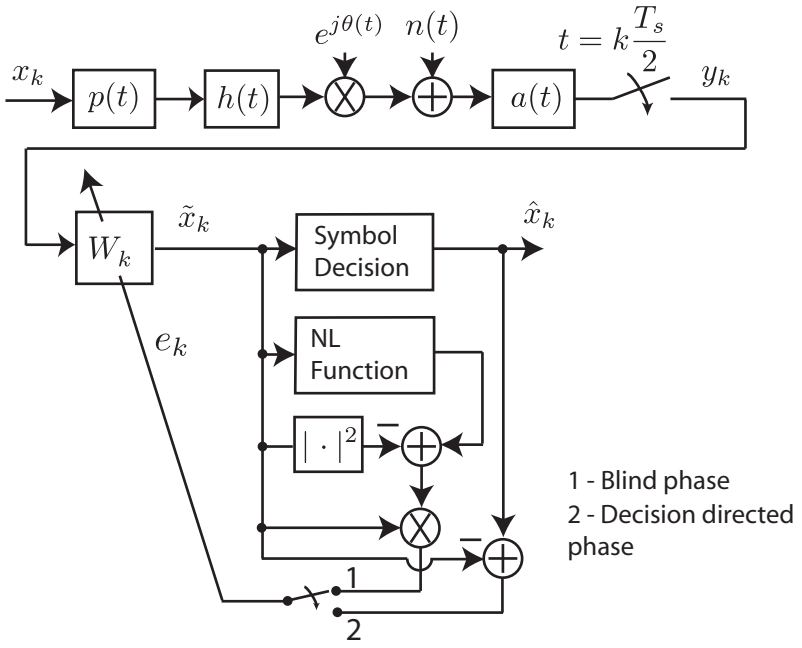

FIGURE 3.7: Diagram of a transmission system employing a CMA equalizer. The block "NL Funtion" calculates the target convergence modulus.

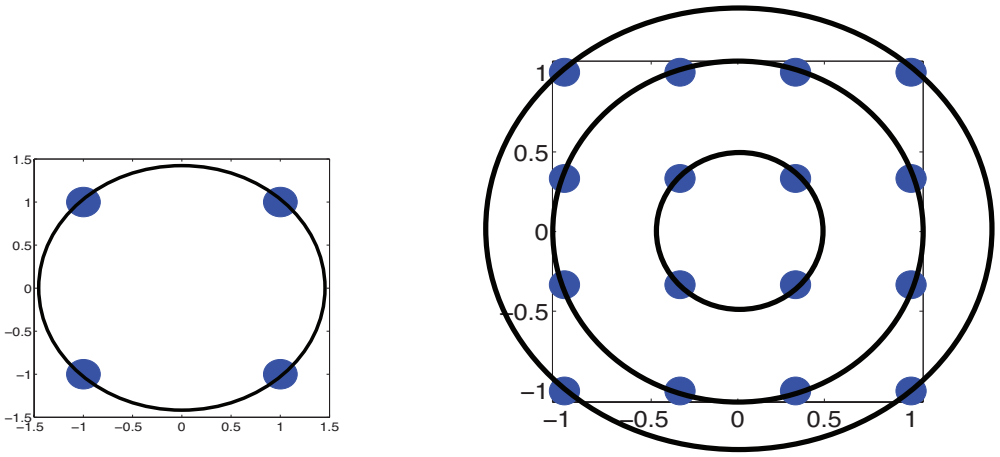

(a) QPSK (b) 16-QAM

FIGURE 3.8: Analysis of QPSK and 16-QAM constellation modulus.

Effectively, the error signal for the CMA algorithm can be expressed as:

$$e_k = (R_2 - |\tilde{x}_k|^2)\tilde{x}_k \tag{3.31}$$

where R_2 represents the output of the non-linear function block of Fig. 3.7, which is given by [10]:

$$R_2 = \frac{E[|x_k|^4]}{E[|x_k|^2]} \tag{3.32}$$

In order to initialize the algorithm, all tap weights W_k are set to zero with the exception of the central tap which is set to one. As soon as convergence is achieved, the equalizer may switch into decision directed mode (LMS-DD algorithm), where the equalizer tries to approximate its output with the nearest constellation symbol.

3.3 Compensation of dispersion impairments

Having discussed the simulation model, it becomes relevant to analyze the issues associated with the compensation of dispersion impairments.

Dispersion compensation on IM/DD systems is not very efficient due to the non-linear O/E conversion in the photodiode, with loss of phase information. In contrast to IM/DD systems, complete equalization of CD and PMD is possible in coherent systems, in the electrical domain, as the equalizer operates on signals proportional to the electric field.

Ip and Kahn showed that a linear FSE can compensate for any linear propagation impairment in a dually polarized coherent optical system, given sufficient oversampling rate, pulse shape and number of equalizer taps are used [3]. The authors state that if the previous conditions are satisfied, any amount of CD and first order PMD can be compensated with less than a 2 dB target penalty (almost entirely due to CD penalty). In order to meet the target penalty, the filter length N_f is directly proportional to the amount of dispersion and satisfies:

$$|\beta_2| L_{fiber} R_s^2 (M/K) \approx 0.15 N_f \tag{3.33}$$

$$N_f = \tau_{DGD} M/K T_s \tag{3.34}$$

for compensating CD and PMD, respectively, where R_s is the data-rate, M/K is the fractional oversampling rate and τ_{DGD} is the DGD. Typically, the required filter length will be imposed by CD, not by PMD. The value of N_f dictated by CD considerations is more than enough to compensate for PMD [31]. Fig. 3.9 shows the filter length required to compensate a specified amount of chromatic dispersion, for two sets of anti-aliasing filters, Bessel and Butterworth, and for three different values of oversampling rate $M/K = \{1, 3/2, 2\}$. It may be confirmed from these results that the most efficient value of oversampling rate is 3/2, since this is the option that allows the compensation of the greatest quantity of fiber dispersion, with the least number of filter coefficients. This

result is also supported by [31]. The observable difference between using a Bessel and a Butterworth filter is not significant. While the Bessel filter induces a linear phase variation, the Butterworth filter induces a nonlinear phase variation; however this nonlinear phase is ultimately compensated by the FSE.

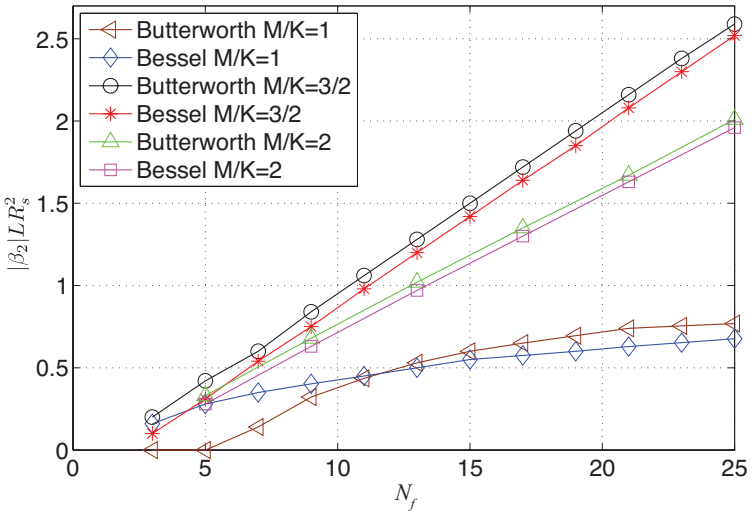

FIGURE 3.9: Amount of compensated fiber dispersion $|\beta_2|LR_s^2$ versus filter length.

Fig. 3.10 plots the maximum tolerable PMD versus filter length. It shows that polarization mode dispersion is also a linear impairment, which can be effectively compensated as long as a FSE with sufficient number of taps is allocated in order to accommodate the length of the impulse response induced by PMD. In fact, a channel with a differential group delay of τ has an impulse response exhibiting two peaks at a distance of $N_f = \tau M/KT_s$ samples. Therefore, since the length of the compensating filter is mainly determined by the chromatic dispersion impairment, the results of Fig. 3.10 simply show the linear impact of PMD for a Bessel antialiasing filter with $M/K = 2$, while the effect of different antialiasing filters and oversampling rates is not assessed, [31] providing further results concerning the mentioned analysis.

3.3.1 Simulation results

In the following simulation results, a NRZ pulse shape $p(t)$ was considered, which was obtained by passing an ideal rectangular pulse train by a 3th order low pass Bessel filter with a 3-dB bandwidth of 80% of the symbol-rate. For the anti-alias filter $a(t)$, 3rd order low pass Bessel filters were used.

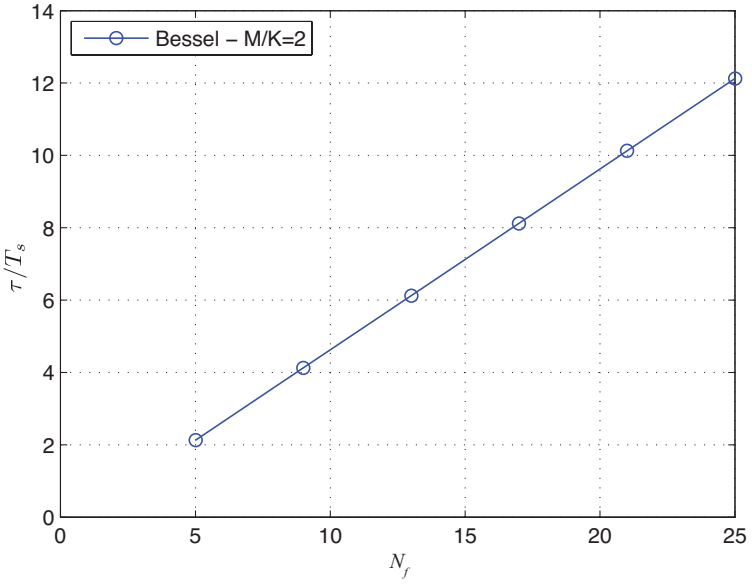

FIGURE 3.10: Maximum amount of tolerable PMD τ/T_s versus filter length.

In Fig. 3.11, the obtained bit error rate versus input SNR per bit is shown, for both QPSK and 16-QAM cases.

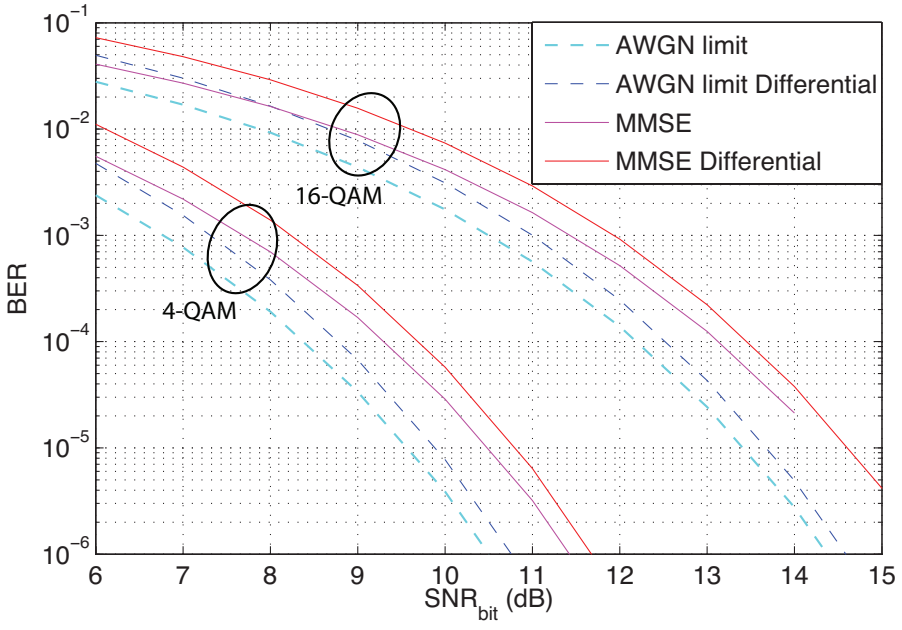

FIGURE 3.11: Bit error rate versus SNR per bit.

By defining the SNR per symbol as:

$$\mathrm{SNR} = \frac{P_{\mathrm{tx}} T_s}{N_0} = \frac{E_s}{N_0} \tag{3.35}$$

where P_x is the mean symbol power, E_s is the mean symbol energy and N_0 is the noise power spectral density, a constant of $10\log_{10}[\log_2(M)]$ dB is subtracted to the SNR to reference it per bit, where M is the constellation size. Therefore, the SNR per bit is defined as:

$$\begin{aligned} \mathrm{SNR}_{\mathrm{bit}} &= \frac{P_x T_b}{N_0} = \frac{E_b}{N_0} \\ \mathrm{SNR}_{\mathrm{bit}}\,(\mathrm{dB}) &= \mathrm{SNR}\,(\mathrm{dB}) - 10\log_{10}[\log_2(M)] \end{aligned} \tag{3.36}$$

The MMSE result (red lines) gives the upper limit on the achievable performance, in the MMSE sense, for a given system pulse response (set of transmission and receiver filters) and signal constellation, obtained by calculating the optimum 13-tap set of coefficients that maximizes the output SNR [31].

Fig. 3.11 also shows results obtained using differential coding, which have poorer performances. The usage of differential coding might be useful in order to cope with situations where the signal is highly affected by phase noise. In such a scenario, it is preferable to make decisions based on differences between consecutive symbol phases rather than on a fixed constellation boundary based approach [6]. The disadvantage of differential encoding is that Gray codes can not be employed, which means that the bit errors to symbol errors relation is increased. For QPSK, the probability of bit error (BER) becomes the same as the probability of symbol error (SER), instead of one half, which leads to a 0.54 dB of penalty at BER= 10^{-3} as can be observed in Fig. 3.11. For 16-QAM, the bit to symbol mapping used was that of [1], where the two least significant bits (LSB) are Gray coded, and mapped in order to provided rotational symmetry, so that even if the constellation rotates 90 degrees, these two bits are still the same. Additionally, the two most significant bits are differentially encoded. In this way, the bit error probability becomes 1/3 of the symbol error probability instead of 1/4 for a fully Gray coded constellation. The symbol error rate also increases, due to the closer phase spacing of 16-QAM mid-amplitude symbols. These two factors lead to 0.5 dB of penalty at BER= 10^{-3} compared to a fully Gray coded constellation.

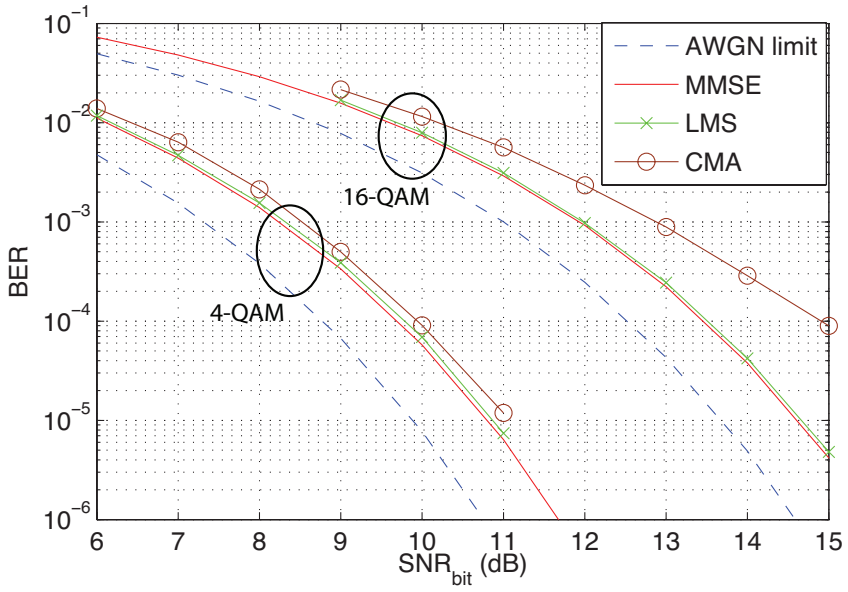

FIGURE 3.12: Bit error rate versus SNR.

Starting in Fig. 3.12, only differential results are considered from hereon, for compatibility reasons with the following chapter. The LMS and CMA results also consider the system pulse response used with the MMSE results, and were obtained by 13-tap adaptive filters evaluated after convergence, using Monte-Carlo simulations. The step size parameter, μ, influences both the convergence speed and residual error and therefore its value was optimized for the specific simulation parameters to $\mu = 1 \times 10^{-3}$. As expected, the LMS curve represented by "$\times$" (green line) closely matches the MMSE result, since it considers the same MSE performance surface, using the steepest descent method to iteratively track the minimum. The result represented by "$\circ$" (brown lines) corresponds to the constant modulus algorithm (CMA). Its performance is fairly good for QPSK, but very poor for 16-QAM. In this case the CMA cost function is not optimized since the constellation has 3 types of points having different modulus, as seen in Fig 3.8(b). In conclusion, although both LMS and CMA algorithms provide similar performance for QPSK , for 16-QAM the CMA performance is affected by the constellation parameters. This fact is considered in the following chapter when comparing the performance of both LMS and CMA algorithms for carrier phase estimation.

3.4 Summary

In this chapter, the main types of linear fiber impairments were investigated, in order to create a valid computer simulation model. Subsequently, the different algorithms suitable for implementation in a digital coherent receiver were studied, focusing on the MMSE criterion. In this context, the LMS and CMA adaptive algorithms were discussed, and their associated theoretical performance bounds were obtained.

Chapter 4

Carrier phase estimation

4.1 Introduction

Coherent optical systems employing compensation of fiber impairments in the digital domain, avoid the usage of optical PLLs, since the implementation of carrier synchronization can be done digitally, allowing for a free running local oscillator, while tolerating 50% to 100% wider laser line-widths than PLL [1].
The constant modulus algorithm is the most used blind adaptive equalization algorithm, essentially because of its robustness and ability to converge prior to phase recovery [62]. In order to cope with laser phase noise, an elegant solution consists in using the CMA for initial adaptation, avoiding training sequences and enabling subsequent independent CPE. Once equalizer convergence has been achieved, there is benefit in switching to decision directed mode, driven from symbol decision errors, which is LMS based, improving the demodulator SNR performance [62]. However, at this point, the phase must be estimated and its value considered in the error signal, precluding the use of independent CPE. Additionally, the equalizer decision feedback might be critical in high-speed parallelized DSP, which would lead to the usage of the CMA algorithm. On the other hand, CMA is not optimized for 16-QAM multiple modulus constellation.

In this chapter the performance of a phase estimation algorithm combined with a DD equalizer in a feedback configuration is assessed and compared to the approach consisting of CMA followed by CPE, both for series and parallel implementations. A recent work [3] suggests the integration of an adaptive digital equalizer with carrier synchronization using decision feedback. Although this concept has been suggested in [3, 62], a detailed study on the algorithms performance has never been done, specially taking into

account the parallelization. This is discussed in this chapter and has been the subject of several publications [63–65]. The actual simulation of the QPSK and 16-QAM coherent optical system was carried out in MATLAB.

4.2 Model description

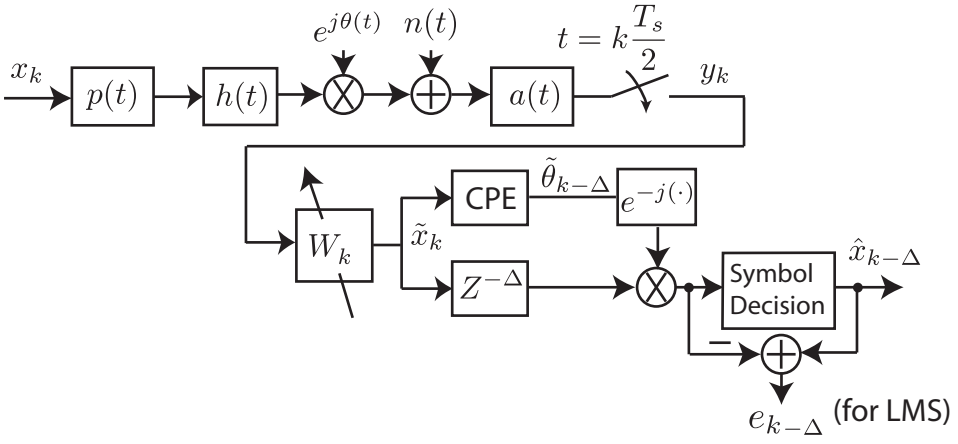

FIGURE 4.1: System canonical model

Figure 4.1 represents the canonical model of a single polarization coherent optical system, where $p(t)$ is the pulse shape and $h(t)$ represents the fiber impulse response, which might include the effects of Chromatic Dispersion and Polarization Mode Dispersion. The signal is noise loaded, with both phase noise $\theta(t)$ and Additive White Gaussian Noise noise (AWGN) $n(t)$. Phase noise is usually characterized as a Wiener process, being modeled as in [1]. The sampling occurs at a rate of 2 samples per symbol, which was previously shown to be sufficient. Actually, 1.5 samples/symbol in conjunction with a 5-th order Butterworth antialiasing filter - $a(t)$, was shown to allow for a penalty of less than 2 dB [31], as seen in Chapter 3. Linear equalization follows, by performing a convolution with a complex valued $T_s/2$ spaced FIR filter. The linear equalizer calculates $\tilde{x}_k$, the minimum-mean-squared-error estimate of the k-th transmitted symbol x_k. The optimum solution for the coefficients is obtainable by the Wiener-Hopf equation [31]. Furthermore, the channel is considered to be time varying due to PMD, so its frequency response is not exactly known and an adaptive equalizer is desirable. Therefore, the least mean squares algorithm can be used to continually adjust the coefficients. The

LMS coefficient update equation is given by:

$$W_{k+1} = W_k + \mu \cdot (e^*_{k-\Delta_1}) \cdot (y_{k-\Delta_1}) \tag{4.1}$$

where W is the equalizer coefficient vector, μ is the algorithm step size, e_k is the conjugated error, y_k is the equalizer input vector [3], and Δ_1 is an arbitrary delay that might be greater than zero if the required coefficient update-rate is lower than the symbol-rate, due to slowly varying impairments such as PMD. The error signal is calculated differently for LMS and CMA, as seen in Chapter 3.

4.3 Carrier phase estimation

In the canonical model of Fig. 4.1, the multiplication by the phase noise $e^{j\phi(t)}$ manifests as a rotation of the received constellation. Additionally, phase noise is a Wiener process with temporal correlation, which means the phase at any symbol period is likely to have a value similar to the phases at adjacent symbols, which allows the usage of signal processing techniques in order to mitigate it. Assuming the signal at the output of the equalizer is perfectly compensated, it is only impacted by phase noise and AWGN, with the following general form:

$$\tilde{x}_k = W_k y_k = x_k e^{j\theta_k} + n_k \tag{4.2}$$

where x_k is the complex valued transmitted symbol at the k-th symbol period, θ_k is the carrier phase, and n_k is AWGN. Figure 4.2 shows a diagram where the components of the received phase are divided in θ_k, the carrier phase, and $n_k^{'}$, the phase perturbation induced by AWGN.

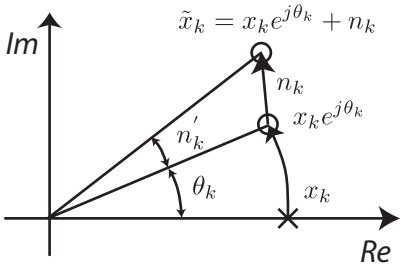

FIGURE 4.2: Diagram showing how phase noise and AWGN affect the transmitted symbols

The goal of the phase estimation process is to obtain $\tilde{\theta}_k$, an estimate of θ_k, which will allow de-rotation of the signal by multiplying it with $e^{-j\tilde{\theta}_k}$, followed by a symbol-by-symbol detector to find $\hat{x}_k$, the estimate of x_k.

Ip and Kahn proposed an algorithm [1], which uses a two stage iteration process for finding the carrier phase (Fig. 4.3). The first stage is a soft decision phase estimator,

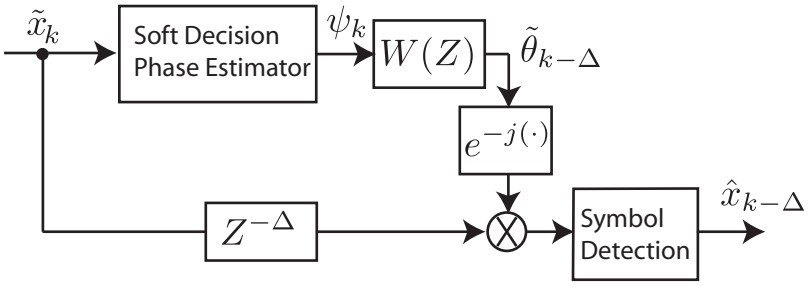

FIGURE 4.3: Two stage iteration carrier phase estimation

which computes soft estimates of the carrier phase without taking into account temporal correlation, followed by a second stage which takes into account temporal correlation to find a phase estimate. The output symbol can be written as follows:

$$\hat{x}_{k-\Delta} = [\tilde{x}_{k-\Delta} e^{-j\tilde{\theta}_{k-\Delta}}]_D \tag{4.3}$$

where $[\cdot]_D$ represents the operation of a decision device.

The soft estimate ψ_k is the phase of $\tilde{x}_k$ referenced to the phase of x_k:

$$\psi_k = \theta_k + n_k^{'} \tag{4.4}$$

where $n_k{}'$ is the projection of n_k onto a vector orthogonal to $x_k e^{j\theta_k}$. This estimate can be obtained either through DD or NDA (Non-Decision Aided, known as M-th power) approaches, shown in Figs. 4.4 and 4.5, respectively. The soft estimate given by the DD estimator is given as follows:

$$\psi_k = \arg(\tilde{x}_k e^{-j\tilde{\theta}_{k-1}}) - \arg(d_{\text{ref}}) \tag{4.5}$$

where d_{ref} is the output of a decision device when its input is $\tilde{x}_k e^{-j\tilde{\theta}_{k-1}}$, given as:

$$d_{\text{ref}} = [\tilde{x}_k e^{-j\tilde{\theta}_{k-1}}]_D \tag{4.6}$$

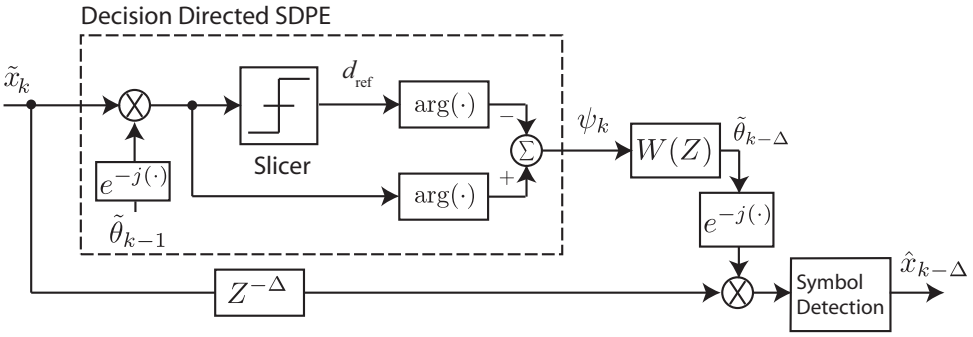

FIGURE 4.4: Two stage iteration carrier phase estimation with the decision-directed soft decision phase estimator

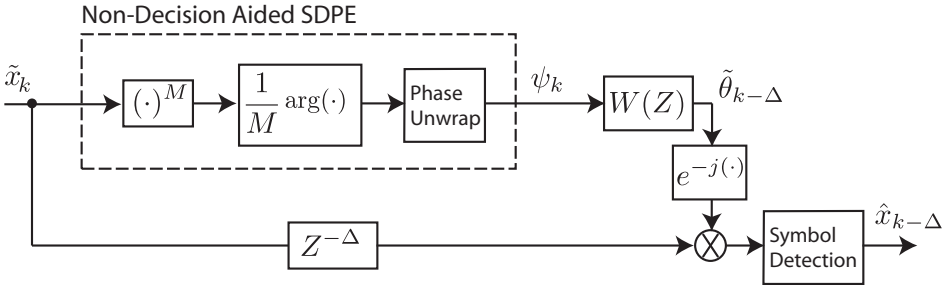

FIGURE 4.5: Two stage iteration carrier phase estimation with the non-decision-aided soft decision phase estimator

Additionally, the soft estimate given by the NDA estimator can be written as:

$$\psi_k = \text{PU}\left(\frac{1}{M}\arg(\tilde{x}_k^M)\right) \tag{4.7}$$

where PU(·) represents a phase unwrapping operation. While in the DD estimator the input signal is firstly de-rotated by an initial estimate of the phase (the previous estimated value), and then the phase difference between the signal at the output of that de-rotation and the nearest constellation point is calculated, producing the soft estimate ψ_k, in the NDA estimator the received signal is raised to the M^{th} power, eliminating the phase modulation, due to the M-fold rotational symmetry of an M-PSK constellation, the output of this operation originating a signal whose phase corresponds to M times the the soft estimate value. In the NDA estimator of Fig. 4.5 phase unwrapping is the operation that follows the arg(·) evaluation. This is a result of the arg(·) function returning values in the range $-\pi$ and π, which after division by M becomes limited between $-\pi/M$ and π/M. In this way, it is necessary to track differences in phases from

consecutive samples that are larger than π/M, in order to keep track of the real phase of the signal. However, the simple comparison between phases of consecutive samples of ψ_k might be inaccurate due to the influence of AWGN. [1] suggested that averaging the last three samples of ψ_k gives reliable performance. However, in this work different possibilities will be explored, in order to evaluate the real impact of an inaccurate phase unwrapping algorithm.

The NDA algorithm is especially well suited to M-ary PSK transmission, since raising the received signal to the M-th power eliminates the phase modulation, allowing θ_k to be estimated without any symbol decisions. However, this algorithm is asymptotically optimal for high SNR. Additionally, the decision directed algorithm replaces the known symbols with the output of a decision device, which is also asymptotically optimal for high SNR. Additionally, if the system constellation is non-PSK (non-constant-envelope), such as a 16-QAM modulation, the NDA algorithm would not be suitable, due to the lack of the M-fold rotational symmetry of the constellation, and the DD algorithm would be the option to live with. However, the DD algorithm requires an initial estimate ($\tilde{\theta}_k$) of the phase noise in order to find ψ_k, which is a disadvantage. In fact, the NDA algorithm has been proposed for 16-QAM in [66], where the mid amplitude symbols (named Class-II) do not contribute to the estimate because of the irregular phase spacing, whereas the remaining symbols, called Class-I, are used, as mentioned in Fig. 4.6. Additionally, an amplitude correction (AC) of the inner symbols must be performed for optimal performance.

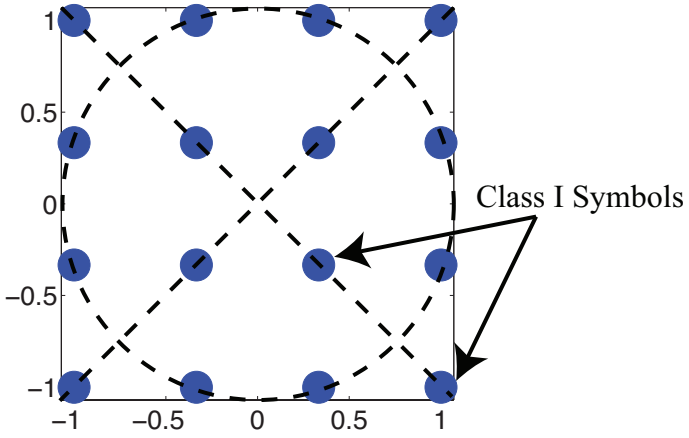

FIGURE 4.6: 16-QAM constellation diagram

Additionally, long sequences of Class-II symbols have to be prevented with appropriate line codes (to avoid cycle slips). However, this has only been done for the simple running average filter. In the following sections, the performance for the Wiener filter is also discussed. An alternative over-performing approach to the NDA was proposed in [67] called alternative NDA (ANDA), by exchanging the order of the filter with the phase unwrapped argument function, as detailed in Fig. 4.7

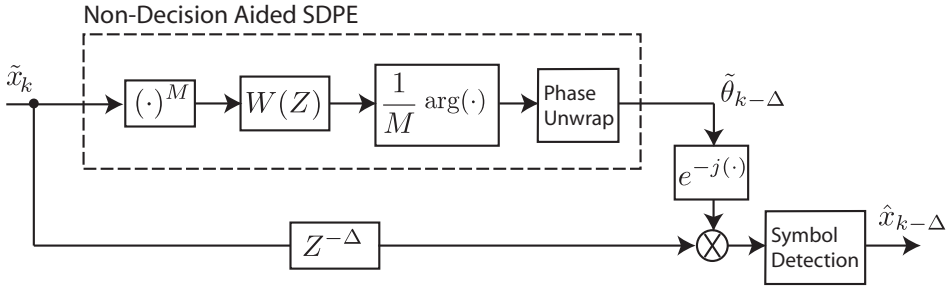

FIGURE 4.7: Two stage iteration carrier phase estimation with the alternative non-decision-aided soft decision phase estimator

After the soft decision phase estimator, the soft estimate ψ_k is passed through the second stage, which is a linear filter whose output is the MMSE estimate of θ_k.

4.3.1 The Wiener filter

The Wiener filter was proposed in [1], as the optimal filter for CPE, since it takes into account the temporal correlation of phase noise. It can be approximated by a Finite Impulse Response (FIR) filter with N taps (typically 10-100), in such a way that coefficients that are less than 5% of the largest coefficient are neglected.

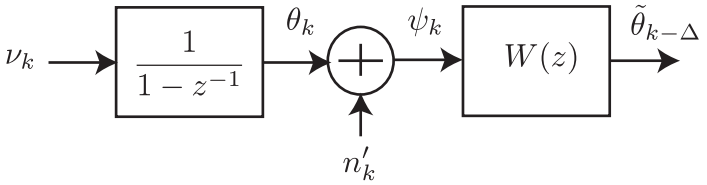

FIGURE 4.8: Modeling of the phase noise and phase estimator [1]

Fig. 4.8 describes the Z domain model for generation of phase noise θ_k, from a gaussian random variable ν_k having a variance of σ_p^2, as detailed in [1]. Additionally, it is shown that ψ_k represents the phase noise corrupted by amplitude noise vector n_k, which causes a perturbation of n'_k in the phase component of the phase noise variable θ_k. Finally, $\tilde{\theta}_{k-\Delta}$ represents an estimate of the delayed actual phase noise $\theta_{k-\Delta}$ and results

from the convolution of the Wiener filter coefficients with the incoming ψ_k variable. By resorting to the Wiener-Hopf equation introduced in the previous chapter, one can easily determine the optimum set of coefficients for $W(Z)$ which minimize the mean squared error between the estimate and the actual value of θ_k. Therefore, $W(Z)$ can be written as:

$$\begin{aligned} W(Z) &= R_{\theta\psi}R_{\psi\psi}^{-1} = E\{\theta(Z)\psi(Z^{-1})\}\cdot E\{\psi(Z)\psi(Z^{-1})\}^{-1} \\ &= E\{\theta(Z)(\theta(Z^{-1})+n(Z^{-1})\}\cdot E\{(\theta(Z)+n(Z))(\theta(Z^{-1})+n(Z^{-1})\}^{-1} \\ &= \frac{E\left\{\dfrac{\nu(Z)}{1-Z^{-1}}\dfrac{\nu(Z^{-1})}{1-Z}\right\}}{E\left\{\dfrac{\nu(Z)}{1-Z^{-1}}\dfrac{\nu(Z^{-1})}{1-Z}\right\}+E\left\{n(Z)n(Z^{-1}\right\}} = \frac{\dfrac{\sigma_p^2}{2-Z-Z^{-1}}}{\sigma_{n'}+\dfrac{\sigma_p^2}{2-Z-Z^{-1}}} \\ &= \frac{rZ^{-1}}{-1+(r+2)Z^{-1}-Z^{-2}} \end{aligned} \tag{4.8}$$

where $r=\sigma_p^2/\sigma_{n'}^2$. σ_p^2 is the variance of the phase noise and $\sigma_{n'}^2$ is the variance of the phase associated with Gaussian noise n_k. The filter given by equation (4.8) has poles located at:

$$z_1, z_2 = 1+\frac{r}{2}\pm\sqrt{\left(1+\frac{r}{2}\right)^2-1} \tag{4.9}$$

which fall symmetrically to the unit circle. Therefore, while z_1 falls inside the unit circle, z_2 falls outside, mapping to causal and anti-causal solutions. Effectively, this filter consists of two exponentially decaying sequences that are symmetric about $n=0$, causal and anti-causal, with an inherent optimum delay of half the filter length ($N/2$). The causal coefficients are given by:

$$w_n = \frac{\alpha r}{1-\alpha^2}\alpha^n,\ n\geq 0 \tag{4.10}$$

where $\alpha = (1+r/2)-\sqrt{(1+r/2)^2-1}$. The parameter r determines the rate of decay of the filter coefficients, which gives decreasing importance to soft estimates made far away from the current symbol.

The expression in (4.10) allows one to determine the optimum set of coefficients for the Wiener filter, while having infinite length. However, in order to determine a limited length set of coefficients, it is necessary to use the conditional probability density function of ψ given $\theta_{k-\Delta}$:

$$p(\psi|\theta_{k-\Delta}) = \frac{1}{(2\pi)^{N/2}|K|^{1/2}}\exp\left(-\frac{1}{2}(\psi-\theta_{k-\Delta}\mathbf{1})^T K^{-1}(\psi-\theta_{k-\Delta}\mathbf{1})\right) \tag{4.11}$$

where $\mathbf{1}$ is a vector of N ones and K is the autocorrelation matrix of ψ, which can be divided in its two components K_p and $K_{n'}$, associated with θ_k and n'_k, respectively, so that $K = K_p + K_{n'}$. In fact, [1] provides expressions for the autocorrelation matrixes K_p:

$$K_p = \sigma_p^2 \cdot \begin{bmatrix} \Delta & \cdots & 2 & 1 & 0 & 0 & \cdots & 0 \\ \vdots & \ddots & \vdots & \vdots & \vdots & \vdots & & \vdots \\ 2 & \cdots & 2 & 1 & 0 & 0 & \cdots & 0 \\ 1 & \cdots & 1 & 1 & 0 & 0 & \cdots & 0 \\ 0 & \cdots & 0 & 0 & 0 & 0 & \cdots & 0 \\ 0 & \cdots & 0 & 0 & 1 & 1 & \cdots & 1 \\ 0 & \cdots & 0 & 0 & 1 & 2 & \cdots & 2 \\ \vdots & & \vdots & \vdots & \vdots & \vdots & \ddots & \vdots \\ 0 & \cdots & 0 & 0 & 1 & 2 & \cdots & N-\Delta-1 \end{bmatrix} \tag{4.12}$$

and $K_{n'}$:

$$K_{n'} = \sigma_{n'}^2 \cdot I_{N\times N} \tag{4.13}$$

where $I_{N\times N}$ is a $N \times N$ identity matrix. One should notice that the upper right and lower left corners of the autocorrelation matrix K_p is filled with zeros due to the values of carrier phase before index $k - \Delta$ being uncorrelated with values after it, given $\theta_{k-\Delta}$ is known. In other words, if $\theta_{k-\Delta}$ is known, only values of phase which are more recent than $k - \Delta$ can be written as a function of values which are older than $k - \Delta$, while the opposite is not possible due to causality. However the correlation between two values of phase where the values belong either to both older or newer phases than $\theta_{k-\Delta}$, is effective, the correlation value being proportional to the smallest index distance to $k - \Delta$. For example, the correlation between $\theta_{k-\Delta+1}$ and $\theta_{k-\Delta+i}$, for $i = \{1, \ldots, \Delta\}$, is always σ_p^2, regardless of i because the $\theta_{k-\Delta+1} = \theta_{k-\Delta} + \nu_{k-\Delta}$, so that the value of phase noise for any given i is only correlated by $\nu_{k-\Delta}$.

The procedure to obtain the optimum set of coefficients involves the minimization of the argument in the exponential function of equation (4.11). This is performed by deriving the natural logarithm of the argument function in order to $\theta_{k-\Delta}$ and subsequently determining the point where it is zero [68]. In this way it is necessary to calculate:

$$\frac{\partial}{\partial\theta_{k-\Delta}} \ln\left[\frac{1}{(2\pi)^{N/2}|K|^{1/2}} \exp\left(-\frac{1}{2}(\psi - \theta_{k-\Delta}\mathbf{1})^T K^{-1}(\psi - \theta_{k-\Delta}\mathbf{1})\right)\right] = 0 \tag{4.14}$$

Since the natural logarithm of the exponential is the argument itself:

$$\frac{\partial}{\partial \theta_{k-\Delta}} \left[-\frac{1}{2} (\psi - \theta_{k-\Delta}\mathbf{1})^T K^{-1} (\psi - \theta_{k-\Delta}\mathbf{1}) \right] = 0 \tag{4.15}$$

By using the following definition for the derivative:

$$\frac{\partial}{\partial \theta}(m^T Q m) = 2 \left(\frac{\partial}{\partial \theta} m^T \right) Q m \tag{4.16}$$

One can determine that:

$$\mathbf{1}^T K^{-1} (\psi - \theta_{k-\Delta}\mathbf{1}) = 0 \tag{4.17}$$

By rearranging the previous equation, it is possible to show that the optimum set of coefficients is given by:

$$w_n = \frac{K^{-1}\mathbf{1}}{\mathbf{1}^T K^{-1}\mathbf{1}} \tag{4.18}$$

Fig. 4.9 compares three different Wiener filters, showing the impact of varying the r factor. If σ_p is too small or $\sigma_{n'}$ is too high, the coefficients of the filter will tend to a series of ones, which is equivalent to the typical running average filter (red line in the plot). Additionally two other cases with a medium and a higher value of r are also shown in the plot (green and blue lines, respectively).

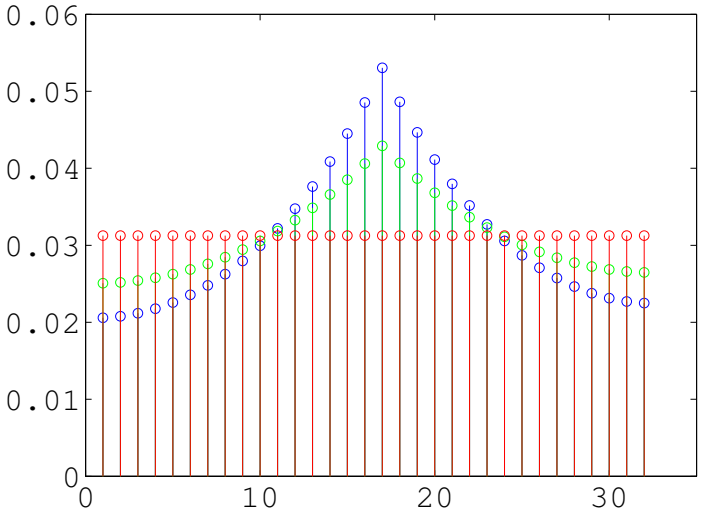

FIGURE 4.9: Superposition of 3 Wiener filters having $N = 32$ coefficients, a delay of $N/2 = 16$ with 3 different r factors.

4.3.2 Decision-directed algorithm issues

The fact that the decision directed soft decision phase estimator needs the feedback from a previous estimate brings additional complexity to the structure. It has been shown that the optimum estimator is a Wiener filter having a delay of half the filter length ($N/2$). In fact, this delay means that at any point in time, the estimate at the output of the filter refers to a sample that entered the estimator $N/2$ samples before. Therefore, this estimate is not optimum to serve as feedback for the DD estimator. In this way, a second filter might be used, having a reduced delay, in order to provide the estimator with a reasonably more accurate estimate. A simulation was undertaken in order to find out the performance difference between the single filter and the two filters approach, while the delay of the main filter was swept between zero and $N = 50$, as depicted in Fig. 4.10, the second filter being set with zero delay.

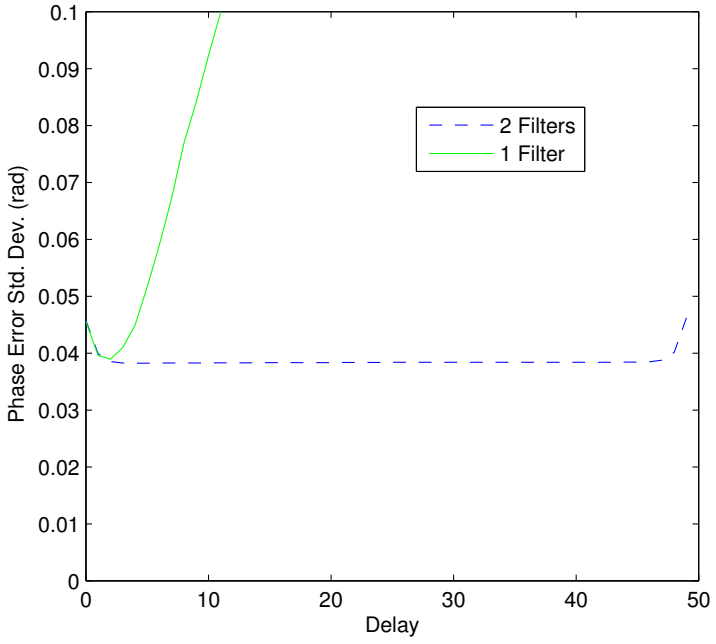

FIGURE 4.10: Phase error standard deviation as a function of the Wiener filter delay. In the case of 2 filters, only the delay of the main filter is varied.

It is clear that unless a very reduced delay is used, the two filters structure becomes necessary in order to maintain a good performance in the phase estimator, since that a large delay in the single filter approach leads to an inaccurate feedback in the DD estimator.

4.4 Novel CPE method

Equalization and carrier phase estimation are two important tasks performed in the receiver, and depending on the equalization algorithm these tasks might need to be executed synchronously with each other. When considering an equalization algorithm such as the blind stochastic gradient algorithm (CMA), these tasks might be decoupled since the algorithm does not use feedback from previous decisions. However, for the case of combined DD equalization and CPE, it has been found through simulation that optimum performance is obtained for zero delay in the CPE filter (assuming the equalizer update-rate equals the symbol-rate), because the value of the estimated phase needs to be fed back into the equalizer's error signal. This stems from a compromise between equalizer delay and CPE accuracy. In fact, the benefit of having a small delay and subsequently a less accurate phase estimate, is higher than having an accurate estimate and a larger delay. Fig. 4.11 shows an example of a set of coefficients representing the response of a wiener filter having zero delay.

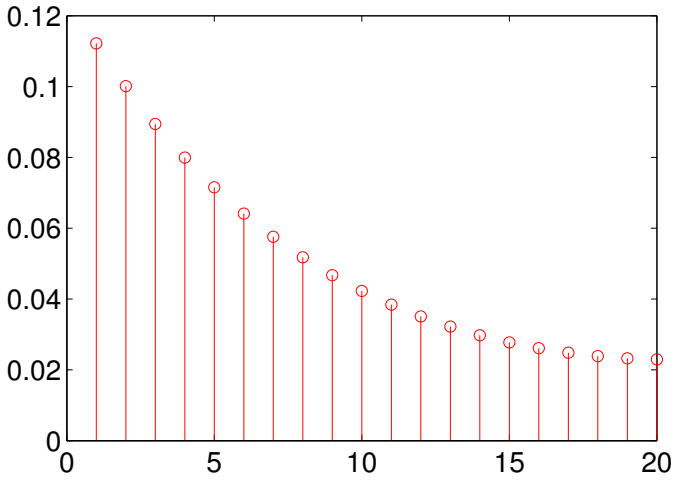

FIGURE 4.11: Example of Wiener filter with 20 coefficients having zero delay.

Here the Kalman filter is proposed, which is a recursive (Infinite Impulse Response - IIR) implementation of the Wiener filter, to implement the zero delay filter, with the advantage of reducing the computational complexity [63]. In fact, while the latter is designed to operate on all of the data directly for each estimate, the former instead, recursively conditions the current estimate on all of the past measurements [13]. There is a complexity reduction from $N/2+1$ multiplications per symbol, N being the length of the FIR Wiener filter, to only 1 multiplication per symbol.

Generically, the Kalman filter is a recursive estimator, which is based on estimates of the internal state of a process given only a sequence of noisy observations. Here, the process is the phase noise where $\theta_k = \theta_{k-1} + \nu_k$, and the observation is perturbed by the noise added by the channel such that $\psi_k = \theta_k + n'_k$. Each state estimate is computed using the estimated state from the previous time step and the current measurement. The Kalman estimator involves several parameters, such as the *a posteriori* error covariance matrix P and the Kalman gain G [69]. The estimate covariance matrix provides a measure of the estimated accuracy of the state estimate, and can be written as a function of the previous time step matrix:

$$P_n = \frac{(P_{n-1} + \sigma_p^2)\sigma_n^2}{P_{n-1} + \sigma_p^2 + \sigma_n^2} \tag{4.19}$$

In order to compute the current estimate, the previous estimate plus a gain factor multiplying the estimated error is used. The gain factor can be written as a function of the previous time step estimate covariance matrix:

$$G = \frac{P_{n-1} + \sigma_p^2}{P_{n-1} + \sigma_p^2 + \sigma_n^2} \tag{4.20}$$

The G factor can be calculated for a stability condition, where $P_n = P_{n-1} = P$. For this condition the gain factor is:

$$\begin{aligned} G &= \frac{1}{1 + \dfrac{\sigma_n^2}{P + \sigma_p^2}} = \frac{1}{1 + \dfrac{2\sigma_n^2}{\sigma_p^2 + \sqrt{\sigma_p^4 + 4\sigma_p\sigma_n}}} \\ &= \frac{1}{1 + \dfrac{2}{r + \sqrt{r^2 + 4r}}} = \frac{\alpha^* - 1}{\alpha^*} = 1 - \alpha \end{aligned} \tag{4.21}$$

In fact, the equivalence between the Kalman filter and the zero-lag Wiener filter can be shown in the following way: first of all, the coefficients of the causal solution of the Wiener filter are normalized to have unitary energy:

$$w_n = \frac{\dfrac{\alpha r}{1-\alpha^2}\alpha^n}{\dfrac{\alpha r}{1-\alpha^2}\left(1 + \sum_{n=1}^{\infty}\alpha^n\right)} = \frac{\alpha^n}{1 - \dfrac{\alpha}{\alpha - 1}} = (1-\alpha)\alpha^n \tag{4.22}$$

The Kalman recursion can be expanded as:

$$\begin{aligned}\tilde{\theta}_{k+1} &= (1-\alpha)\psi_k + \alpha\tilde{\theta}_k \\ &= (1-\alpha)\psi_k + (1-\alpha)\alpha\psi_{k-1} + \cdots + (1-\alpha)\alpha^N\psi_{k-N} \\ &= (1-\alpha)\sum_{n=0}^{N}\alpha^n\psi_{k-n} = \sum_{n=0}^{N} w_n\psi_{k-n} \end{aligned} \tag{4.23}$$

Effectively, equation (4.23) shows that the estimate given by the Kalman recursion is mathematically equivalent to the convolution with the coefficients given by the zero-lag Wiener filter.

For DD phase estimation, the soft estimate error is given by:

$$\begin{aligned}\psi_k - \tilde{\theta}_k &= \arg(\tilde{x}_k) - \arg(d_{ref}) - \tilde{\theta}_k \\ &= \arg(\tilde{x}_k e^{-j\tilde{\theta}_k}\cdot \mathrm{conj}(d_{ref})) \end{aligned} \tag{4.24}$$

Including the result of (4.24) the Kalman recursion is given by:

$$\begin{aligned}\tilde{\theta}_{k+1} &= \tilde{\theta}_k + G\cdot(\psi_k - \tilde{\theta}_k) \\ &= \tilde{\theta}_k + (1-\alpha)\cdot\arg(\tilde{x}_k e^{-j\tilde{\theta}_k}\cdot\mathrm{conj}(d_{ref})) \end{aligned} \tag{4.25}$$

where $\alpha = (1 + r/2) - \sqrt{(1 + r/2)^2 - 1}$ and $r = \sigma_p^2/\sigma_{n'}^2$ [1] is the ratio between the magnitude of phase noise and AWGN, which determines the rate of decay of the filter coefficients. G is the Kalman filter gain, which would be determined adaptively if the input variables were not stationary. However, because the inputs are stationary its steady state value can be pre-computed, which can be shown to give $G = 1 - \alpha$, as determined in equation (4.21) and then considered in equation (4.25).

Fig. 4.12 shows the proposed diagram of the equalizer and subsequent carrier phase estimation, where the error signal for the equalizer is derived after carrier "de-spin", so that the equalizer output is still a constellation with ringed shape. As the picture shows, the error signal for the equalizer is calculated as follows:

$$e_k = (d_{ref} - \tilde{x}_k e^{-j\tilde{\theta}_k})\cdot e^{j\tilde{\theta}_k} \tag{4.26}$$

Instead of determining the soft estimate ψ_k as in [1], here the approach of [70] is followed, where the difference $\psi_k - \tilde{\theta}_k$ is calculated directly without the need to perform

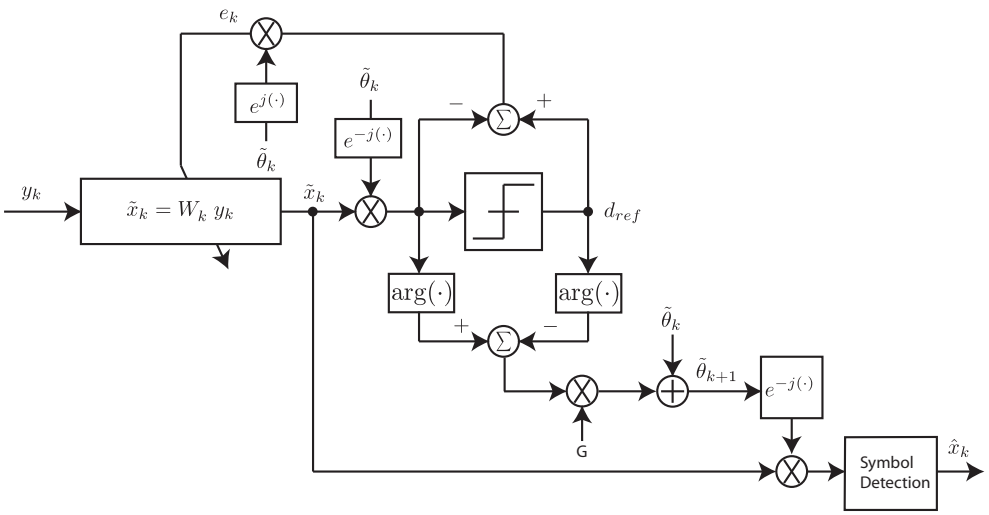

FIGURE 4.12: Diagram of the equalizer and subsequent carrier phase estimation

phase unwrapping. This is the reason for the lack of phase unwrapping block in Fig. 4.4. Additionally, a novel way of calculating the value of $\sigma_{n'}^2$ is introduced. In [1] it is calculated from the SNR. However, as the SNR might be unknown, it was found that this parameter might be determined iteratively, by periodically evaluating the variance of a statistical sufficient window size of the quantity: $\arg(\tilde{x}_k e^{-j\tilde{\theta}_k} \cdot \mathrm{conj}(d_{ref}))$. This might be a disadvantage for the Kalman approach, if the convergence of the estimation takes too long. Furthermore, recursive filters are sensitive to both parallelization and quantization issues. In Fig. 4.13 it is shown that at least 8 bits are required in order to avoid performance degradation above 2 dB stemming from fixed point quantization, while above 10 bits both FIR and IIR tend to the same performance.

4.5 Simulation results - carrier phase estimation

Simulations were performed employing a non-Gray differential bit encoding scheme (proposed in [1]) for all cases, preventing catastrophic bit error propagation when phase noise is high, due to the cycle slips phenomenon. All simulations were performed considering an $Eb/N0 = 12$ dB which is 1 dB above the differential AWGN limit of BER $= 1 \times 10^{-3}$. In Fig. 4.14, the phase unwrapping operation is analyzed for a QPSK signal using the NDA soft decision phase estimator, for different laser line-widths. As mentioned previously, the phase unwrapping operation requires a previous soft estimate in order to determine whether the phase difference between two consecutive samples is greater than π/M, in order to track the signal phase without any phase jumps, which means cycle

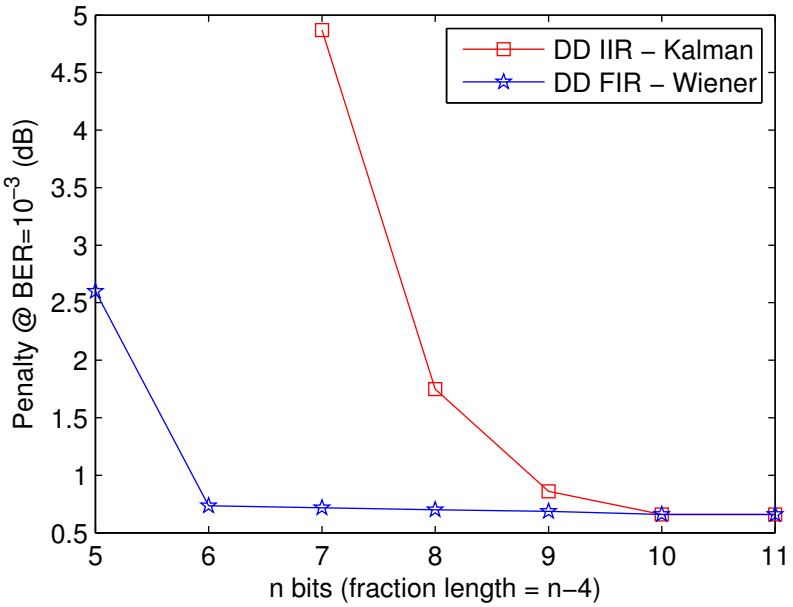

FIGURE 4.13: Penalty for a target BER=1e-3. $\Delta\nu T_b = 10^{-5}$.

slips are avoided. As said before, [1] suggested that averaging the last three samples of ψ_k gives reliable performance. In this way, in order to evaluate the impact of an averaging of previous samples, a filter structure composed of only ones, having variable length, was simulated, which is represented by dashed lines in Fig. 4.14. In fact, as depicted, a reduced length of the averaging (around 3 samples) filter provides optimal performance, specially in high phase noise scenarios. However, there is a better approach which can be implemented by applying a Wiener filter to the previous samples, instead of simple averaging (results in full lines). Effectively, when a Wiener filter is used, as soon as 5 samples are accommodated in the filter window, optimal performance is achieved, over-performing the simple averaging filter.

Concerning the phase unwrapping operation, an additional simulation was performed, whose result can be observed in Fig. 4.15(a), where the r factor was swept by varying its denominator, the variance of the phase oscillations induced by AWGN (n' in Fig. 4.2). In this case three different configurations for the phase unwrapping operation were simulated: averaging the last three samples, a Wiener filter with 5 samples and an additional result where the perfect value was used, since it is known within the simulation environment. As one can see, the Wiener filter approach provides a similar performance to the limit performance. However, the objective of varying the r factor, was also to discover whether an optimum value would exist, which is confirmed by the

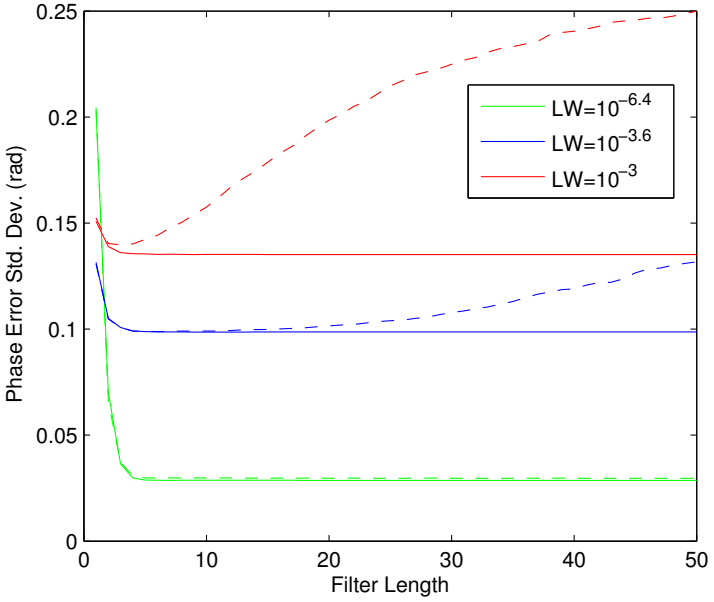

FIGURE 4.14: Phase error standard deviation versus filter length. LW is the laser line-width given by $\Delta\nu T_b$. Dashed lines represent the case of a running average filter (all the coefficients to one) and solid lines are for the case of a Wiener filter having zero delay.

shape of curves in the results. Furthermore, the optimum value for the variance of n' is found to be approximately the same regardless of the type of soft phase estimator used. Fig. 4.15(b) shows the results of the same analysis, for a 16-QAM transmission. The same conclusions can be made regarding the existence of an optimum value. As expected, the performance difference between DD and NDA based approaches is much larger than for QPSK due to the fact that only Class-I symbols can be used in the estimation.

Fig. 4.16 provides results for the bit error rate as a function of laser line-width for 16-QAM. The green line represents the performance for decision directed soft phase estimator, using an infinite impulse response strategy (the Kalman filter). For comparison purposes, other two results using a decision directed approach as well were obtained, however using a Wiener filter in the estimation block. The red line corresponds to using a zero delay Wiener filter, yet with a limited length of 20 taps. If an unlimited number of taps would be allowed the performance would approach exactly the same as in the IIR case. Additionally, another result is plotted in orange, where a Wiener filter having an optimum delay of half the filter length was used, and the number of taps considered is sufficiently high so that any effects stemming from the limited length of the filter can

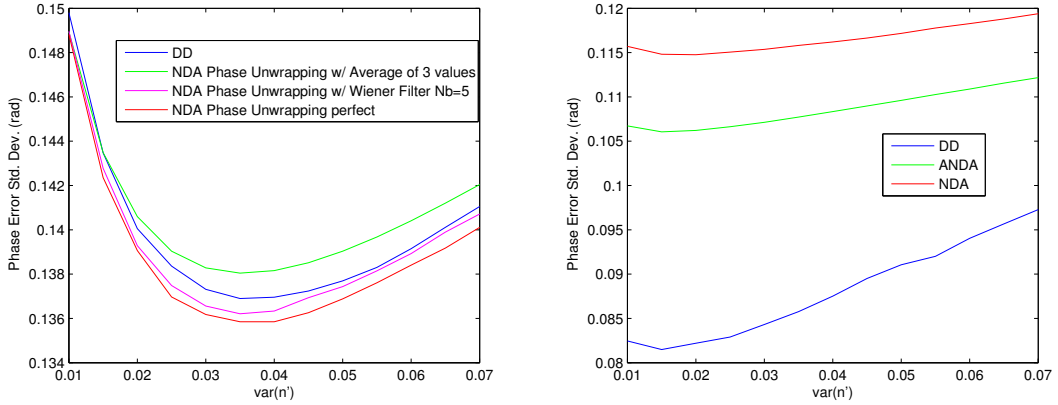

(a) QPSK. $\Delta\nu T_b = 10^{-3}$

(b) 16-QAM. $\Delta\nu T_b = 10^{-4}$

FIGURE 4.15: Phase error standard deviation versus the variance of n' used in the r factor.

be neglected. This shows that both the effects of limited length of the Wiener filter and selected delay of the filter have an impact on the bit error rate performance. In the former the impact is higher for reduced values of laser line-width, while in the latter the impact is more significant in an intermediate window of the laser line-width.

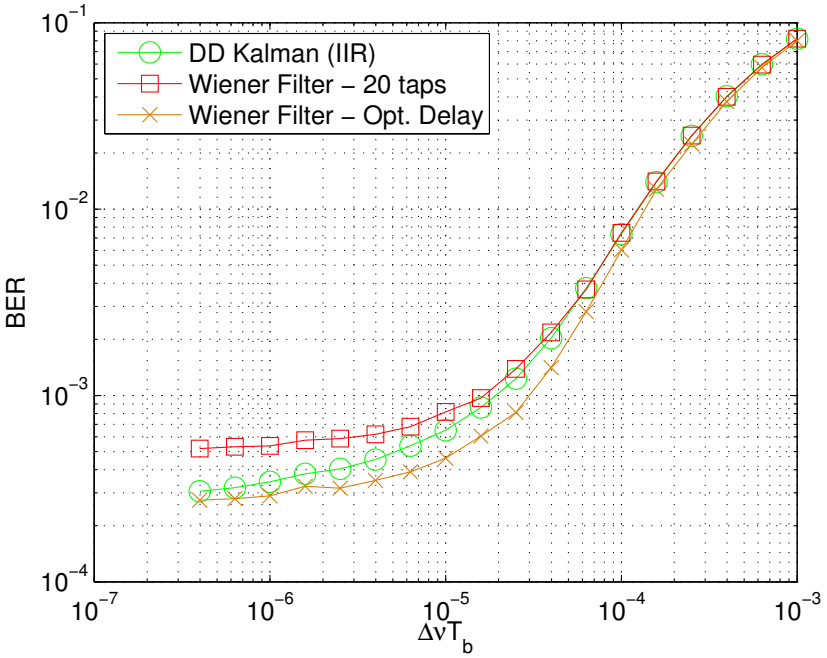

FIGURE 4.16: Bit error rate versus laser line-width per bit-rate, for 16-QAM.

A complete analysis on the impact of a limited Wiener filter length compared to the Kalman (IIR) filter, was also obtained for both QPSK – Fig. 4.17(a) – and 16-QAM –

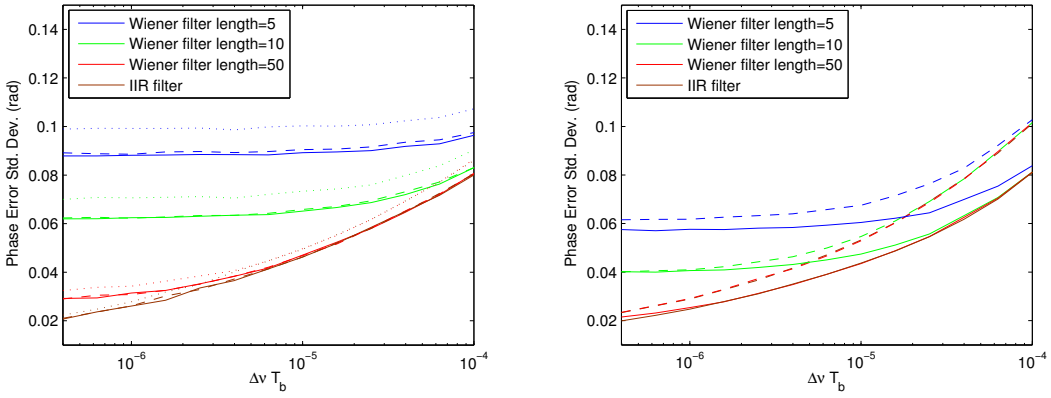

(a) QPSK (b) 16-QAM

FIGURE 4.17: Phase error standard deviation versus line-width per bit-rate product $\Delta\nu T_b$. Solid lines correspond to DD, dashed lines to ANDA and dotted lines to NDA

Fig. 4.17(b) – constellations.

As one can determine from the results, there is a significant impact on limiting the length of the Wiener filter, whereas this impact is reduced as the number of coefficients increases to 50, and approaches the performance of the IIR result. As depicted, the ANDA algorithm provides a result equivalent to DD for QPSK, while the usage of NDA impairs a significant penalty. On the other hand, for 16-QAM the ANDA almost matches the performance of DD for low line-widths while leading to higher penalties at larger line-widths. The NDA result is not plotted for 16-QAM due to its poor performance with this constellation.

Finally, Fig. 4.18 shows the results of the analysis made to both DD – Fig. 4.18(a) – and ANDA – Fig. 4.18(b) – soft estimators for 16-QAM modulation. This result describes the phase error standard deviation as a function of the Wiener filter length, indicating that the higher the line-width, the shorter the filter length needs to be in order to approach the IIR limit performance. Additionally, although the ANDA algorithm provides a slightly worse performance than the DD, especially for higher line-widths, it approaches the limit IIR performance with a lower number of coefficients.

4.6 Implementation issues - Parallelization

In order not to compromise the performance of the proposed algorithm, it is expected that the carrier phase does not change significantly over the memory length of the equalizer, and its length should be minimized. In fact, the analysis presented along the

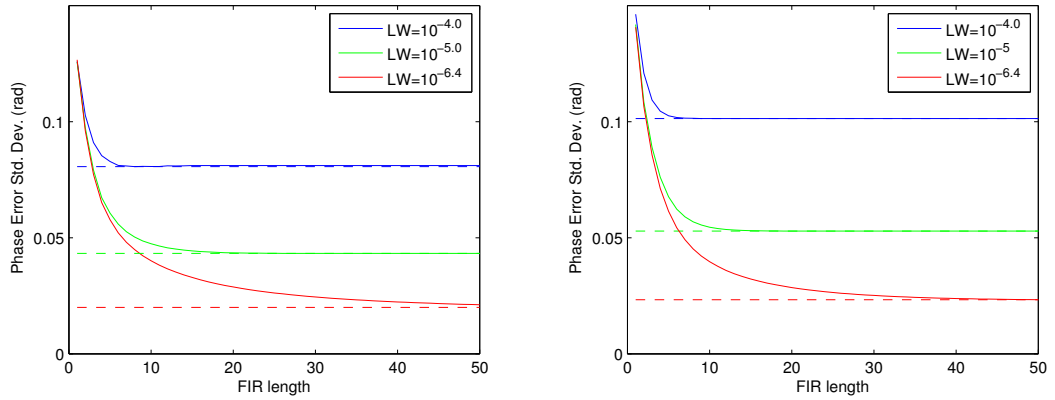

(a) DD (b) ANDA

FIGURE 4.18: Phase error standard deviation versus Wiener filter length (solid lines) for a $\Delta\nu T_b = [10^{-4}, 10^{-5}, 10^{-6.4}]$, in blue, green and red, respectively. Dashed lines represent the IIR limit. 16-QAM.

present Chapter considers that the transmission channel includes optical dispersion compensation. However, the usage of Dispersion Compensating Fiber (DCF) carries several disadvantages [16], such as loss and nonlinearity which eventually lead to a reduced system performance. Although not studied in the present work, a practical implementation of an uncompensated optical transmission system could use a long filter for CD compensation of long fiber distances (*e.g.* 512-tap), implemented in the digital domain. It should be noticed that this approach also leads to a certain penalty, depending on the data-rate and transmission length, stemming from receive laser phase noise enhanced by the electronic equalization [61], as mentioned in Chapter 3. The coefficients of this filter could be either static or slowly updated, and then a subsequent small filter (*e.g.* 13-tap of length has been considered by several authors [5]) with rapid updates could be used, to mitigate the residual uncompensated CD and track dynamic polarization changes, as suggested in Chapter 3. This concept has been validated in [5], for both LMS and CMA. Furthermore, as the time-scales associated with dispersion and phase noise are different, parallelization techniques can be introduced up to a certain extent in the phase noise estimation algorithm.

Effectively, the discussed algorithms should be implemented with a high degree of parallelism, otherwise it is not possible to implement them in real-time with the currently available technology [71]. The algorithms might be modified to accomplish this, with a look ahead computation [72] to refer the feedback to a result obtained L symbols before, at the expense of extra feedforward (FF) taps, yielding the following Z transform of the

zero lag Wiener filter coefficients:

$$W(Z) = \frac{(1-\alpha)\sum_{k=0}^{L-1}\alpha^k Z^{-k}}{1-\alpha^L Z^{-L}} \tag{4.27}$$

By calculating the corresponding difference equation, the Kalman recursion to obtain the estimated phase is given by [64]:

$$\tilde{\theta}_{k+1} = (1-\alpha)\sum_{n=0}^{L-1}\alpha^n \psi_{k-n} + \alpha^L \tilde{\theta}_{k-L+1} \tag{4.28}$$

The calculation of $\tilde{\theta}_{k+2}$ can be started before the previous $\tilde{\theta}_{k+1}$ is complete which supports the parallel implementation. In this way, cycle slips will have the same impact as in a serial system. Fig. 4.19, shows an example of a parallel implementation with $L = 3$. In this scheme, 3 processing units might operate simultaneously and independently from each other because they only need information from 3 symbols behind in time. Additionally, each PU has 3 times more time available to execute the calculations than what it would have if no parallelization was used at all.

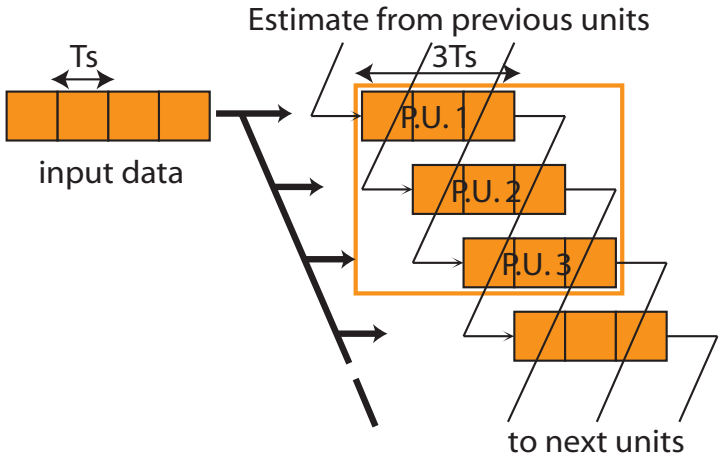

FIGURE 4.19: Diagram of a parallel implementation. P.U. designates Processing Unit. T_s is the symbol duration.

Figure 4.20 describes the coefficients of an estimation filter where parallelization is implemented with $L = 32$. In this way, the Kalman filter will need to operate with a delay of 32 samples, so that an anti-causal tail will be applied to the samples which are forward in time, in a feedforward manner, exactly as performed by the Wiener filter. However, the coefficients in the causal tail which are applied to samples backward in time, might be implemented in a Kalman approach.

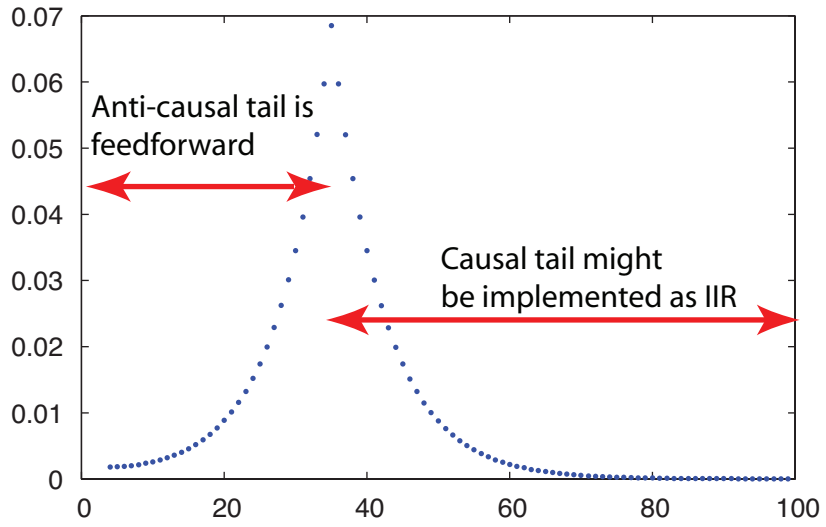

FIGURE 4.20: Coefficients of the estimation filter having $L = 32$

Fig. 4.21 shows simulation results of a 16-QAM transmission, where both the decision directed and alternative non-decision-aided approaches are compared. The parallelization factor is varied from 1 to 8 and 32. The DD approach with $L = 32$ is always worse than NDA, which shows that DD is not well suited for parallelization. One should emphasize that the NDA approach might be parallelizable with no loss in performance since it involves no CPE feedback.

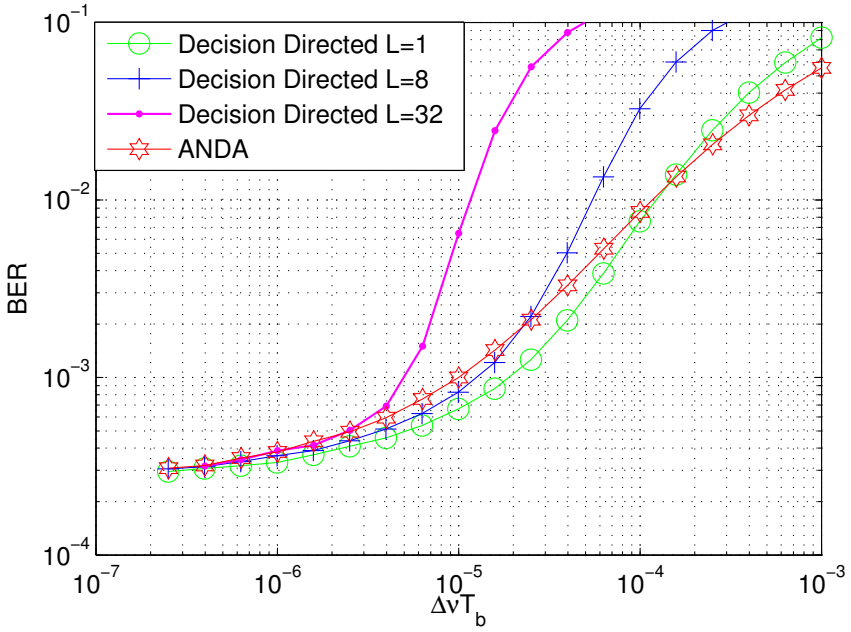

FIGURE 4.21: Bit error rate versus laser line-width per bit-rate, for 16-QAM

4.7 Results - Equalization combined with CPE

For the simulations where equalization was performed, a 3rd order low pass Bessel filter for $p(t)$ and anti-alias (AA) filter $a(t)$ was considered. The results were found through the Monte-Carlo technique and evaluated after convergence with a step size of $\mu = 10^{-3}$. The simulations were conducted for 16-QAM transmission and analyzed the following equalizer / phase estimation filter pair configurations [65]:

Equalizer	Estimation Filter
LMS-DD	DD
	ANDA
CMA	DD
	ANDA

While the LMS result was obtained by using the proposed method of Fig. 4.12, where the phase is estimated at the output of the equalizer and then included in the error signal, the CMA result corresponds to using separate equalizer convergence and subsequent ideal phase estimation through the FIR Wiener filter.

Figures 4.22 and 4.23 compare the performance of several scenarios involving both equalization and phase estimation, in terms of both bit error rate and power penalty, respectively.

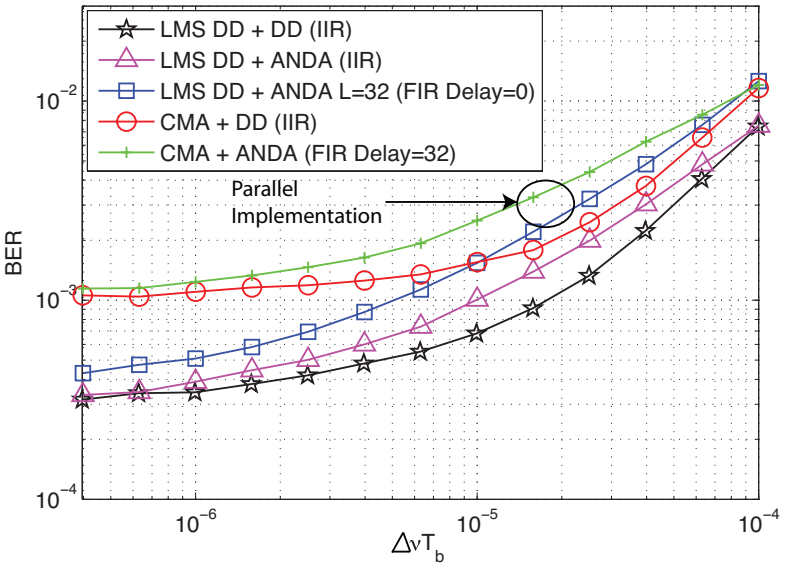

FIGURE 4.22: Bit error rate versus laser line-width per bitrate.

The results in Fig. 4.23 correspond to taking the values of Fig. 4.22 at a bit error rate of 10^{-3} and then increase the signal to noise ratio as the line-width increases in order to maintain the desired target BER. This SNR additions are accounted as penalties.

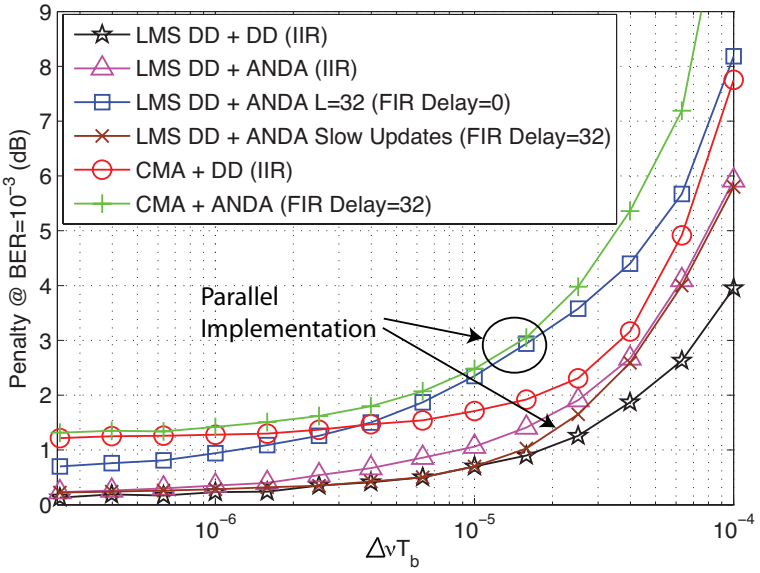

FIGURE 4.23: Penalty versus laser line-width per bitrate. Reference E_b/N_0 of 12dB (BER $= 1 \times 10^{-3}$ sensitivity point for LMS)

Although CMA is not optimized for 16-QAM, it still converges at a cost of a higher penalty than LMS (1.2 dB opposed to 0.1 dB, respectively, at low line-widths). In the result represented by "$*$" (black line), the phase is estimated at the output of the LMS-DD equalizer, with the IIR-DD CPE filter, and then fed-back in the error signal. In curves "$\triangle$" and "$\square$" (pink and blue lines, respectively), the CPE was changed to IIR-NDA with $L = 1$ and FIR-NDA with $L = 32$ respectively. In the latter, IIR was still employed to the other $N - L$ taps, as suggested by equation 4.28. Curve "$\times$" (brown line in Fig. 4.23) refers to a LMS-DD equalizer with slow updates ($\Delta_1 \gg 32$), using the optimized CPE filter with Delay=32. The observable difference to "$\triangle$" (pink line) is due to the CPE delay only. Additionally, this approach might be parallelized with no penalty due to the negligible equalization feedback. The "$+$" and "$\circ$" results (green and red lines, respectively), correspond to separate CMA equalization and subsequent CPE through the IIR-DD and FIR-NDA approaches, respectively. While the former is not efficiently parallelizable as seen before (Fig. 4.20), the latter may be parallelized and can benefit from using a finite delay while not causing any penalty due to the absence of equalization feedback. It is relevant to notice that the filters used for the parallel

versions were named FIR in the legends, because the L feedforward taps are intrinsic to the parallel implementation. Depending on the maximum speed of available DSP chips, the required parallelization level will dictate which approach should be chosen. If no parallelization is required the LMS-DD+DD should be chosen based on a good compromise between complexity and performance. If a parallelization level $L \leqslant 32$ is necessary, both approaches have similar complexities, the LMS-DD+NDA approach being preferable based on performance, but if the requirement is greater than 32, then CMA+NDA is the best option, because its performance does not depend on L. A table summarizing the major strengths and weaknesses of the several approaches is shown in Fig. 4.24.

Eq.	CPE Filter	Strengths	Weaknesses	
LMS-DD	DD	Small penalty, specially for small linewidths. IIR filter can be used, reducing the computational complexity. Phase unwrapping is more robust than for NDA.	Not Parallelizable due to CPE Feedback.	Equalizer Feedback. When used, IIR is susceptible to feedback issues.
	NDA Serial / Parallel	No CPE Feedback. IIR filter can still be used in the non-feedforward part of the filter tail. If slow updates are allowed, it is the best option for parallel processing.	FF filter section needed for parallel implementation. For L>32, CMA approaches are preferable.	
CMA	DD	Smaller penalty than CMA+NDA for large linewidths. IIR filter can be used, reducing the computational complexity. Phase unwrapping is more robust than for NDA.	Not Parallelizable due to CPE Feedback. Higher penalty than LMS-DD+DD.	CMA equalizers can not achieve as low MSE as LMS based, specially for the 16-QAM non-constant modulus constellation.
	NDA Serial / Parallel	No CPE Feedback. Penalty is independent from L. IIR filter can still be used in the non-feedforward part of the filter tail.	1dB worse than LMS-DD+NDA. FF filter section needed for parallel implementation.	

FIGURE 4.24: Table summarizing the strengths and weaknesses of each algorithm combination

4.8 Summary

The current chapter focused on the topic of carrier phase estimation and equalization algorithms. Decision directed and non-decision-aided carrier phase estimation algorithms were analyzed for both 4 and 16-QAM modulation formats. Then the issues associated with the combination of equalization and carrier phase estimation were investigated, in terms of performance and parallelization possibilities. In fact, the performance of

a phase estimation algorithm operating in feedback with a LMS-DD equalizer was assessed, for both decision directed and non-decision-aided carrier phase estimation. The performance of this configuration was compared to the CMA algorithm having separate carrier phase estimation. It was found that up to $L = 32$ the LMS-DD using equalization feedback still outperforms the equivalent CMA approach, while having similar computational complexity levels. Additionally, if the system design requirements allow for slow equalizer updates, LMS-DD in conjunction with NDA is always the best option for parallel processing.

Chapter 5

Back-Propagation

5.1 Introduction

The ultimate limits of transmission capacity are determined by the nonlinear impairments arising in optical fiber communication links. In fact, it is in the transition from the linear to the nonlinear regime that the highest capacity can be achieved. Therefore, the compensation of fiber nonlinearity allows an increase of the capacity by tolerating an higher launched power within the linear regime. Back-propagation [14] is a method for fiber nonlinearity mitigation based on the inversion of the signal propagation equation, which will be thoroughly assessed within this chapter. With this aim, firstly the implementation of the nonlinear propagation equation will be studied, and then the details of a simulation model for a long-haul transmission system will be focused, considering both single channel and OFDM modulation formats. Subsequently, the back-propagation algorithm will be analyzed in terms of design rules, in order to determine its computational complexity requirements for different system configurations. Finally, the performance of the back-propagation algorithm will be assessed in a study comparing single channel and OFDM transmission formats.

5.2 Fiber Impairments

A coherent optical system is generally affected by impairments stemming from both the transmitter and local oscillator lasers, mainly laser phase noise, which can be effectively compensated due to its correlation, as addressed in chapter 4. In these systems, the transmission channel is typically long-haul, which requires optical amplifiers. EDFAs

generate white noise due to amplified spontaneous emission, which can not be compensated in the receiver. Additionally, the optical fiber introduces both linear and nonlinear impairments. CD and PMD are unitary linear impairments, therefore enabling lossless compensation. Opposed to the unitary impairments, polarization dependent loss is non-unitary, implying loss for its compensation. The symbol timing offset in the receiver and the optical filtering operations are additional linear impairments present in the system, with a unitary and non-unitary characteristic, respectively. Opposed to linear impairments, there are nonlinear impairments caused by the fiber Kerr effect, which accounts for the fiber refractive index change proportional to the optical power. These effects can be classified in two categories: signal-signal and signal-noise depending on the type of interference that generates the impairment. The signal-signal interference includes the effects of self-phase modulation (SPM), cross-phase modulation (XPM) and four-wave mixing (FWM), which can be compensated more effectively. The main effect originated by a signal-noise interference is nonlinear phase noise (NLPN), which results from the conversion of random amplitude fluctuations (due to ASE) into phase fluctuations. Therefore this effect is stochastic and can be compensated less effectively.

The refractive index change with optical intensity is the main source of nonlinear effects in optical fibers. The refractive index can be written as the sum of a linear part with a nonlinear part [54]:

$$\tilde{n}_r(\omega, |E|^2) = n_r(\omega) + n_{r,2}|E|^2 \tag{5.1}$$

where $n_r(\omega)$ is the linear frequency dependent refractive index, at low powers, which is responsible for chromatic dispersion, and $n_{r,2}$ is the nonlinear coefficient that scales the weight of the square of the optical field $|E|^2$ on the refractive index.

SPM, XPM and FWM are the most studied nonlinear impairments associated with this phenomenon. SPM accounts for the optical field phase change due to its own intensity variation during propagation. The nonlinear phase shift induced by SPM over a length of fiber L, is given by:

$$\phi_{NL} = n_{r,2} k_0 L |E|^2 \tag{5.2}$$

where $k_0 = 2\pi/\lambda$ denotes the wavenumber. XPM is a nonlinear phenomenon which occurs when two or more optical waves co-propagate in the optical fiber due to the refractive index change induced by each wave, which in turn induces a nonlinear polarization-dependent phase shift on the other co-propagating waves [54]. Assume the total electric field is written as the sum of two optical waves at ω_1 and ω_2:

$$E = \frac{1}{2}\hat{x}\left[E_1 \exp(-j\omega_1 t) + E_2 \exp(-j\omega_2 t)\right] \tag{5.3}$$

propagating simultaneously in the fiber along the $\hat{x}$ polarization axis. Complex conjugate terms were not represented for simplicity. It can be shown that the nonlinear phase shift at ω_1 is given by:

$$\phi_{NL} = n_{r,2} k_0 L(|E_1|^2 + 2|E_2|^2) \tag{5.4}$$

where terms at newly generated frequencies have been neglected, because phase matching is not satisfied. It is important to notice that the phase shift contribution from the optical field at ω_2 (due to XPM) is two times stronger than the contribution by the optical field at ω_1 itself (due to SPM). FWM accounts for the beating between light-waves at different frequencies, leading to phase modulation of the channels, and therefore generation of modulation sidebands at new frequencies.

The propagation of a pulse $A(z,t)$ through a single mode optical fiber is governed by the generalized nonlinear Schrödinger equation (GNSE), assuming a slowly varying envelope approximation [54]:

$$\frac{\partial A}{\partial z} + \beta_1 \frac{\partial A}{\partial t} + \frac{1}{2} j\beta_2 \frac{\partial^2 A}{\partial t^2} - \frac{1}{6}\beta_3 \frac{\partial^3 A}{\partial t^3} + \frac{\alpha}{2} A = j\gamma |A|^2 A \tag{5.5}$$

where, for simplicity, the z and t dependences of A have been omitted. The nonlinear parameter γ is given by:

$$\gamma = \frac{n_{r,2}\omega_0}{cA_{\text{eff}}} \tag{5.6}$$

in which ω_0 is the center frequency of the optical pulse, n_2 is the fiber nonlinear refractive index coefficient, c is the speed of light and A_{eff} is the fiber effective core area. The fiber attenuation is accounted through α and nonlinearity through γ. The parameters β_1, β_2, and β_3 are obtained from the Taylor series expansion of the propagation constant $\beta(\omega)$. While β_1 is related with the inverse of the group velocity of the pulse envelope, β_2 is the GVD parameter. The effect of the third order dispersion β_3 (dispersion slope),

accounting for the change of GVD with angular frequency can be neglected as long as transmission is not in the vicinity of the zero dispersion wavelength (1.3 μm) where β_2 is negligible. In this thesis, transmission is considered in the 1.5 μm window, known as anomalous dispersion region, where β_2 is approximately $-20\,\mathrm{ps}^2/\mathrm{km}$. When both attenuation and third order dispersion parameters can be neglected, and considering β_2 is independent of z, the GNSE is known as the nonlinear Schrödinger equation (NLSE).

It is useful to bear in mind several length scales inherent to nonlinear transmission. Firstly, one should recall the characteristic lengths, which are the lengths required to induce a phase distortion of one radian, specifically L_{NL} is a length scale related to power only (SPM) and L_{wo} is the walk-off length related to chromatic dispersion only [73–75]:

$$L_{\mathrm{NL}} = \frac{1}{\gamma P_p} \tag{5.7}$$

$$L_{\mathrm{wo}} = \frac{2}{\beta_2 \omega_{\mathrm{max}}^2} \tag{5.8}$$

where P_p is the signal peak power and ω_{max}^2 is the highest frequency component of the modulated signal, within a 3 dB bandwidth. It is often necessary to calculate the nonlinear phase shift of a signal induced by nonlinearity, over a span of fiber with several kilometers. However, as the signal attenuates, the induced phase rotation will become negligible after a certain length of fiber. In fact, the propagation of the signal field $A(z,t)$ in the presence of loss and Kerr nonlinearity (neglecting dispersion) can be represented as [54]:

$$\frac{\partial A}{\partial z} + \frac{\alpha}{2} A = j\gamma |A|^2 A \tag{5.9}$$

Equation (5.11) has the following exact solution:

$$A(z,t) = A(0,t)\exp(-\alpha z/2)\exp(j\phi_{NL}) \tag{5.10}$$

where nonlinear phase shift is written as:

$$\phi_{NL} = \gamma |A(0,t)|^2 L_{\mathrm{eff}} \tag{5.11}$$

where L_{eff} is the effective length defined as:

$$L_{\mathrm{eff}} = \frac{1 - \exp(-\alpha L)}{\alpha} \tag{5.12}$$

The quantity L_{eff} plays the role of a effective length which is smaller than L because of fiber losses.

Another physical length of interest is the walk-off length L_{wo}, which gives the distance after which the relative delay between pulses from two spectral components of interest separated by $\Delta\nu_{\text{ref}}$ is equal to the pulse width, which means they have fully walked through each other:

$$L_{\text{wo}} = \frac{1}{2\pi|\beta_2|\Delta\nu_{\text{ref}}R_s} \tag{5.13}$$

where R_s is the symbol-rate (equivalent to the inverse of the pulse width).

The several length scales given in the previous equations quantify the impact of different impairments on signal propagation. However, one can not generalize which impairments are dominant, since these length scales depend on symbol-rate, channel spacing, modulation format, input power, type and length of fiber, dispersion management, amplifier spacings, among others. Therefore, each set of system parameters has to be evaluated separately to infer which length scale is the most influent.

The NLSE is a nonlinear partial differential equation, which due to a complex interplay between nonlinearity and dispersion has only analytic solution for some specific cases, such as solitons, being typically solved numerically. The split-step Fourier (SSF) method, also designated by SSFM, introduced by Tappert in 1973 [76] is considered one the fastest numerical techniques for this purpose, being approximately one order of magnitude faster than finite-difference methods [54]. The SSFM has become the most widely accepted technique for the simulation and analysis of signal propagation in both single and multi-channel optical fiber systems.

5.3 Split-Step Fourier Method

The GNSE in (5.5) can be simplified in the following manner:

$$\frac{\partial A}{\partial z} = (\hat{D} + \hat{N})A \tag{5.14}$$

where $\hat{D}$ is a differential operator accounting for dispersion and attenuation, and $\hat{N}$ is the nonlinear operator governing nonlinear effects in the propagating signal. $\hat{D}$ and $\hat{N}$ are respectively given by:

$$\hat{D} = -\frac{1}{2}j\beta_2\frac{\partial^2}{\partial t^2} + \frac{1}{6}\beta_3\frac{\partial^3}{\partial t^3} - \frac{\alpha}{2} \tag{5.15}$$

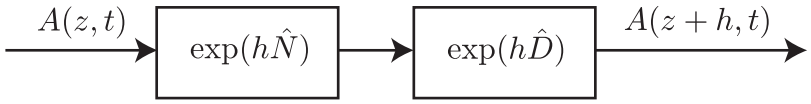

FIGURE 5.1: Asymmetric SSFM diagram

$$\hat{N} = j\gamma|A|^2 \tag{5.16}$$

As the signal travels along the fiber, the effects of dispersion and nonlinearity interact with each other. However, the numerical solution given by the SSF method involves dividing the optical fiber into small segments of length h, wherein the effects of dispersion and nonlinearity are considered independently, which is an approximation. An exact solution to the previous equation (5.14) can be shown to be, after one simulation step h:

$$A(z+h,t) = \exp\left[h(\hat{D}+\hat{N})\right] A(z,t) \tag{5.17}$$

There are two common strategies of propagating the optical field through the split-step method, either by dividing the propagation from z to $z+h$ into two (asymmetric) or three (symmetric) steps.

5.3.1 Asymmetric SSFM

The asymmetric method can be implemented either by performing first the nonlinear operator and then the linear operator, or the reverse:

$$A^{DN}(z+h,t) = \exp[h\hat{D}]\exp[h\hat{N}]A(z,t) \tag{5.18}$$

$$A^{ND}(z+h,t) = \exp[h\hat{N}]\exp[h\hat{D}]A(z,t) \tag{5.19}$$

As one can see in Fig. 5.1, the calculations consist of a product of two noncommuting operators. Therefore, an expansion of this product is required in order to analyze the errors involved in the approximation. The Baker-Hausdorff formula [54, 77, 78] provides a mechanism in order to expand the product of two noncommuting operators:

$$\exp(\hat{a})\exp(\hat{b}) = \exp\left(\hat{a}+\hat{b}+\frac{1}{2}[\hat{a},\hat{b}]+\frac{1}{12}\left[\hat{a}-\hat{b},[\hat{a},\hat{b}]\right]+...\right) \tag{5.20}$$

where $[\hat{a}, \hat{b}] = \hat{a}\hat{b} - \hat{b}\hat{a}$. By substituting $\hat{a}$ with $h\hat{D}$ and $\hat{b}$ with $h\hat{N}$, one can find that:

$$A^{DN}(z+h,t) = \exp\left(h(\hat{D}+\hat{N}) + \frac{h^2}{2}[\hat{D},\hat{N}] + \frac{h^3}{12}\left[\hat{D}-\hat{N},[\hat{D},\hat{N}]\right] + ...\right) A(z,t) \quad (5.21)$$

and a similar expression holds for $A^{ND}(z+h,t)$. By inspection of the previous equation (5.21), and comparison with (5.17), one can see that all terms apart from $h(\hat{D}+\hat{N})$ are error terms, and that the dominant error term is found from the single commutator $\frac{h^2}{2}[\hat{D},\hat{N}]$, therefore proportional to h^2.

Although [78] discusses that the pulse-width of the accurate solution $A(z+h,t)$ is bounded by the pulse-widths of the two approximate solutions $A^{DN}(z+h,t)$ and $A^{ND}(z+h,t)$, it was shown in [16] that the order of operations that maximizes the accuracy of the algorithm is to apply first the nonlinear operator, as nonlinear effects have a stronger impact at the beginning of a fiber segment when the power is highest, and then the dispersion operator.

5.3.2 Simulation error for the asymmetric SSFM

The design of an optical communication system requires long simulations in order to explore a multidimensional design space, requiring the repetition of multiple loops for each design parameter of interest, such as launched power, symbol-rate, number of channels, among others. This fact motivated research into more efficient techniques of solving the NLSE, either by increasing the computational efficiency or the simulation accuracy. Additionally, one has to avoid the usage of a excessively small step size to provide high simulation accuracy for all the varying system parameters, because it represents a significant waste of computation. In [78] a procedure has been found to determine the length of the simulation step in order to provide a comparable global simulation accuracy for varying system parameter values. The local simulation error has been derived using the difference between the two approximate solutions to the asymmetric SSF method, which is valid for both single channel and WDM cases. The error can be represented by:

$$\epsilon = \gamma P_p D B_\lambda R_s h^2(z) \quad (5.22)$$

where P_p represents the peak power, D is the dispersion parameter, B_λ is the signal bandwidth in the wavelength domain and R_s is the symbol-rate (approximate bandwidth in the frequency domain). One can solve the previous equation in order to provide the

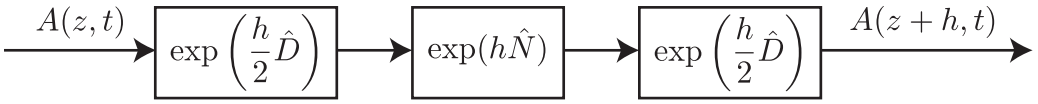

FIGURE 5.2: Symmetric SSFM diagram

step size h_k as a function of the electric field intensity on the previous step $|E(z_{k-1})|^2$:

$$h_k = \left[\frac{\epsilon}{\gamma|E(z_{k-1})|^2(2\pi|\beta_2|B_f^2)}\right]^{1/2} \tag{5.23}$$

A value of ϵ of 10^{-4} was considered throughout this thesis which is within the required accuracy range of current WDM communication systems [79].

5.3.3 Symmetric SSFM

The symmetric SSF method is presented in [54] as an improved technique of propagating the signal from z to $z+h$. This approach consists in mapping the effect of nonlinearity to the middle of the segment (Fig. 5.2) such that:

$$A(z+h,t) = \exp\left(\frac{h}{2}\hat{D}\right)\exp\left(\int_z^{z+h}\hat{N}(z')dz'\right)\exp\left(\frac{h}{2}\hat{D}\right)A(z,t) \tag{5.24}$$

The name of the method derives from the symmetry of the exponential dispersion operators. As the nonlinear operator has a dependence on z, lumping it to the middle of the segment is useful. If the step size is small enough it can be approximated by $\exp(h\hat{N})$, which was considered in the derivations of [78]. Therefore, by resorting again to (5.20), one can expand the product of the three operators as:

$$\exp(h\hat{D}/2)\exp(h\hat{N})\exp(h\hat{D}/2) = \exp\left(h(\hat{D}+\hat{N}) + \frac{h^3}{6}\left[\frac{\hat{D}}{2}+\hat{N},\left[\frac{\hat{D}}{2},\hat{N}\right]\right] + ...\right) \tag{5.25}$$

By comparing the previous equation with (5.21) it can be found that the leading error terms are proportional to h^3, and that no h^2 terms are present. This is the explanation for the symmetric algorithm to be more accurate than the asymmetric one. Using a procedure similar to the previously mentioned for the asymmetric SSF method, [78] obtained the local simulation error after one step of propagation as:

$$\epsilon = \gamma P_{\max}(z)h(z)(DB_\lambda R_s h(z))^2 \tag{5.26}$$

which can again be solved to provide the step size h_k during propagation:

$$h_k = \left[\frac{\epsilon}{\gamma|E(z_{k-1})|^2(2\pi|\beta_2|R_s^2)^2}\right]^{1/3} \tag{5.27}$$

For modern communication systems having moderate nonlinearity, the only parameter that changes during propagation is the intensity of the electric field, due to fiber attenuation, since the signal bandwidth does not change significantly. Instead of making the step size very small, in order to approximate the nonlinear operator by $\exp(h\hat{N})$, an elegant alternative consists in approximating the integral of equation (5.24) with a trapezoidal rule such that:

$$\int_z^{z+h} \hat{N}(z')dz' \approx \frac{h}{2}\left[\hat{N}(z) + \hat{N}(z+h)\right] \tag{5.28}$$

where $\hat{N}(z)$ and $\hat{N}(z+h)$ is the nonlinear operator evaluated both at the beginning and at the end of the step, respectively. However, the nonlinear operator is unknown at the end of the step when the propagation was only performed up to the middle of the segment. Therefore, an iterative procedure is used (Fig. 5.3), where initially $\hat{N}(z+h)$ is replaced by $\hat{N}(z)$, so that a good approximation of the electric field at the end of the step $A(z+h,t)$ can be found, and consequently an accurate approximation of $\hat{N}(z+h)$ is obtained. Thereafter, the calculation of the nonlinear operator can be repeated, with the number of iterations depending on the convergence of the results. The work presented along this thesis has systematically resorted to using one repetition, which has shown to be enough to assure convergence of the performance.

The implementation of the dispersion operator can be accomplished efficiently by evaluating it in the frequency domain, using the fast Fourier transform algorithm:

$$\exp(h\hat{D})A(z,t) = \Im^{-1}(\Im[\exp(h\hat{D})]\Im[A(z,t)]) \tag{5.29}$$

$$= \Im^{-1}\left(\exp\left(h\left[-\frac{1}{2}j\beta_2\omega^2 + \frac{1}{6}\beta_3\omega^3 - \frac{\alpha}{2}\right]\right)A(z,\omega)\right) \tag{5.30}$$

where $\Im$ denotes the Fourier transform operation, and therefore, $A(z,w)$ represents the Fourier transform of $A(z,t)$. Conversely, the most efficient approach to evaluate the nonlinear operator is the time domain, being easily represented as a phase rotation:

$$\exp(h\hat{N})A(z,t) = \exp(j\gamma|A(z,t)|^2h)A(z,t) \tag{5.31}$$

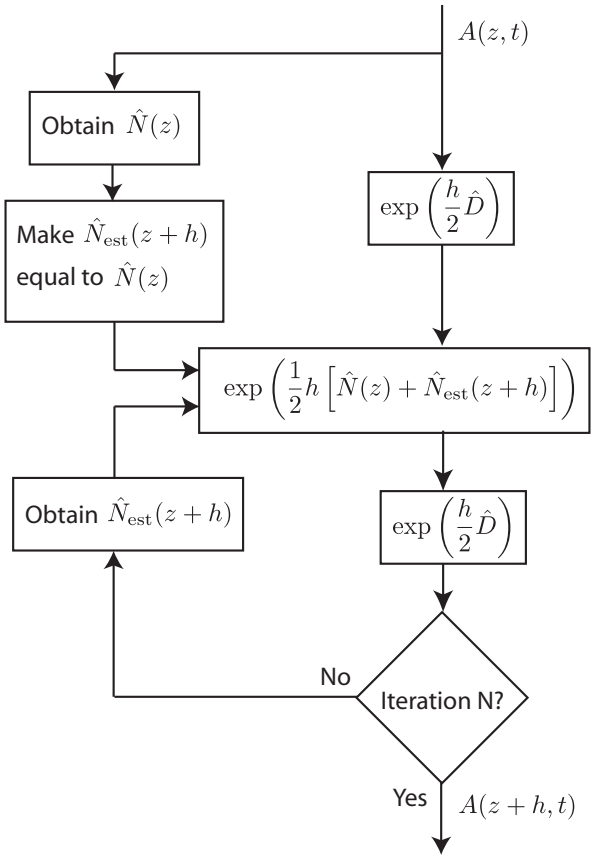

FIGURE 5.3: Diagram illustrating the iterative procedure to propagate one step of the electric field in the Symmetric SSFM

In a nutshell, the implementation of the symmetric split-step Fourier method requires dividing the fiber in a given number of sections or steps, depending on the accuracy required. In each step, the field $A(z,t)$ is first propagated through a linear part of length $h/2$, consisting of dispersion only. Then, in the middle of the step, the field is multiplied by a phase rotation operator, which introduces the nonlinear component representing the effect of the whole segment h. After that the dispersion operator is performed again. In this process there is the need to switch successively between time and frequency domains. This is accomplished through the FFT algorithm, to switch from the time to the frequency domain, and its inverse, the IFFT, to switch from the frequency to the time domain. This is the most computationally complex operation of the algorithm, requiring, in a N_{FFT} point FFT, $O(N_{\text{FFT}}\log N_{\text{FFT}})$ computations, while filtering and phase rotation operations require only $O(N_{\text{FFT}})$ operations. In the asymmetric SSF algorithm there is only one dispersion operator, representing two FFT computations. In the symmetric SSF, besides the two symmetric dispersion operators in the first and second parts of the segment, there is one extra operator due to the required iteration. This accounts

for a total of six FFT computations, three times more computations compared to the asymmetric approach. Although not analyzed in this work, in [75] a procedure has been described that leads to a computational saving compared to the standard SSF method, for WDM systems, when propagation of the individual WDM channels is performed separately. His approach consists in calculating the middle dispersion operator (the one required to increase the accuracy of the nonlinear operator), as a delay operator, accounting solely for the walk-off between channels, since, opposed to the second operator, the first and the third dispersion operators are effectively responsible for physical dispersion propagation.

5.4 Transmission model

In this chapter, a transmission channel representative of a periodically amplified long haul system is considered. Furthermore, the transmitter is considered to be capable of generating an arbitrary waveform, while the receiver is also capable of manipulating an arbitrary signal, in order to recover the transmitted symbols (Fig. 5.4). In this way, the operations necessary to combat signal distortion by the channel are performed by the receiver DSP, specifically, linear equalization, backward propagation, clock recovery and carrier phase estimation. The transmitter side DSP is responsible for the required IFFT operations when an OFDM signal is generated, while the respective FFT operation is performed by the receiver DSP. Additionally, when single carrier formats are used, pulse shaping can also be performed in the digital domain by the transmitter DSP.

5.4.1 Optical Amplifiers

A long haul fiber optic communication system is eventually limited by fiber losses. This loss limitation is typically overcome through the use of optical amplifiers, which amplify the optical signal directly on the fiber, without requiring any conversion to the electrical domain, this technique becoming widespread during the nineties. An optical amplifier amplifies incident light by stimulated emission, which is accomplished through a pump that leads to population inversion [56].

An optical amplifier generates amplified spontaneous emission noise during signal amplification. As a signal propagates along the transmission fiber, the noise is accumulated leading to a reduction of system performance, due to signal-to-noise ratio worsening. The SNR degradation is quantified through the amplifier noise figure parameter,

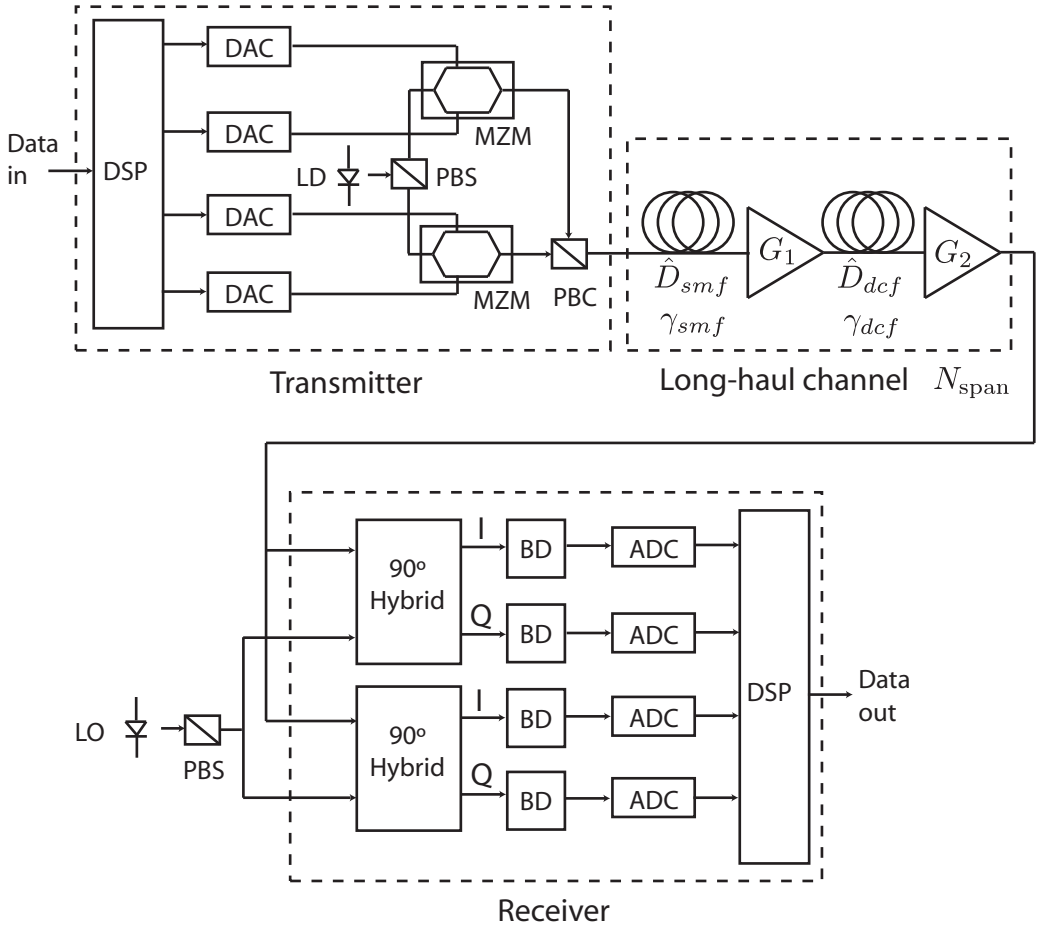

FIGURE 5.4: Diagram describing the transmitter, channel and receiver of a polarization multiplexed coherent optical system, employing digital signal processing functions at both ends.

which is defined by:

$$F = \frac{\text{SNR}_{\text{in}}}{\text{SNR}_{\text{out}}} \tag{5.32}$$

where SNR_{out} refers to the electric power generated when the optical signal is converted into an electric current.

The spectral density of spontaneous-emission-induced noise at the output of an optical amplifier is proportional to the gain and is given by [54]:

$$N_0 = h\nu n_{sp}(G-1) \tag{5.33}$$

where $h\nu$ is photon energy, h the Planck constant and ν the optical frequency. G is the amplifier gain in linear units and n_{sp} is the spontaneous emission factor which is related with the degree of atomic population inversion between the ground and excited states.

Subsequently, the amplifier noise figure can be written as [56]:

$$F = \frac{1 + 2n_{sp}(G-1)}{G} \tag{5.34}$$

For a large gain, the noise figure is approximately 3 dB, considering a perfect amplifier. In a real amplifier, the noise figure is typically around 6 dB [54, 56]. However, this definition assumes the input signal in the optical domain and the output signal in the electrical domain, after photo-detection. In [80] a different definition for the noise figure is provided, which is independent of the signal. Standard noise measurement equipment takes advantage of this fact by measuring the output noise power within a bandwidth with no signal applied at the input, the input being terminated with the source impedance. In this way the excess noise figure is defined as the output noise power within the signal bandwidth divided by the gain, normalized to the thermal noise power at standard room temperature. According to this definition, the noise spectral density at the amplifier output becomes:

$$N_0 = (F-1)h\nu G \tag{5.35}$$

Additionally, if one needs to considerer the effect of the concatenation two optical amplifiers, it is possible to apply the following formula to the excess noise figure:

$$F - 1 = F_1 - 1 + \frac{F_2 - 1}{G_1} \tag{5.36}$$

where the subscripts 1 and 2 refer to the first and second amplifiers, respectively. This development will be useful to find the total excess noise figure of the system in Section 5.4.3.

5.4.2 Dispersion Management

Dispersion management consists in precisely placing DCFs along the optical link, in order to reduce the impact of fiber nonlinearity, specifically four wave mixing, being one of the most powerful and widely used techniques for that purpose. With this technique, the total accumulated dispersion is small at any point in the fiber, but the absolute dispersion is always non-zero, causing a phase mismatch between different wavelength channels, therefore destroying the possibility of FWM [56]. The signal optical field at any given point in the fiber depends on the accumulated dispersion experienced by the

signal from the transmitter up to that point; additionally the optical field waveform influences the impact of fiber nonlinearity on transmission. In fact, since the effect of the optical nonlinearity is small on a local scale, its effects require many tens of hundred of kilometers in order to make a significant impact on performance. Therefore, as the nonlinear interaction length is long, the local chromatic dispersion assumes great importance. Supposing a signal 1 is propagated near the zero dispersion wavelength of the fiber (λ_0), and that another signal 2 having a different wavelength is co-propagated, during propagation, these signals mix and generate sidebands resulting from inter-modulation distortion. This mixing product will fall symmetrically on the other side of λ_0, therefore traveling at the same group velocity than signal 2. This allows for a long interaction length between signal 2 and its mixing product, during which they can exchange energy, leading to a degradation on signal performance. In this way, WDM systems typically operate far from the zero-dispersion wavelength, so that each channel has a finite value of dispersion, which unfortunately leads to pulse broadening. It is in this context that dispersion management is used, so that the total accumulated dispersion is zero after some distance, but the absolute dispersion per length is nonzero at all points along the fiber, providing a solution to this dilemma. This nonzero local dispersion can reduce phase matching, or the propagation distance over which different wavelengths can interact, thereby destroying the efficiency of the four wave mixing process. Therefore, by constructing an amplifier chain with concatenated optical fibers having specific lengths and opposite signs of dispersion, a dispersion map is created where phase-matching lengths are short, and the end-to-end dispersion is small or even zero in order to minimize the effects of pulse spreading.

A periodic dispersion map is typically used with a period equal to the amplifier spacing (typically 50-100 km). An 80 km spacing has been considered in this work. Amplifiers compensate for accumulated fiber losses in each section. The most common fiber type already installed in current fiber optic systems has anomalous GVD, with a parameter $D = 17\,\text{ps/(nm-km)}$, and its dispersion can be compensated by using a segment of dispersion-compensating fiber (DCF), having normal GVD with a dispersion parameter value on the order of $D = \{-80, -100\}\,\text{ps/(nm-km)}$ [54]. In this work the selected value was $D = -80\,\text{ps/(nm-km)}$. The usage of DCF has several drawbacks. Firstly, a segment of DCF can only compensate for a segment of SMF 5 to 10 times longer. One should have into account that DCF losses are relatively high in the $1.55\,\mu m$ window, typically 3 times higher than SMF. Additionally, due to the relatively small

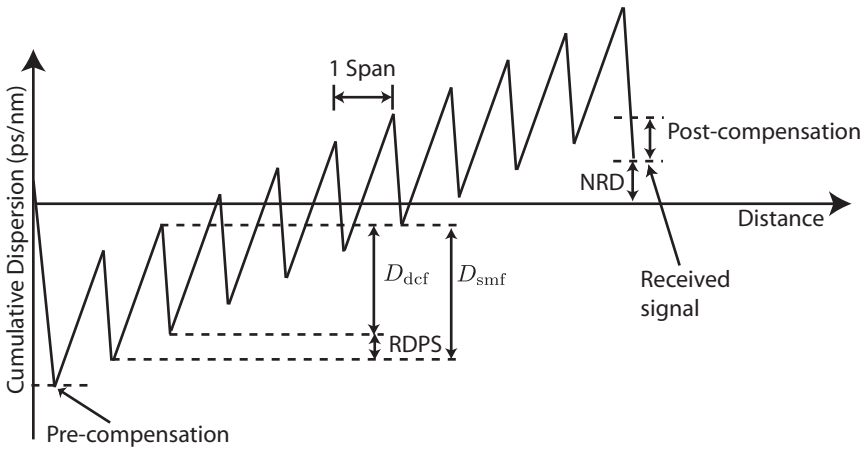

FIGURE 5.5: Cumulative dispersion map.

mode diameter of DCF, the optical intensity is larger at any given input power, resulting in enhanced nonlinear effects, with the typical nonlinear coefficient being 4 times higher than for SMF. Additionally, it is important to notice that not only the nonlinearity of DCF imposes constraints on the system performance, but also its loss and its introduced propagation delay.

Residual dispersion per span

By precisely placing the DCFs along the link, according to a specified target residual dispersion per span (RDPS), the accumulated dispersion can be controlled to provide the desired RDPS. When the residual dispersion is constant for every span in the link, it is called *singly periodic dispersion map*. DCF is typically inserted between two optical amplifiers and can either work in a pre-compensation scheme, when it is located before the transmission fiber, or in a post-compensation scheme when it is located after the transmission fiber. Additionally it can be placed at both ends in a hybrid configuration, leading to a certain degree of pre-compensation and net residual dispersion (NRD). Defining the RDPS, the amount of pre-compensation and the amount of net residual dispersion, is enough to completely describe the dispersion map characteristics. Fig. 5.5 illustrates a typical dispersion map, and provides a clear perspective about dispersion mapping concepts.

In general, it is possible to optimize the three mentioned parameters for a given set of fiber characteristics, bit-rate, channel spacing and modulation format, so that the system operating point is optimized in terms of launched power, allowing for better

Parameter	SMF	DCF
Attenuation (α)	0.2 dB/Km	0.6 dB/Km
Dispersion (D)	17 ps/(nm-km)	-80 ps/(nm-km)
Nonlinear parameter (γ)	0.0013 $\mathrm{m}^{-1}\mathrm{W}^{-1}$	0.0053 $\mathrm{m}^{-1}\mathrm{W}^{-1}$

TABLE 5.1: Specification of parameters for both SMF and DCF.

Parameter	Amplifier 1 (dB)	Amplifier 2 (dB)
Noise figure (F)	5	5
Gain (G)	$g\left(\alpha_{\mathrm{smf}}L_{\mathrm{smf}} + \alpha_{\mathrm{dcf}}L_{\mathrm{dcf}}\right)$	$(1-g)\left(\alpha_{\mathrm{smf}}L_{\mathrm{smf}} + \alpha_{\mathrm{dcf}}L_{\mathrm{dcf}}\right)$

TABLE 5.2: Specification of parameters for the amplifiers of the long haul link.

signal to noise ratios at the receiver, and therefore the best performance. For the work presented here, the considered optical fiber parameters are summarized in Table 5.1.

Additionally, the considered amplifier parameters are given Table 5.2.

The factor g is a design parameter which can be adjusted between 0 and 1, and is nominally 0.5 in the simulation results presented in the following sections, which gives $G_1 = G_2$.

5.4.3 Total system noise

By referencing the noise to the output of the first span of SMF, the amplifier concatenation formula [80] shown in Section 5.4.1 can be used to obtain the total noise figure of the system:

$$F_{\mathrm{total}} - 1 = N_{\mathrm{span}}\left[(F_1 - 1) + \frac{(F_2 - 1)}{G_1 \exp(-\alpha_{\mathrm{dcf}}L_{\mathrm{dcf}})}\right] \tag{5.37}$$

where $G_1 \exp(-\alpha_{\mathrm{dcf}}L_{\mathrm{dcf}})$ is the equivalent gain of lumping the DCF attenuation inside the gain of the first amplifier, in order to allow for the use of the concatenation formula. In this way, the total noise spectral density at the output of the last amplifier is given by:

$$N_{0,\mathrm{total}} = (F_{\mathrm{total}} - 1)h\nu \exp\left(\alpha_{\mathrm{smf}}L_{\mathrm{smf}}\right) \tag{5.38}$$

where $\alpha_{\mathrm{smf}}L_{\mathrm{smf}}$ is the equivalent gain of the two amplifiers (G_1 and G_2) with a DCF segment in between. The noise power at the receiver is then obtained by multiplying the total noise spectral density by the bandwidth of the received signal which is approximately equal to the symbol-rate. Therefore, the optical signal to noise ratio of the received signal is given by:

$$\mathrm{OSNR} = \frac{P_{\mathrm{tx}}}{N_{0,\mathrm{total}}R_s} \tag{5.39}$$

where P_{tx} is the power of the transmitted signal, which is maintained down to the receiver since the distributed amplifiers compensate for all the path losses. It is important to notice that the OSNR is defined differently from typical laboratory measurement equipment, which consider a reference bandwidth of 12.5 GHz.

5.4.4 Measures of system performance

The most commonly used metric to evaluate the performance of a digital light-wave system is the Q-factor, which corresponds to the electrical signal to noise ratio at the input of the receiver's decision circuit. Although the bit error rate represents the ultimate estimate of performance, time consuming Monte Carlo simulations are required in order to capture the low probability events, and therefore the Q factor metric is much more adequate. In this work, an adaptation of the definition proposed in [81] is used, where the Q factor is defined for QAM signaling, by extracting its value from the constellation points, using the Cartesian axes as decision thresholds. In this way, here, the Q factor is defined in the same way for QAM signals, but it is averaged in both dimensions and through all the constellation clusters, in order to provide an accurate estimate in the presence of constellation clouds distorted by nonlinear phase noise. The usage of the Q factor metric assumes the noise is Gaussian distributed, which is a good approximation when nonlinearity is compensated [82], while being a poor approximation for the tail of the probability density function when it is not compensated. The Q factor expression can be written as:

$$\mathrm{Q}_{(\mathrm{dB})} = 20\log_{10}(q) \tag{5.40}$$

where q is written as:

$$q = \sqrt{\frac{1}{2}\frac{\mu_x^2}{\sigma_x^2} + \frac{1}{2}\frac{\mu_y^2}{\sigma_y^2}} \tag{5.41}$$

for a given cluster, where μ is the mean value of a particular cluster from a decision threshold, and σ^2 is the variance in that direction [81] . Furthermore, the bit error rate of the system can be derived from the Q factor through the complimentary erf function, in the following way:

$$\mathrm{BER} = \frac{1}{2}\mathrm{erfc}\left(\frac{q}{\sqrt{2}}\right) \tag{5.42}$$

Additionally, for QPSK signals, the Q factor for the calculation of the theoretical noise limit performance can be written as:

$$\mathrm{Q}_{(\mathrm{dB})} = 20\log_{10}\left(\frac{A}{\sqrt{N_{0,\mathrm{total}}R_s}}\right) \tag{5.43}$$

where A represents the one-dimensional amplitude of the transmitted constellation points (and also its mean value in that dimension), and $\sqrt{N_{0,\mathrm{total}}R_s}$ represents the standard deviation of the added noise.

5.4.5 Theoretical performance limits

In order to provide a perspective on how the Q factor varies with the launched power, an analysis on the theoretical performance has been made. As can be seen in Fig. 5.6, two sets of results are plotted, one for 10 GSymbols/s and another for 25 GSymbols/s, which are the symbol-rates with more significance in the current research for optical communication systems [17], which allow for 40 Gb/s and 100 Gb/s systems, when polarization division multiplexing and QPSK modulation are considered. The red and pink lines are for the single channel case, with 100% RDPS and 0% RDPS, respectively, where approximately 1.2 dB of penalty arises with the introduction of DCF, due to its loss. The blue line corresponds to OFDM transmission, having $N_c = 128$ carriers and a guard interval of 1/8 of the observation period, where a penalty is incurred due to the usage of cyclic prefix, in this case 0.58 dB.

It is also of relevance to analyze the impact of varying the factor g, the amplification distribution factor between amplifier 1 and amplifier 2, for the long haul amplified link in consideration. In order to understand the impact of this factor on system performance, firstly it is relevant to obtain the power profile within the amplified long-haul system. Fig. 5.7 presents an overview of the power evolution along the fiber span.

The amplification distribution factor g can be varied between 0 and 1, as long as the total gain $G_1 + G_2$ is equal to the total loss $L_1 + L_2$ induced by both SMF and DCF. As depicted in Fig. 5.8, the analysis considers three different RDPS scenarios and two different data-rates. As expected, there is no performance difference for $g = 1$ between the several RDPS cases, since the total gain is lumped to amplifier 1. This is explained considering that the total noise figure for the concatenation of two amplifiers given in (5.37), takes the contribution of amplifier 2 as being inversely proportional to the gain of amplifier 1. Therefore, if the gain of amplifier 1 is high, the noise figure of amplifier

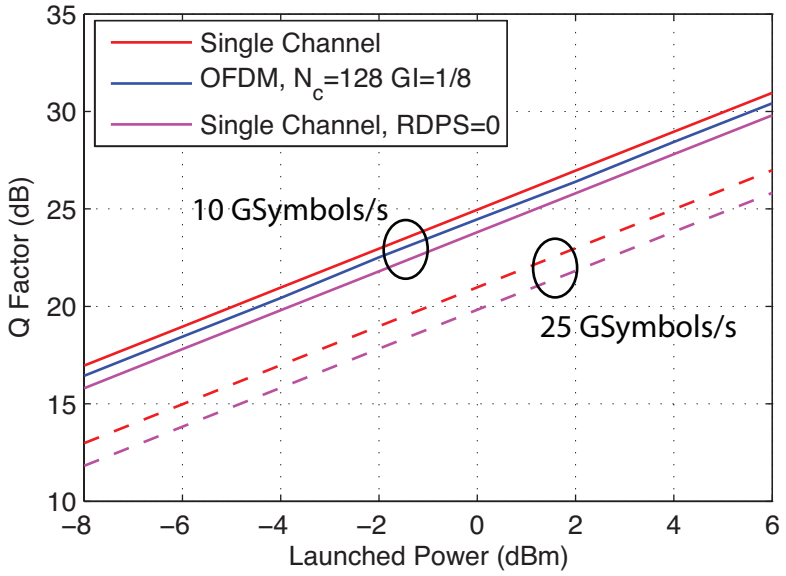

FIGURE 5.6: Q factor vs Launched Power for 10 GSymbols/s (solid lines) and 25 GSymbols/s (dashed lines)

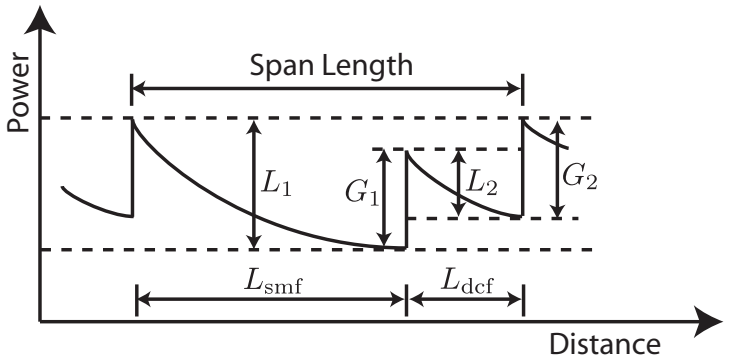

FIGURE 5.7: Diagram of the power profile. L_1 and L_2 represent the loss incurred by SMF and DCF lengths, with $L_1 = \alpha_{\text{smf}} L_{\text{smf}}$, and $L_2 = \alpha_{\text{dcf}} L_{\text{dcf}}$, respectively. G_1 and G_2 represent the gain of amplifiers 1 and 2, respectively.

2 is low, and the dependence on the amount of DCF used is cancelled by the varying gain of amplifier 1. On the other hand, when $g = 0$, the gain of amplifier 1 is unitary leading to an increased contribution of amplifier 2 to the total noise figure, which is increased proportionally to the loss induced by the amount of DCF used. In this way, the performance worsens as the amount of DCF increases (equivalent to a decreasing value of RDPS). Additionally, Fig. 5.9 analyzes the Q factor as a function of the RDPS, while considering three different values of $g = \{0, 0.5, 1\}$. As expected the values on Fig. 5.8 and 5.9 for a value of $g = 0.5$, match those in Fig. 5.6 for a launched power of +4 dBm. The major conclusion that can be obtained from these results is the fact that

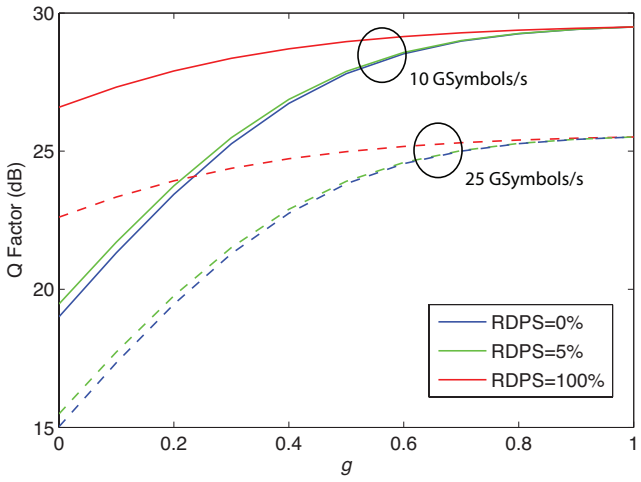

FIGURE 5.8: Q factor vs g for 10 GSymbols/s (solid lines) and 25 GSymbols/s (dashed lines), at +4 dBm Launched Power

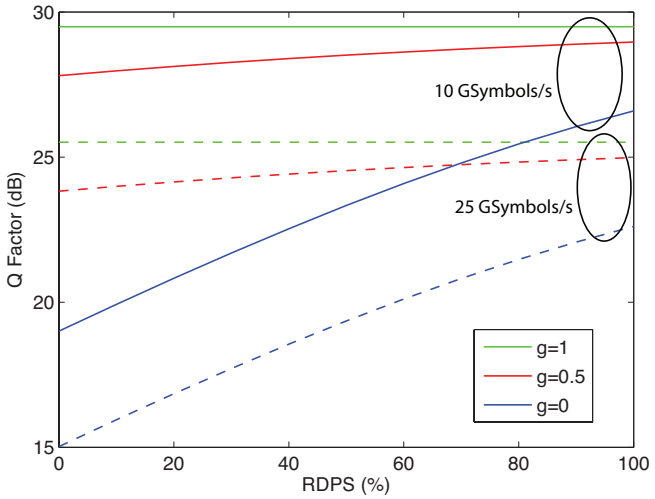

FIGURE 5.9: Q factor vs RDPS for 10 GSymbols/s (solid lines) and 25 GSymbols/s (dashed lines), at +4 dBm Launched Power

as far as only the noise impact is considered, the ideal scenario would be to use a g factor near the unity, which means lumping the most part of the gain to the first amplifier, in order to obtain the best performance, regardless of the RDPS value. Further in the current chapter, a similar analysis will be performed taking into account the impact of nonlinearity, which will lead to different conclusions.

5.5 Back propagation algorithm

Whereas in the linear transmission regime, the total system capacity increases with launched power, in the nonlinear regime the capacity is reduced, because fiber nonlinearity scales with the square of the power while SNR grows linearly with the power. The highest capacity is observed in the transition from the linear to the nonlinear regime. The compensation of both linear and nonlinear fiber impairments allows for the improvement of the highest capacity point due to an increase of the optimum launched power. The best method known for fiber nonlinearity mitigation is backward propagation [14], which consists in passing the received signal through a virtual fiber with opposite signs of dispersion and nonlinearity, yielding an estimate of the transmitted signal. In the absence of noise and limited computation power and provided the characteristics of the transmission channel are known, this technique can recover exactly the signal that was transmitted. While BP was firstly used in pre-compensation schemes [83, 84], the availability of the full electric field in a coherent optical receiver allows for BP to be used as a post-compensation technique. Since the BP algorithm works with the electric field of the signal, it can be applied to single carrier, wavelength division multiplexing (WDM) and OFDM signals.

In fact, back-propagation has been proposed as a universal technique for jointly compensating linear and nonlinear impairments for WDM systems using coherent detection, DSP and DCF, enabling higher launched power and longer transmission reach. It has been proposed independently by [15] and [16]. BP calculates a solution for the NLSE, which is generally numerically solved using the Split Step Fourier Method (SSFM), having inverse signs for the dispersion and nonlinearity operators:

$$\frac{\partial E}{\partial z} = (\hat{D} + \hat{N})E \tag{5.44}$$

Notice that for back-propagation equations the nomenclature for the electric field is expressed as $E(z,t)$, while for forward simulation of the optical system it is considered as $A(z,t)$. In terms of the structure of the transmission channel, Fig. 5.10 provides a description of the pathway which the electric field follows from the transmission up to the reception, where the signal should recover its original form. The complete equation

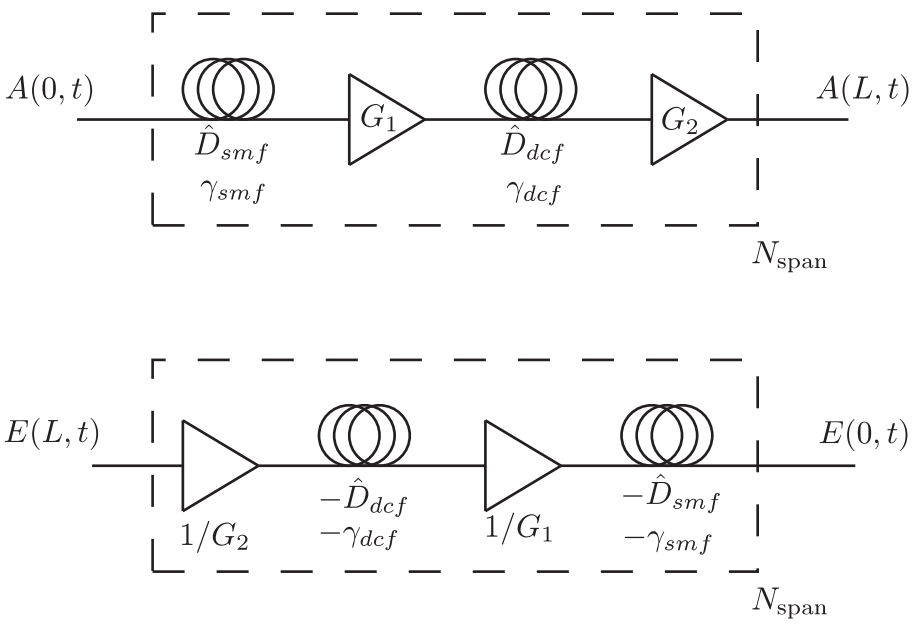

FIGURE 5.10: Forward and backward transmission diagrams

for the back-propagation algorithm is as follows:

$$-\frac{\partial E}{\partial z}+\frac{1}{2}j\beta_2\frac{\partial^2 E}{\partial t^2}-\frac{1}{6}\beta_3\frac{\partial^3 E}{\partial t^3}+\frac{\alpha}{2}E=j\gamma|E|^2E \tag{5.45}$$

Back-propagation can be used as a pre-compensation technique, resulting in the transmission of a distorted signal that the fiber characteristics end up restoring, which might be useful if full information of the electric field is not available at the receiver. However, the topic of this work explores the usage of post-compensation, since the signal is considered to be down-converted in the receiver using a coherent approach. Additionally, as back-propagation focus on the numerical solving of the NLSE, the previously discussed asymmetric and symmetric algorithms are also valid, as well as the step size selection rules.

In fact, the main drawback with back-propagation compared to forward propagation is that the output signal can not be calculated to arbitrary precision due to the effect of noise. Therefore, the equation governing the calculation of the back-propagated electric field after one step size needs to suffer an adjustment in the nonlinear operator:

$$E(z,t)=\exp\left[-h(\hat{D}+\zeta\hat{N})\right]E(z+h,t) \tag{5.46}$$

The parameter ζ is the amount of nonlinearity compensated, reflecting the uncertainty

of the signal amplitude used to undo the nonlinear phase rotations. The mathematical model of the back-propagation algorithm is shown in Fig. 5.11 for the asymmetric case.

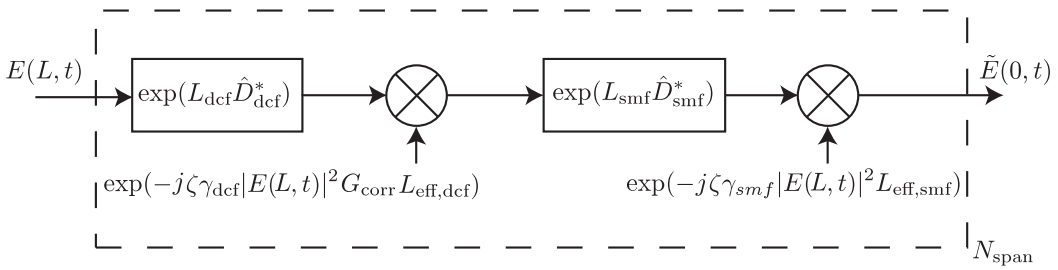

FIGURE 5.11: Asymmetric BP diagram. The operators $\hat{D}^*_{\mathrm{dcf}}$ and $\hat{D}^*_{\mathrm{smf}}$ denote the complex conjugate of $\hat{D}_{\mathrm{dcf}}$ and $\hat{D}_{\mathrm{smf}}$, respectively.

As shown in Fig. 5.11, for the part of SMF compensation, the nonlinear phase de-rotations are proportional to:

$$L_{\mathrm{eff,smf}}\gamma_{\mathrm{smf}}|E(L,t)|^2 \tag{5.47}$$

Additionally, the DCF compensation part includes a gain correction factor of:

$$G_{\mathrm{corr}} = G_1 \exp(-\alpha_{\mathrm{smf}} L_{\mathrm{smf}}) \tag{5.48}$$

in order to correctly reference the power level in the DCF section. Equation (5.47) considers that only one section per span is performed. If more than one step is to be performed, then the phase de-rotation for each step i of SMF is proportional to:

$$L_{\mathrm{eff,smf}_i}\gamma_{\mathrm{smf}}|E(L,t)|^2 \exp\left(\frac{-\alpha_{\mathrm{smf}} L_{\mathrm{smf}}(i-1)}{N_{\mathrm{sec}}}\right) \tag{5.49}$$

where N_{sec} is the total number of sections, and:

$$L_{\mathrm{eff,smf}_i} = \frac{1-\exp(-\alpha_{\mathrm{smf}} L_{\mathrm{smf}}/N_{\mathrm{sec}})}{\alpha_{\mathrm{smf}}} \tag{5.50}$$

Therefore, the effective length is modified to reflect the reduced segment length of fiber. Furthermore, the exponential term in equation (5.49) reflects the change in the signal power from step to step. In this way, the index i should be varied from N_{sec} down to 1, so that the signal power grows along the fiber span, symmetrically to its variation when it was first forward propagated. Additionally, Fig. 5.12 shows a diagram of the

implementation of the BP algorithm considering multiple sections per span, as explained above.

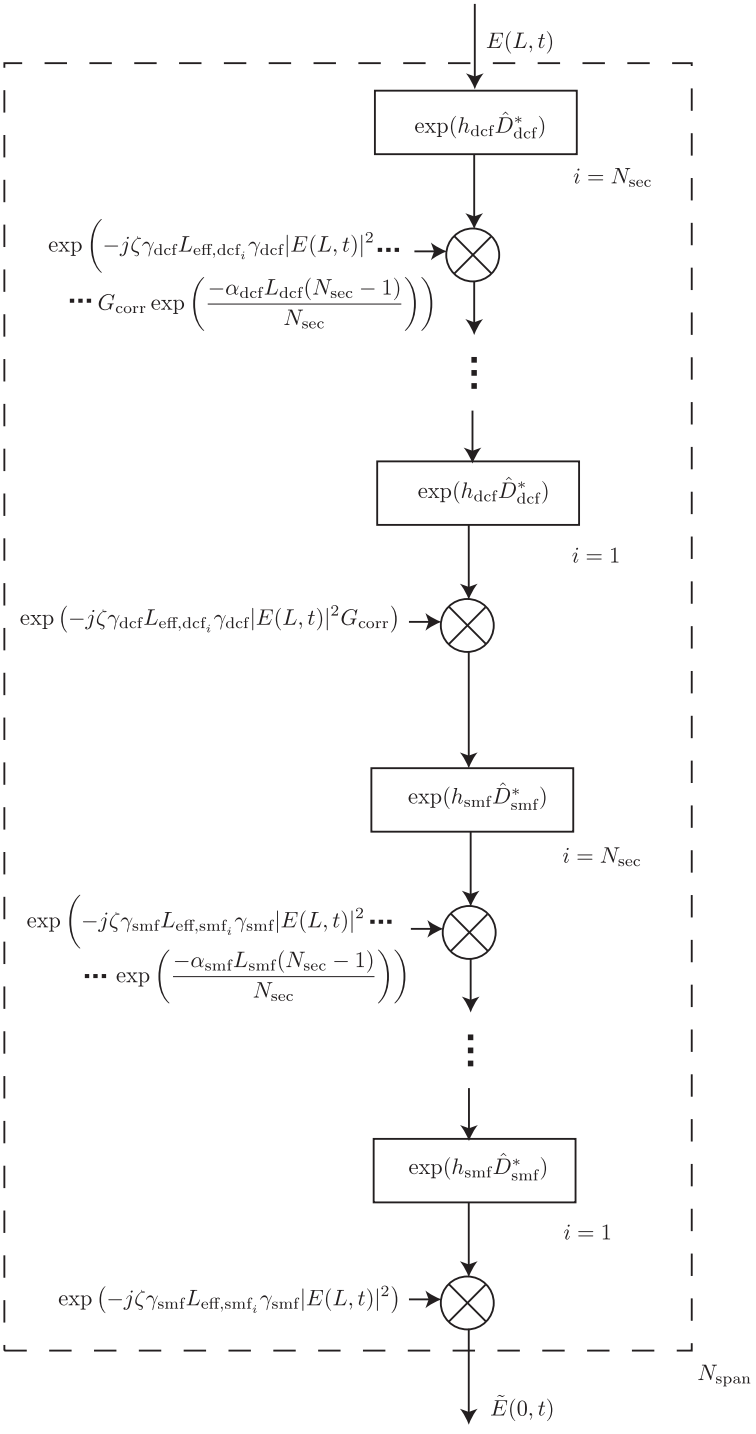

FIGURE 5.12: Asymmetric BP diagram, considering N_{sec} sections per span. Variables h_{dcf} and h_{smf} denote the length of each section of DCF and SMF, respectively.

For a typical transmission case, the weight of the dispersion operator is much higher than the weight of the nonlinear operator. In fact, the nonlinear operator contributes

with a small perturbation on what is mainly a dispersive scenario. Therefore, if the estimation of the electric field after each BP step is accurate enough, one can perform the nonlinear phase de-rotation admitting the nonlinear operator is a good estimate of the true value, which is equivalent to set ζ near 1, because it is likely that this phase de-rotation will make the output signal closer to the original signal. On the other hand, if the calculation of electric field is inaccurate due to noise or numerical error, it is desirable to take only a small contribution of the nonlinear operator weight for the phase de-rotation. Otherwise, an error in amplitude would be converted into a random phase rotation, leading to a even worse estimation of the signal electric field. This parameter depends on the launched power, dispersion map, oversampling rate and number of steps used for BP. The best value of ζ is found by numerical simulation, and generally is small (tends to zero) for low residual dispersion per span, and approaches 1 for dispersion unmanaged transmission (100% RDPS). Additionally, the parameter tends to 1 for an increasing number of BP steps.

The numerical error mentioned in the previous paragraph leads to a divergence between the output of the digital SSFM and the true solution of the propagation equation. The two main reasons leading to this phenomenon are an insufficiently small step size length, and the sample rate not satisfying Nyquist's criterion, when taking into account the new frequencies generated by the nonlinearity. In [16] it has been found that an oversampling rate of three may be required for back-propagation in order to avoid aliasing effects, due to the electric field being third order on the propagation equation. The step size requirements were discussed in [78]. Furthermore, one should notice that any inaccuracies in the representation of the FIR linear filter responsible for dispersion compensation operation, would result in a numerical error, due to error accumulation at each iteration. It is therefore essential to minimize the amplitude distortion of the linear equalizer [85].

5.5.1 Performance impact induced by ζ parameter

At this point, it is relevant to gain insight on the influence of the parameter ζ on system performance, while varying the value of RDPS. Furthermore, since the DCF also contributes to both dispersion and nonlinearity phenomena, it is also useful to notice the system sensitivity to these parameters, specifically, how performance is affected by turning off these parameters in the simulations. Fig. 5.13 demonstrates three sets of

results for $\zeta \in \{0, 0.5, 1\}$, for a typical scenario referred as "A" (solid lines), for a scenario "B" where the DCF dispersion effect is turned off (dashed lines), while maintaining its nonlinearity and finally for the case "C" where the DCF nonlinearity effect is turned off (dotted lines), while maintaining its dispersion. Notice that for scenario "B" the effective residual dispersion per span does not correspond to its nominal value, since the dispersion effect is not cancelled by the DCF. However, the objective is to investigate the interplay between dispersion and nonlinearity, in order to quantify the contribution of each effect separately. These simulations were performed using QPSK modulation, with an oversampling rate of $M/K = 3$, a launched power of +4 dBm, and 3 sections per span. Additionally, Fig 5.14 shows the results of the same analysis but using a continuous variation of parameter ζ, which is therefore represented in a three dimensional surface.

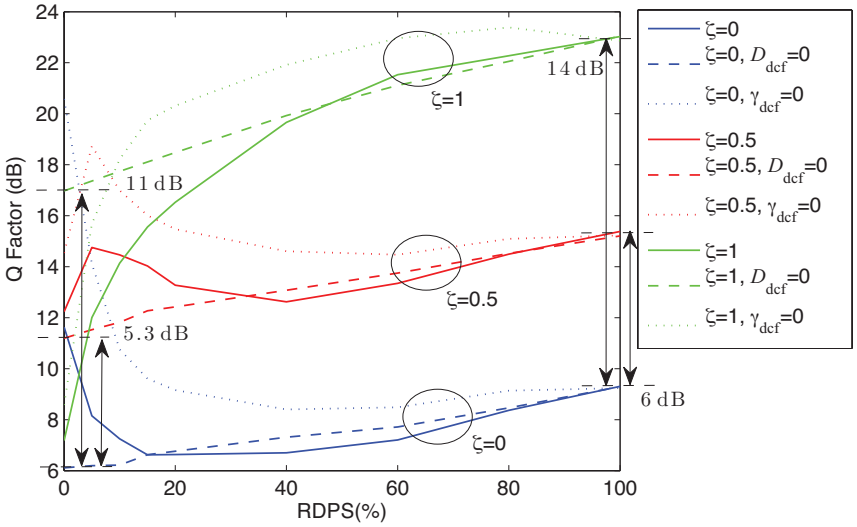

FIGURE 5.13: Performance comparison on the influence of $D_{\text{dcf}} = 0$ (dashed lines) and $\gamma_{\text{dcf}} = 0$ (dotted lines) at +4 dBm Launched Power

In the first place, the results with $\zeta = 0$ should be looked at. If starting from the 100 % RDPS point, considering scenario "A", one can see that the performance degrades as the RDPS decreases, since the DCF length is increased, which on its turn increases the loss and DCF nonlinearity, thus leading to a worse performance. Additionally, a reduction of SMF dispersion (by adding DCF) can increase the impact of nonlinear effects. In fact, the presence of dispersion reduces the impact of nonlinearity because it induces the noise to walk-off from the signal, reducing the nonlinear interactions between them [16]. However, in spite of these mentioned effects that lead to performance worsening, one

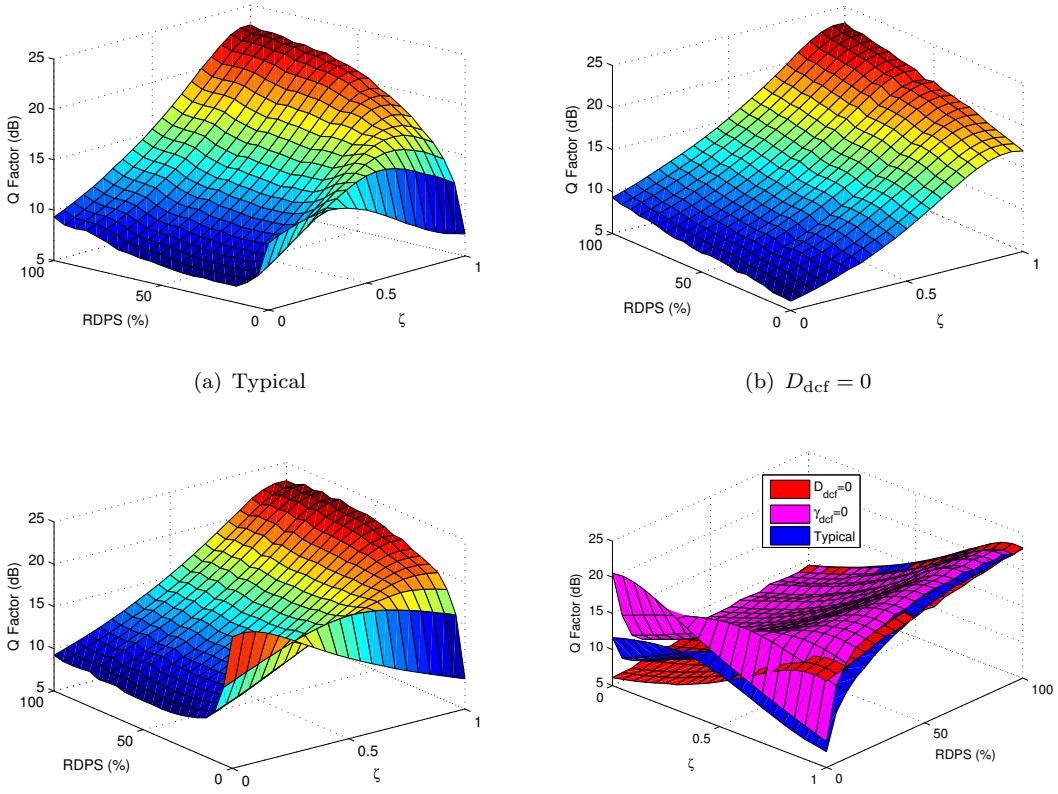

(a) Typical

(b) $D_{\mathrm{dcf}} = 0$

(c) $\gamma_{\mathrm{dcf}} = 0$

(d) Superposition of results of (a), (b) and (c)

FIGURE 5.14: Q factor versus ζ parameter versus RDPS value, for 3 sections of asymmetric BP algorithm at 10 GSymbols/s. Typical (a), $D_{\mathrm{dcf}} = 0$ (b), $\gamma_{\mathrm{dcf}} = 0$ (c), and superposition of the previous three (d)

might notice that when approaching 20 % RDPS the Q factor starts improving continuously up to 0 % RDPS. This indicates that another effect starts dominating, which is the fact that the nonlinear phase rotations occur closer to points of zero dispersion, therefore affecting the signal at instants where its original constellation form is nearly recovered. Therefore, at the receiver, if no nonlinear compensation is performed along with dispersion reversal (for $\zeta = 0$), the signal constellation is still reasonably acceptable, exhibiting a spiral effect from nonlinear phase rotations, as shown in Fig. 5.15. On the other hand, when nonlinear phase rotations systematically occur at points of high dispersion (for higher RDPS values), nonlinearity impacts a signal which is largely distorted by dispersion, therefore, after dispersion reversal the signal remains still very distorted, as also shown by the comparison given in Fig. 5.15.

Scenario "B" gives slightly better performance than "A" for high RDPS values. While in "A", the increase of DCF length leads to a reduction of the SMF dispersion effect and consequent reduction of the advantageous noise walk-off effect, in "B" there

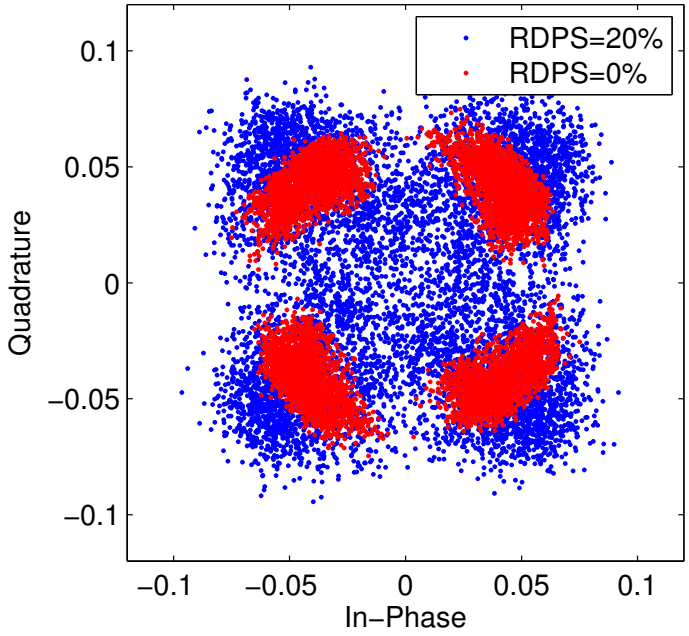

FIGURE 5.15: Performance comparison between 0 % and 20 % RDPS, for $\zeta = 0$, at +4 dBm of launched power.

is no reduction of the SMF dispersion because DCF dispersion is not activated, and therefore this effect does not occur again. Additionally, in "B", there is no performance improvement near 0 % of RDPS, because the effect of SMF dispersion cancellation does not happen. In this way, the performance linearly degrades from 100 % to 0 % RDPS, with the only effect contributing to this degradation being the DCF loss (requiring an increased level of amplification, and therefore higher noise) and also the induced nonlinearity. Finally, for scenario "C", the best performance compared to scenarios "A" and "B" is obtained. When comparing to scenario "A", the tendencies are the same (performance degradation for high RDPS values and performance improvement for low RDPS values), but a general improvement is obtained which goes from 0 dB at 100 % to approximately 8 dB at 0 % RDPS, due to the impact of the DCF nonlinearity being removed. The decreasing performance when RDPS goes from 100 % downwards is due to the above mentioned reduction of the noise walk-off effect.

Regarding the results for $\zeta = 0.5$, the curves tendencies are similar to the $\zeta = 0$ case, the Q factor being shifted by 6 dB at 100 % RDPS, due to the impact of the back-propagation algorithm on the compensation of the nonlinear phase. However, when approaching 0 % RDPS, the performance does not keep the 6 dB of advantage, for all scenarios. In scenario "B" it is approximately 5.3 dB above at RDPS=0 %, showing that

the penalty of the BP algorithm in compensating the DCF nonlinearity is approximately 0.7 dB. However, for scenarios "A" and "C" where the DCF dispersion is activated, the BP algorithm does not bring significant advantages, being even worse for case "C". This is due to the phase matching phenomenon, which consists in phase de-rotations adding coherently after each span (near zero RDPS), and proportionally to power, leading to a degradation of the Q factor. Therefore, as the RDPS deviates from 0 % the phase additions loose coherence, due to the averaging effects of chromatic dispersion, leading to a performance improvement.

Finally for $\zeta = 1$, as expected from the previous explanation, the performance is the best at 100 % RDPS, compared to the results for $\zeta = 0$ and $\zeta = 0.5$. For 0 % RDPS, the performance is only improved for scenario "B". In this scenario, the performance gain is approximately 14 dB at 100 % RDPS and 11 dB at 0 % RDPS, compared to the $\zeta = 0$ case.

The above presented results suggest that the optimum value of ζ reduces with RDPS reduction, which indicates that the compensation uncertainty is higher for lower RDPS values, where the low values of dispersion lead to an higher impact of noise and phase matching.

5.5.2 Analysis of pre-compensation impact

The pre-compensation reflects the amount of dispersion placed at the transmitter in order to shift the dispersion map in the positive or negative direction depending on positive or negative dispersion being used for that purpose, respectively, which can be visualized by recalling Fig. 5.5, where a negative amount of dispersion is used for pre-compensation. Since chromatic dispersion and nonlinearity interact with each other, the amount of pre-compensation is expected to have an impact on the resulting performance. In Fig. 5.16 the Q factor performance for the specific pre-compensation values of $P_c = \{+1, 0, -1/2, -1, -2\}$ relative to the dispersion of a single span of SMF, is shown for both cases of $\zeta = 0$ (a) and (b) where the nonlinearity is not compensated, and $\zeta =$ optimum (c) and (d), where nonlinearity is compensated using the BP algorithm with a tuned value of ζ. In (b) and (d) the DCF nonlinearity is turned off in order to facilitate the analysis of the results. The considered launched power was +4 dBm and the number of sections per span for the BP algorithm was set to 5.

Regarding the non-compensated cases, it can be concluded that using a more negative value of pre-compensation (to a certain extent) results in a better Q factor, especially for lower RDPS values, where the cumulative dispersion has a small variation from span to span, therefore crossing the zero dispersion point more times. It should be noticed that as the pre-compensation value decreases, the Q factor curves start exhibiting a maximum, which is related with the RDPS value for which the average cumulative dispersion is closer to zero. In case (b) where $\gamma_{\text{dcf}} = 0$ the results are generally better as expected, due to the absence of DCF nonlinearity. Additionally, the fact that the best Q factor at zero RDPS is for zero pre-compensation indicates that it is at the beginning of each span that nonlinearity has stronger impact due to the higher signal power after amplification, as expected. Therefore, at zero RDPS, when moving from zero pre-compensation to $P_c = -1/2$, the point where SMF nonlinearity is stronger moves away from zero dispersion, leading to a worse performance.

Considering the cases of compensated nonlinearity (c) and (d), one can observe that the Q factor is essentially affected by the amount of pre-compensation for low RDPS values. There is a small performance improvement in Q factor with reducing RDPS (below 10 %), for $P_c = -1$ in (c) and $P_c = \{-1/2, -1\}$ in (d), which occurs due to the cumulative dispersion map being near zero at those specific pre-compensation values. As seen previously, this leads to a high Q factor without compensation, and subsequently the observed improvement in the case of compensated nonlinearity is relative to this non-compensated case. In fact, the performance difference from the compensated to the non-compensated case does not vary significantly with pre-compensation. Therefore the maximum achievable Q factor for low RDPS values is possible with a pre-compensation between $P_c = 0$ and $P_c = -1$.

5.5.3 Analysis of BP step size requirements

Ip and Kahn [14, 16] have discussed that the step size requirements for BP are much more relaxed than those required to model communication systems (forward propagation). It has been shown that the step size can take values in such a range that the numerical error stays small compared to the impact of AWGN. It has also been shown that the presence of noise (and consequent amplitude fluctuations) leads to phase de-rotation values being proportional to the noisy amplitude, which makes the algorithm solution to diverge from the original value, this divergence being proportional to the

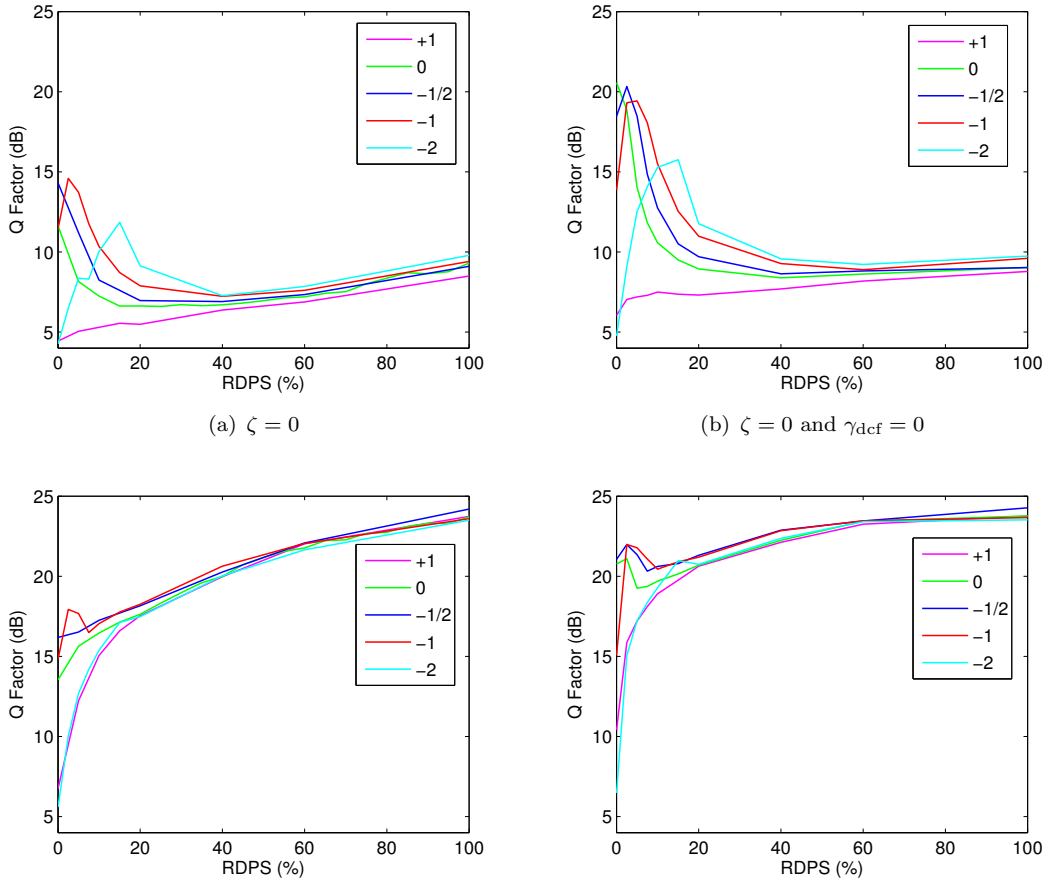

(a) $\zeta = 0$

(b) $\zeta = 0$ and $\gamma_{\text{dcf}} = 0$

(c) $\zeta =$ optimum

(d) $\zeta =$ optimum and $\gamma_{\text{dcf}} = 0$

FIGURE 5.16: Q Factor versus RDPS for varying amounts of pre-compensation, specifically $P_c = \{+1, 0, -1/2, -1, -2\}$ relative to the dispersion of a single span of SMF, with (a) $\zeta = 0$, (b) $\zeta = 0$ and $\gamma_{\text{dcf}} = 0$, (c) $\zeta =$ optimum and (d) $\zeta =$ optimum and $\gamma_{\text{dcf}} = 0$

number of sections. This fact may support the hypothesis that an optimum number of sections should exist, which should be validated later in this chapter. The step size is the most significant parameter in determining the complexity of the BP algorithm. Therefore, an extensive analysis of the effect of varying the number of sections used in the back-propagation algorithm was performed, for 100%, 5% and 0% RDPS, when considering a launched power of +4 dBm, as shown in figs. 5.17, 5.18 and 5.19, respectively. The values of RDPS considered were chosen empirically by simulation results showing that the most significant performance differences are located near 0% RDPS. Lines represented by "dash-dot" are for an oversampling rate of two, dotted lines are for an oversampling rate of three, while dashed lines are for an oversampling rate of four. Additionally, solid lines correspond to using the maximum of the available samples used

in simulation and therefore should represent the best case. The symmetric and asymmetric SSFM algorithms are distinguished by blue and pink colors, respectively. A red dashed horizontal line is additionally depicted for the 100%RDPS case, representing the theoretical limit performance, for referencing purposes. The careful analysis of these plots carries a lot of useful information, that allows one to understand the influence of the oversampling rate, RDPS value and type of algorithm used, while gaining sensitivity to the importance of each of these parameters. The maximum number of sections used was 10, because it is possible to achieve a stable Q factor within this limit, regardless of the oversampling rate. First of all, it is clear that an oversampling rate of two is honestly insufficient, in all cases, since the performance is clearly poor in terms of Q factor, and additionally the ζ parameter stays away from one indicating that numerical error has a significant impact. An oversampling rate of three is preferable, since it provides better results, but the RDPS value should be analyzed. In fact, for low values of RDPS, it is clear that an oversampling rate of four tends to be necessary. The results corresponding to using all of the samples available, provide an indication on how far is the performance of each of the different oversampling rate from the limit. In particular, for 100% RDPS case, an oversampling rate of four has practically the same performance as the limit, indicating there is no benefit in increasing the oversampling rate beyond this value. However, this does not hold for cases of low RDPS, where more than four times of oversampling would be required to achieve a performance near the limit, which would lead to high computational complexity. For the specific case of 0% RDPS, an additional result is presented, corresponding to the scenario of turning off the AWGN in the simulation. Bold lines in blue and pink colors, corresponding to the symmetric and asymmetric algorithms, respectively, are represented. The results indicated that it is effectively the presence of noise that leads to numerical error in the simulation. The noise does not have a significant impact for uncompensated transmission, because the dispersion effect leads the noise to walk-off from the signal, while for dispersion managed transmission the noise stays in band with the signal, increasing nonlinear interactions between noise and signal.

5.5.4 Computational complexity comparison

At this point, with the quantity of information given in previous figures, one may find difficult to determine how is the complexity of each algorithm related to the system

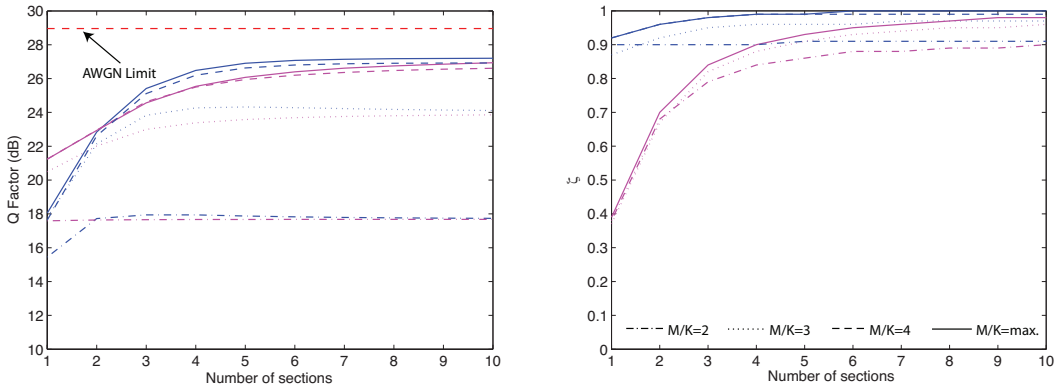

(a) Q factor (b) ζ parameter analysis

FIGURE 5.17: (a) Q factor and (b) optimum ζ parameter versus the number of sections of the BP algorithm at 10 GSymbols/s and 100% RDPS

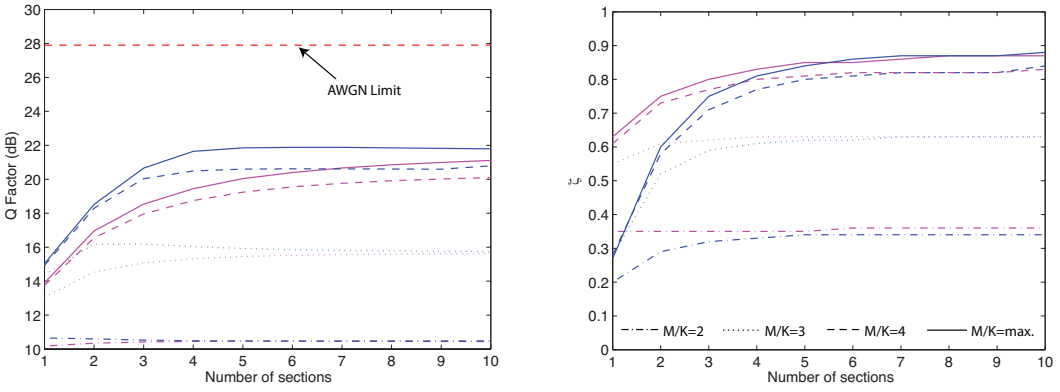

(a) Q factor (b) ζ parameter analysis

FIGURE 5.18: (a) Q factor and (b) optimum ζ parameter versus the number of sections of the BP algorithm at 10 GSymbols/s and 5% RDPS

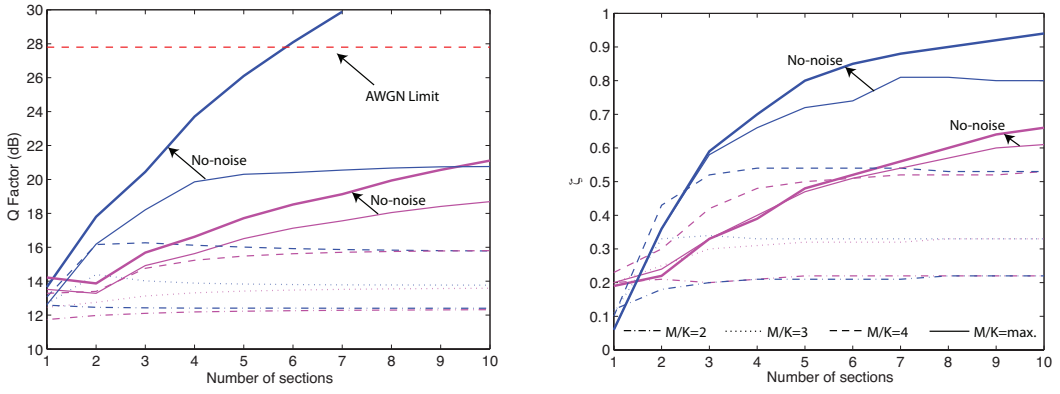

(a) Q factor (b) ζ parameter analysis

FIGURE 5.19: (a) Q factor and (b) optimum ζ parameter versus the number of sections of the BP algorithm at 10 GSymbols/s and 0% RDPS

performance. Therefore, it is of relevance to provide a means of comparing the performance gain with the complexity increase, as a function of the oversampling rate. One important remark is that the computational complexity of the symmetric algorithm is three times higher than its asymmetric counterpart, essentially because of the iterative operation associated with the splitting of the dispersion operator in two parts. In the following results given in Fig. 5.20, the asymmetric algorithm has been used as reference, having a "1x" of computational complexity, which corresponds to having a single section (or equivalently a span length section). The results in red and pink solid lines are for three and nine sections, respectively. Additionally, the results represented by dashed lines correspond to the symmetric algorithm, using 1, 3, and 5 sections, represented by the red, pink and green colors, respectively, which translates in a "3x", "9x" and "15x" complexity due to the three times factor of comparison to the asymmetric case. It can be concluded that the asymmetric algorithm outperforms the symmetric algorithm for similar complexity levels, with the performance difference gradually vanishing as the RDPS decreases.

The performance analysis as a function of the number of sections used in the BP algorithm was also carried out for a data-rate of 25 GSymbols/s. The results are presented in Figs. 5.21, and 5.22. Similar conclusions to the 10 GSymbols/s analysis can be obtained by carefully observing each of the plots. The noticeable difference is only concerned with the increased requirements in terms of minimum number of sections necessary to achieve the best performance, therefore it was necessary to analyze the results up to 20 sections, at 25 GSymbols/s. Additionally, Fig. 5.23 presents three dimensional plots showing the previous results in a different perspective where the tendencies of the curves can be more easily analyzed. It can be concluded that a higher number of sections is required for the higher data-rate of 25 GSymbols/s, where compared to the 10 GSymbols/s, as expected from the previously shown step size requirements in equation (5.23), which translates into a smaller step the higher the signal bandwidth. Furthermore, for low RDPS regimes, the performance at 25 GSymbols/s benefits from higher ζ values than for 10 GSymbols/s, which can be attributed to the higher intensity of chromatic dispersion (due to the higher data-rate), which attenuates the noise impact and the phase matching issue.

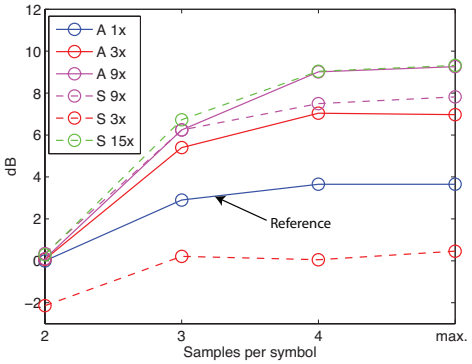

(a) 100% RDPS

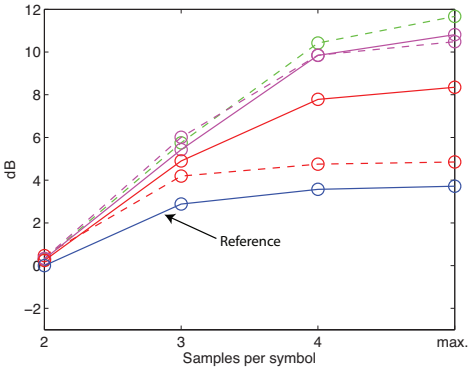

(b) 5% RDPS

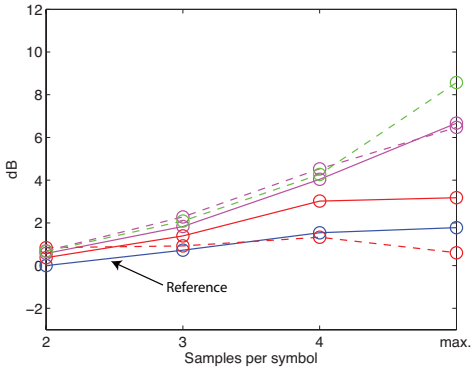

(c) 0% RDPS

FIGURE 5.20: Q factor as a function of the oversampling rate, comparing several computation complexity efforts of both symmetric and asymmetric algorithms at 100% RDPS (a), 5% RDPS (b), 0% RDPS (c), at 10GSymbols/s

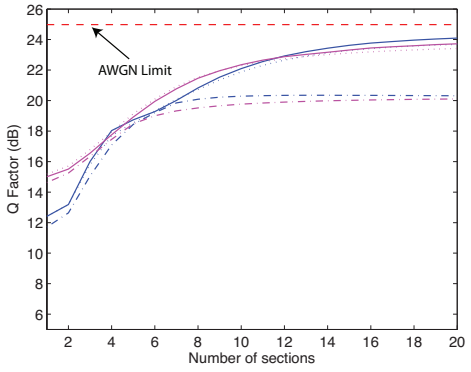

(a) Q factor

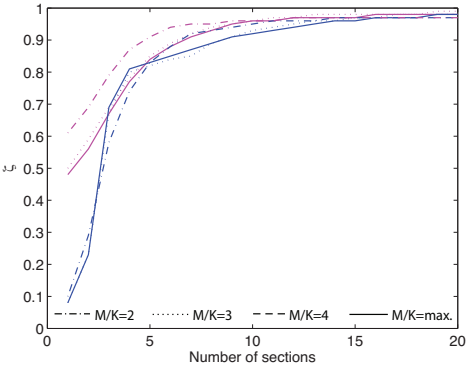

(b) ζ parameter analysis

FIGURE 5.21: (a) Q factor and (b) optimum ζ parameter versus number of sections of BP algorithm at 25 GSymbols/s and 100% RDPS

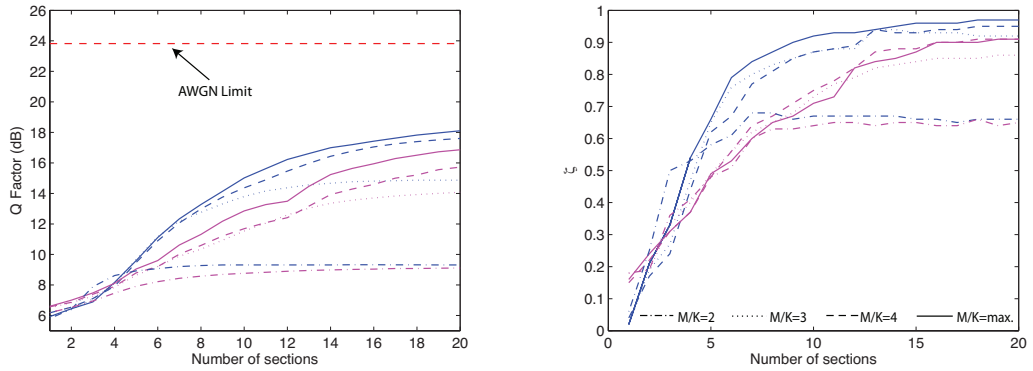

(a) Q factor (b) ζ parameter analysis

FIGURE 5.22: (a) Q factor and (b) optimum ζ parameter versus number of sections of BP algorithm at 25 GSymbols/s and 0% RDPS

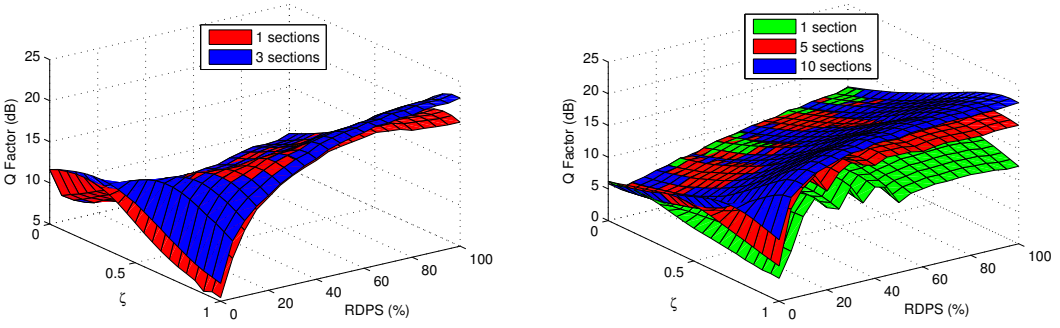

(a) 10 GSymbols/s (b) 25 GSymbols/s

FIGURE 5.23: Q factor versus ζ parameter versus RDPS value, at 10 GSymbols/s(a) and 25 GSymbols/s(b)

5.5.5 Performance impact induced by g factor

Previously in this chapter, the performance impact of the g factor was analyzed in theoretical terms, in Figs. 5.8 and 5.9, for a long-haul transmission system where the only considered impairment was the noise from amplifiers. However, when considering the channel dispersion and nonlinearity and their subsequent compensation through the BP algorithm, another analysis becomes pertinent. Fig. 5.24 presents the results on the performance impact of g factor as a function of ζ, for RDPS={0, 5,100} % and for both 10 GSymbols/s and 25 GSymbols/s transmission rates. Although theoretically the optimum g value tends towards 1 regardless of the RDPS value, after BP this holds only at 100 % RDPS. In fact, for 100 % RDPS the performance does not depend on the g factor, since, for this specific case, there is no DCF. However, for lower values of RDPS the optimum g factor decreases to approximately 0.3, independently of the data-rate;

this is due the to fact that the DCF nonlinearity becomes significant and therefore it is preferable to give higher amplification to the signal after the DCF rather than before, in order to avoid its nonlinearities. This effect is also proportionally dependent on the signal launched power. In this way, simulations were conducted in order to determine the optimum g factor as the launched power is varied, for the worst RDPS scenario of 0 % (when DCF has the most significant impact). Fig. 5.25 presents the performance results as a function of g and ζ. For low launched powers (-8 dBm) the optimum g factor is approximately 0.7, indicating that a higher gain for amplifier 1 is beneficial leading to a increase on the OSNR, before the signal is again attenuated by the DCF. In fact, for this power level the system is still operating in the linear regime, and therefore the power level on the DCF is of no concern. Furthermore, as the launched power increases, the system performance increasingly moves towards the nonlinear regime, and therefore the optimum g moves towards 0. The optimum values found were $g = 0.5$ for -2 dBm, $g = 0.3$ for +4 dBm, and $g = 0.2$ for +6 dBm, which confirms the increasing impact of DCF nonlinearity.

5.6 BP for single channel versus OFDM

In this section the nonlinear performance of the two main modulation candidates for long haul optical transmission is studied, namely Polarization Division Multiplexed Quadrature Phase Shift Keying (PDM-QPSK) and Coherent Optical OFDM (CO-OFDM), focusing on both dispersion management and computational requirements analysis. The following analysis neglects the effect of polarization inherent to the PDM-QPSK format, for simplicity. OFDM signals typically exhibit high peak values, compared to single channel modulated signals. This basic signal characteristic is generally quantified through the peak to average power ratio (PAPR). In long haul single mode optical fiber, the high PAPR of OFDM may be a fundamental disadvantage, but the difference is only likely to be significant in systems with dispersion compensation [86, 87]. In such high-capacity systems, the maximization of the signal to noise ratio is achieved through the maximization of the launched power per span, which induces fiber nonlinearities, especially for high peak values that are strongly impacted. In systems without dispersion compensation, signal dispersion will cause the power distribution of OFDM and other modulation schemes to become similar at points distant from the transmitter, reducing the impact

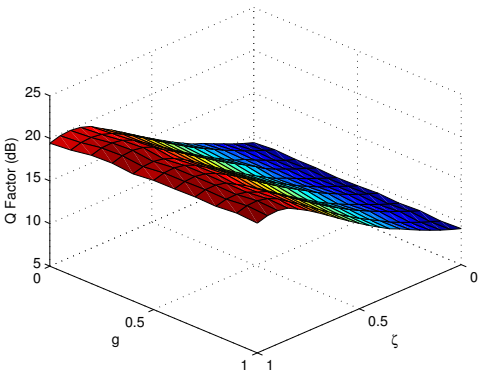

(a) 100% RDPS - 10 GSymbols/s

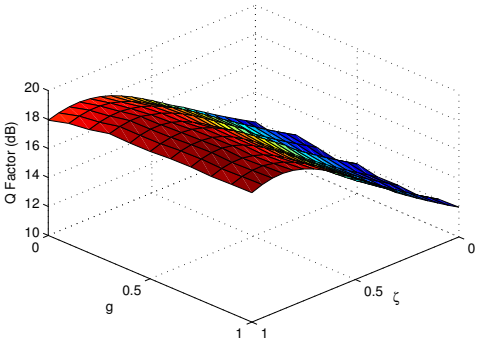

(b) 100% RDPS - 25 GSymbols/s

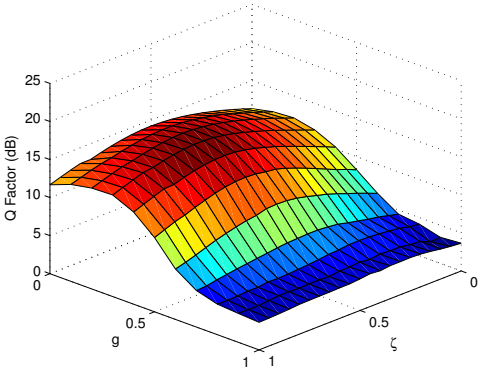

(c) 5% RDPS - 10 GSymbols/s

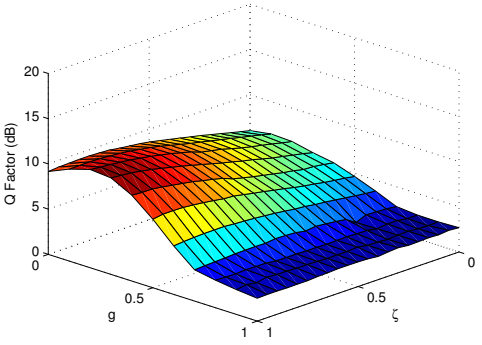

(d) 5% RDPS - 25 GSymbols/s

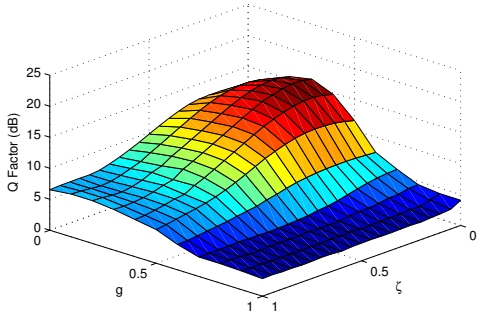

(e) 0% RDPS - 10 GSymbols/s

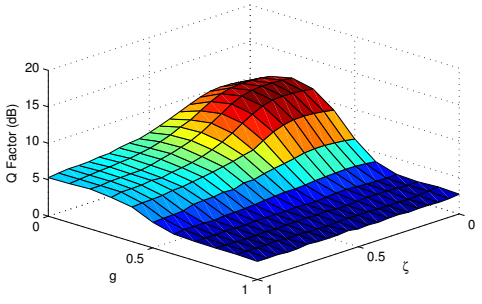

(f) 0% RDPS - 25 GSymbols/s

FIGURE 5.24: Q factor versus g factor versus ζ parameter for 100% (a), 5% (c) and 0% RDPS (d) at 10 GSymbols/s and 100% (b), 5% (d) and 0% RDPS (f) at 25 GSymbols/s

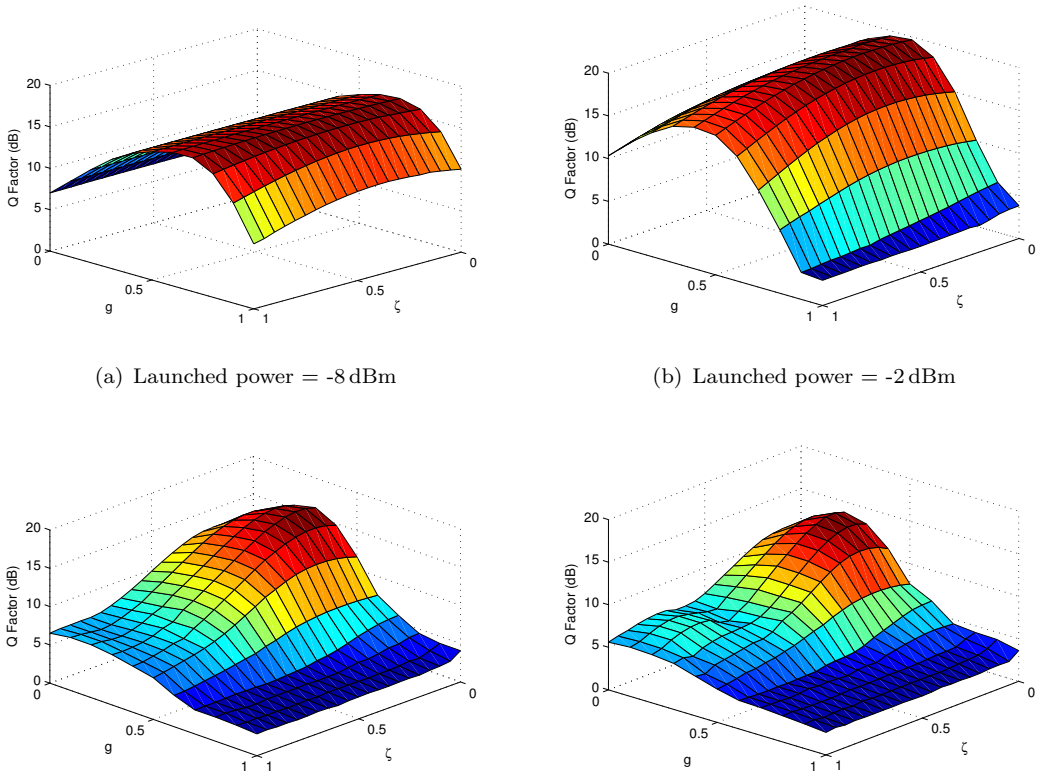

(a) Launched power = -8 dBm

(b) Launched power = -2 dBm

(c) Launched power = +4 dBm

(d) Launched power = +6 dBm

FIGURE 5.25: Q factor versus g factor versus ζ parameter for 0% RDPS at 10 GSymbols/s for a launched power of -8 dBm (a), -2 dBm (b), +4 dBm (c), +6 dBm (d)

of nonlinearity. For systems with dispersion compensation, clipping of the OFDM signal before transmission may significantly reduce the effect of fiber nonlinearity [88].

The 10 GSymbols/s long haul transmission link previously introduced in section 5.4 is used. Two dispersion management configurations are analyzed: 100 % RDPS corresponding to dispersion unmanaged transmission, and a dispersion managed link with residual dispersion of 5 % per span. The analyzed oversampling rate (OR) for single channel transmission was $M/K = \{3, 4\}$ samples per symbol. A reference OFDM signal was considered, having $N_c = 128$ carriers, with $N_u = 96$ of them being used for transmission of QPSK symbols, representing a zero padding factor of 4/3 and having a guard interval of 1/8 of the observation period. The oversampling rates of {2, 3, 4} samples per symbol were analyzed, taking into account the zero padding factor.

5.6.1 OFDM computational complexity analysis

The performance of the BP algorithm can be compared between both SC and OFDM transmission if a similar computational complexity level is considered. Therefore, it is relevant to understand how the oversampling rate and step size parameters affect the performance of the BP algorithm for OFDM signals. Figs. 5.26 and 5.27 show the Q factor as a function of the number of sections in the BP algorithm, revealing the impact of varying the oversampling rate for both 5 % and 100 % RDPS cases, respectively, considering a high launched power of +4 dBm. One should notice the fact that at 100 % RDPS an OR of 3 is sufficient, and further increasing the OR does not bring additional benefit to performance, whereas at 5 % RDPS an OR increase from 3 to 4 brings a significant improvement in performance of approximately 7 dB. The fact that for lower RDPS scenarios the computational complexity requirements are increased is due to the increased impact of noise, as previously explained, which enhances the phase matching phenomenon, leading to a smaller improvement in performance with increasing number of sections of the BP algorithm. Furthermore, the results are also compared in terms of number of sections (or steps) used in the BP algorithm, and whether symmetric or asymmetric SSFM is used. It can be verified that the performance stabilizes around 5 sections for both symmetric and asymmetric approaches, the former providing worse performance when the number of sections is small. Increasing the number of sections above that point is not worth in terms of performance gain/computational effort.

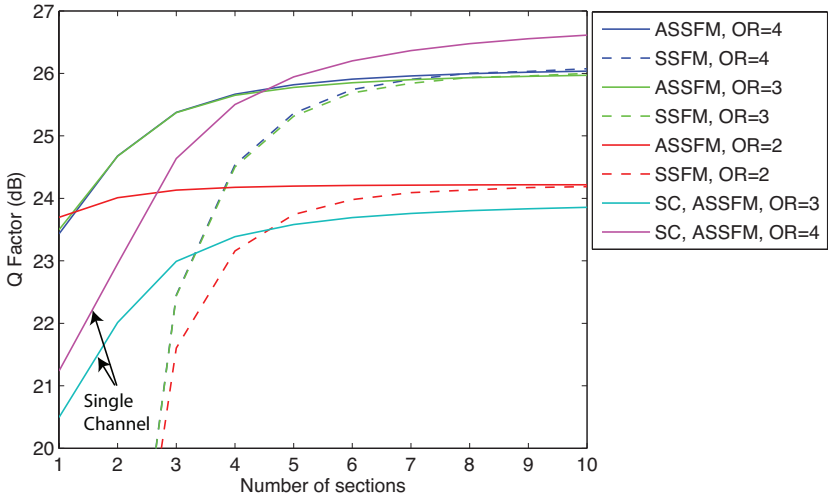

FIGURE 5.26: Q factor as a function of the number of sections used in the BP algorithm for 100 % RDPS, at +4 dBm of launched power

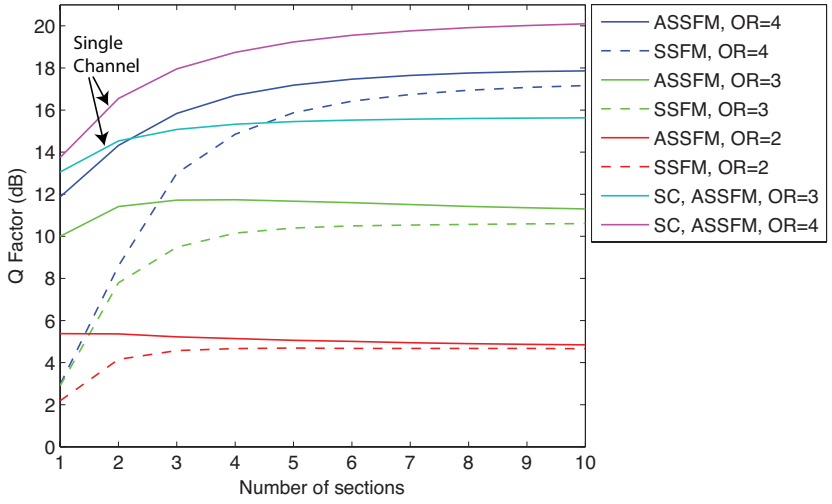

FIGURE 5.27: Q factor as a function of the number of sections used in the BP algorithm for 5 % RDPS, at +4 dBm of launched power

Considering 100 % RDPS in Fig. 5.26, and for an $OR < 4$ it is possible to observe that the performance of OFDM is better than SC, for a similar number of sections, while for $OR = 4$, SC starts outperforming OFDM above 5 sections. In general terms, to achieve optimum performance SC requires more computational complexity, which can be attributed to the larger bandwidth occupation compared to OFDM. For 5 % RDPS in Fig. 5.27, SC clearly outperforms OFDM for similar levels of complexity.

5.6.2 OFDM versus SC for varying RDPS

In order to understand how the dispersion management affects the signal performance, a detailed analysis was carried out, where the residual dispersion per span was varied from 0 % up to 100 %, as shown in Fig. 5.28. A constant number of five sections was used for both SC and OFDM transmission, and a launched power of +4 dBm. First of all, in order to quantify the nonlinearity compensation performance, results are shown where the nonlinearity was left uncompensated. As explained before for SC, the performance tends to improve for low RDPS values due to the fact that the nonlinear phase rotations occur closer to points of zero dispersion, therefore affecting the signal at instants where its original constellation form is nearly recovered, originating spiral shaped constellation due to the nonlinear phase noise. However, for OFDM, this improvement does not occur due to its high sensitivity to phase deviations stemming from the nonlinearity. Additionally, a result is shown for $N_c = 8$ subcarriers, indicating that the reduced PAPR resulting from a reduced number of subcarriers effectively leads to higher tolerance to

nonlinearity, especially for higher values of RDPS. It was verified that the oversampling rate does not change the results significantly, therefore, only one result is shown for both SC and OFDM.

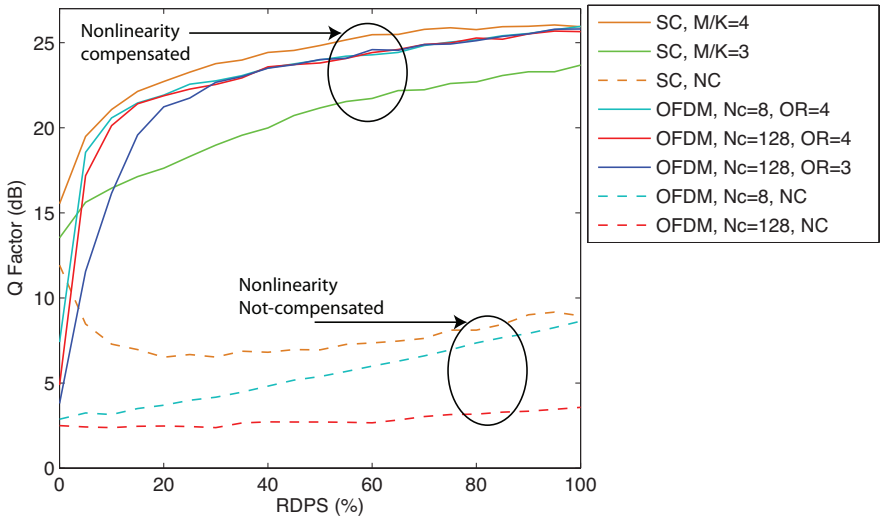

FIGURE 5.28: Q factor versus RDPS for both single channel and OFDM, considering 5 sections per span and +4 dBm of launched power. Both compensated and non-compensated (NC) cases are plotted, with solid and dashed lines, respectively.

Regarding the results where nonlinearity is compensated, one can conclude that for higher RDPS values the performance of OFDM is insensible to the oversampling rate (within the range in analysis of $OR = 3, 4$), its Q factor being approximately 2 dB better than SC for $OR = 3$ and similar for $OR = 4$. For low RDPS values (below 20 %), OFDM performance starts worsening more rapidly than that of SC. For this low RDPS cases, the OR used starts affecting performance. At 5 % RDPS a Q factor difference of 5.5 dB is observed between $OR = 3$ and $OR = 4$. Furthermore, an additional improvement of 1.5 dB is obtained if the PAPR is reduced through the reduction of the number of subcarriers from $N_c = 128$ to $N_c = 8$. This indicates that the high PAPR of OFDM induces a difference on the nonlinear performance for low RDPS values. In fact, the high peak signal values of OFDM lead to larger nonlinear phase rotations, which are impacted by the increased in-band noise when dispersion is low, therefore its compensation being less effective due to enhanced phase matching after each span.

While the previous analysis considered a fixed launched power of + 4dBm, it is also pertinent to compare the results for varying launched power, subsequently looking at two reference RDPS values of 5 % and 100 %. The performance of both OFDM and SC is obtained as a function of launched power (LP) from -8 dBm to +8 dBm, at 100 %

RDPS (in Fig. 5.29) and from -8dBm to +6dBm, at 5 % RDPS (in Fig. 5.30). In both cases, the Q factor for uncompensated nonlinearity is also shown.

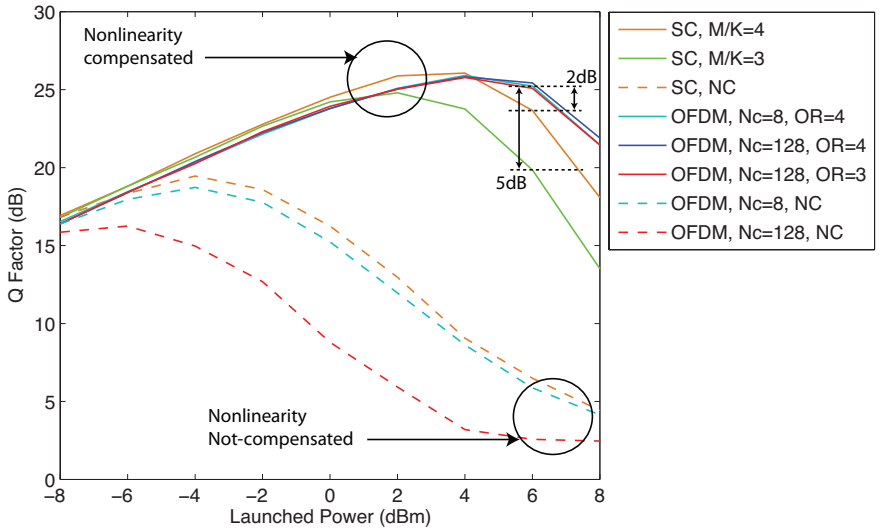

FIGURE 5.29: Q factor as a function of launched power. Single Channel vs OFDM for 100 % RDPS

At 100 % RDPS, one can conclude that the results for OFDM are all similar, with an optimum launched power of +4 dBm, while for SC, the optimum launched power is +2 dBm with $OR = 3$, increasing to +4 dBm with $OR = 4$. Considering an $OR = 3$, OFDM provides a considerable higher tolerance to nonlinearity, having a Q factor approximately 5 dB above at +6 dBm, this difference being reduced to 2 dB for an $OR = 4$.

At 5 % RDPS, the optimum launched power is reduced to 0 dBm, the performance of OFDM being worse than that of SC for similar complexities. For $OR = 3$, OFDM gradually loses performance from a similar Q factor at 0 dBm up to a 5 dB penalty at +6 dBm. For $OR = 4$, this penalty is 1.5 dB at 0 dBm up to a 5 dB at +6 dBm. For $N_c = 8$ this penalty of 5 dB is reduced to approximately 2 dB, therefore indicating that the high PAPR of OFDM is a critical factor at low RDPS values, which has a considerable impact in performance. Effectively, it can be concluded that OFDM has higher tolerance for dispersion unmanaged transmission, losing this advantage for dispersion managed systems.

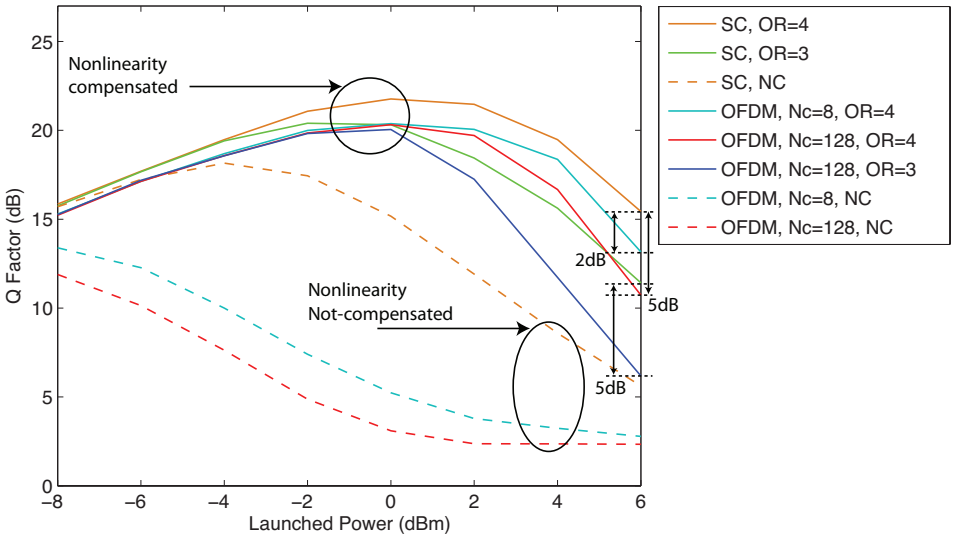

FIGURE 5.30: Q factor as a function of launched power. Single Channel vs OFDM for 5 % RDPS

5.7 Summary

The current chapter thoroughly analyzed the symmetric and asymmetric implementation of the nonlinear propagation equation. Subsequently, the simulation model of a long-haul transmission system was investigated, results being presented on the optimized dispersion map characteristics for an amplified long-haul channel, and theoretical performance bounds being obtained for both single channel and OFDM modulation formats.

The back-propagation algorithm was studied in detail, and optimum design rules were determined from simulation results, where the dispersion map, oversampling rate, launched power and computational complexity were the parameters of interest. It was concluded that the optimum value of the nonlinear phase de-rotation parameter, ζ, varies with the RDPS, indicating that the compensation uncertainty is higher for lower RDPS values, where the low values of dispersion lead to a higher impact of noise and phase matching issues. Moreover, the analysis of dispersion pre-compensation has shown an optimum value of dispersion between $P_c = 0$ and $P_c = -1$, relative to the dispersion of a single span of SMF. Concerning the analysis of computational complexity, it was found that oversampling requirements increase with decreasing RDPS, which results from the noise impact on the simulation numerical error. Additionally, the asymmetric algorithm was found to out-perform the symmetric algorithm for similar complexity levels, with the performance difference gradually vanishing as the RDPS decreases. From the comparison

of results at 10 GSymbols/s and 25 GSymbols/s, it was concluded that an higher number of sections is required for higher bandwidth signals, while higher optimum ζ values are obtained with the higher data-rate signals due to the stronger impact of chromatic dispersion. Furthermore, the influence of the amplifier gain splitting ratio g was assessed, its optimum value decreasing with increasing launched power, for low RDPS values, due to the fact that the DCF nonlinearity becomes significant and therefore it is preferable to give higher amplification to the signal after the DCF rather than before, in order to avoid its nonlinearities.

Finally, a comparison on the performance of the back-propagation algorithm between single channel and OFDM transmission formats was conducted, where it was concluded that OFDM has higher tolerance for dispersion unmanaged transmission, losing this advantage for dispersion managed systems, due to its high PAPR, which is problematic due to phase matching.

Chapter 6

Back-propagation for Multi-band OFDM signals

6.1 Introduction

Chapter 5 has shown that the interplay between fiber chromatic dispersion, intra-channel nonlinearities and amplifier noise is determinant in limiting the maximum system capacity. However, when moving from single channel to multichannel (WDM) systems attention must be paid to nonlinear inter-channel effects. Traditionally, the optical communications community has solved the problem of inter-channel nonlinearities resorting to dispersion management and mid-span phase conjugation techniques [89]. More recently, increasing attention has been put into electronic impairment compensation techniques, either using pre or post compensation [83, 90], essentially due to the progress in coherent detection, ADC (for post-compensation) and DAC (for pre-compensation) devices, associated with digital signal processing techniques, which are the building blocks to impairment compensation in the electronic domain.

This work concentrates on post compensation techniques, which have the added value that the algorithms might operate in an adaptive manner, which is effective to accommodate any modifications performed in the physical layer of the system. However, there is one inherent disadvantage in the deployment of multichannel back-propagation for mesh networks, which is related with the dynamic nature of signal routing through reconfigurable optical add/drop multiplexers (ROADMs). In fact, when the receiver performs back-propagation, it is assumed that all the channels have traveled all the way from the transmitter, which in general is not the case in these networks, because the signal

can be dropped before the receiver; in such case the receiver has no information about that channel which was dropped, but it has interacted with the other channels during propagation and needed to be taken into account. Additionally, there might be channels that were added after the transmitter, which would lead to huge errors in the receiver, because it would also back-propagate those channels up to the transmitter. Therefore, for mesh networks it is preferable to perform single channel back-propagation combined with dispersion unmanaged transmission in order to minimize inter-channel nonlinearities. In this context, the topic of multichannel back-propagation is more adequate to point-to-point links as studied in [75].

In this Chapter, the topic of multichannel back-propagation will be addressed considering OFDM signals having multiple bands. The performance of two different implementations will be compared, namely the total field and the coupled field approaches, focusing on the computational complexity issues. Furthermore, the coupled field algorithm will be extended to include the effect of Four Wave Mixing, in order to provide an improvement in performance while maintaining its computational complexity.

6.2 Multi-band OFDM

One of the main challenges associated with the investigation of electronic compensation of optical system distortions has been the fact that the bandwidth requirements of state of the art research systems is always much higher than the what the best capabilities of ADC/DAC can meet. Shieh [39] has demonstrated that this electronics bottleneck can be overcome by using the concept of orthogonal band multiplexing to divide the entire OFDM spectrum into multiple orthogonal bands (orthogonal-band-multiplexed OFDM – OBM-OFDM), which can coexist with a small or even zero guard band between them, since the orthogonality condition allows for band de/multiplexing without inter-band interference. Additionally, this approach provides other advantages relying on the fact that two OFDM subbands can be simultaneously demultiplexed using a single FFT operation whereas three (I)FFTs would be required otherwise. It is also of great importance to notice that OBM-OFDM provides inherently high spectral efficiency, since very small guard bands might be used. This OBM-OFDM scheme should not be confused with the multi-band OFDM (MB-OFDM) used for ultra-wide band circuits (UWB), where only one band is transmitted at any point in time. Although, for simplicity, the OBM-OFDM signal is referred to as multi-band OFDM signal from hereon.

In the OBM-OFDM approach, the entire OFDM spectrum is divided into N OFDM bands, each having a subcarrier spacing f_d. Therefore, in order to achieve orthogonality between bands, it is enough to use a guard band that is an integer multiple of the subcarrier spacing f_d. In this way, each OFDM band is an orthogonal extension of another band. In the receiver, the laser should be tuned to the center of each band, and then the signal is filtered by an anti-alias filter having a bandwidth slightly larger than the band itself.

The OBM-OFDM modulation scheme adopted in this work was implemented in Matlab, having a total number of subcarriers of 128, QPSK encoding, a guard-interval of 1/8 of the observation period, and the middle 88 subcarriers filled with information. Each OFDM band carries a 5 GSymbols/s stream of useful data. The anti-alias filter used accommodates a bandwidth equivalent to the frequency spectrum occupied by 138 subcarriers, which gives the equivalent to 10 subcarriers of tolerance, since each band has 128 subcarriers. Although this possibly includes spurious components from neighboring bands, since these are orthogonal to the subcarriers of interest, the interference degradation is negligible.

6.2.1 Variable band spacing

In order to evaluate the impact on system performance of varying the OFDM band spacing, a simulation was performed showing the validity of this approach. Fig. 6.1 shows the Q factor of one band de-multiplexed out of a OBM-OFDM signal, as a function of the band spacing, normalized to the subcarrier spacing (f_d).

It is clear that as soon as the band spacing rises to zero, corresponding to a band spacing equal to f_d, which is equivalent to zero guard-band, the Q factor gets above 25 dB. The band spacing is varied in 0.5 dB steps, which leads to a poor Q factor whenever the band spacing is not an integer multiple of f_d. However, as the band spacing approaches 8, the performance tends to become insensible to the orthogonal condition, since the in-band interference is reduced after that point.

A perspective of the signals that will be used in the next sections is given now, in Fig. 6.2, where OBM-OFDM signal are plotted having a normalized band spacing varying between 8 and 200, which have significantly different characteristics in order to provide an analysis regarding the performance of nonlinearity compensation algorithms.

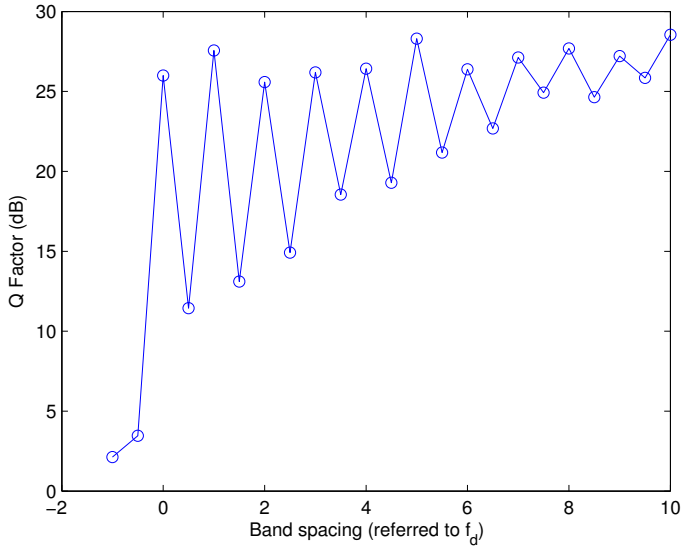

FIGURE 6.1: Q factor versus band spacing.

6.3 Total field Back-propagation

When considering a generic WDM multichannel signal, its bandwidth is generally much larger than the electrical bandwidth of a single photo-receiver. Additionally, not only the photodiode is a restriction factor but also the analogue to digital converter, whose sample rate is not enough to accommodate the whole bandwidth of a WDM signal. Therefore a structure composed by a bank of local oscillators tuned to the center frequencies of each of the channels of the WDM signal, is required in order to translate each of those channels to baseband. The receiver could now perform back-propagation using the digitized electric field from each WDM band. However, the full electric field of the WDM signal might be reconstructed through a coherent sum such that:

$$E(z,t) = \sum_{m=1}^{N} E_m(z,t)\exp(jm\Delta\omega t) \tag{6.1}$$

where N is the total number of channels, and $\Delta\omega = 2\pi\Delta f$ is the channel spacing. In fact, the signal has to be up-sampled before the optical field reconstruction can take place. The phases of the several local oscillators have to be synchronized in order to preserve the relative phase of the reconstructed WDM channels after coherent addition, which can be achieved possibly by using mode-locked lasers [74]. The reconstructed optical field can be used as an input to the back-propagation algorithm in order to compensate for the transmission impairments, as shown in Fig. 6.3, which has been named the total

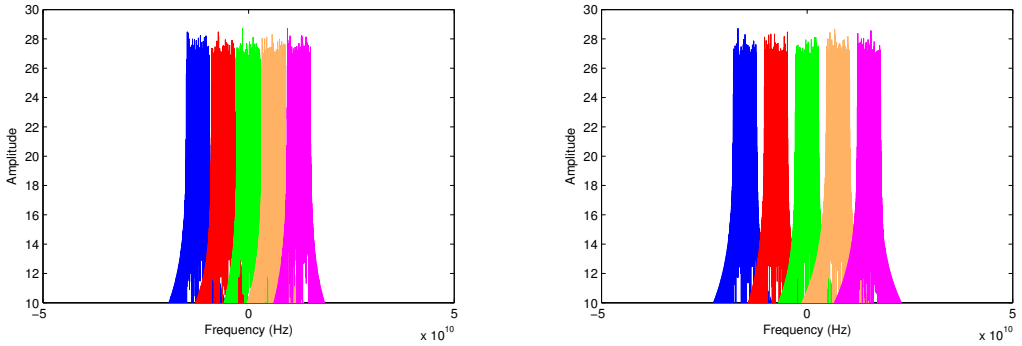

(a) Band spacing = $8f_d$ (b) Band spacing = $30f_d$

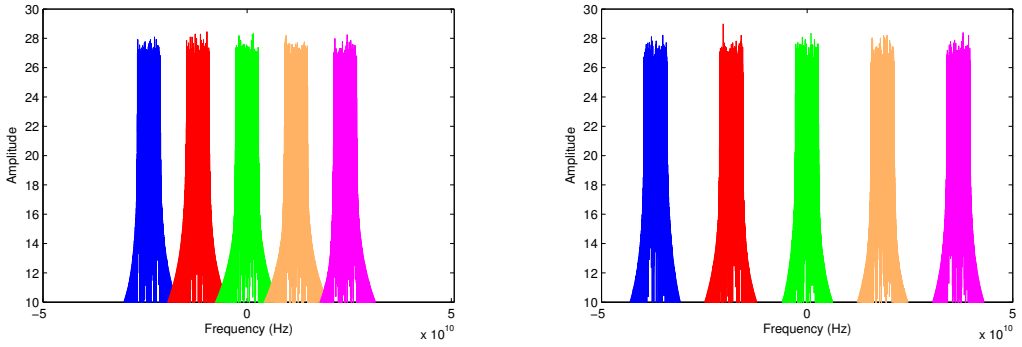

(c) Band spacing = $100f_d$ (d) Band spacing = $200f_d$

FIGURE 6.2: OFDM multi-band amplitude spectrum, with varying band spacing.

field algorithm [15, 74].

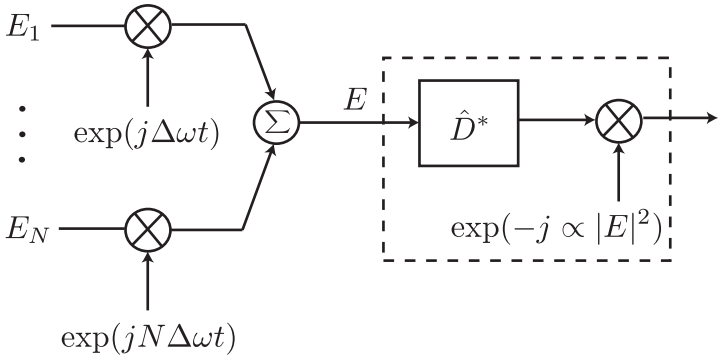

FIGURE 6.3: Diagram of total field back-propagation.

The back-propagation equation is given in the same way as in Chapter 5:

$$-\frac{\partial E}{\partial z}+\frac{1}{2}j\beta_2\frac{\partial^2 E}{\partial t^2}-\frac{1}{6}\beta_3\frac{\partial^3 E}{\partial t^3}+\frac{\alpha}{2}E=j\gamma|E|^2E \tag{6.2}$$

This equation describes the back-propagation evolution of the total field, including SPM, XPM and FWM compensation. By taking the amplified long-haul channel of Chapter 5,

simulations were performed in order to discover the behavior of the multi-band signals, with varying band spacings, in the total field back-propagation algorithm, for a RDPS of 100%, and a launched power of +4 dBm in order to operate in a strongly nonlinear region. Fig. 6.4 provides the results of this analysis.

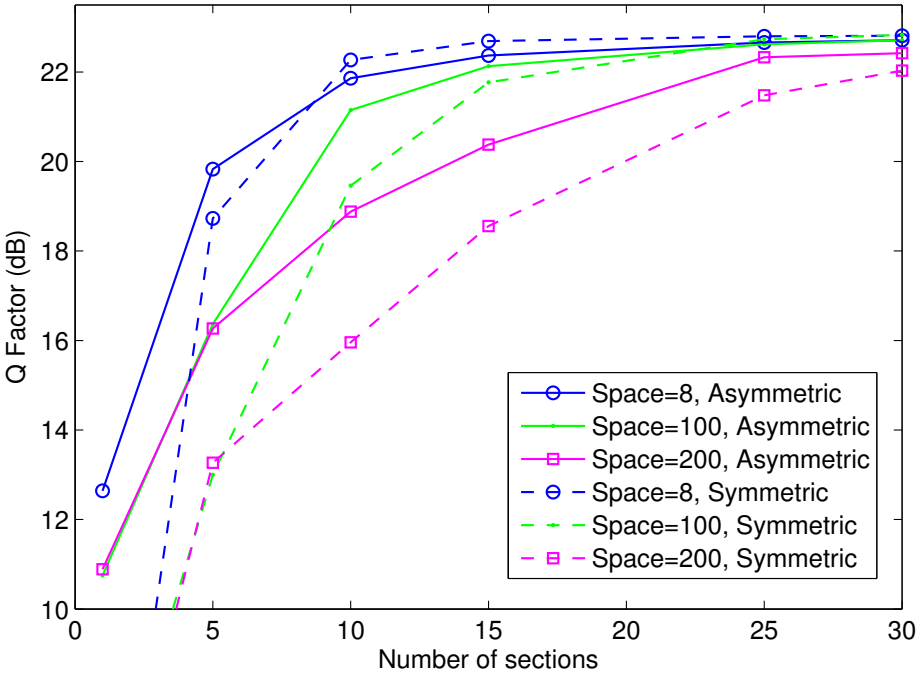

FIGURE 6.4: Q factor versus number of steps used for back-propagation, using the total field approach for the asymmetric and symmetric algorithms, at 5 GSymbols/s per band. Symmetric SSFM (dashed lines) and Asymmetric SSFM (solid lines)

As the results show, the signals with larger bandwidth, or equivalently larger band spacing, have poorer performance for a reduced number of steps, due to the fact that a larger bandwidth requires more precision in the calculations of the back propagated field, as can be recalled from the minimum required step size equation given in Chapter 5. As one might infer from the results, the Q factor performance achieves a stable plateau for a sufficiently high number of sections of BP. The poor behavior observed for a low number of sections is due to the numerical error of the algorithm. Only after the number of steps is enough to overcome the algorithm uncertainty, the performances stabilizes with the number of steps. Additionally, if a sufficiently high number of steps would be allowed (above 30), the best performances would be achieved by the signals with larger band spacing, due to the reduced interference between bands. The asymmetric algorithm performance outperforms that of the symmetric approach for a lower number of sections, as expected from the analysis in Chapter 5.

6.4 Coupled field Back-propagation

The coupled field back-propagation method consists in considering the electric field backward evolution of each band separately. Furthermore, all bands are back-propagated in simultaneous, enabling the contribution of the terms of cross phase modulation between bands to be accounted in the nonlinear phase de-rotation of each band, for each back-propagation step. The mathematical derivation of the cross phase modulation terms is as follows: by substituting in E of equation (6.2) into the expression for the electric field given by (6.1), and expanding the $|E|^2$ term, while neglecting FWM terms, it holds that:

$$-\frac{\partial E_m}{\partial z}+\Delta\beta_{1,m}\frac{\partial E_m}{\partial t}+\frac{1}{2}j\beta_2\frac{\partial^2 E_m}{\partial t^2}-\frac{1}{6}\beta_3\frac{\partial^3 E_m}{\partial t^3}+\frac{\alpha}{2}E_m=j\gamma\left(2\sum_{i=1}^{N}|E_i|^2-|E_m|^2\right)E_m \tag{6.3}$$

The right end side of equation (6.3) represents the nonlinear phase compensation term, which can be written as:

$$j\gamma\left(2P_{\text{Sum}}-|E_m|^2\right)E_m \tag{6.4}$$

where P_{Sum} represents the power summation of the electric fields from all channels. Fig. 6.5 details the implementation of the coupled field back-propagation algorithm where the nonlinear phase rotation term is given as in equation 6.4.

As a means of evaluating the performance of the BP algorithm when using the coupled field approach, a simulation was conducted, the Q factor being obtained as a function of the number of sections (Fig. 6.6), for both symmetric and asymmetric algorithms and with varying space between bands.

As noticed in previous results comparing the symmetric with the asymmetric algorithms, there is also a clear performance advantage of the asymmetric approach when the number of sections is low. The results presented in Fig. 6.6 can also be represented in a different manner, where the Q factor is shown as a function of the band spacing for selected values of number of sections used in the BP algorithm as shown in Fig. 6.7.

Both plots contain the same information, but presented in different ways. As can be understood from the results, for a reduced band spacing, the performance is approximately independent of the number of sections used, which shows the limitations of the coupled field algorithm in dealing with very closely spaced bands/channels. This can be

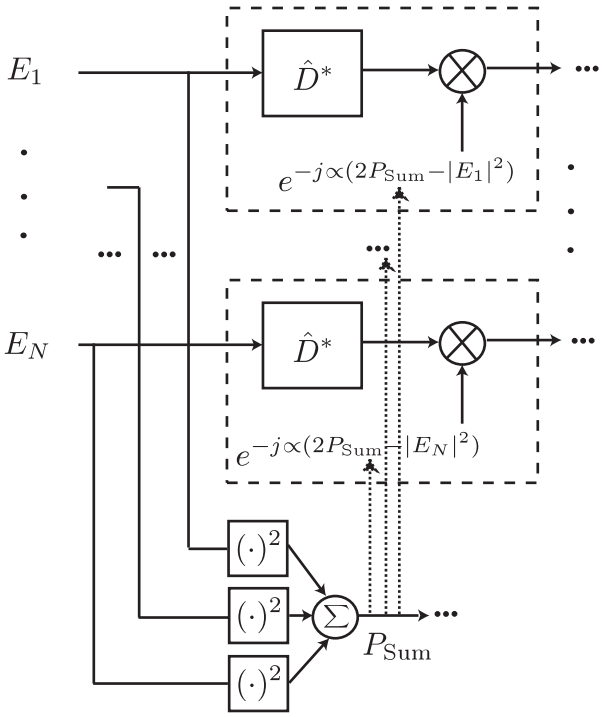

FIGURE 6.5: Diagram of coupled field back-propagation.

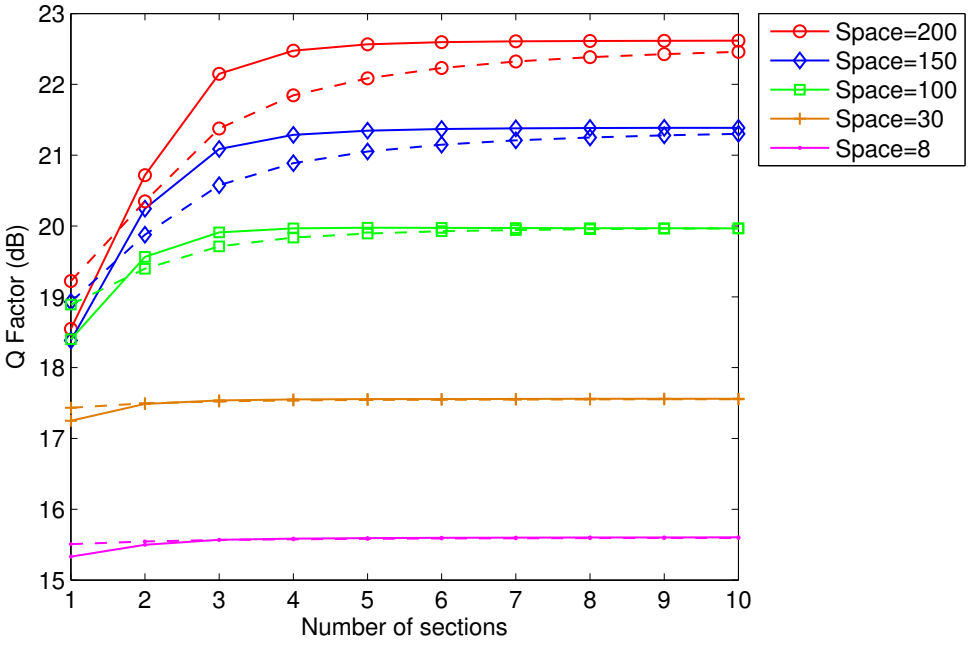

FIGURE 6.6: Q factor versus number of steps used in the back-propagation algorithm, using the coupled field technique, for band spacings of $\{8, 20, 100, 150, 200\}$ times the subcarrier spacing. Symmetric SSFM (solid lines) and Asymmetric SSFM (lines in dashed)

explained by the fact that the back-propagation algorithm takes as its input each of the filtered bands of the signal available in the receiver. However, during fiber propagation

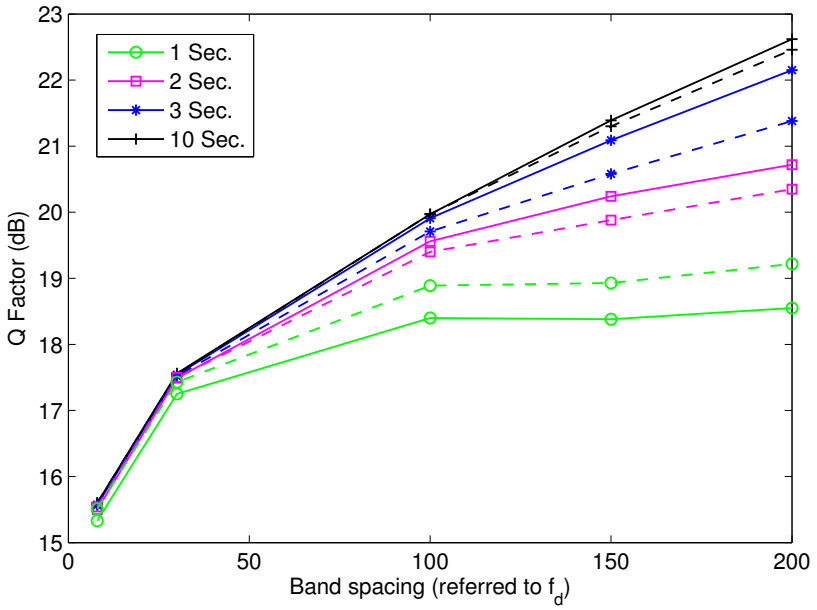

FIGURE 6.7: Q factor versus band spacing. Symmetric SSFM (solid lines) and Asymmetric SSFM (lines in dashed)

there are newly generated frequency components (inter-modulation products) that fall outside of the nominal bandwidth of the bands, as can be seen in Fig. 6.8. As these components are not taken into account in the coupled field algorithm, this leads to its poor performance for scenarios of very closely spaced bands.

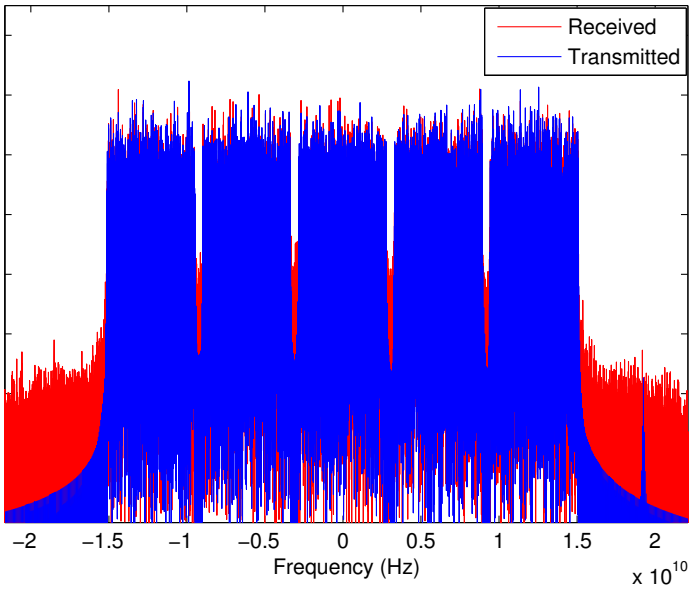

FIGURE 6.8: Power spectrum of the multi-band signal at the receiver input versus power spectrum of the transmitted signal

The electric field signal of each band requires an anti-aliasing filter preceding the sampler in order to avoid interference between bands. As one could expect, using a larger anti-aliasing filter bandwidth could improve the receiver performance, since more information can be taken into account in the back-propagation equation, namely the distortion products. Fig. 6.9 shows the impact of increasing the anti-aliasing filters bandwidth. Three different bandwidths were used, specifically having an additional tolerance compared to the nominal bandwidth of $10 f_d$ (the standard case), namely {20, 30, 40} times the subcarrier spacing. As can be concluded from the results, there is effectively a slight benefit (up to 0.4 dB) in increasing their bandwidth. For a band spacing below $30 f_d$, there is a penalty for filter bandwidths larger than $10 f_d$ due to inter-band interference.

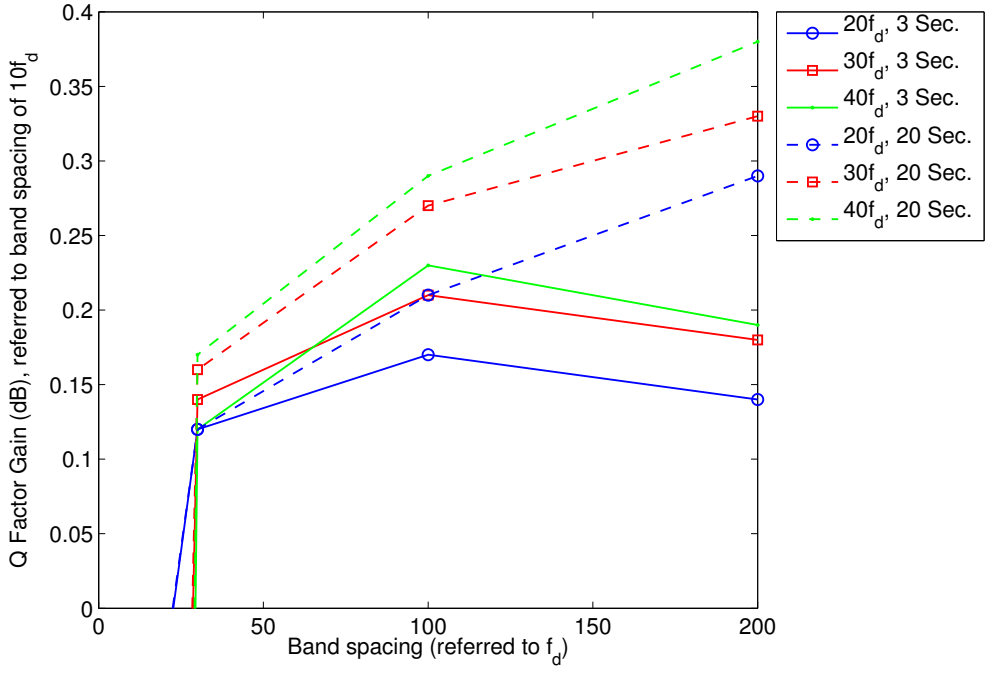

FIGURE 6.9: Q factor versus band spacing for 3 different bandwidths for the anti-aliasing filter, namely {20, 30, 40} f_d. Asymmetric SSFM using 3 (solid lines) and 20 sections (dashed lines).

Additionally, Fig. 6.6 also shows that as the band spacing increases, there is an increasing benefit in using an higher number of sections in the BP algorithm, due to the reduction of the inter-modulation products. For very large band spacings (above $200 f_d$), it has been verified that the performance approaches the limit of transmitting a single band, due to the absence of XPM interference.

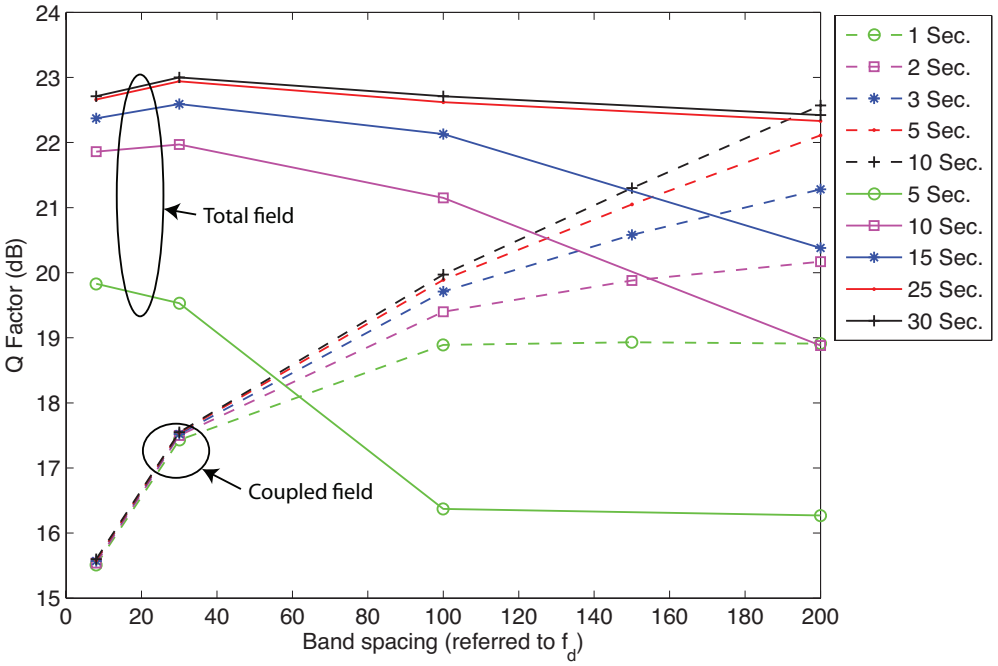

FIGURE 6.10: Q factor versus band spacing. Asymmetric algorithm.

Fig. 6.10 provides an additional comparison between the coupled field and the total field approaches, with a number of sections varying from 1 up to 10 for the former and from 5 to 30 for the latter, this difference originating from the fact that the computational complexity of the total field algorithm is higher than the coupled field, by a factor equal to the number of bands, which will be analyzed in the next section. In this way, one can conclude that for a band spacing below $60 f_d$, the performance of the total field approach is always better. Additionally, the coupled field approach over-performs the total field for signals having band spacings above $60 f_d$, provided 5 sections are used for the total field. This advantage decreases as the number of sections for the total field approach is increased. For the case of 25 sections the total field approach provides better Q factor for up to the maximum band spacing considered in the simulation of $200 f_d$.

6.5 Computational complexity comparison - coupled field vs total field

It is of relevance to analyze the differences in terms of computational complexity between the coupled field method and the total field method. Mateo [75] has derived an expression

that relates the number of computations of both approaches, in the following form:

$$\frac{C_{\text{total}}}{C_{\text{coupled}}} = \frac{h_{\text{coupled}}}{N h_{\text{total}}} = \frac{\pi k}{2} \frac{(N-1)\Delta f}{N R_s} \tag{6.5}$$

where C represents the total number of computations of the algorithm, R_s represents the symbol-rate, and k is a constant that depends on the type of algorithm selected. Additionally, it is considered that the number of operations is inversely proportional to the step size. One should notice that h_{coupled} is inversely proportional to the number of operations per channel, which justifies the multiplication by a factor of N, the total number of channels. Therefore, the total field computation cost is directly proportional to the ratio between channel spacing and the symbol-rate, which means that, as seen in Fig. 6.10, for a fixed number of computations and symbol-rate, the performance decreases with the increase of channel spacing. In an inverse manner, the coupled field computational cost is inversely proportional to the ratio between channel spacing and the symbol-rate, justifying the performance increase with increasing channel spacing as seen in the same plot. This computational complexity rule is also valid for dispersion managed systems, as long as the dominant characteristic lengths are related to dispersive effects, as noticed in [75].

Another parameter of relevance is the required latency of the back-propagation algorithm, if particularly the aim is a real time implementation. Regarding this parameter, there is a fundamental difference between the coupled and total field approaches, in the sense that the coupled field approach is inherently parallelizable, which reduces the system latency. In fact, the latency is proportional to the number of operations per step and per channel, while for the total field approach, the latency is proportional to the number of operations per step. The following expression can be written for the processing latency ratio [75]:

$$\frac{\tau_{\text{total}}}{\tau_{\text{coupled}}} = \frac{h_{\text{coupled}}}{h_{\text{total}}} = \frac{\pi k}{2} \frac{(N-1)\Delta f}{R_s} \tag{6.6}$$

This equation is similar to (6.5), the only difference being that the number of channels has vanished from the denominator. Therefore, the latency of the total field approach is proportional to the total optical bandwidth $(N-1)\Delta f$. This means that as the channel spacing increases, there is a point after which the coupled field approach becomes the most efficient compensation technique, because its latency is inversely proportional to

the total optical bandwidth. Additionally, the same phenomenon should also be true in terms of Q factor performance, since that for a fixed number of sections, the performance of the coupled field approach increases with the total optical bandwidth, while the total field approach behaves in an inverse manner.

6.5.1 Analysis for constant symbol-rate

It should be of relevance to analyze the difference in performance between the coupled field and total field implementations while using the same computational complexity in both algorithms. The results of Fig. 6.11 show the results of the mentioned analysis, which has been performed as a function of the number of bands for a constant symbol-rate. The analysis of these algorithms performance in terms of number of bands could be potentially relevant in a scenario of application to a multi-user access network. The lines in blue represent a result of similar complexity between both algorithms, since the coupled field compensation is performed with 1 section per span while the total field is carried with a number of sections equal to the number of bands in consideration. It can be concluded that for a small band spacing ($8f_d$) the total field approach is better performing for any number of bands. Concerning the coupled field approach, the performance degradation with increasing number of bands, is a result of the higher numerical error, which accumulates faster when more bands are considered in the estimate of the electric field in each BP step. For an higher band spacing ($100f_d$ in this case) the coupled field approach is outperforming for a number of bands up to five. The results in red were plotted for an indication of the performance bound of both algorithms, considering 10 sections for the coupled field method and and a considerably high number of sections (above 50), for the total field approach. One could conclude that the total field approach provides an approximately constant Q factor of 23 dB as long as high number of sections is used, while the coupled field would only benefit from an higher number of sections for a reduced number of bands and high band spacing as depicted in Fig. 6.11(b) for the red line represented with squares.

Therefore, from the previous analysis it can be concluded that the coupled field algorithm is an interesting option in terms of performance/computational complexity, if the system is allowed to have a relatively large band spacing and a reduced number of bands. Such an analysis had never been performed before, its results being extremely

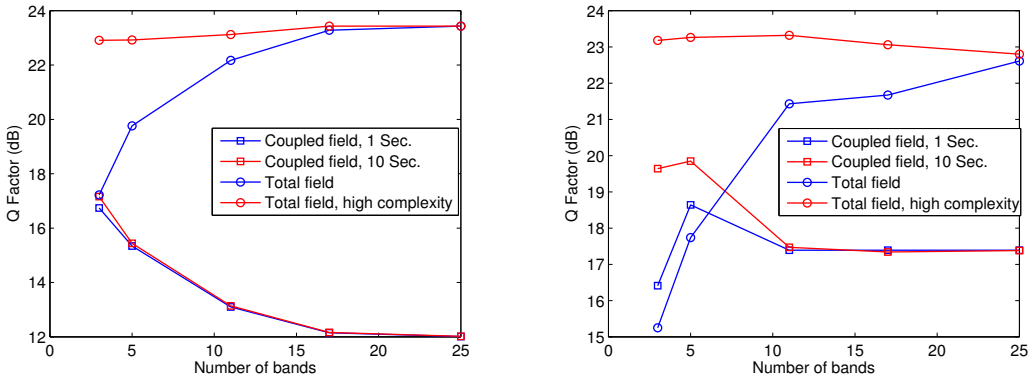

(a) Band spacing = $8f_d$ (b) Band spacing = $100f_d$

FIGURE 6.11: Q factor versus number of bands for a constant symbol-rate of 25 GSymbols/s, having a band spacing of $8f_d$ (a) and $100f_d$ (b). Lines in blue represent a similar computational complexity between both algorithms. Lines in red represent the performance limit of both algorithms.

relevant in the context of system design for optical systems employing real-time digital signal processing.

6.6 Dispersion managed transmission

It is of relevance to analyze the performance of the coupled and total field algorithms when the system in consideration uses dispersion management, in order to complement the analysis of Chapter 5 concerning this topic. Simulations were performed, where the RDPS was varied from 25% to 100%, and the Q factor was obtained for both the coupled and the total field algorithms, for three different band spacings, namely $30f_d$, $100f_d$ and $200f_d$, as shown in Fig. 6.12.

In terms of the coupled field results, it is possible to conclude that the Q factor incurs a higher penalty for lower RDPS values. Additionally, a higher number of sections makes only a significant impact for the case of larger band spacing, as for the case of a spacing of 200 times f_d. In terms of the total field results, when compared to the coupled field, one can conclude that its performance is more dependent on the selected number of sections for the BP algorithm. If a fair comparison in terms of computational complexity is to be made, one should compare the coupled field algorithm with the corresponding total field with the former having a number of sections five times higher than the latter. The reason is a result from the computational complexity of the coupled field algorithm which depends on the number of bands of the signal, as seen previously. This means that one

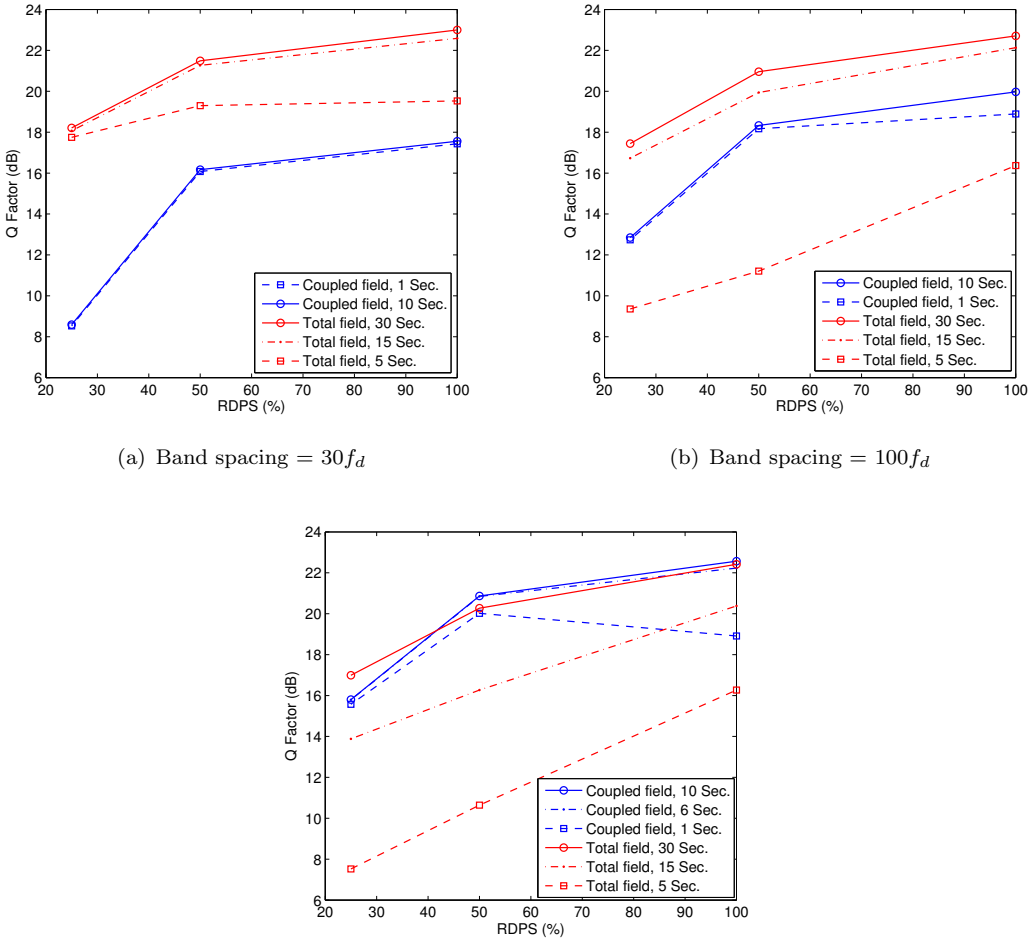

(a) Band spacing = $30f_d$

(b) Band spacing = $100f_d$

(c) Band spacing = $200f_d$

FIGURE 6.12: Q factor versus RDPS for a varying number of sections used for back-propagation, using the coupled field approach (blue lines) and the total field approach (red lines), considering the asymmetric BP algorithm, with a band spacing of (a) $30f_d$, (b) $100f_d$ and (c) $200f_d$.

section in the coupled field approach corresponds to the same complexity as five sections on the total field approach. In general terms, it can be concluded that for a band spacing of 200 times f_d the coupled field approach has a clear performance advantage regardless of the RDPS value, when comparing 1 section in the coupled field with 5 sections in the total field (same complexity level). If the number of sections is increased, both algorithms approach a similar performance. Furthermore, for a band spacing of 100 times f_d, the coupled field approach only outperforms the total field for the minimum number of sections (at low complexity), the total field becoming preferable for an higher number of sections (at higher complexity). Finally for a band spacing of 30 times f_d the total field approach is preferable regardless of the RDPS. The coupled field algorithm performance

suffers from the increased nonlinearity introduced by the DCF, which is enhanced by the increased phase matching phenomenon near low RDPS values, leading to interference among the different bands as they back-propagate independently. Additionally, the total field algorithm performance is reasonably less affected by the RDPS reduction, since the signal is back-propagated as a single band, therefore being barely perturbed by the phase matching phenomenon. Subsequently, for an higher complexity level (solid lines), the total field algorithm provides the best performance, for all RDPS scenarios, which is more pronounced for lower band spacings up to negligible for higher band spacings. However, the design engineer would have to consider the tradeoff between the higher cost of this algorithm in terms of implementation latency and its performance, when choosing between the coupled and total field approaches.

6.7 Four Wave Mixing

In an optical fiber, nonlinearities stem from the third order susceptibility $\chi^{(3)}$, which accounts for the effects of third harmonic generation, four-wave mixing and nonlinear refraction index [54]. The nonlinear refraction index refers to the previously mentioned intensity dependence of the refractive index, which is responsible for most of the nonlinear effects in optical fibers. Third harmonic generation and FWM are considered third order parametric processes, generally involving interaction among four optical waves. In order to understand the FWM process, it is necessary to take into account that the response of an optical fiber to an applied field is not linear in the electric field E. In fact, there is an induced polarization given by:

$$P_{NL} = \epsilon_0 \chi^{(3)} \vdots EEE \tag{6.7}$$

which represents the third order polarization term, where ϵ_0 is the vacuum permitivity, E is the applied electric field and P_{NL} is the induced nonlinear polarization. Now, one should consider that the applied electric field is composed by four linearly polarized optical waves oscillating at frequencies w_1, w_2, w_3, w_4, such that:

$$E = \sum_{m=1}^{4} E_m \exp[j(k_m z - w_m t)] \tag{6.8}$$

where the propagation constant is given by $k_m = n_{r,m}\omega_m/c$, with $n_{r,m}$ being the refractive index in channel m. It is now possible to express P_{NL} exactly in the same form as E, and therefore notice that the P_m (m varying between 1 and 4), is composed by a large number of terms involving the product of three electric fields. In this way, as an example, P_4 can be represented as:

$$\begin{aligned} P_4 = \frac{3\epsilon_0}{4}\chi^{(3)}[&|E_4|^2E_4 + 2(|E_1|^2 + |E_2|^2 + |E_3|^2)E_4 \\ &+ 2E_1E_2E_3\exp(j\theta_+) + 2E_1E_2E_3^*\exp(j\theta_-) + ...] \end{aligned} \tag{6.9}$$

with θ_+ and θ_- defined as:

$$\theta_+ = (k_1 + k_2 + k_3 - k_4)z - (\omega_1 + \omega_2 + \omega_3 - \omega_4)t \tag{6.10}$$

$$\theta_- = (k_1 + k_2 - k_3 - k_4)z - (\omega_1 + \omega_2 - \omega_3 - \omega_4)t \tag{6.11}$$

In equation (6.9), the first term refers to SPM, the following three terms refer to XPM effects and the remaining terms refer to FWM. However, the effectiveness of the parametric coupling depends on the phase mismatch between E_4 and P_4 governed by θ_+ and θ_-, which is referred as phase-matching, which requires a specific choice of the frequencies and the refractive indices, so that the phase mismatch nearly vanishes in order to produce significant FWM. While the term θ_+ is associated with phenomena such as third harmonic generation, and the corresponding phase matching condition is very difficult to satisfy, the term θ_- is associated FWM, in the sense that two photons at frequencies ω_1 and ω_2 are annihilated with simultaneous creation of two photons at frequencies ω_3 and ω_4, which can be written as:

$$\omega_3 + \omega_4 = \omega_1 + \omega_2 \tag{6.12}$$

Additionally, the phase matching requirement can be stated as:

$$\delta_k = k_3 + k_4 - k_1 - k_2 = \frac{1}{2}\beta_2[(\omega_3 - \omega_0)^2 + (\omega_4 - \omega_0)^2 - (\omega_1 - \omega_0)^2 - (\omega_2 - \omega_0)^2] \tag{6.13}$$

The partially degenerate case in which $\omega_1 = \omega_2$ is the most relevant for optical fibers, since it easily satisfies the phase matching condition. The introduction to the four wave mixing phenomenon made here will be considered in the next section to support its analysis in the context of multichannel back-propagation.

6.8 Multichannel back-propagation for FWM

The previous analysis in the expansion of (6.2) has not considered the FWM terms. However, if the FWM terms are neglected, there are intermodulation products that are not taken into account in the backward propagation. Additionally, the field fluctuations induced from FWM distortion might vary faster than those caused by XPM, which could require a smaller step size. The mathematical derivation of the FWM terms in the nonlinear propagation equation can be obtained by rewriting the total optical field as:

$$E = \sum_{m=1}^{N} E_m \exp(jk_m z) \tag{6.14}$$

where k_m is the linear propagation constant of the m-th channel. Again, by substituting in the electric field E (in equation 6.2) the expression for the electric field given by (6.14), one can write the nonlinear term, including the FWM part [75]:

$$j\gamma \left(2\sum_{i=1}^{N} |E_i|^2 - |E_m|^2 \right) E_m + j\gamma \left[\sum_{[rslm]\in I} E_r E_s E_l^* \exp(j\delta k_{rslm} z) \right] \tag{6.15}$$

with $l = r + s - m$, in order to neglect fast time oscillating terms, and respecting $\{r, s, m\} \in \{..., -2, -1, 0, 1, 2, ...\}$ the index of each channel, so that the newly generated waves stay within the WDM band and finally $r \neq s \neq m$ so that SPM and XPM terms are not considered twice. The phase mismatch parameter δk_{rslm} can be expanded as follows:

$$\delta k_{rslm} = k_r + k_s - k_l - k_m = \frac{1}{2}\beta_2 \Delta w^2 [r^2 + s^2 - (r + s - m)^2 - m^2] \tag{6.16}$$

where l was substituted according to $l = r+s-m$. This expression can be maximized in order to find the maximum phase mismatch, which is contributed by the edge channels over the central channel, originating the fastest field fluctuations, subsequently requiring the smallest step size. Therefore, by setting $r = 1$, $m = (N + 1)/2$ and $s = N$, which represent the first, the middle and the last channels, respectively, it holds that:

$$\delta k_{\max} = \frac{1}{4}|\beta_2|(N-1)^2 \Delta w^2 = \pi^2 |\beta_2|(N-1)^2 \Delta f^2 \tag{6.17}$$

Although computer simulations have allowed the determination of the required step size in order to obtain a stable performance for the BP algorithm, as seen in the previous

sections, it is possible to use mathematical derivations that support the step size selection for each case. In fact, by taking the inverse of the maximum phase mismatch shown in equation (6.17), [91] has derived the following expression for the FWM length:

$$L_{\text{fwm}} = \frac{1}{\pi^2 |\beta_2| (N-1)^2 \Delta f^2} \tag{6.18}$$

which represents the length after which the the fastest z-fluctuations over the mth channel are shifted by one radian, which means that significant power fluctuations start building up. This expression is useful for the total field case. However, the coupled field step size is not governed by the FWM characteristic length, but instead by the walk-off characteristic length. In fact, it is also of interest to extend the definitions provided in Chapter 5 for the nonlinear and walk-off characteristic lengths [75]:

$$L_{\text{NL}} = \frac{1}{\gamma P_p \frac{2N-1}{N}} \tag{6.19}$$

$$L_{\text{wo}} = \frac{1}{2\pi |\beta_2| (N-1) \Delta f R_s} \tag{6.20}$$

In this way, all the relevant physical lengths are defined, which provide a useful mathematical upper bound on the step size used by each algorithm.

6.9 Partial FWM compensation

The analysis made in the previous sections has shown that the compensation through the total field approach requires more computational complexity, while imposing higher latency times, which is not favorable to a real-time implementation of the algorithms. On the other hand, the compensation through the coupled field method does not give optimum results for all cases, being particularly limited for signals with very closely spaced bands.

Mateo [91] proposed a technique which allows for partial compensation of FWM by improving the equations of the coupled field algorithm with additional calculations reflecting FWM interaction leading to nonlinear mixing between neighboring channels. In this way, the FWM terms including the interaction between 2 and 4 neighbors are given by, respectively:

$$F_{2m} = 2E_{m+1}E_{m-1}E_m^* \tag{6.21}$$

$$\begin{aligned} F_{4m} = {} & E_{m+1}^2 E_{m+2}^* + E_{m-1}^2 E_{m-2}^* + 2E_{m-1}E_{m+2}E_{m+1}^* \\ & + 2E_{m+1}E_{m-2}E_{m-1}^* + 2E_{m+2}E_{m-2}E_m^* \end{aligned} \tag{6.22}$$

Here, the phase mismatch exponential has been omitted for simplicity. The same restrictions as in equation 6.15 need to be taken into account, in order to neglect fast time oscillating terms, that newly generated waves stay within the band and so that SPM and XPM terms are not considered twice. Furthermore, by resorting again to equation 6.15, expressions for the interaction of 6 and 8 neighbors are also derived in this work:

$$\begin{aligned} F_{6m} = {} & E_{m-3}E_m E_{m-3}^* + E_{m+3}E_m E_{m+3}^* + 2E_{m-3}E_{m+3}E_m^* + 2E_{m-3}E_{m+1}E_{m-2}^* \\ & + 2E_{m-3}E_{m+2}E_{m-1}^* + 2E_{m+3}E_{m-1}E_{m+2}^* + 2E_{m+3}E_{m-2}E_{m+1}^* \end{aligned} \tag{6.23}$$

$$\begin{aligned} F_{8m} = {} & E_{m-4}E_m E_{m-4}^* + E_{m+4}E_m E_{m+4}^* + 2E_{m-4}E_{m+4}E_m^* + 2E_{m-4}E_{m+1}E_{m-3}^* \\ & + 2E_{m-4}E_{m+2}E_{m-2}^* + 2E_{m-4}E_{m+3}E_{m-1}^* + 2E_{m+4}E_{m-1}E_{m+3}^* \\ & + 2E_{m+4}E_{m-2}E_{m+2}^* + 2E_{m+4}E_{m-3}E_{m+1}^* \end{aligned} \tag{6.24}$$

Therefore, the nonlinear term in the BP equation is now written as:

$$j\gamma \left(2P_{\text{sum}} - |E_m|^2\right) E_m + j\gamma(F_{2m} + F_{4m} + F_{6m} + F_{8m}) \tag{6.25}$$

In fact, these FWM terms are highly phase matched, having the potential to improve the results without compromising the computational complexity. Additionally, [91] suggests a perturbative implementation to solve equation (6.25), such that the nonlinear operator for step i is approximated as:

$$E_m^{i+1} = E_m^i \exp\left[j\gamma h(2P_{\text{sum}} - |E_m|^2)\right] + \gamma h(F_{2m}^i + F_{4m}^i + F_{6m}^i + F_{8m}^i) \tag{6.26}$$

where h represents the BP step size. However, this approximation is only valid if the number of neighboring channels considered for FWM compensation is a small fraction (below 20 %) of the total number of channels interacting through XPM. This is required so that the phase mismatch length (L_{fwm}) becomes larger than the walk-off length (L_{wo}), implying that field variations due to FWM are slower than the variations due to XPM. However, this could preclude the usage of this algorithm when the number of transmitted bands is reduced, therefore a solution is provided in the next section.

6.10 Partial FWM compensation method for multi-band OFDM signals

In this work, a novel strategy of implementing a partial FWM compensation scheme is proposed. Instead of performing the the perturbative compensation as suggested in [91], which is suitable for WDM transmission with a large number of channels, equation (6.26) is modified in order to reduce the numerical error, due to a small number of bands being considered. The BP step is then computed as follows:

$$E_m^{i+1} = E_m^i \exp\left[-j\gamma\zeta L_{\text{eff}}(2P_{\text{sum}} - |E_m^i|^2)\right] + \xi\gamma L_{\text{eff}}(F_{2m}^i + F_{4m}^i + F_{6m}^i + F_{8m}^i) \quad (6.27)$$

where ζ represents the nonlinear phase rotation parameter, as seen previously and $0 \leqslant \xi \leqslant 1$ represents an empirical parameter which is introduced here in order to control the amount of FWM compensation, its optimum value being found through simulation.

The Q factor performance using the new partial FWM compensation method with the coupled field approach for a signal with 5 bands is shown in Fig. 6.13 for a band spacing of 30 and Fig. 6.14 for a band spacing of 50 times f_d, considering the interaction of both 2 and 4 neighbor bands.

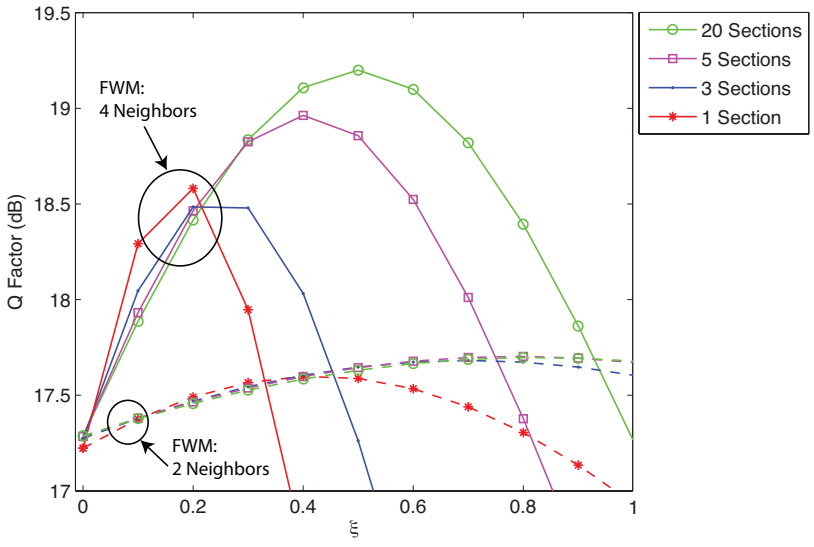

FIGURE 6.13: Q factor versus ξ, for bands spaced at $30f_d$, compensating the FWM interaction of 2 neighbors (dashed lines) and 4 neighbors (solid lines). The asymmetric BP algorithm was used.

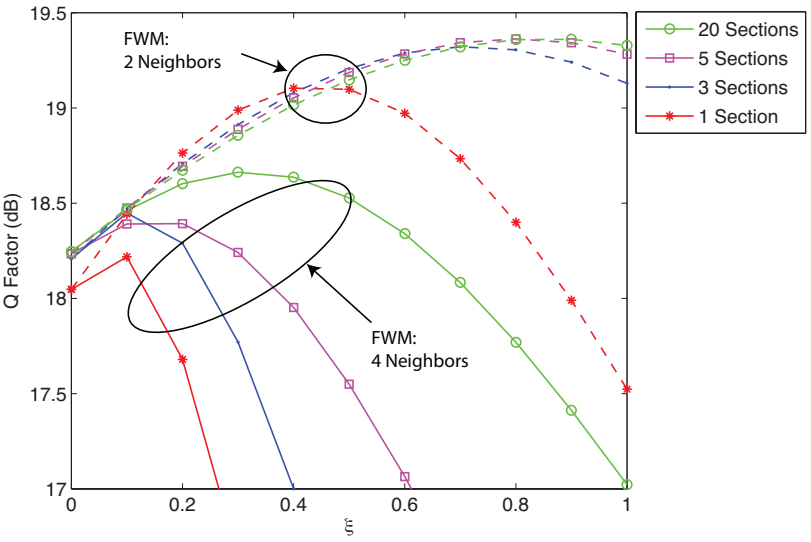

FIGURE 6.14: Q factor versus ξ, for bands spaced at $50 f_d$, compensating the FWM interaction of 2 neighbors (dashed lines) and 4 neighbors (solid lines). The asymmetric BP algorithm was used.

From the analysis of Figs. 6.13 and 6.14, it can be seen that the proposed algorithm effectively provides a performance gain, compared to using only the coupled field algorithm, which corresponds to the performance at the $\xi = 0$ point. Additionally, increasing the number of sections used in the BP algorithm, the higher the performance gain, although above 20 sections the improvement is negligible. Additionally, the ξ parameter increases with the number of sections used, becoming constant above 20 sections. The original method from which this new partial compensation method was derived, was reported to provide a performance gain up to 1.5 dB for the center channels of a 24 WDM channel setup using 16-QAM. In the present work, performance improvements above 2 dB were observed, depending on the band spacing considered, for the case of five closely spaced OFDM bands.

In order to evaluate the performance variation as a function of the the band spacing, a simulation was performed, where the spacing between bands was varied from $8 f_d$ up to $200 f_d$. The results are shown in Fig. 6.15. The ξ parameter used in the simulations corresponds to the optimum value found for each case.

The analysis of the results present in Fig. 6.15 show that the advantage of using the partial FWM compensation is more effective for reduced band spacings, gradually vanishing as the band spacing increases, regardless of the number of sections used in the BP algorithm. The reason behind this behavior is related with the effect of FWM

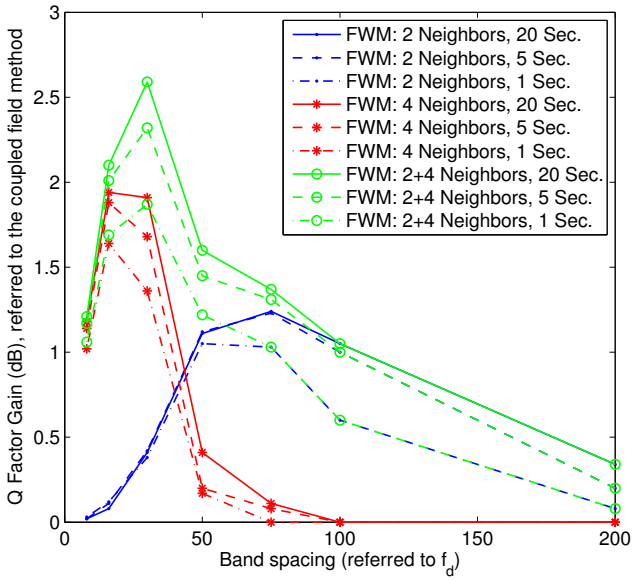

FIGURE 6.15: Q factor versus band spacing, for the interaction of 2 neighbors (blue lines), 4 neighbors (red lines) and the combination of both (green lines), for {1, 5, 20} sections in the asymmetric BP algorithm.

impairment itself, whose the strength decreases as the channels are further away from each other. Furthermore, the strength of the interaction between 2 neighbors is only significant for a band spacing above $20f_d$, starting to decrease above $80f_d$ whereas the strength of the interaction between 4 neighbors is only significant for small band spacings up to $50f_d$. This is due to the strength of the FWM field variations, which are stronger for the interaction of signals more distant in frequency [75].

For the specific case of band spacing equal to $30f_d$, Fig. 6.16 shows the performance improvement obtained for each band, comparing the case of using the coupled field algorithm alone (blue line) with that of using the coupled field with FWM compensation including 2 neighbor bands (red line), 4 neighbor bands (green line) and the combination of both (pink line), the Q factor improvement being 0.4 dB, 1.7 dB and 2.2 dB, respectively. Notice that the 4 neighbor FWM result only shows improvement for the central band, which is the only band having 4 interacting neighboring bands.

The impact of varying the number of sections is shown in Fig. 6.17 for a band spacing of $100f_d$, comparing the relative performance of using {1, 5, 20} sections in the BP algorithm. The dashed lines represent the result of using the coupled field method alone, while the solid lines represent the result of using the coupled field method combined with the FWM compensation of 2 neighbor channels. As shown, the performance increase affects not only the central band but also the two neighboring bands where the algorithm

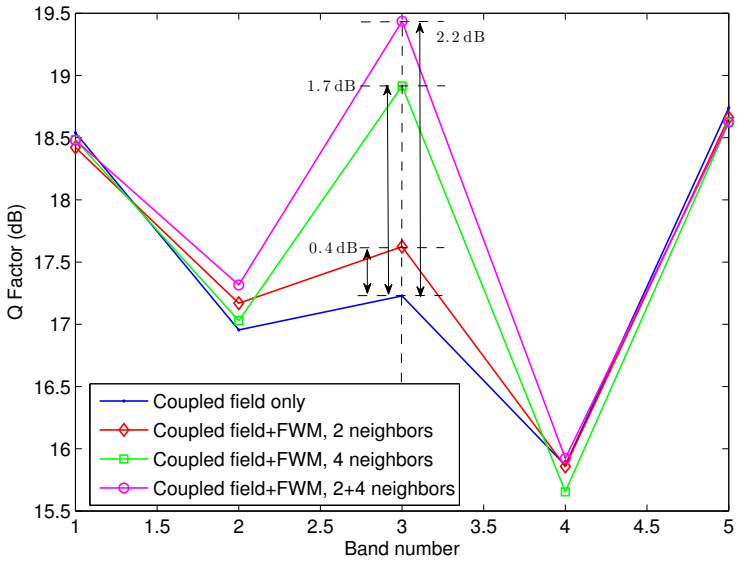

FIGURE 6.16: Q factor versus band number comparing the performance of using only the coupled field algorithm (blue line) with that of using the coupled field algorithm in combination with the partial FWM compensation, using 2 neighbors (red line), 4 neighbors (green line) and the combination of both (pink line), in the asymmetric BP algorithm.

is also applied. The improvement increases with the number of sections, improving from 0.6 dB up to 1.05 dB, for an increase from 1 to 20 sections, which confirms that the FWM compensation effectively becomes more precise due to the numerical error reduction when the number of sections is increased.

6.10.1 Variable number of bands

It is pertinent to investigate the performance of the proposed partial FWM compensation algorithm for OFDM signals having more than 5 bands. Therefore, different signals having a number of bands between 5 and 25 were generated, while maintaining the total bandwidth of the signal, in order to consider a 25 GSymbols/s data-rate. Fig. 6.18 shows the Q factor as a function of the band number for each of the multi-band signals, having a band spacing of 8 times f_d. The Q factor performance of the coupled field algorithm alone is plotted in blue lines and is compared to that of using the coupled field algorithm in combination with the partial FWM compensation using 2 neighbors (green line), 4 neighbors (red line), considering a complexity of 5 sections. It should be noticed that the performance of the center bands tends to be worse than those bands in the edge, due to the fact that the middle ones suffer from stronger FWM, since they have a higher number of neighbors. Furthermore, the performance of the partial FWM compensation method

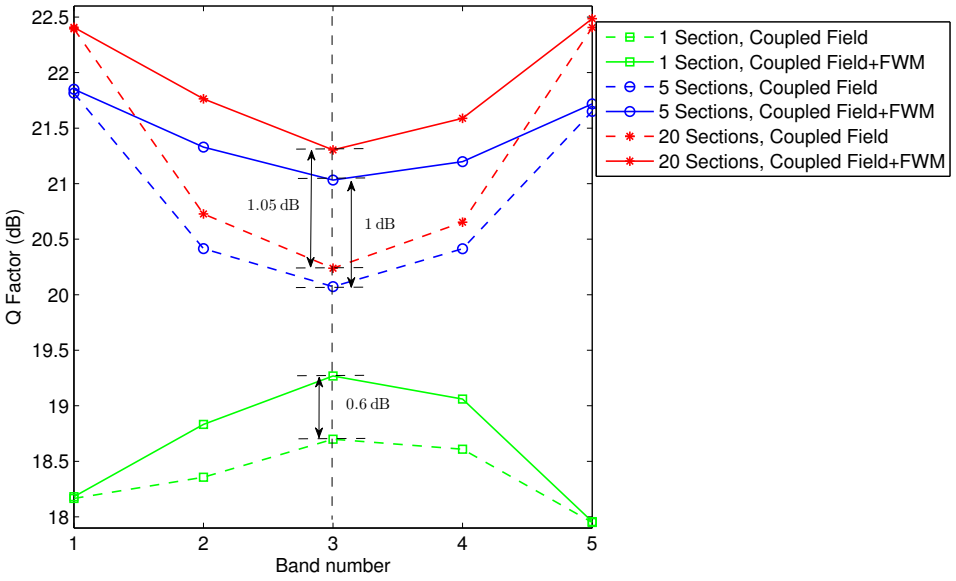

FIGURE 6.17: Q factor versus band number comparing the performance of using only the coupled field algorithm with that of using the coupled field algorithm in combination with the partial FWM compensation, for $\{1, 5, 20\}$ sections and band spacing equal to $100 f_d$.

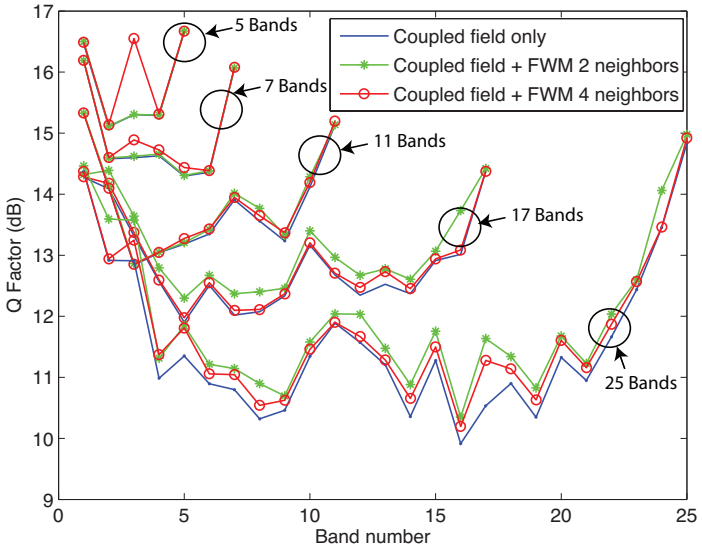

FIGURE 6.18: Q factor versus band number comparing the performance of using only the coupled field algorithm with that of using the coupled field algorithm in combination with the partial FWM compensation, for 5 sections of the BP algorithm.

provides better results for 5 bands, when considering the interaction with 4 neighbor bands, its performance reducing as the number of bands increases. This shows that the proposed algorithm is more effective in signals with reduced number of bands. However, the partial FWM compensation method provides a slight performance improvement for

a number of bands above 17. Recall from the previous analysis in section 6.5.1 that the higher the number of bands considered in the BP algorithm the higher its numerical error becomes, since it accumulates faster when more bands are considered in the estimate of the electric field in each BP step. This fact explains the slight performance improvement given by the FWM partial compensation method when the number of bands increases. The partial FWM compensation using the equations for the interaction of 6 and 8 bands has also been simulated but with no observable performance advantages for the optical transmission setup in consideration. In fact, an improvement was found only for shorter lengths of fiber, having less than 5 spans, which shows that the interaction between largely spaced bands is reduced by dispersion walk-off. Therefore this case is potentially interesting for implementation in different network configurations than those discussed here.

6.11 Summary

The present chapter analyzed the back-propagation algorithm for OFDM multi-band transmission focusing on the comparison between coupled field and total field back-propagation. These algorithms have been compared based on computational complexity where it was concluded that the coupled field algorithm is an interesting option, if the system is allowed to have a relatively large band spacing and a reduced number of bands. Additionally, it was concluded that the coupled field approach is more affected by low RDPS values, while allowing for a more efficient practical implementation in terms of its latency. Additionally, four wave mixing was considered within the coupled field method to provide simplified means of multichannel nonlinearity compensation. A compensation method was proposed in this context, which allows for a considerable performance improvement when using a relatively small band spacings and a reduced number of bands.

Chapter 7

Back-propagation for polarization multiplexed transmission

7.1 Introduction

Digital Signal Processing techniques are gaining increasing importance as they allow for robust long-haul transmission with full compensation at the receiver. Furthermore, it was concluded in Chapter 5, that systems employing in-line dispersion compensating fiber, perform worse than those with only digital compensation, as suggested by [16]. This Chapter will discuss whether this still holds for WDM and polarization multiplexed transmission.

The employment of advanced DSP functions implies that sufficient sampling rates are satisfied. However, the lack of suitable ADC-DAC technology has originated the need for reducing the symbol rate while increasing spectral efficiency, leading to the investigation of multilevel modulation formats in conjunction with polarization multiplexing.

The main nonlinear impairments limiting long haul WDM systems are the inter-channel effects, specifically cross-phase modulation and four wave mixing [3]. However, if sufficient channel spacing is allocated, these impairments are reduced and then the major impairments become intra-channel effects, namely self-phase modulation and also a linear impairment, chromatic dispersion.

It is relevant to recall from Chapter 5, that XPM is a nonlinear phenomenon which occurs when two or more optical waves co-propagate in the optical fiber due to the refractive index change induced by each wave, which in turn induces a nonlinear polarization-dependent phase shift on the other co-propagating waves [54]. When the interaction

takes place between intensity modulated waves, the nonlinear phase shift becomes time dependent leading to phase and polarization modulation of the other waves.

Back-propagation has been proposed as a universal technique for jointly compensating linear and nonlinear impairments for WDM systems using coherent detection, DSP and DCF, enabling higher launched power and longer transmission reach [15]. In this Chapter the asymmetric SSFM BP algorithm is adopted, while considering polarization division multiplexing (PDM), for 10 GSymbols/s RZ-QPSK transmission in a 25 $\times$ 80 Km spans of single mode fiber and variable length of inline DCF. The cases of single polarization transmission and time interleaved (TI) PDM are also considered.

7.2 System modeling

When a signal carries channels in a polarization division multiplexed or polarization interleaved scheme, it becomes mandatory to include those polarization effects in the nonlinear propagation equation. The coupled nonlinear Schrödinger equations that describe the propagation in a linearly birefringent optical fiber are given by [92]:

$$\begin{aligned}
\frac{\partial u_x}{\partial z} + \left\{\frac{\alpha_x}{2} + j\beta_{0x} + \beta_{1x}\frac{\partial}{\partial t} + \frac{j}{2}\beta_{2x}\frac{\partial^2}{\partial t^2}\right\}u_x &= j\frac{\gamma}{3}(3|u_x|^2 + 2|u_y|^2)u_x + j\gamma\frac{1}{3}u_x^* u_y^2 \\
\frac{\partial u_y}{\partial z} + \left\{\frac{\alpha_y}{2} + j\beta_{0y} + \beta_{1y}\frac{\partial}{\partial t} + \frac{j}{2}\beta_{2y}\frac{\partial^2}{\partial t^2}\right\}u_y &= j\frac{\gamma}{3}(3|u_y|^2 + 2|u_x|^2)u_y + j\gamma\frac{1}{3}u_y^* u_x^2
\end{aligned} \tag{7.1}$$

where α, $\beta_{0x,y}$, $\beta_{1x,y}$ and $\beta_{2x,y}$ account for the attenuation, birefringence, differential group delay and CD, respectively, while u_x and u_y represent the electric field components in the x and y polarizations, respectively. Higher order nonlinear terms can be neglected because the birefringent beat length (typically a few meters) is considered much shorter than the nonlinear length (typically several kilometers), leading to a random scattering of the polarization of the electric field in length scales shorter than 100 m [58]. Moreover, given the fast changes in the polarization state of the electric field, the resulting nonlinearity is averaged over the entire poincaré sphere [93]. Furthermore, β_0 and β_1 are set to zero, because birefringence does not affect the nonlinear term [92] and polarization mode dispersion can be neglected at 10 GSymbols/s [31], respectively. In this way, the averaging of equation (7.1) over the fast polarization changes leads to

the Manakov equation, which can be written as [54, 58]:

$$\begin{aligned}\frac{\partial u_x}{\partial z} + \left\{\frac{\alpha_x}{2} + \frac{j}{2}\beta_{2x}\frac{\partial^2}{\partial t^2}\right\}u_x = j\frac{8\gamma}{9}(|u_x|^2 + |u_y|^2)u_x \\ \frac{\partial u_y}{\partial z} + \left\{\frac{\alpha_y}{2} + \frac{j}{2}\beta_{2y}\frac{\partial^2}{\partial t^2}\right\}u_y = j\frac{8\gamma}{9}(|u_y|^2 + |u_x|^2)u_y\end{aligned} \tag{7.2}$$

Equation (7.2) shows that the signal carried on the orthogonal polarization makes a contribution to the nonlinear phase, as significant as the signal propagating on that polarization, which means the polarization multiplexing operation may induce a significant penalty in the system performance. Additionally, this equation assumes that the relative orientations of polarizations among the several channels remains unchanged during propagation, which can only be assumed if the bandwidth of the total field in propagation is narrow enough to allow the polarization mode dispersion to be negligible. Therefore, in order to take into account this requirement, only a reduced number of channels could be simulated in this work. Additionally, [93] shows that the BP method to compensate for nonlinear impairments does not affect the operation of channel demultiplexing, so that these tasks might be decoupled.

The numerical implementation of equation (7.2) is achieved using the SSFM, either for the forward and backward propagation directions. Therefore, the methods presented in Chapter 5 are valid also for this case, so that the implementation of the total field back-propagation is straightforward. Additionally, the coupled field back-propagation technique used in Chapter 6 for a multichannel signal is here extended to the polarization multiplexed transmission scenario, which has not been reported yet. The nonlinear term in the x axis, $j\frac{8\gamma}{9}(|u_x|^2 + |u_y|^2)u_x$ can be expanded as follows:

$$NL_x \propto u_x u_x^* u_x + u_y u_y^* u_x \tag{7.3}$$

Then, as an example, by considering that the signal in each polarization carries 3 independent channels, the previous expression becomes:

$$\begin{aligned}NL_x \propto (u_{1,x} + u_{2,x} + u_{3,x})(u_{1,x} + u_{2,x} + u_{3,x})^*(u_{1,x} + u_{2,x} + u_{3,x}) + \\ (u_{1,y} + u_{2,y} + u_{3,y})(u_{1,y} + u_{2,y} + u_{3,y})^*(u_{1,x} + u_{2,x} + u_{3,x})\end{aligned} \tag{7.4}$$

which can be calculated for each of the channels. For channel $u_{1,x}$, the nonlinear term can be shown to be proportional to:

$$\begin{aligned}&[|u_{1,x}|^2 + 2(|u_{2,x}|^2 + |u_{3,x}|^2) + (|u_{1,y}|^2 + |u_{2,y}|^2 + |u_{3,y}|^2)]u_{1,x} \\ &+ [u_{1,x}u_{2,x}^* + u_{3,x}u_{2,x}^* + u_{1,x}u_{3,x}^* + u_{2,x}u_{3,x}^*]u_{1,x} \\ &+ [u_{2,y}u_{1,y}^* + u_{3,y}u_{1,y}^* + u_{1,y}u_{2,y}^* + u_{3,y}u_{2,y}^* + u_{1,y}u_{3,y}^* + u_{2,y}u_{3,y}^*]u_{1,x}\end{aligned} \tag{7.5}$$

which can be written in generalized form for $u_{i,x}$ as:

$$\left[2\sum_{j=1}^{N}|u_{j,x}|^2 - |u_{i,x}|^2 + \sum_{j=1}^{N}|u_{j,y}|^2\right]u_{i,x} + \text{FWM terms} \tag{7.6}$$

where the FWM terms are the ones given by the second and third lines of equation (7.5). Figure 7.1 shows a schematic of the coupled field implementation of the asymmetric BP algorithm for WDM polarization division multiplexed transmission, in accordance with the above equations. As can be inferred from the analysis of the schematic, the contribution to the nonlinear rotation at polarization x stemming from the power summation from each channel of the same polarization is approximately twice compared to the contribution from the orthogonal polarization. In other words, the nonlinear impact resulting from the channels traveling in the orthogonal polarization is only half of that contributed by the co-polarized channels.

The considered WDM system model is shown in Fig. 7.2 for the case of 3 WDM channels. WDM channels are typically multiplexed using an arrayed waveguide grating (AWG), having a super-gaussian amplitude transfer function, and a 3-dB bandwidth equal to 80 % of the channel spacing, which has been considered in the presented model as given in [16].

The detailed schematic of each transmitter structure is represented in Fig. 7.3 [94].

The transmitter includes a delay Δ which can be set to half the symbol period if time-interleaving between the two polarizations is desired.

7.3 Simulation results

The performance of the 10 GSymbols/s RZ-QPSK transmission system was evaluated, considering the same amplified long-haul optical channel used in Chapter 5. The pulse shape was adjusted for 50% RZ. The oversampling rate m is set to 3 in the simulations

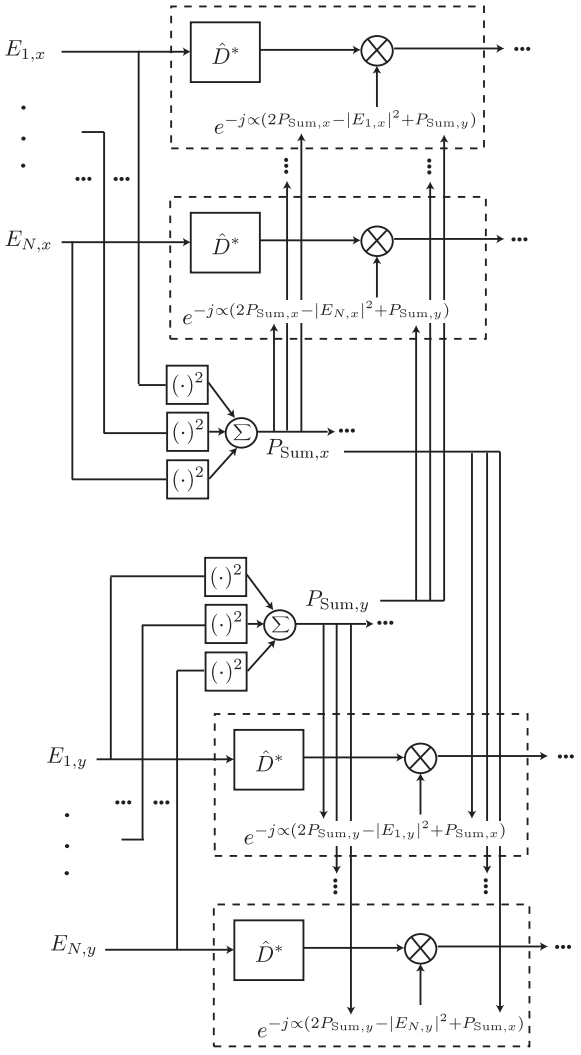

FIGURE 7.1: Block diagram of the coupled field asymmetric BP PDM scheme

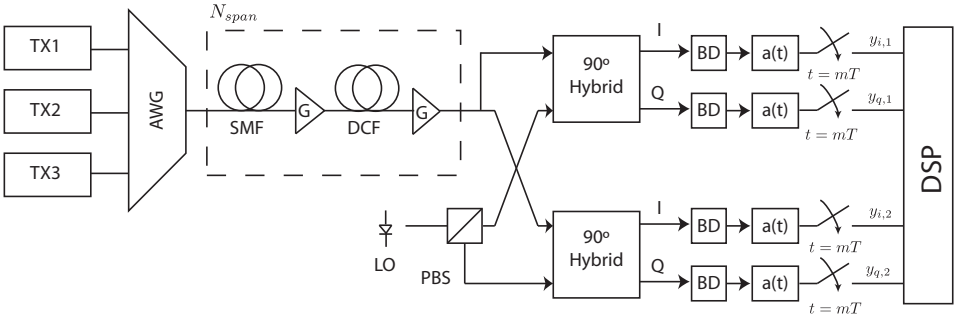

FIGURE 7.2: Block diagram of 3 channel WDM transmitter, transmission channel and digital coherent receiver with subsequent digital signal processing

according to results of Chapter 5. The antialias filters were set as lowpass 5th order Butterworth with a bandwidth of 40% of the oversampling rate. The DSP performs the functions of back-propagation and carrier phase estimation. However, for simplicity

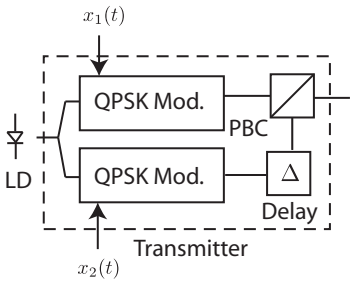

FIGURE 7.3: Block diagram of the PDM transmitter

phase noise was not included in the simulations, therefore, the carrier phase estimation corresponds to a single phase rotation, in order to compensate for accumulated residual phase rotations resulting from dispersion and nonlinearity mitigation. A simple moving average filter with length 64 was used [66], which was placed in the last step of the algorithm just before the Q factor calculation. First the performance of a system with no inline dispersion compensation is discussed. Then the impact of varying the residual dispersion of inline DCF is addressed in section 7.3.2

7.3.1 No inline dispersion compensation

Figures 7.4 and 7.6 show how the Q factor of the constellation after detection varies with launched power, when both cases of single polarized (SP) and polarization division multiplexed (PDM) transmission are analyzed. A Q factor of 10 dB is the minimum required to employ forward error correction, and therefore it is important to keep this value in mind. The AWGN limit curve corresponds to the ideal case when all other impairments are turned off, and a matched filter is used at the receiver to compensate the transmitter pulse shape.

Through the analysis of the results in Fig. 7.4, it is clear that the BP algorithm performance is far better than that of the linear equalization algorithm. As for the BP algorithm, in terms of PDM transmission, one can see that up to -2 dBm of launched power there is no observable difference to the single polarization case, whereas after this point the PDM result exhibits a penalty due to the nonlinear interaction between the two polarizations, as the nonlinear threshold is reached. Additionally, while for a single section the optimum operation power is 0 dBm, this point increases to +2 dBm for a higher number of sections, specifically 5, providing a Q factor improvement of approximately 1.5 dB at +2 dBm and 3 dB at +4 dBm, as noticed in Fig. 7.4. Simulations showed no significant additional benefit in further increasing the number of sections.

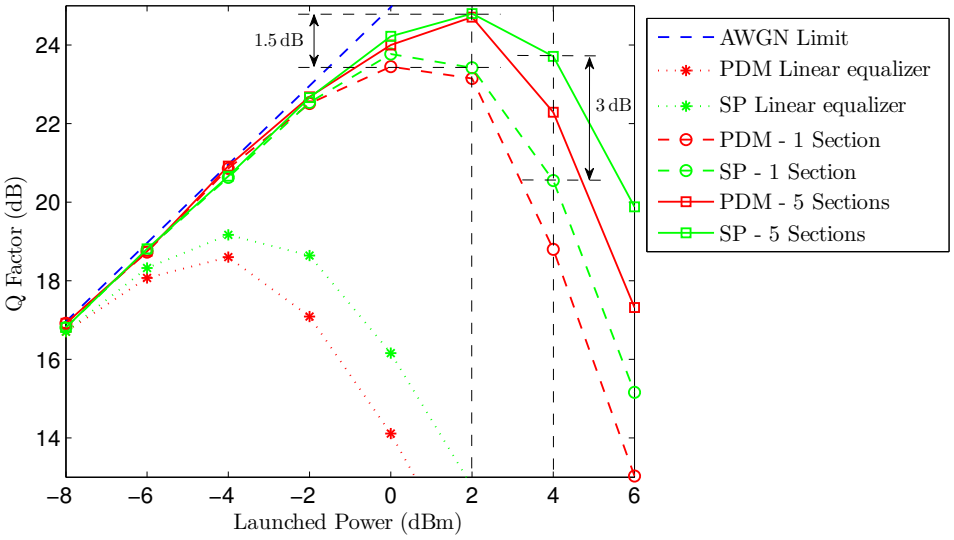

FIGURE 7.4: Q factor versus launched power. Single channel transmission comparing both BP and linear equalization algorithms. 100% RDPS.

The result of linear equalization (LE) is also shown for the cases of SP and PDM. It is clear that LE performs much worse when nonlinearity is present, for both SP and PDM formats. This means that not only SP, as in [16], but also PDM systems may benefit from the BP algorithm.

7.3.2 Impact of inline dispersion compensation

The performance impact of varying the residual dispersion per span through the simulation of varying lengths of inline DCF has also been assessed. Fig. 7.5 shows the impact of varying the number of sections used in the BP algorithm in a single channel SP transmission, at +4 dBm of launched power, this value being set slightly above the optimum operation point of +2 dBm in order to clearly observe the impact of nonlinearities. As expected, the Q factor decreases when the RDPS value is decreased. Furthermore, the penalty is higher near the 100% RDPS scenario, for a lower number of sections. If only one section was to be used (span length compensation), the performance would even benefit from a reduced value of RDPS, its maximum being approximately 65% RDPS. Additionally, a 3 dB improvement is obtained at 100% RDPS, when moving from 1 to 5 sections, as also seen in Fig. 7.4.

In Fig. 7.6 the BP performance for several RDPS scenarios was investigated, specifically, 0%, 5% and 100%, as a function of launched power. These results consider additionally the case of PDM with time-interleaving. The time-interleaving format was

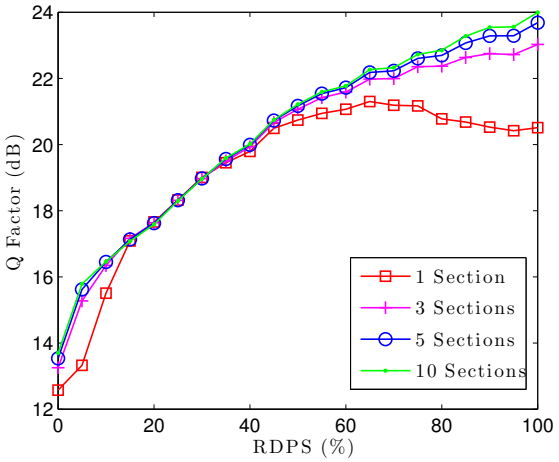

FIGURE 7.5: Q factor versus RDPS with varying number of sections in the BP algorithm, for single channel SP transmission.

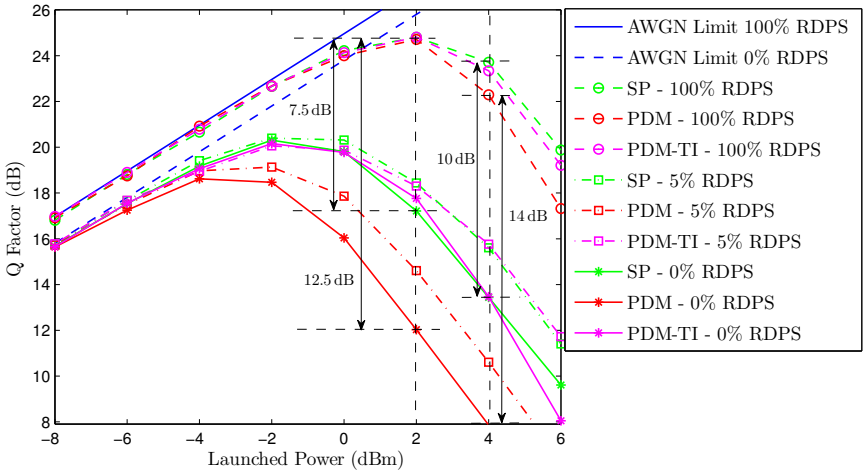

FIGURE 7.6: Q factor versus launched power. Single Channel Back-propagation, for 0%, 5% and 100% RDPS.

suggested in [95, 96], for RZ pulses in WDM transmission, because it helps reducing the nonlinear polarization scattering in dispersion-managed system, due to the state of polarization of the signal becoming data independent, causing alternating opposite nonlinear polarization rotations. The principle of the TI format consists in using RZ pulses in opposition of phase between polarizations, so that the signal intensity in one polarization does not lead to a phase rotation in the orthogonal polarization and vice-versa, as shown by the drawings of Fig. 7.7.

Due to the relevance of the TI format it was also implemented in the simulations. In

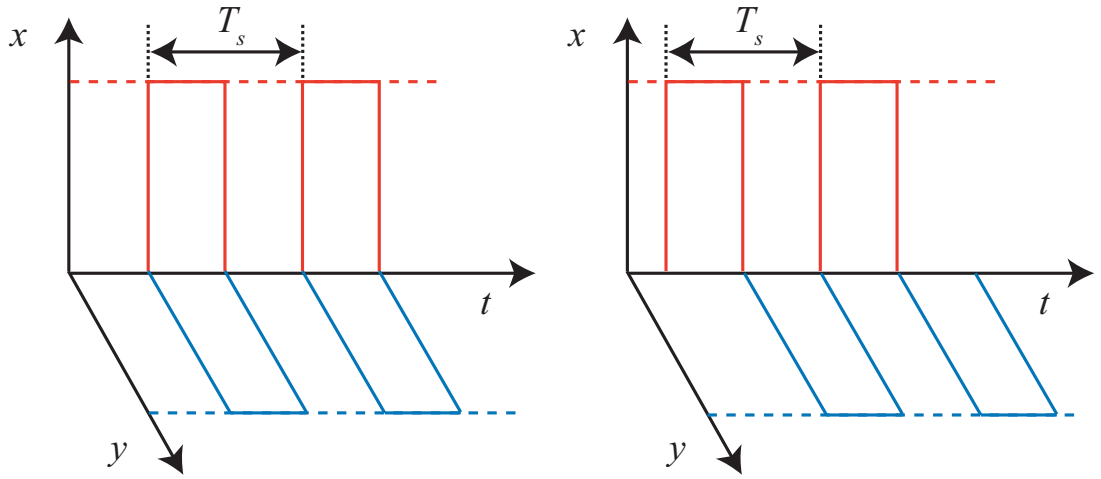

(a) Synchronized RZ-PDM-QPSK (b) Time-interleaved RZ-PDM-QPSK

FIGURE 7.7: Dashed lines represent the profile of NRZ pulses. RZ pulses transmitted in polarizations x and y, synchronized (a) and time-interleaved (b)

spite of this format having been proposed for WDM transmission, for the sake of completeness, it is also considered in the simulations for the single channel case and it will be shown that it still provides a significant improvement. As depicted in Figure 7.6, a rising penalty between the performance of SP and PDM is apparent with increasing SMF dispersion compensation (decreasing RDPS). At +2 dBm, this penalty is approximately 7.5 dB for SP and 12.5 dB for PDM, when comparing 0% RDPS with 100% RDPS, originating a 5 dB gap, which decreases to 4 dB at +4 dBm. Actually the TI format exhibits a similar performance as the SP format. Additionally, the TI format is slightly less effective in scenarios of unmanaged dispersion, because the pulses broaden rapidly in propagation due to dispersion, therefore loosing the synchronism between polarizations. As an extension of the results plotted in Figure 7.6, Figure 7.8 compares the Q factor performance of single channel, PDM and PDM-TI cases for a constant launched power of +4 dBm with varying RDPS. It is shown in all cases that the ideal level of RDPS is 100%, which means that no DCF is used and all the compensation is done digitally in the receiver, independently of the system being SP or PDM, the PDM-TI having a Q factor very close to the SP case. The same conclusion was found in [16] regarding the SP case, and [97] for the PDM case. Here, the PDM-TI format is evaluated for the first time using the BP algorithm and is shown to provide optimum performance for dispersion unmanaged transmission.

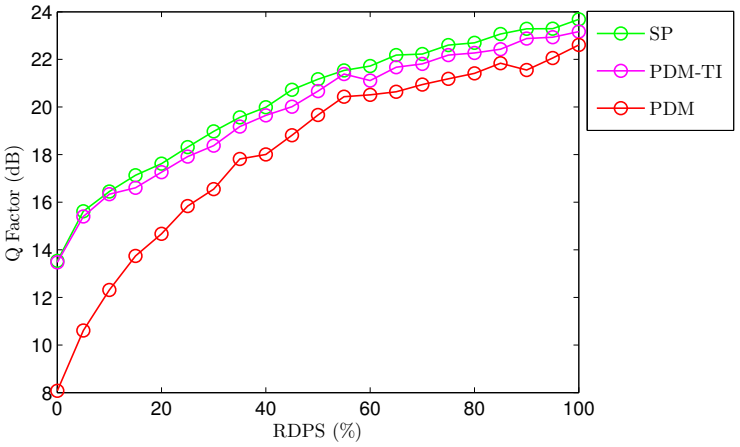

FIGURE 7.8: Q factor versus RDPS. Single Channel Back-propagation, having single polarization (green line), PDM (red line) and PDM-TI (pink line).

7.3.3 WDM transmission system

The analysis of digital back propagation for WDM transmission of three and five channels was carried out, where two channel spacing values were considered according to the ITU-T standards for WDM systems, specifically 25 GHz and 50 GHz, for the same long-haul optical channel as in previous sections. Figure 7.9 shows the results of varying the number of sections in the BP algorithm, for both SP and PDM-TI transmission, for one, three and five channel cases, using the coupled field algorithm in the multichannel cases. It is seen that the step size requirements are directly related to the number of channels. The minimum number of sections that allows for a penalty below 0.5 dB compared to using 80 sections is 5, 20 and 30 sections for one, three and five channels, respectively. These values are used as reference in the subsequent simulations. It is also observed that PDM-TI performance degrades significantly with an increasing number of channels.

An additional comparison regarding the number of sections has been performed, its results being presented in Fig. 7.10 where the Q factor is plotted as a function of the variable ζ for both three and five channels, where ζ is the nonlinear phase rotation parameter introduced in Chapter 5. Through the analysis of the presented results, it can be concluded not only that the optimum value of ζ is dependent on the selected number of sections, but also that its optimum value is lower when more channels are transmitted, which is due to the increased nonlinear interactions originating more compensation uncertainty.

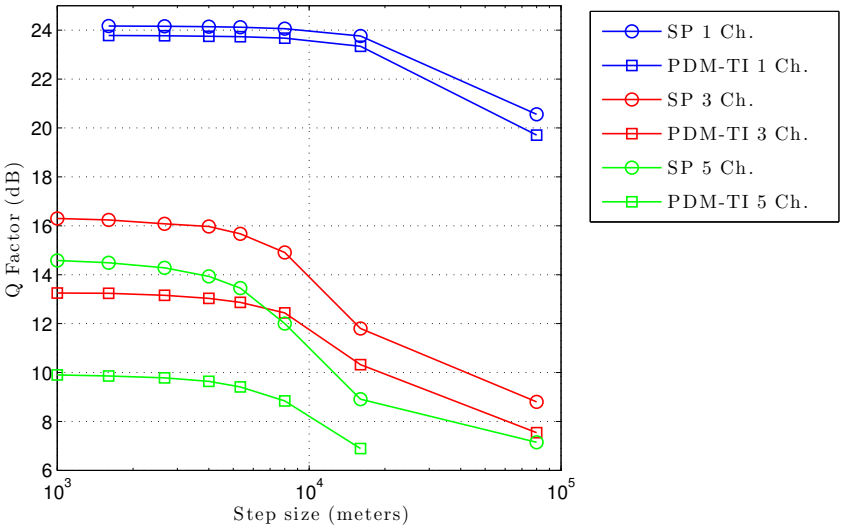

FIGURE 7.9: Q factor versus step size at 25 GHz channel spacing, for one (blue), three (red) and five WDM channels (green). SP is represented by circles while PDM-TI is represented by squares. Step sizes in the x axis of $\{1000, 1600, 2667, 4000, 5333, 8000, 16000$ and $80000\}$ meters which correspond to $\{80, 50, 30, 20, 15, 10, 5$ and $1\}$ sections, respectively.

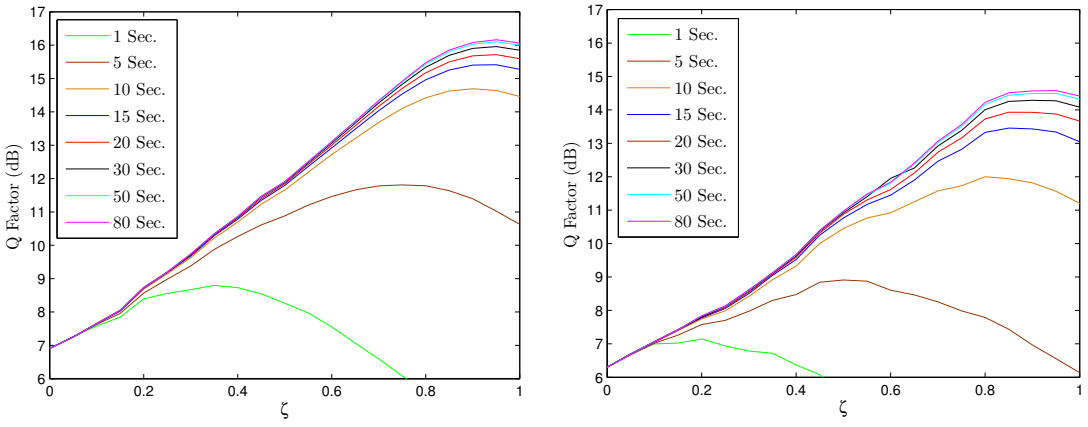

(a) 3 Channels (b) 5 Channels

FIGURE 7.10: Q factor as a function of variable ζ for (a) 3 WDM channels and (b) 5 WDM channels.

Figure 7.11 extends the previously shown comparison of Fig. 7.4 to WDM transmission of both three and five channels, spaced at 25 GHz, for 100 % RDPS, using the coupled field back-propagation.

Through the analysis of Fig. 7.11, one can observe that while the optimum launched power for the single channel SP case is +2 dBm, this is reduced to 0 dBm per channel, when considering both three or five channels. Moreover a reduction of the Q factor of approximately {6.5 dB, 7.5 dB} at +2 dBm and {8 dB, 9.6 dB} at +4 dBm is observed for

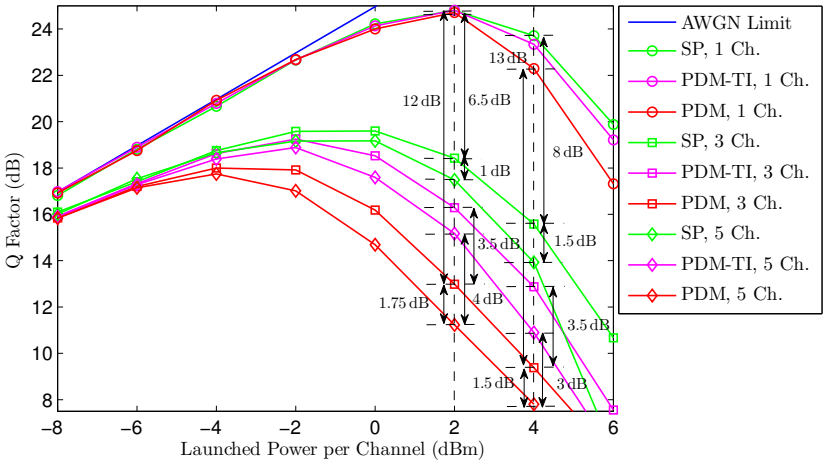

FIGURE 7.11: Q factor versus launched power at 100% RDPS and 25 Ghz channel spacing, for one (circles), three (squares) and five WDM channels (diamonds). Single polarization is represented by green lines, PDM by red lines and PDM-TI by pink lines.

three or five channels, respectively. For PDM transmission, the optimum launched power is reduced to -4 dBm per channel, where a penalty of approximately {12 dB,13.75 dB} at $+2$ dBm and {13 dB, 14.5 dB} at $+4$ dBm is obtained for three and five channels, respectively. Additionally, PDM-TI format is able to improve the performance for both three and five WDM channel cases. An improvement of approximately 3.5 dB, 4 dB} at $+2$ dBm and 3.5 dB, 3 dB} at $+4$ dBm is attained for three and five channels, respectively. A similar analysis was also conducted for three and five WDM channels spaced at 50 GHz. The results are shown in Figure 7.12.

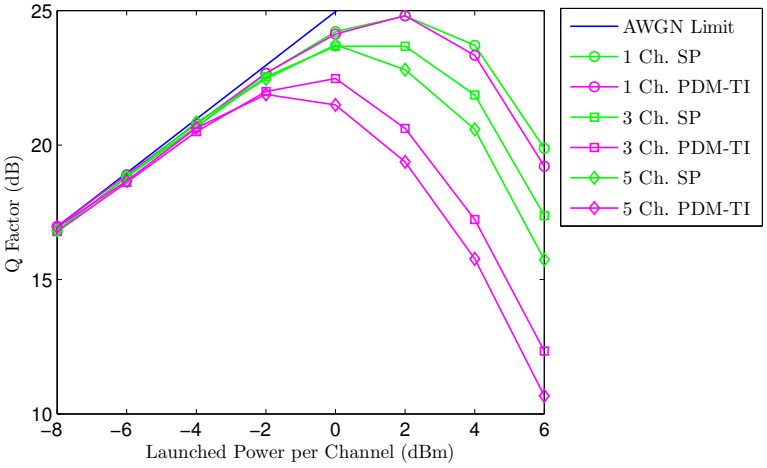

FIGURE 7.12: Q factor versus launched power at 100% RDPS and 50 Ghz channel spacing, for one (circles), three (squares) and five WDM channels (diamonds). Single polarization is represented by green lines and PDM-TI by pink lines.

Additionally, in order to allow for a proper comparison, Figure 7.13, superimposes both results of 25 GHz and 50 GHz spaced channels. The main conclusions are as follows: increasing the channel spacing to 50 GHz enables a large improvement in the SP performance for both three and five channel cases, of approximately {5.25 dB, 6.25 dB} at +2 dBm and +4 dBm, respectively, whereas the performance for PDM-TI only improved approximately 4.25 dB, essentially due to the distortion induced by the nonlinear polarization interaction.

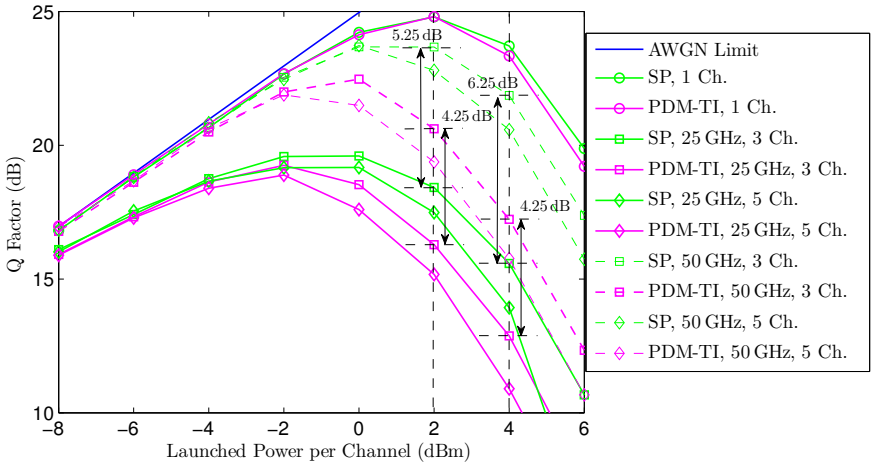

FIGURE 7.13: Q factor versus launched power at 100% RDPS for one (circles), 3 (squares) and 5 WDM channels (diamonds). Single polarization is represented by green lines and PDM-TI by pink lines. Dashed lines represent channels with 50Ghz spacing.

Figure 7.14 establishes a comparison between the scenarios of one, three and five channels, for the cases of SP, PDM and PDM-TI, showing the Q factor when the RDPS value is swept from 0% to 100%, at +4 dBm of launched power. When looking at SP transmission only, it is apparent that the Q factor as a function of RDPS varies differently in single channel compared to the multi-channel coupled field case. While in single channel the Q factor increases as the RDPS increases, for multichannel coupled field the Q factor increases from 0% to 50% RDPS, where an optimum point is achieved, decreasing between the 50% point up to 70% and increasing again up to 100% RDPS. The Q factor is approximately the same at 50% and 100% RDPS. A similar result was found by [95], for a linearly equalized receiver, where the usage of DCF is said to have positive impact in the system performance for WDM transmission. While for single channel transmission, the noise walk-off induced by increasing SMF dispersion has a positive impact due to the fact that the noise walking off from the signal decreases nonlinear

interactions, for a multi-channel signal when the noise walks off from the signal it starts interfering with adjacent channels which might even worsen the performance.

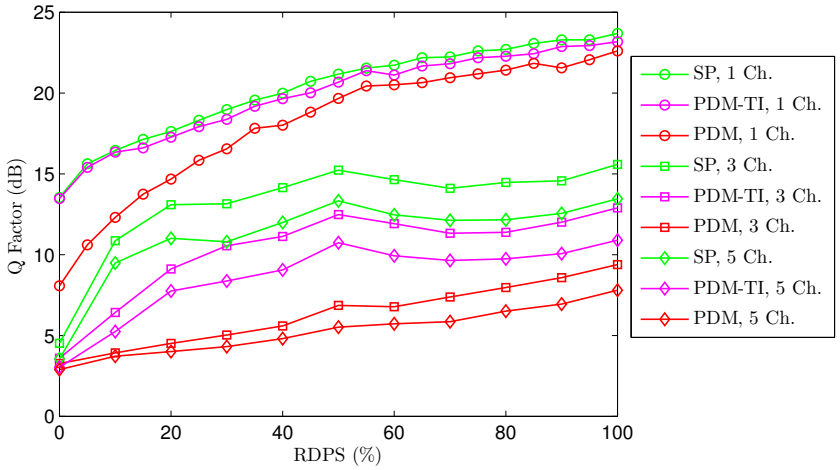

FIGURE 7.14: Q factor versus RDPS and 25 GHz channel spacing, for one (circles), three (squares) and five WDM channels (diamonds). Single polarization is represented by green lines, PDM-TI by pink lines and PDM by red lines.

For the polarization multiplexed transmission without time interleaving in Fig. 7.14, the discussed performance worsening above 50 % RDPS is barely noticeable, for both three and five channels. However, if time interleaving is used, this effect is well noticed, which indicates that when the nonlinear polarization interaction is reduced (through the usage of TI) the performance exhibits a behavior similar to the SP case. In [96] it is suggested that it is the interaction between polarizations that leads the dispersion managed system to perform worse than the system without DCF, for a linearly equalized WDM transmission. That is in agreement with the fact that the time-interleaved format leads to the inversion of that behavior, as shown in these results, since the nonlinear interaction between polarizations is significantly reduced.

In order to verify the separate impact of DCF dispersion and DCF nonlinearity on a multi-channel signal a simulation has been conducted where each of this effects has been considered independently. The simulation results are shown in Fig. 7.15. When DCF dispersion is turned off, the performance increases with increasing RDPS, due to an lower amount of DCF nonlinearity being present. On the other hand, when DCF nonlinearity is turned off, the performance improves as the RDPS increases up to 40 %, resulting from the reduction of the phase matching phenomenon near 0 % RDPS. Additionally, the performance starts worsening above the 40 % point towards 100 %, which is the result of the previously mentioned noise walk-off interacting with adjacent channels. Finally,

when both DCF nonlinearity and dispersion are combined, the resulting performance is bounded between the contribution from each of these effects.

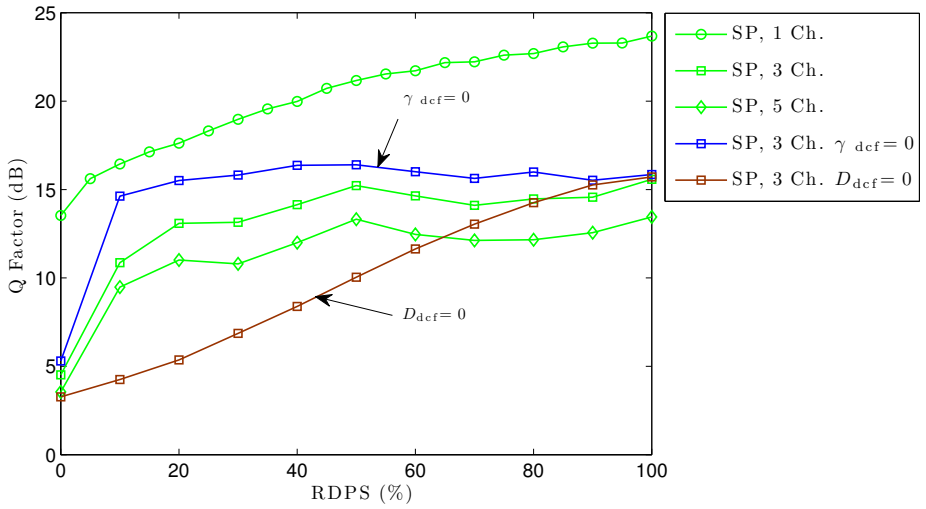

FIGURE 7.15: Q factor versus RDPS and 25 GHz channel spacing, for one (circles), three (squares) and five WDM channels (diamonds). Blue line corresponds to $D_{\mathrm{dcf}} = 0$ and brown line corresponds to $\gamma_{\mathrm{dcf}} = 0$, both for three WDM channels.

Figure 7.16 shows the results of the previous analysis considering three WDM channels spaced at both 25 GHz and 50 GHz. It is shown that the performance of three 50 GHz spaced WDM SP channels, induces a penalty of approximately 2 dB compared to the single channel SP case. Moreover the increase in performance is approximately linear with the increase in RDPS. Hence the walk-off issue for multi-channel transmission does not play a significant impact (compared with using 25 GHz spacing), which can be explained based on the higher channel spacing. However, the TI polarization multiplexed case does not follow the same tendency as the SP case, the penalty increasing with the RDPS, opposed to what is seen with 25 GHz spaced channels, where the PDM-TI case follows the tendency of the SP case. In fact, the PDM-TI case with 50 GHz spacing is still affected by the noise walk-off issue in spite of the high channel spacing, which in principle, is due to the increased nonlinear effects stemming from polarization interaction. Additionally, the performance in the PDM case is severely limited by the nonlinear polarization interaction, while over-performing its 25 GHz counterpart, as expected.

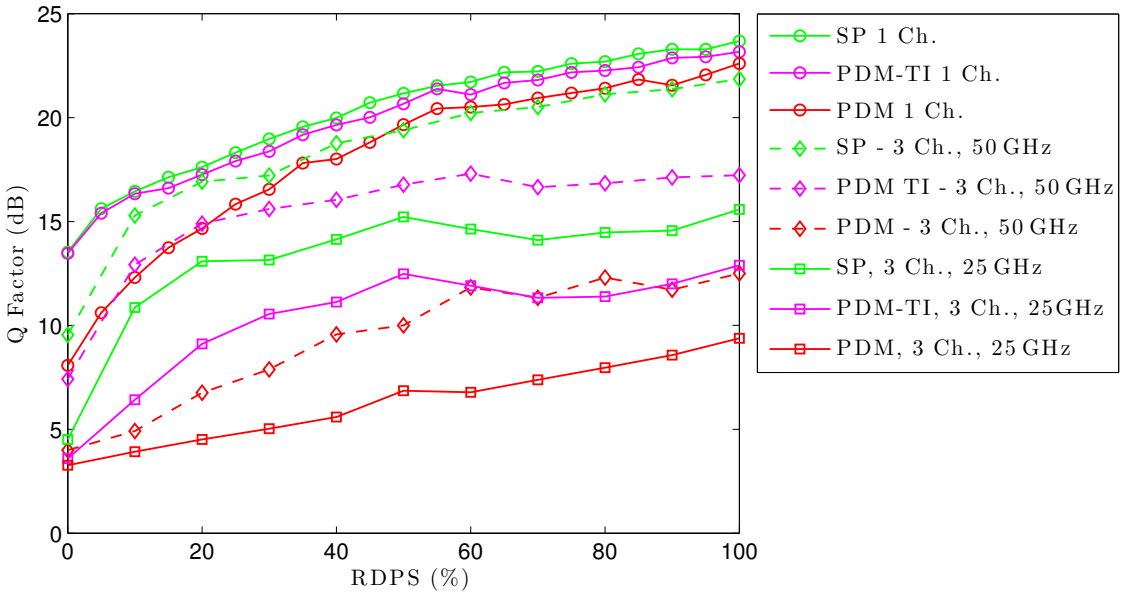

FIGURE 7.16: Q factor versus RDPS, for one and three WDM channels. Single channel results are represented in circles while channels with 25 GHz and 50 GHz spacing are represented by squares and diamonds, respectively.

7.3.4 Oversampling requirements

The analysis of the oversampling requirements for both coupled and total field algorithms for 3 WDM channels is discussed in this section for both 25 GHz and 50 GHz channel spacing. The analysis considers also the variation of the RDPS value in order to assess its impact on the performance. This is a very pertinent study which has never been reported before. The Q factor as a function of RDPS value, Fig. 7.17(a), and as a function of the oversampling rate, Fig. 7.17(b), was obtained for 25 Ghz spaced channels, for both the coupled field algorithm (with 'squares') and the total field (with 'circles') algorithms, considering single polarization transmission. The conclusions found here also apply to polarization multiplexed signals, as simulations have shown, but its results are omitted for simplicity. The coupled field approach provides best performance for low oversampling rates, while the total field approach eventually outperforms for higher oversampling rates. In fact, the coupled approach does not provide significant benefits above 6 samples per symbol, for 100% RDPS. For 20% RDPS the performance of the coupled field algorithm decreases for an oversampling rate above 4 samples per symbol, contrarily to the slight increase seen for 100 % RDPS. This is due to the excess bandwidth of the back-propagating signal due to the oversampling, which accumulates a phase matching interference from the other channels as it back-propagates from span to

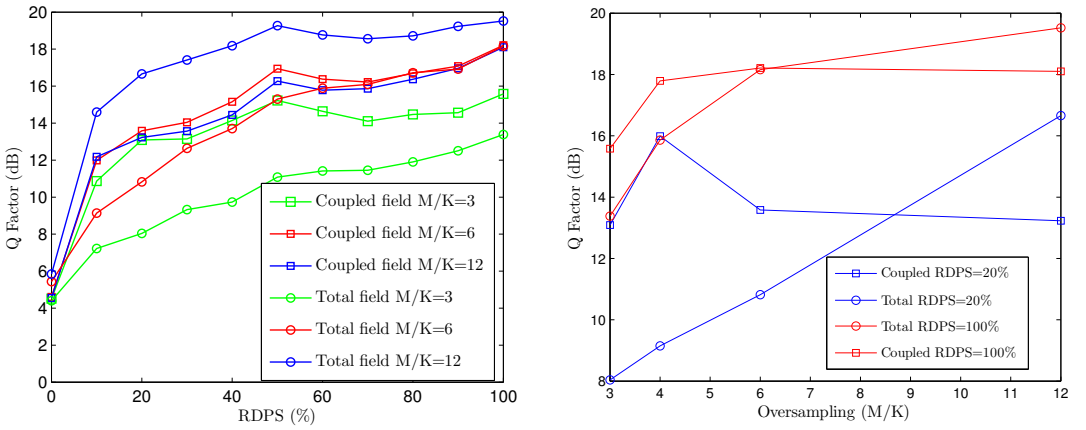

(a) RDPS sweep for $M/K = \{3, 6, 12\}$ (b) Oversampling rate sweep for RDPS $= \{20, 100\}\%$

FIGURE 7.17: Q factor as a function of RDPS (a) and oversampling rate (b) for 25 GHz spaced channels. Squares correspond to to coupled field algorithm and circles correspond to the total field algorithm.

span. However, the most relevant case in terms of practical implementation is the lower oversampling rate, and it is for $M/K = \{3, 4\}$ that the coupled field implementation provides the most significant gains compared to the total field approach.

The results of Fig. 7.18 evaluate the extension of the previous analysis to 50 GHz spaced channels. It can be concluded that, for 100% RDPS and reduced oversampling rate, the coupled field and total field algorithms have a similar performance. Since the lower the oversampling rate, the most practical, in terms of implementation, the system becomes, the coupled field algorithm is then preferable due to its lower latency. Additionally, for lower RDPS values (below 40%) the coupled field approach is always preferable, regardless of the oversampling rate. In this case the performance does not degrade with the higher oversampling rate due to the higher channel spacing mitigating this interference. Therefore, it can be concluded that for 50 GHz spaced channels, the coupled field approach is better performing at low RDPS values, while being similar (at reduced oversampling) or slightly worse (at higher oversampling) for 100% RDPS.

7.4 Summary

The equations of the back-propagation algorithm from Chapter 5 were extended to polarization multiplexed transmission, considering both single channel and WDM scenarios. The BP performance was compared for both SC and WDM polarization multiplexed transmission, while considering the impact of the system dispersion map and the step size requirements. Additionally, the analysis has also considered a time interleaved

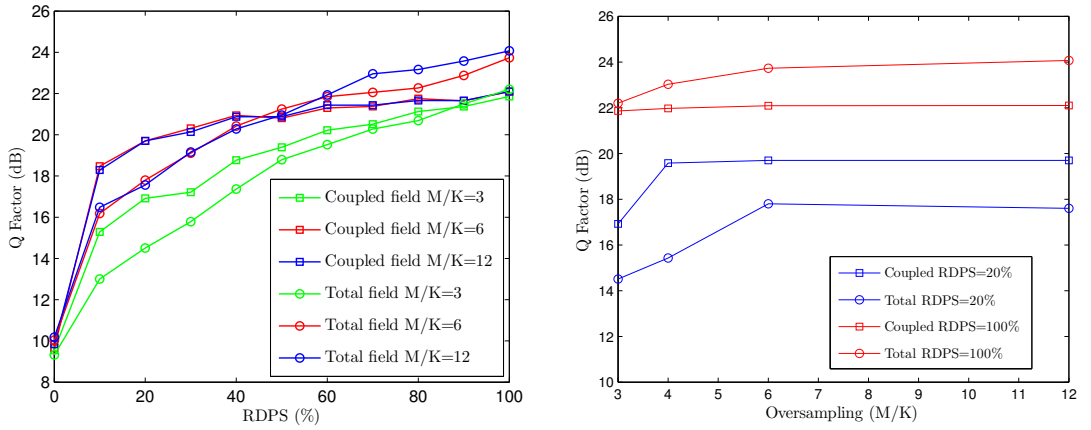

(a) RDPS sweep for $M/K = \{3, 6, 12\}$ (b) Oversampling rate sweep for RDPS $= (20, 100)\%$

FIGURE 7.18: Q factor as a function of RDPS (a) and oversampling rate (b) for 50 Ghz spaced channels. Squares correspond to to coupled field algorithm and circles correspond to the total field algorithm.

version of the polarization multiplexed signals, where a reduction of the nonlinear polarization interaction was observed. Furthermore, the analysis of two different channel spacings was conducted, as well as an evaluation of the RDPS value influence on system performance. The performed analysis allowed to determine that the noise walk-off induced by the RDPS increase leads to different results between single channel and WDM transmission cases, being positive for single channel, while for WDM it causes a performance reduction. Additionally, PDM transmission was found to be limited by nonlinear polarization interaction in the case of WDM, although the usage of time interleaving mitigates this interaction, whereas an higher channel spacing adds a contribution to that mitigation.

Chapter 8

Conclusions

This thesis has presented the main digital signal processing functions inherent to a coherent optical receiver enabling an optical transmission system. Special attention was directed to the equalization, carrier recovery and nonlinearity mitigation. The principles of a coherent optical transmission system were reviewed and different coherent optical receiver structures were analyzed. Linear fiber transmission impairments were successfully modeled in MATLAB, namely CD, PMD and phase noise. The LMS and CMA equalizer structures were investigated, and theoretical performance bounds were obtained for 4 and 16-QAM modulation formats. Additionally, differential encoding schemes were studied, which are suitable for high phase noise scenarios, providing immunity to catastrophic error propagation resulting from cycle slips. The decision directed and the non-data-aided soft decision phase estimators were analyzed, and an improvement of the phase unwrapping function associated with the NDA phase estimation algorithm was proposed which uses the Wiener filter to provide an estimate of the previous value.

The integration of equalization functions with carrier phase estimation algorithms was evaluated, and a new structure was proposed which uses an infinite impulse response implementation of the Wiener filter in a feedback configuration with a LMS equalizer, which provides optimum results and reduced computational complexity. Additionally, the issues associated with a parallel implementation of the discussed algorithms were investigated, in order to determine the restrictions and strategies that allow for an effective practical implementation. The DD and NDA phase estimators can be modified using a look-ahead computation to allow for parallelization. It was concluded that DD is not well suited for parallelization, due to internal phase estimator feedback, and the NDA approach might be parallelizable with no loss since it involves no feedback. The

LMS and CMA algorithms were combined with the mentioned phase estimators, and depending on the maximum speed of available DSP chips, the required parallelization level will dictate which approach should be chosen. If no parallelization is required the LMS-DD+DD should be chosen based on a good compromise between complexity and performance. If a parallelization level $L \leqslant 32$ is necessary, both LMS-DD+DD and LMS-DD+NDA approaches have similar complexities, the latter being preferable based on performance; but if the requirement is greater than 32, then CMA+NDA is the best option, because its performance does not depend on L.

The joint mitigation of both dispersion and nonlinear effects can be partially achieved through the back-propagation algorithm providing an improvement of performance. The symmetric and asymmetric implementation of the nonlinear propagation equation was investigated in detail. Additionally, the simulation model of a long-haul transmission system was successfully created, and theoretical results were presented on the optimized dispersion map characteristics for an amplified long-haul channel. Theoretical performance bounds were obtained for both single channel and OFDM modulation formats. Furthermore, the back-propagation algorithm was analyzed in detail, and optimum design rules were determined from simulation results, where the dispersion map, oversampling rate, launched power and computational complexity parameters were considered. It was concluded that the optimum value of the nonlinear phase de-rotation parameter, ζ, varies with the RDPS, indicating that the compensation uncertainty is higher for lower RDPS values, where the low values of dispersion lead to an higher impact of noise and phase matching issues. Moreover, the analysis of dispersion pre-compensation has shown an optimum value of dispersion between $P_c = 0$ and $P_c = -1$, relative to the dispersion of a single span of SMF. Concerning the analysis of computational complexity, it was found that the oversampling requirements increase with decreasing RDPS, which results from the noise impact on the simulation numerical error. The performance and computational complexity requirements of the symmetric and asymmetric implementation of the back-propagation algorithm was assessed, and optimum design options regarding the dispersion map characteristics were addressed. Having into account that the computational complexity of the symmetric algorithm is 3 times higher than its asymmetric counterpart, it was concluded that the asymmetric algorithm over-performs the symmetric algorithm for similar complexity levels, with the performance difference gradually vanishing as the RDPS decreases. Additionally, the influence of the amplifier gain splitting ratio g was assessed, its optimum value decreasing with increasing

launched power, for low RDPS values, due to the fact that the DCF nonlinearity becomes significant and therefore it is preferable to give higher amplification to the signal after the DCF rather than before, in order to avoid its nonlinearities. A comparison on the performance of the back-propagation algorithm between single channel and OFDM transmission formats was conducted, where it was concluded that OFDM has higher tolerance for dispersion unmanaged transmission, losing this advantage for dispersion managed systems, due to its high PAPR, which is problematic due to phase matching.

The back-propagation algorithm for OFDM multi-band transmission was implemented and a comparison between the coupled field and total field back-propagation was conducted, where computational complexity and dispersion management were considered variables. It was concluded that for reduced band spacings the performance of the total field approach is always better. Additionally, the coupled field approach overperforms the total field for signals having large band spacings (above $60 f_d$), provided 5 sections are used for the total field. This advantage decreases as the number of sections for the total field approach is increased. Compared to the coupled field approach, the compensation through the total field approach requires more computational complexity, while imposing higher latency times, which is not favorable to a real-time implementation of the algorithms. In fact, the it was concluded that the coupled field algorithm is an interesting option in terms of performance/computational complexity, if the system is allowed to have a relatively large band spacing and a reduced number of bands. In this context, the four wave mixing was considered within the coupled field method to improve its performance regarding multi-band nonlinearity compensation. A compensation method was proposed for multi-band OFDM signals, where a previously suggested equation is modified in order to reduce the numerical error, due to a small number of bands in consideration. The partial FWM compensation considering the interaction of 2 and 4 neighbor bands is shown to effectively provide a performance gain proportional to the number of sections used in the BP algorithm, compared to using the coupled field algorithm only. However, the advantage of using the partial FWM compensation is more effective for reduced band spacings/number of bands, gradually vanishing as the band spacing increases.

Finally, the equations of the back-propagation algorithm were extended to polarization multiplexed transmission, considering both single channel and WDM scenarios. The BP performance was compared for both SC and WDM polarization multiplexed transmission, while considering the impact of the system dispersion map. It was found

that not only SP but also PDM systems may benefit from the BP algorithm. The performed analysis allowed to determine that the noise walk-off induced by the RDPS increase leads to different results between single channel and WDM transmission cases, being positive for single channel, while for WDM it causes a performance reduction. Additionally, PDM transmission was found to be limited by nonlinear polarization interaction in the case of WDM, although the usage of time interleaving mitigates this interaction, whereas an higher channel spacing adds a contribution to that mitigation.

Future research directions include:

- While the analysis presented in this work compared the performance of different equalization algorithms in combination with different carrier phase estimation algorithms, considering a parallel implementation, it is pertinent to perform a further assessment on the performance of the different studied approaches while focusing on the adaptation of the equalizer coefficients in the presence of dynamic polarization effects of different magnitudes. Additionally, such analysis should also investigate the performance of the different algorithms measured as a function of the parallelization level, while also including a graphical result on the variation of the algorithm computational complexity.

- Further study of the implementation issues concerning the parallelization of the carrier phase estimation algorithm, considering the case of an optical transmission system with an uncompensated link, where the memory length of the fixed equalizer is expected to induce a non-negligible penalty.

- Investigate the performance of the back-propagation algorithm in the case of distributed Raman amplification, instead of discretely placed EDFAs, since the signal intensity profile is completely different and therefore nonlinearities will have a different impact.

- While the analysis presented in this work has systematically resorted to obtain the system Q factor performance as a function of different parameters while having a fixed long haul channel, it would be also extremely insightful to analyze the maximum achievable distance as a function of those same parameters but having a fixed target limit Q factor performance.

- Study of the optimum network scenarios that would take advantage of the coupled field BP compensation considering the interaction of up to 8 neighbor bands, in the context of OFDM multi-band transmission.

- The partial FWM compensation methods would also have the potential to improve the performance of the coupled field algorithm for polarization multiplexed WDM signals, which deserves special attention due to the recent increased interest in spectrally efficient modulation formats.

Bibliography

[1] E. Ip and J.M. Kahn. Feedforward carrier recovery for coherent optical communications. *Journal of Lightwave Technology*, 25(9):2675–2692, 2007.

[2] M. Seimetz. Performance of coherent optical square-16-QAM-systems based on IQ-transmitters and homodyne receivers with digital phase estimation. In *Proc. and the 2006 National Fiber Optic Engineers Conference Optical Fiber Communication Conference OFC 2006*, page 10pp., March 5–10, 2006.

[3] E. Ip, A.P.T. Lau, D.J.F. Barros, and J.M. Kahn. Coherent detection in optical fiber systems. *Opt. Express*, 16:753–791, 2008.

[4] S.L. Jansen, B. Spinnler, I. Morita, S. Randel, and H. Tanaka. 100GbE: QPSK versus OFDM. *Optical Fiber Technology*, 15(5-6):407–413, 2009.

[5] S.J. Savory. Digital filters for coherent optical receivers. *Optics Express*, 16(2): 804–817, 2008.

[6] D. E. Crivelli, H. S. Carter, and M. R. Hueda. Adaptive digital equalization in the presence of chromatic dispersion, PMD, and phase noise in coherent fiber optic systems. In *Proc. IEEE Global Telecommunications Conference GLOBECOM '04*, volume 4, pages 2545–2551, November 29–December 3, 2004. doi: 10.1109/GLOCOM.2004.1378465.

[7] D.-S. Ly-Gagnon, K. Katoh, and K. Kikuchi. Unrepeated 210-km transmission with coherent detection and digital signal processing of 20-Gb/s QPSK signal. In *Proc. Technical Digest Optical Fiber Communication Conference OFC/NFOEC*, volume 2, page 3pp., March 6–11, 2005.

[8] M. Seimetz. Multi-format transmitters for coherent optical M-PSK and M-QAM transmission. In *Proc. 7th Int Transparent Optical Networks Conf*, volume 2, pages 225–229, 2005. doi: 10.1109/ICTON.2005.1506139.

[9] S. J. Savory, G. Gavioli, V. Mikhailov, R. I. Killey, and P. Bayvel. Ultra Long-Haul QPSK Transmission using a Digital Coherent Receiver. In *Proc. Digest of the IEEE LEOS Summer Topical Meetings*, pages 13–14, July 23–25, 2007. doi: 10.1109/LEOSST.2007.4288307.

[10] D.N. Godard. Self-recovering equalization and carrier tracking in two-dimensional data communication systems. *IEEE transactions on communications*, 28(11):1867, 1980.

[11] J. R. Treichler, M. G. Larimore, and J. C. Harp. Practical blind demodulators for high-order QAM signals. *Proceedings of the IEEE*, 86(10):1907–1926, 1998. doi: 10.1109/5.720245.

[12] J. Yang, J.J. Werner, and G.A. Dumont. The multimodulus blind equalization algorithm. In *Proceedings of 13th International Conference on Digital Signal Processing '97.*, volume 1, pages 127 –130 vol.1, jul. 1997. doi: 10.1109/ICDSP.1997.627988.

[13] K. Banović, M.A.S. Khalid, and E. Abdel-Raheem. A configurable fractionally-spaced blind adaptive equalizer for QAM demodulators. *Digital Signal Processing*, 17(6):1071–1088, 2007.

[14] E.M. Ip and J.M. Kahn. Fiber Impairment Compensation Using Coherent Detection and Digital Signal Processing. *Journal of Lightwave Technology*, 28(4):502–519, 2010.

[15] X. Li, X. Chen, G. Goldfarb, E. Mateo, I. Kim, F. Yaman, and G. Li. Electronic post-compensation of WDM transmission impairments using coherent detection and digital signal processing. *Opt. Express*, 16:880–888, 2008.

[16] E. Ip and J. M. Kahn. Compensation of Dispersion and Nonlinear Impairments Using Digital Backpropagation. *Journal of Lightwave Technology*, 26:3416–3425, October 2008. doi: 10.1109/JLT.2008.927791.

[17] S. J. Savory. Digital Signal Processing Options in Long Haul Transmission. In *Proc. Conference on Optical Fiber communication/National Fiber Optic Engineers Conference OFC/NFOEC 2008*, pages 1–3, February 24–28, 2008. doi: 10.1109/OFC.2008.4528650.

[18] Mohammed Sabih Chaudhry. *Microwave IF Signal Processing Strategies For Coherent Optical Communications*. PhD thesis, University College of North Wales, 1993.

[19] T. OKOSHI. Coherent optical fiber communications. *Modern radio science*, page 59, 1988.

[20] BM Oliver. Signal-to-noise ratio in photoelectric mixing. *Proceedings of the IEEE*, 49, 1961.

[21] H.P. Yuen and V.W.S. Chan. Noise in homodyne and heterodyne detection. *Optics letters*, 8(3):177–179, 1983. ISSN 0146-9592.

[22] John G. Proakis. *Digital Communications*. McGraw-Hill, 4 edition, August 2001. ISBN 0072321113.

[23] TG Hodgkinson, RA Harmon, and DW Smith. Demodulation of optical DPSK using in-phase and quadrature detection. *Electronics Letters*, 21(19):867–868, 1985. ISSN 0013-5194.

[24] L. G. Kazovsky. Phase- and polarization-diversity coherent optical techniques. *Journal of Lightwave Technology*, 7(2):279–292, 1989. doi: 10.1109/50.17768.

[25] NG Walker and JE Carroll. Simultaneous phase and amplitude measurements on optical signals using a multiport junction. *Electronics Letters*, 20(23):981–983, 1984. ISSN 0013-5194.

[26] M. Seimetz and C.-M. Weinert. Options, feasibility, and availability of 2×4 90° hybrids for coherent optical systems. *Journal of Lightwave Technology*, 24(3):1317–1322, 2006. doi: 10.1109/JLT.2005.863251.

[27] M. Seimetz. *High-order modulation for optical fiber transmission*. Springer Verlag, 2009.

[28] K.P. Ho. *Phase-modulated optical communication systems*. Springer Verlag, 2005.

[29] E. Ip and J.M. Kahn. Power spectra of return-to-zero optical signals. *Lightwave Technology, Journal of*, 24(3):1610–1618, 2006. ISSN 0733-8724.

[30] K.P. Ho and J.M. Kahn. Spectrum of externally modulated optical signals. *Journal of Lightwave Technology*, 22(2):658, 2004.

[31] E. Ip and J. M. Kahn. Digital Equalization of Chromatic Dispersion and Polarization Mode Dispersion. *Journal of Lightwave Technology*, 25(8):2033–2043, 2007. doi: 10.1109/JLT.2007.900889.

[32] R.W. Chang. Synthesis of band-limited orthogonal signals for multichannel data transmission. *Bell Syst. Tech. J*, 45(10):1775–1796, 1966.

[33] R. Prasad. *OFDM for wireless communications systems*. Artech House Publishers, 2004.

[34] W. Shieh and I. Djordjevic. *OFDM for optical communications*. Academic Press, 2009.

[35] D.J.F. Barros and J.M. Kahn. Optimized dispersion compensation using orthogonal frequency-division multiplexing. *Journal of Lightwave Technology*, 26(16):2889, 2008.

[36] B. J. C. Schmidt, A. J. Lowery, and J. Armstrong. Experimental Demonstrations of Electronic Dispersion Compensation for Long-Haul Transmission Using Direct-Detection Optical OFDM. *Journal of Lightwave Technology*, 26(1):196–203, 2008. doi: 10.1109/JLT.2007.913017.

[37] Wei-Ren Peng, Xiaoxia Wu, V. R. Arbab, B. Shamee, Jeng-Yuan Yang, L. C. Christen, Kai-Ming Feng, A. E. Willner, and Sien Chi. Experimental Demonstration of 340 km SSMF Transmission Using a Virtual Single Sideband OFDM Signal that Employs Carrier Suppressed and Iterative Detection Techniques. In *Proc. Conf. Optical Fiber communication/National Fiber Optic Engineers Conf. OFC/NFOEC 2008*, pages 1–3, 2008. doi: 10.1109/OFC.2008.4528409.

[38] W.-R. Peng, B. Zhang, K.-M. Feng, X. Wu, A. E. Willner, and S. Chi. Spectrally Efficient Direct-Detected OFDM Transmission Incorporating a Tunable Frequency Gap and an Iterative Detection Techniques. *Journal of Lightwave Technology*, 27 (24):5723–5735, 2009. doi: 10.1109/JLT.2009.2033304.

[39] W. Shieh, Q. Yang, and Y. Ma. 107 Gb/s coherent optical OFDM transmission over 1000-km SSMF fiber using orthogonal band multiplexing. *Opt. Express*, 16(9): 6378–6386, 2008.

[40] N. Kaneda, Qi Yang, Xiang Liu, S. Chandrasekhar, W. Shieh, and Young-Kai Chen. Real-Time 2.5 GS/s Coherent Optical Receiver for 53.3-Gb/s Sub-Banded OFDM. *Journal of Lightwave Technology*, 28(4):494–501, 2010. doi: 10.1109/JLT.2009.2031126.

[41] B. Schmidt, A. J. Lowery, and L. B. Du. Low sample rate transmitter for direct-detection optical OFDM. In *Proc. Conf. Optical Fiber Communication - incudes post deadline papers OFC 2009*, pages 1–3, 2009.

[42] B.J.C. Schmidt, Z. Zan, L.B. Du, and A.J. Lowery. 100 Gbit/s transmission using single-band direct-detection optical OFDM. In *Optical Fibre Communication/-National Fibre Optic Engineers Conference (OFC/NFOEC),(OSA, 2009), Paper PDPC3*, 2009.

[43] J. M. Tang, P. M. Lane, and K. A. Shore. High-speed transmission of adaptively modulated optical OFDM signals over multimode fibers using directly Modulated DFBs. *Journal of Lightwave Technology*, 24(1):429–441, 2006. doi: 10.1109/JLT.2005.860146.

[44] Tektronics. *Tektronics DPO72004*, 2007. URL `http://www2.tek.com/cmswpt/psdetails.lotr?ct=PS&ci=13305&cs=psu&lc=EN`.

[45] Microelectronics Gmbh Germany MICRAM. *VEGA Signal Convertors*, 2009. URL `http://www.micram.com/index.php/products/vega`.

[46] H. Sun, K.T. Wu, and K. Roberts. Real-time measurements of a 40 Gb/s coherent system. *Opt. Express*, 16:873–879, 2008.

[47] R. Waegemans, S. Herbst, L. Holbein, P. Watts, P. Bayvel, C. Furst, and R.I. Killey. 10.7 Gb/s electronic predistortion transmitter using commercial FPGAs and D/A converters implementing real-time DSP for chromatic dispersion and SPM compensation. *Optics Express*, 17(10):8630–8640, 2009.

[48] P. Watts, M. Glick, R. Waegemans, Y. Benlachtar, V. Mikhailov, S. Savory, P. Bayvel, and R. I. Killey. Experimental demonstration of real-time DSP with FPGA-based optical transmitter. In *Proc. 10th Anniversary Int. Conf. Transparent Optical Networks ICTON 2008*, volume 1, pages 202–205, 2008. doi: 10.1109/ICTON.2008.4598407.

[49] R. P. Giddings, X. Q. Jin, H. H. Kee, X. L. Yang, and J. M. Tang. First experimental demonstration of real-time optical OFDM transceivers. In *Proc. 35th European Conf. Optical Communication ECOC '09*, pages 1–2, 2009.

[50] J. M. Cioffi. *EE 379A Digital Communication: Signal Processing*. Stanford University, 2007. URL `http://www.stanford.edu/class/ee379a/`. Course Reader.

[51] L. M. Pessoa, H. M. Salgado, and I. Darwazeh. Adaptive Electrical Equalization of Optical Impairments in Coherent Optical Systems. In *Proc. Digest of the Symposium on Enabling Optical Networks and Sensors*, June 28, 2007.

[52] M. G. Taylor. Coherent detection method using DSP for demodulation of signal and subsequent equalization of propagation impairments. *IEEE Photonics Technology Letters*, 16(2):674–676, 2004. doi: 10.1109/LPT.2003.823106.

[53] L. M. Pessoa, H. M. Salgado, and I. Darwazeh. Algorithms for DSP implementation in coherent optical systems. In *Proc. CMC 2008 - Cranfield Multi-Strand Conference: Creating Wealth Through Research and Innovation*, May 5–6 2008.

[54] G. Agrawal. *Nonlinear Fiber Optics*. Academic Press, 3 edition, January 2001. ISBN 0120451433.

[55] C. Francia, F. Bruyere, D. Penninckx, and M. Chbat. PMD second-order effects on pulse propagation in single-mode optical fibers. *Photonics Technology Letters, IEEE*, 10(12):1739–1741, 1998.

[56] G. Keiser. *Optical fiber communications*. McGraw-Hill Science/Engineering/Math, 2000. ISBN 0072360763.

[57] A. O. Dal Forno, A. Paradisi, R. Passy, and J. P. von der Weid. Experimental and theoretical modeling of polarization-mode dispersion in single-mode fibers. *IEEE Photonics Technology Letters*, 12(3):296–298, 2000. doi: 10.1109/68.826919.

[58] D. Marcuse, C. R. Manyuk, and P. K. A. Wai. Application of the Manakov-PMD equation to studies of signal propagation in optical fibers with randomly varying birefringence. *Journal of Lightwave Technology*, 15(9):1735–1746, 1997. doi: 10.1109/50.622902.

[59] C. Henry. Theory of the phase noise and power spectrum of a single mode injection laser. *Quantum Electronics, IEEE Journal of*, 19(9):1391–1397, 1983.

[60] N. Wiener. *Extrapolation, interpolation, and smoothing of stationary time series*. MIT Press, 1964.

[61] W. Shieh and K.P. Ho. Equalization-enhanced phase noise for coherent-detection systems using electronic digital signal processing. *Optics Express*, 16(20):15718–15727, 2008.

[62] J.R. Treichler, M.G. Larimore, JC Harp, A.S.T. Inc, and CA Sunnyvale. Practical blind demodulators for high-order QAM signals. *Proceedings of the IEEE*, 86(10): 1907–1926, 1998.

[63] L. M. Pessoa, H. M. Salgado, and I. Darwazeh. Joint mitigation of optical impairments and phase estimation in coherent optical systems. In *Proc. Digest of the IEEE/LEOS Summer Topical Meetings*, pages 169–170, July 21–23, 2008. doi: 10.1109/LEOSST.2008.4590543.

[64] L. M. Pessoa, H. M. Salgado, and I. Darwazeh. Assessment of parallel equalizer/phase estimation algorithms in coherent optical systems. In *Proc. IEEE/LEOS Summer Topical Meeting LEOSST '09*, pages 79–80, July 20–22, 2009. doi: 10.1109/LEOSST.2009.5226259.

[65] L. M. Pessoa, H. M. Salgado, and I. Darwazeh. Performance Evaluation of Phase Estimation Algorithms in Equalized Coherent Optical Systems. *IEEE Photonics Technology Letters*, 21(17):1181–1183, 2009. doi: 10.1109/LPT.2009.2024003.

[66] M. Seimetz. Laser Linewidth Limitations for Optical Systems with High-Order Modulation Employing Feed Forward Digital Carrier Phase Estimation. In *Proc. Conference on Optical Fiber communication/National Fiber Optic Engineers Conference OFC/NFOEC 2008*, pages 1–3, February 24–28, 2008. doi: 10.1109/OFC.2008.4528637.

[67] E. Ip and J.M. Kahn. Addendum to Feedforward Carrier Recovery for Coherent Optical Communications. *Journal of lightwave technology*, 27(13):2553, 2009.

[68] H. Meyr, M. Moeneclaey, and S.A. Fechtel. *Digital communication receivers*. Wiley Online Library, 1998. ISBN 0471502758.

[69] L.L. Scharf. *Statistical signal processing*. Addison-Wesley Reading, MA, 1991.

[70] Liang Zhao and Won Namgoong. A novel phase-noise compensation scheme for communication receivers. *IEEE Transactions on Communications*, 54(3):532–542, 2006. doi: 10.1109/TCOMM.2006.869788.

[71] N. M. Pinto, L. M. Pessoa, and H. M. Salgado. FPGA Implementation of Signal Processing Algorithms in Coherent Optical Systems. In *Proc. Digest of the Symposium on Enabling Optical Networks and Sensors*, 2009.

[72] M. G. Taylor. Accurate digital phase estimation process for coherent detection using a parallel digital processor. In *Proc. 31st European Conference on Optical Communication ECOC 2005*, volume 2, pages 263–264, September 25–29, 2005.

[73] RJ Essiambre, G. Raybon, and B. Mikkelsen. Pseudo-linear transmission of high-speed signals: 40 and 160 Gbit/s. *Optical Fiber Telecommunications IV-B*, 2002.

[74] E. Ip and J.M. Kahn. *Nonlinear impairment compensation using backpropagation.* In-Tech, Vienna Austria, December 2009.

[75] E. Mateo, L. Zhu, and G. Li. Impact of XPM and FWM on the digital implementation of impairment compensation for WDM transmission using backward propagation. *Optics Express*, 16(20):16124–16137, 2008.

[76] A. Hasegawa and F. Tappert. Transmission of Stationary Nonlinear Optical Physics in Dispersive Dielectric Fibers I: Anomalous Dispersion. *Appl. Phys. Lett.*, 23(3): 142–144, 1973.

[77] GH Weiss and AA Maradudin. The Baker-Hausdorff Formula and a Problem in Crystal Physics. *Journal of Mathematical Physics*, 3:771, 1962.

[78] Q.Z.M.I. Hayee. Symmetrized split-step Fourier scheme to control global simulation accuracy in fiber-optic communication systems. *J. Lightwave Technol*, 26:302–316, 2008.

[79] E. Ip. Nonlinear Compensation Using Backpropagation for Polarization-Multiplexed Transmission. *Lightwave Technology, Journal of*, 28(6):939–951, 2010.

[80] HA Haus. The noise figure of optical amplifiers. *IEEE Photonics Technology Letters*, 10(11):1602–1604, 1998.

[81] A.J. Lowery, L.B. Du, and J. Armstrong. Performance of optical OFDM in ultralong-haul WDM lightwave systems. *Lightwave Technology, Journal of*, 25(1): 131–138, 2007.

[82] K.P. Ho. Probability density of nonlinear phase noise. *JOSA B*, 20(9):1875–1879, 2003.

[83] K. Roberts, C. Li, L. Strawczynski, M. O'Sullivan, and I. Hardcastle. Electronic precompensation of optical nonlinearity. *IEEE Photonics Technology Letters*, 18 (2):403–405, 2006.

[84] R.J. Essiambre, P.J. Winzer, X.Q. Wang, W. Lee, C.A. White, and E.C. Burrows. Electronic predistortion and fiber nonlinearity. *IEEE Photonics Technology Letters*, 18(17):1804–1806, 2006.

[85] G. Goldfarb and G. Li. Efficient backward-propagation using waveletbased filtering for fiber backward-propagation. *Optics Express*, 17(11):8815–8821, 2009.

[86] K. Forozesh, S.L. Jansen, S. Randel, I. Morita, and H. Tanaka. The influence of the dispersion map in coherent optical OFDM transmission systems. In *Proc. Digest of the IEEE/LEOS Summer Topical Meetings*, pages 135–136, July 21–23, 2008.

[87] J. M. B. Oliveira, L. M. Pessoa, H. M. Salgado, and I. Darwazeh. Signal processing techniques for transmission impairments compensation in optical systems. In *Proc. 12th International Conference on Transparent Optical Networks (ICTON) 2010*, pages 1 –4, jun. 2010. doi: 10.1109/ICTON.2010.5549064.

[88] F. Buchali, R. Dischler, X. Liu, A. Arkarachinores, and O. Strobel. Nonlinear limits for high bit-rate O-OFDM systems. In *Summer Topical Meeting, 2009. LEOSST'09. IEEE/LEOS*, pages 83–84. IEEE, 2009.

[89] A. Chowdhury and R.J. Essiambre. Optical phase conjugation and pseudolinear transmission. *Optics letters*, 29(10):1105–1107, 2004.

[90] A.J. Lowery. Fiber nonlinearity pre-and post-compensation for long-haul optical links using OFDM. *Opt. Express*, 15:12965–12970, 2007.

[91] E.F. Mateo and G. Li. Compensation of interchannel nonlinearities using enhanced coupled equations for digital backward propagation. *Applied optics*, 48(25):F6–F10, 2009.

[92] A. Carena, V. Curri, R. Gaudino, P. Poggiolini, and S. Benedetto. A time-domain optical transmission system simulation package accounting for nonlinear and polarization-related effects in fiber. *IEEE Journal on Selected Areas in Communications*, 15(4):751–765, 1997. doi: 10.1109/49.585785.

[93] F. Yaman and G. Li. Nonlinear impairment compensation for polarization-division multiplexed WDM transmission using digital backward propagation. *IEEE Photonics Journal*, 1(2):144–152, 2009.

[94] L. M. Pessoa, H. M. Salgado, and I. Darwazeh. Simplified backpropagation equalization in WDM coherent polarization multiplexed systems. In *Proc. 11th International Conference on Transparent Optical NetworksICTON '09*, pages 1–5, June 2009. doi: 10.1109/ICTON.2009.5185082.

[95] C. Xie. WDM coherent PDM-QPSK systems with and without inline optical dispersion compensation. *Optics express*, 17(6):4815, 2009.

[96] C. Xie. Interchannel Nonlinearities in Coherent Polarization-Division-Multiplexed Quadrature-Phase-Shift-Keying Systems. *IEEE Photonics Technology Letters*, 21 (5):274–276, 2009.

[97] V. Curri, P. Poggiolini, A. Carena, and F. Forghieri. Dispersion Compensation and Mitigation of Nonlinear Effects in 111-Gb/s WDM Coherent PM-QPSK Systems. *IEEE Photonics Technology Letters*, 20(17):1473–1475, 2008.